Cascaded Wavelength Conversion Processes in Lithium Niobate Waveguide Structures

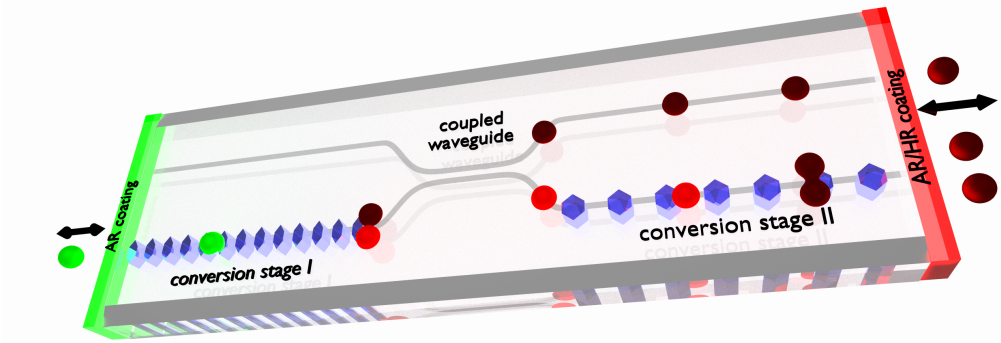

Der Naturwissenschaftlichen Fakultät
der Universität Paderborn
zur Erlangung des Doktorgrades
Dr. rer. nat.
vorgelegte Dissertation

von
Stephan Krapick
aus Gehofen

For my family.

Contents

CHAPTER 1

Summary

Integrated quantum optics is a young field of research, and its impact on real-world quantum applications is growing rapidly. Efficient, compact, scalable and long-term-stable sources for quantum-optical states play an important role within that framework. The functionality of the sources is intended to guarantee the quality and quantity of the generated states, while high integration densities are desired. Mature technologies and the development of novel measurement methods and apparatus build the basis.

In this dissertation we describe the fabrication and thorough characterization of a nonlinear optical photon source. Its compact design, based on titanium-diffused, periodically poled waveguide structures in lithium niobate allows for the energy-efficient and long-term-stable operation. Several passive and active optical components on a single chip provide us with the generation of photon pairs with high brightness, and we are able to herald single photons with high efficiencies. We show that the functionalities of our photon-pair source suffices the prerequisites of applicable passive-decoy-state quantum cryptography, by which the photon-number-splitting attack of an eavesdropper can be detected and averted.

The main focus lies on cascaded nonlinear frequency conversion processes in periodically poled waveguide structures on the very same device. We show that cascaded sum-frequency generation from the telecom wavelength range to the visible is possible, and that we realized a tunable green laser source in this way. Using cascaded parametric down-conversion we generate almost noise-less three-photon quantum states on a single chip for the first time. Up to now, this was only possible using hybrid systems not benefiting from the prospects of integrated quantum optics in terms of compactness, interface-loss reduction, scalability, and long-term stability. In the outlook we propose an integrated four-photon source as one logic extension.

Zusammenfassung

Die integrierte Quantenoptik ist ein junges Forschungsfeld, dessen Bedeutung für Anwendungen im täglichen Leben stetig zunimmt. Effiziente, kompakte, skalierbare und langzeitstabile Quellen quantenoptischer Zustände spielen dabei eine tragende Rolle. Die Funktionalität der Quellen soll bei hohen Intgrationsdichten auf einem einzigen Chip die Qualität und Quantität der erzeugten Zustände garantieren. Eine ausgereifte Technologie sowie die Entwicklung moderner Messmethoden und -instrumente stellen dafür die Basis dar.

In dieser Dissertation beschäftigen wir uns mit der Herstellung und der Charakterisierung einer nichtlinear-optischen Photonenquelle. Ihr kompaktes Design auf Basis Titan-diffundierter, periodisch gepolter Wellenleiterstrukturen in Lithiumniobat erlaubt einen energieeffizienten und langzeitstabilen Betrieb. Mehrere passive und aktive optische Komponenten auf einem einzigen Chip ermöglichen es, Photonenpaare mit hoher Ausbeute zu erzeugen und einzelne Photonen mit hoher Effizienz anzukündigen. Es wird gezeigt, dass die Funktionalität unserer Photonenpaarquelle den Anforderungen der Quantenkryptographie genügt, um photonenzahlbedingte Angriffe eines Störers zu erkennen und mittels passiver Köderzustände zu umgehen.

Das Hauptaugenmerk dieser Arbeit liegt auf der Kaskadierung zweier nichtlinearer Frequenzkonversionsprozesse durch gepolte Wellenleiterstrukturen auf dem selben Bauelement. Es wird gezeigt, dass die kaskadierte Summenfrequenzerzeugung von klassischem Licht bei Telekommunikationswellenlängen hin zu sichtbarem Licht möglich ist, und dass damit eine abstimmbare grüne Laserquelle realisiert werden kann. Zudem wird die kaskadierte parametrische Fluoreszenz verwendet, um besonders rauscharme quantenoptische Drei-Photonen-Zustände erstmalig auf einem einzigen Chip zu erzeugen. Dies war bisher nur in hybriden Systemen möglich, die von den Vorteilen der Integrierten Quantenoptik im Hinblick auf Kompaktheit, Kompatibilität, Skalierbarkeit und Langzeitstabilität nicht profitieren. Wir geben einen Ausblick auf eine Vier-Photonen-Quelle als logische Erweiterung dieser Arbeit.

CHAPTER 2

Introduction

Contents

We introduce the kind reader to the interesting research field of quantum optics, which has been developed only about 120 years ago. By giving a brief overview on the conceptual and experimental milestones of the earlier days, we guide to the most important research results in quantum optics of the last thirty years relevant for this thesis. We also point out why integrated quantum optics is one of the most promising sub-fields of quantum physics and why it is -in our opinion - closest to the real-world-applicability of the fundamental achievements in quantum optics. Additionally, the outline and structure of this thesis is given.

2.1. A State-of-the-Art-View on nonlinear quantum optics

In 1900 Max Planck shook up the world of physics by introducing h, which we nowadays know as the constant named after him, as a universal constant of nature in his work on the energy distribution law in the normal spectrum (*Ueber das Gesetz der Energieverteilung im Normalspektrum*) [1]. This ground-breaking conceptual trick lead to the solution of the discrepancy between Wien's radiation law [2] and the radiation law of Rayleigh and Jeans [3, 4]. The idea of Planck was that a black body absorbs and emits radiation energy only in quantized portions. Albert Einstein exploited Planck's concept for his explanation of the photoelectric effect (re-)defining the absorbed quantized energy as the product of h and the radiation frequency.

In the following years the physical society seemingly split into two enemy camps, which fought against each other by means of scientific battles, whether or not this novel theory is right or wrong. Many famous researchers have contributed to the manifestation of quantum physics as a complement to what physics had been those days. The work of Max Born and Niels Bohr, as well as Paul Dirac's and Louis de Broglie's activities, continuously improved the standing of quantum mechanics within the community.

The wave-particle dualism had been key to the contradictory opinions in the 1920's, when Werner Heisenberg and Erwin Schrödinger pursued different paths to describe quantum states by matrix mechanics [5] on the one hand and wave mechanics on the other hand [6]. Likewise, the question whether or not the introduced wave-function has a physical meaning arose. In 1927 Max Born proposed the solution to this issue by calling the wave-function as yield function (*Ausbeutefuntion*) [7], which is thought to be the cornerstone of the Copenhagen interpretation of quantum mechanics given by Schrödinger in 1935 [8]: the wave-function is an equivalent of the probabilities of quantum phenomena, which means that quantum physics is inherently probabilistic.

Although the Copenhagen interpretation had become more and more of a common sense in the physics community, Einstein, Podolsky and Rosen raised the question: *Can quantum-mechanical description of physical reality be considered complete?* in 1935 [9]. Their philosophical concern raised the famous paradox named after them (EPR-paradox), which had been unsolved for decades. The paradox includes what makes quantum physics to some extend hard to understand: entanglement or the *spooky long-range interaction* is the non-classical resource to overcome the necessity to violate Heisenberg's uncertainty relation [10], which Einstein and his co-workers claimed for determinism of quantum theory. John Bell proposed the solution to the EPR-paradox by introducing inequalities [11], the experimental violation of which can prove that the concept of quantum mechanics is a non-local, not a classical, but a complete theory.

Meanwhile, the stimulated emission of microwave and visible radiation had been discovered by Townes' group and Maiman in 1955 and 1960 [12,13], respectively. The theoretical description of these coherent light sources in the framework of quantum optics was contributed by Glauber in 1963 [14], who also clarified how to determine whether light is classical or quantum. Both developments, the MASER and the LASER, were key to a cascade of new developments in the following years, but here we will concentrate more on the optical version of these most classical light sources.

During the 60's and 70's of the last century, the development and application of more powerful and also pulsed laser systems have lead to very important discoveries on the nonlinear optical response of dielectric media. Armstrong and co-workers [15] as well as Franken and Ward [16] have found that specific materials allow for the frequency conversion of light with light, which can be called the cradle of nonlinear optics. Besides the remarkable developments on telecommunication and laser physics, the concept of nonlinear optics also paved the way for Burnham's and Weinberg's demonstration on the first generation of photon pairs in nonlinear crystals by

parametric down-conversion in 1970 [17]. Shortly after, Freedman's and Clauser's experiment showed the violation of Bell's inequality for the first time and, thus, the lack of hidden variables in quantum theory [18, 19]. Besides, nonlinear optics had discovered the usefulness of optical waveguides for increasing of the nonlinear conversion efficiencies and to integrate multiple functionalities on optical chips [20–25].

Further improvements to all kinds of measurement apparatus allowed Aspect and co-workers in 1981 to violate the Bell inequalities with very small statistical errors, after Kimble has demonstrated the anti-bunching of single photons in 1977 to [26]. It soon became clearer that specific processes can provide single quanta of light, which could be tested for their classical or quantum characteristics. In 1987 Hong, Ou and Mandel demonstrated the famous interference effect of anti-bunching photons at a beam-splitter, which is nowadays a standard method to prove the indistinguishability of entangled photons [27]. Their findings, in combination with the development of novel single photon emitters, paved the way for what quantum optics has become: closer to meaningful and useful applications for our everyday life.

For the theoretical and experimental work during the last three decades, we want to give only a brief overview on achievements in quantum optics being relevant to this thesis. We present our research results for an integrated quantum light source based on parametric down-conversion (PDC). Previous major developments on this kind of state preparation have been made by Rarity and co-workers [28], Huang and Kumar [29], Kwiat and co-workers [30, 31], and U'Ren and co-workers [32], who continuously improved the brightness and fidelity of the generated photon states. Theirs as well as the work and achievements of Greenberger et al. and Pan et al. [33, 34] can be seen as inspiration and also incentive for this work. In particular, in the latter two works it has been proposed and verified that the novel class of Greenberger-Horne-Zeilinger states (GHZ) can be deployed for the deterministic proof that quantum theory is non-local.

The application of parametric down-conversion for generating single-photon states is by far not a stand-alone method. Other groups have successfully demonstrated sources of single photons by using trapped ions [35–37], angular orbital momentum of photons [38–40], cold atoms [41, 42], quantum dots [43, 44], and vacancy centers in diamond [45–47]. The latter two appear to have the potential, next to guided-wave parametric down-conversion [48–50], for being deployed in real-world applications.

Quantum information processing (QIP) appears to be the fundamental direction of applied quantum optics, and it deals with the bright generation of pure single photons, with the low loss transmission of the states over long distances and with the processing of the carried information in local and wide-area quantum networks. In particular, the application of quantum computation [51, 52] and the implementation of unconditionally secure quantum key distribution (QKD) schemes [53] will rely on the synchronization of environmentally independent, robust, bright, and pure or multiplexed single photon sources as well as on low-loss transmission lines and interfaces [41, 54–56]. Therefore it is necessary to concentrate on the development of elementary building bocks, which combine multiple functionalities at short distances, and which are mutually compatible with other components of the quantum networks.

2.2. Why integrated quantum optics?

In the field of quantum optics, a multitude of integrated devices has been developed [57–61], since they offer several advantages in comparison to free-space experimental setups with bulk optic components [62]. The miniaturization of systems and increasing complexity drastically reduces the required space and paves the way for future the application and commercialization of the aforementioned quantum technologies. It also enables the implementation of optical networks with low loss, a large number of optical modes and high stability.

In 2008 Politi and co-workers [63] have demonstrated quantum interference and photonic gates on-chip. Many groups have developed sophisticated and integrated experiments with two-photon interference [64, 65] or photon-entanglement [66, 67], controlled qubit-operations [68] as well as controlled phase shifts in linear optical circuits [60,69]. In 2012 Metcalf et al. have realized the first three-photon experiment inside a linear optical network [70] and research on Boson sampling in an integrated device has demonstrated four-photon quantum interference [71].

The preparation of the photon states has mostly been performed outside the integrated devices employing traditional bulk crystal parametric down-conversion sources. The efficient coupling between these sources and the integrated circuit remains one bottleneck for designing systems with increasing complexity. Fortunately, remarkable efforts have been devoted to the development of integrated parametric down-conversion sources for photon pair generation inside channel waveguides [48, 72–79] over the last two decades. The main benefits of guided-wave PDC processes can be found in high conversion efficiencies, spatial and spectral mode control, robustness against environmental influences and their compatibility to optical fiber network technology. Among several fabrication techniques with different nonlinear materials used for the implementation of PDC sources (see for example [72, 80–83]), titanium-indiffusion is a standard method to manufacture waveguides in lithium niobate. It provides extremely low loss [84] and the guiding of both polarizations.

In addition, the frequency up-conversion of quantum states using nonlinear optics has been successfully pursued by several groups. They discovered in guided-wave and bulk approaches that almost unit conversion efficiency to visible wavelengths can be achieved [85, 86] and that the properties of the input quantum states are preserved [87–90].

Only very recently, the semi-integrated generation of photon-triplet states as fundamental resources for the preparation of lowest-order GHZ has been achieved by Hübel et al., Shalm et al. and Hamel et al. [91–93]. In their works they combined two different parametric down-conversion sources in a cascaded fashion such that effectively three photons are be generated from one input photon. However, implementing such a quantum state source in an integrated manner has not been shown to date, but it could reduce losses at the interfaces of the cascaded PDC sources and, thus, could yield improved long-term stability, reliability, and robustness.

In this thesis we aim for the implementation of a reliable fully monolithic device, which is capable of generating photon triplets with verified high purity and brightness.

Our work is structured as follows: in Chapter 3 we introduce the reader to the theoretical background of this work, including nonlinear interactions in dielectric media and the requirements of quasi-phase-matched processes. Recapitulating the theoretical fundamentals of quantum light in general and parametric down-conversion in particular there, we move on and provide a brief overview on the basics and the technology of our deployed nonlinear material: titanium-diffused waveguides in periodically poled lithium niobate (Ti:PPLN) in Chapter 4. After having described the design parameters of our integrated cascaded PDC device, we characterize its linear optical and basic non-linear optical functionalities in Chapter 5 in terms of loss, spectral emission characteristics, tunability, and the behavior of the implemented directional coupler.

In Chapter 6 we make use of parts of the implemented building blocks and show that the bright and highly efficient generation of heralded single photons can be achieved with or device. Besides, we prove that our bright source is capable of being applied as a building block in passive decoy-state quantum key distribution [94] in order to circumvent the photon-number-splitting attack of an eavesdropper.

Chapter 7 is dedicated to the application of the full number of on-chip functionalities in terms of cascaded frequency conversion processes, where the main focus lies on the generation of photon-triplet states vis integrated cascaded parametric down-conversion. Having presented and discussed our results, we summarize our work in the conclusion in Chapter 8. Furthermore, we provide an outlook on possible future activities including the fabrication and testing of a four-photon source as the logical extension of the device described here.

CHAPTER 3

Nonlinear frequency conversion - theoretical considerations

Contents

An introduction to the theory of conversion processes, based on second-order nonlinear materials, is provided in this chapter. We give an overview on the different types of three-wave-mixing processes caused by the nonlinear polarization in dielectric media. The requirement of quasi-phase-matching for co-linear sum-frequency generation and second-harmonic generation is studied with classical theory. We model titanium-diffused channel waveguides in lithium niobate and give a brief introduction on the effective-index method. Additionally, we anticipate the behavior of passive directional coupler structures by applying the local normal mode method. Finally, conventional and cascaded parametric down-conversion are discussed employing quantum theory.

3.1. Optical $\chi^{(2)}$-nonlinear media and three-wave-mixing processes

In classical and quantum optics, second-order nonlinear materials, commonly referred to as $\chi^{(2)}$-nonlinear media, play an important role due to their large dielectric susceptibility tensor elements. When electromagnetic waves propagate through such a dielectric medium, their electric field interacts with the electronic structure of the material and leads to polarization of the atoms. As long as the incoming waves have low electric field strengths, the interaction with the electrons is similar to a harmonic oscillator, which means that the polarization-causing, accelerated electrons return to their initial state, while electromagnetic radiation is emitted due to the relaxation. The generated wave can interfere with the driving light wave and causes so-called linear optical effects like absorption, refraction, reflection, and dispersion. For strongly confined light, i. e. very high field amplitudes, the interaction of the light and the matter gets more and more into an anharmonic regime, where the polarization of the atoms has a non-linear dependency on the field strength and intensity. This causes the nonlinear optical effects described in this section.

3.1.1. Nonlinear Polarization in dielectric materials

We can introduce the induced nonlinear polarization $\vec{P}$, which describes the dipole moment per unit volume and depends on the external electric field $\vec{E}$ and the field-dependent electric susceptibility $\chi\left(\vec{E}\right)$. The vacuum permittivity acts as the coefficient of proportionality and we write

$$\vec{P} = \varepsilon_0 \chi\left(\vec{E}\right)\vec{E}. \tag{3.1}$$

Due to the fact that the susceptibility depends on the field in a nonlinear fashion it is appropriate to develop the relation in Eq. 3.1 in terms of a Taylor series

$$\vec{P} = \varepsilon_0 \left(\chi^{(1)}\vec{E} + \chi^{(2)}\vec{E}\vec{E} + \chi^{(3)}\vec{E}\vec{E}\vec{E} + ...\right), \tag{3.2}$$

where the individual $\chi^{(i)}$ are described by tensors of rank $i+1$. This means that first-order susceptibility is a matrix and dimensionless, and it has values of the order of $\chi^{(1)} \approx 1$. It relates to the relative permittivity of non-magnetic dielectric materials as $\chi^{(1)} = \varepsilon_r - 1$ with $\varepsilon_r = n^2(\omega)$, where $n(\omega)$ is the refractive index of the material. The first-order susceptibility is responsible for the harmonic interaction of light with the medium, and the first term of the Taylor series in Eq. 3.2 describes the linear contribution to the polarization, which reads

$$\vec{P}_{\mathrm{L}} = \varepsilon_0 \chi^{(1)}\vec{E}. \tag{3.3}$$

By contrast, the remaining higher-order terms in Eq. 3.2 can be referred to as the nonlinear polarization

$$\vec{P}_{\mathrm{NL}} = \varepsilon_0 \left(\chi^{(2)}\vec{E}\vec{E} + \chi^{(3)}\vec{E}\vec{E}\vec{E} + ...\right). \tag{3.4}$$

As an example, we have a look at the units and typical absolute values of the nonlinear susceptibilities of a standard nonlinear material, i. e. lithium niobate [95–97]:

$$\chi^{(2)} \approx 3 \cdot 10^{-11}\,\mathrm{m\,V^{-1}}$$
$$\chi^{(3)} \approx 2 \cdot 10^{-21}\,\mathrm{m^2\,V^{-2}}.$$

The impact of an electric field of, say $10^5\,\mathrm{V\,m^{-1}}$ of field strength, leads to induced contributions to the nonlinear polarization for both susceptibility tensors. But the second-order contribution overcomes the third-order contribution by more than five orders of magnitude. Thus, we neglect the response of media like lithium niobate in terms of third-order nonlinearities.

Let us assume that a second-order nonlinear medium is illuminated by electromagnetic radiation. The electric field thereof shall be constructible as the superposition of two fields at different frequencies, which reads

$$\vec{E} = E_1 e^{-i\omega_1 t} + E_1 e^{-i\omega_1 t} + c.c.. \tag{3.5}$$

Inserting this equation to the second-order contribution to the polarization, $\vec{P}^{(2)}$, yields

$$\begin{aligned}
\vec{P}^{(2)} \;=\; & \varepsilon_0\chi^{(2)}\left[E_1^2 e^{-2i\omega_1 t} + c.c.\right] \\
& +\varepsilon_0\chi^{(2)}\left[E_2^2 e^{-2i\omega_2 t} + c.c.\right] \\
& +\varepsilon_0\chi^{(2)}\left[2E_1E_2 e^{-i(\omega_1+\omega_2)t} + c.c.\right] \\
& +\varepsilon_0\chi^{(2)}\left[2E_1E_2 e^{-i(\omega_1-\omega_2)t} + c.c.\right] \\
& +2\varepsilon_0\chi^{(2)}\left[E_1E_1^* + E_2E_2^* + c.c.\right].
\end{aligned} \tag{3.6}$$

From Eq. 3.6 we can extract different contributions to the polarization involving three fields, two at the input and one as the output, and the corresponding processes are commonly referred to as *three-wave mixing*. The first two terms describe second-harmonic generation (SHG) of radiation at twice the frequencies of the illuminating field components, i. e. $\omega_{\mathrm{SHG}} = 2\omega_1$ and $\omega_{\mathrm{SHG}} = 2\omega_2$, when the electrons of the medium relax to the ground state. The third term accounts for sum-frequency generation (SFG), which is the more general case of SHG with two different input frequencies. We get $\omega_{\mathrm{SFG}} = \omega_1 + \omega_2$. The fourth term describes difference-frequency generation (DFG), where the generated light is emitted at the frequency $\omega_{\mathrm{DFG}} = \omega_1 - \omega_2$. The last term of Eq. 3.6 does not contribute to the generation of light at new frequency components. This component is called optical rectification and is responsible for the build-up of static electric fields inside the $\chi^{(2)}$-nonlinear medium [98, 99]. All the aforementioned frequency-dependent processes fulfill the law of energy conservation

$$\sum \hbar\omega_{\mathrm{in}} = \sum \hbar\omega_{\mathrm{out}}. \tag{3.7}$$

The process of DFG appears similar to that of SFG, but a closer look on the processes at the single photon level offers insights to the differences. For SFG two photons at low frequencies ω_1 and ω_2 are annihilated, while a new photon at the sum-frequency ω_{SFG} is created. By contrast, the process of DFG requires the annihilation of a high-energy photon at ω_1 for the generation a photon at the difference-frequency $\omega_1 - \omega_2$, because of the energy conservation law. At the same time, another photon at ω_2 is also created. This means that effectively not only a new frequency component is generated, but the low-frequency component of the input field gets amplified. In other words: the presence of light at ω_2 stimulates the decay of light at ω_1, which leads to a photon pair at ω_2 and ω_{DFG}. The DFG process is therefore often called optical parametric amplification (OPA) [99].

We assume that our nonlinear medium is lossless and that the total power in the DFG process is preserved. The Manley-Rowe relations [99, 100] describe the variation of the total intensity along the propagation direction of the mixing waves through the nonlinear medium. In conjunction with the conservation of energy, the Manley-Rowe relations require also the conservation of the photon flux. This fact has important consequences for the work in this thesis: consider a DFG process, in which the low-frequency component at ω_2 is initially *not* injected to the nonlinear medium. The driving field can couple to vacuum fluctuations, and the generation of two photons at lower frequencies takes place. Herein, the sum of energies after the decay process is equal to the energy of the injected field. This process is called optical parametric fluorescence or parametric down-conversion (PDC), and it is explained in more detail in Sec. 3.3. The involved photons are usually referred to as pump (p), signal (s) and idler (i). By convention the signal has the higher frequency of the two generated photons. The energy conservation rule for the PDC case is given by the shortened formula $\omega_{\mathrm{p}} = \omega_{\mathrm{s}} + \omega_{\mathrm{i}}$.

In Fig. 3.1 we represent the frequency-dependent $\chi^{(2)}$-nonlinear processes by term schemes. We infer in the following section the conditions, under which the generated frequency components are emitted by the nonlinear medium with significant intensities.

3.1.2. Phase-matching and quasi-phase-matching

Our considerations in the previous section dealt with the frequency-dependent generation of light in a dielectric medium. Describing the involved electric fields as in Eq. 3.5 allows for considering the temporal evolution of the fields, but so far we have neglected their propagation in space. In this section we include also the spatial evolution of the electric fields and replace Eq. 3.5 by the time- and space-dependent fields

$$\vec{\tilde{E}}_j\left(t,\vec{r}\right) = A_j\left(z\right)\vec{\mathcal{E}}_j\left(x,y\right)\cdot e^{i\vec{k}_j\cdot\vec{r}}\cdot e^{-i\omega_j t} + c.c., \tag{3.8}$$

where $A_j\left(z\right)$ is the space-dependent field amplitude, $\vec{\mathcal{E}}_j\left(x,y\right)$ is the spatial mode distribution, and $\vec{k}_i$ is the wave-vector of the propagating field. In the following we concentrate on the uni-directional propagation of the involved light waves along

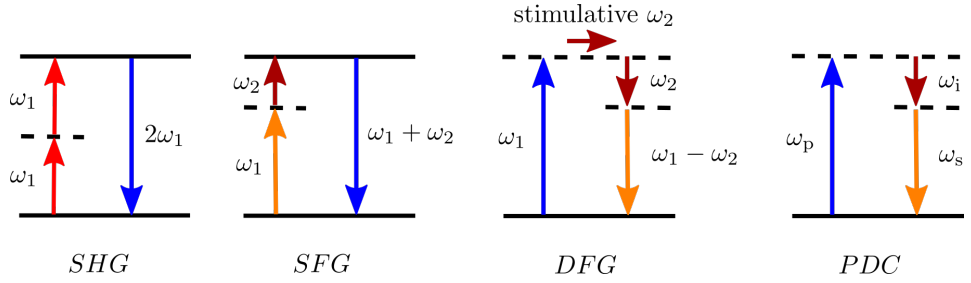

Figure 3.1.: The frequency-dependent $\chi^{(2)}$-nonlinear three-wave mixing processes are shown. I the case of second-harmonic generation (SHG) two identical waves at low frequency mix to an output wave at double the input frequency. Sum-frequency generation (SFG) represents the more general case, where the two input waves have different frequencies and sum in the three-wave-mixing process. Difference-frequency generation (DFG) requires two input waves, the low-frequency wave of which (ω_2) stimulates the generation of a third wave at the frequency $\omega_1 - \omega_2$ and a second wave at ω_2. Parametric down-conversion (PDC) is a special case of DFG, where only the high-frequency (pump-) wave is injected to the nonlinear medium and couples to vacuum fluctuations. This process generates a pair of photons from a virtual energy level, while the energy conservation has to be fulfilled.

the z-direction, which corresponds to the special case of co-linear propagation. This is very important for our later technological processing relying on waveguides in nonlinear lithium niobate crystals. However, for now we also assume identical mode distributions $\mathcal{E}_j(x,y) = 1$ for all three interacting fields for simplicity. With these simplifications the wave-vector can be reduced to a wave number, i. e.

$$\vec{k}_i \rightarrow k_{\mathrm{z},i} = k(\omega_i) = \frac{\omega_i}{c} n_i(\omega_i), \tag{3.9}$$

which is equivalent to a phase delay of the propagating wave. Here, c is the vacuum speed of light, and $n_i(\omega_i)$ represents, again, the frequency-dependent refractive index, which is related to the dispersive properties of the dielectric medium determined by $\chi^{(1)}$. Note that $k(\omega_i)$ in the presented form is equal to what is elsewhere referred to as the propagation constant β_i, because we included the refractive index in the definition of Eq. 3.9.

In a derivation similar to the considerations in the previous section we can infer the relative phase between the interacting fields in the second-order nonlinear processes. This leads to the following phase relations for the individual conversion processes:

$$\textbf{SHG}: \quad \Delta k_{\mathrm{SHG}} = k(2\omega_1) - 2 \cdot k(\omega_1), \tag{3.10}$$

$$\textbf{SFG}: \quad \Delta k_{\mathrm{SFG}} = k(\omega_1) + k(\omega_2) - k(\omega_1 + \omega_2), \tag{3.11}$$

$$\textbf{DFG}: \quad \Delta k_{\mathrm{DFG}} = k(\omega_1) - k(\omega_2) - k(\omega_1 - \omega_2), \tag{3.12}$$

$$\textbf{PDC}: \quad \Delta k_{\mathrm{PDC}} = k(\omega_\mathrm{p}) - k(\omega_\mathrm{s}) - k(\omega_\mathrm{i}), \tag{3.13}$$

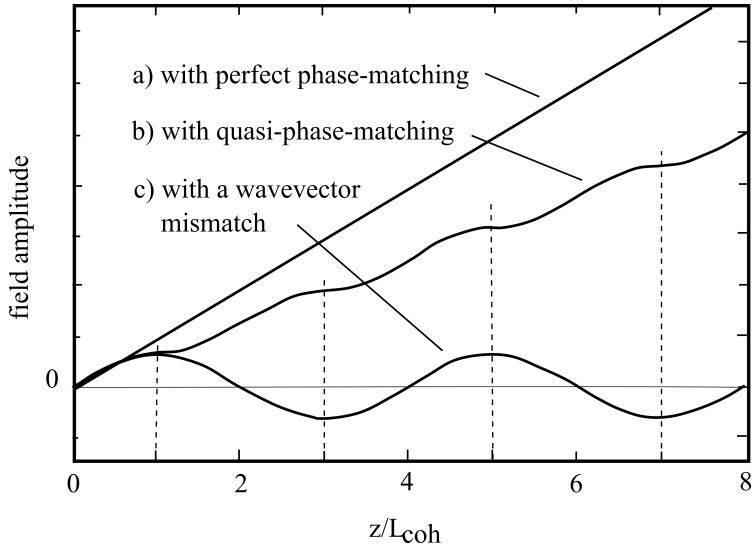

Figure 3.2.: The graph, taken from Ref. [99], shows the output field amplitude of $\chi^{(2)}$-nonlinear conversion processes dependent on the propagation length in units of the coherence length. We see that a) for perfect phase-matching the output intensity grows linearly with propagation length, whereas b) for quasi-phase-matched processes the effective increase is shallower and modulated with periods of the double coherence length. For non-phase-matched process (c)) the generated field amplitude oscillates around zero with periods of four times the coherence length.

where the specific Δk represent the relative phase mismatch of the involved fields. Since the wave numbers k_i are related to the absolute values of the photon momenta inside the nonlinear medium by $p_i = \hbar \cdot k_i$, Eq. 3.10 to Eq. 3.13 represent the respective laws of momentum conservation. Due to the fact that all three-wave-mixing processes are interference effects of the illuminating and the generated fields, the phase mismatch must be $\Delta k = 0$ over the propagation length inside the nonlinear medium. This case is usually called phase-matching. Given this coherent interaction condition, the constructive interference leads to a build-up of significant output field amplitudes and powers/intensities. Otherwise, the power of the output field amplitudes will oscillate around zero. This is shown in Fig. 3.2 [99], where the coherence length for constructive interference has been defined:

$$L_{\mathrm{coh}} = \frac{\pi}{\Delta k}. \tag{3.14}$$

As a consequence no significant amount of output power can be measured at the exit of the nonlinear medium.

We only consider the co-linear propagation of light here, since it denotes a major prerequisite for conversion processes in waveguides later on in this thesis. Since most

of the $\chi^{(2)}$-nonlinear media like lithium niobate show normal dispersion, genuinely phase-matched processes in a co-linear configuration can be achieved by exploiting the birefringence of the material. In this case we can make use of the different dispersion for orthogonally polarized light, if the corresponding nonlinear optical tensor element

$$d_{ijk} = \frac{1}{2}\chi^{(2)}_{ijk} \tag{3.15}$$

exhibits a non-zero contribution in the considered nonlinear material. However, the dispersive properties of typical nonlinear crystals forbid the choice of arbitrary frequency or wavelength triples to mix. Thus, we have to find other ways to make use of the largest nonlinear optical tensor elements in combination with arbitrary wavelength combinations, which have to fulfill both energy and momentum conservation. Fortunately it is possible to manipulate the spontaneous polarization of ferroelectric nonlinear materials such that we can inscribe a periodic grating to the crystal, in which the signs of the nonlinear susceptibility and the nonlinear optical tensor element change periodically. The grating period Λ_G corresponds to an artificial wave number or phase term, which has to fulfill the condition $\Lambda_\mathrm{G} = 2 \cdot L_\mathrm{coh} = 2\pi/\Delta k$. Assuming that the periodic grating shows square-wave behavior in space, we can describe the spatial dependence of the nonlinear optic tensor elements, $d_{ijk}(z)$, in terms of a Fourier series:

$$d_{ijk}(z) = d_{ijk} \sum_{m=-\infty}^{\infty} G_m e^{iK_m z}, \tag{3.16}$$

with $K_m = 2\pi m/\Lambda_\mathrm{G}$ being the wave number of the grating associated with the m-th Fourier component of the nonlinear optic tensor element. For rectangular modulation of the grating we have

$$G_m = 4 \cdot \frac{\sin(m\pi/2)}{(m\pi/2)}, \tag{3.17}$$

and the first-order amplitude is given by $G_1 = 2/\pi$. We further concentrate on this fundamental case and obtain for the effective nonlinear optic tensor element

$$d^\mathrm{eff}_{ijk} = \frac{2}{\pi} d_{ijk}. \tag{3.18}$$

Likewise, we get for the first-order grating wave number

$$K_{\mathrm{G},1} = \frac{2\pi}{\Lambda_{\mathrm{G},1}}, \tag{3.19}$$

which we introduce as an additional term to Eq. 3.10 to Eq. 3.13. By choosing the grating wave numbers such that the phase mismatch is $\Delta k = 0$, we get the conditions for what is commonly referred to as **quasi-phase-matching (QPM)**. We write

down the quasi-phase-matching conditions for the three-wave-mixing processes:

$$\textbf{SHG}: \quad k(2\omega_1) - 2 \cdot k(\omega_1) \pm \frac{2\pi}{\Lambda_{\mathrm{G,SHG}}} = 0, \tag{3.20}$$

$$\textbf{SFG}: \quad k(\omega_1 + \omega_2) - k(\omega_1) - k(\omega_2) \pm \frac{2\pi}{\Lambda_{\mathrm{G,SFG}}} = 0, \tag{3.21}$$

$$\textbf{DFG}: \quad k(\omega_1) - k(\omega_2) - k(\omega_1 - \omega_2) \pm \frac{2\pi}{\Lambda_{\mathrm{G,DFG}}} = 0, \tag{3.22}$$

$$\textbf{PDC}: \quad k(\omega_\mathrm{p}) - k(\omega_\mathrm{s}) - k(\omega_\mathrm{i}) \pm \frac{2\pi}{\Lambda_{\mathrm{G,PDC}}} = 0. \tag{3.23}$$

Knowing the dispersion relation of a ferroelectric $\chi^{(2)}$-nonlinear medium we can conveniently extract the grating periods, by which the spontaneous polarization and, thus, the nonlinear susceptibility must be periodically inverted. This is fundamental for our technological effort to tailor nonlinear ferroelectrics like lithium niobate for the sake of application as wavelength converters in classical and quantum nonlinear optics.

3.2. Modeling of Ti-diffused waveguide structures in lithium niobate

Our device, the fabrication and characterization of which is carried out in this thesis, relies on titanium-diffused waveguide structures in periodically poled lithium niobate. While the nonlinear optical properties and prospects of $\chi^{(2)}$-nonlinear media in terms of co-linear three-wave mixing processes are already covered by the theoretical modeling in the previous sections, we now concentrate on the special case of guided waves. As we pointed out above, second-order frequency conversion processes require large electric field strengths to take place. The conventional focusing of Gaussian beams can already cause nonlinear effects in bulk materials like our lithium niobate [101].The effective nonlinear interaction length L, having a major impact on the overall conversion efficiency in terms of energy consumption, typically suffers from effects related to defocussing of the interacting fields. In waveguides, however, we can maintain the required high intensities over comparatively long distances, because total internal reflection of the beams is provided, if the refractive index inside the waveguide is larger than the refractive index of the surrounding media. Here, we concentrate on the modeling of titanium-diffused waveguides by means of diffusion, the relation of the local refractive index change, the effective refractive index modeling, and on the behavior of coupled waveguide structures.

3.2.1. Titanium diffusion in lithium niobate

We rely on the local diffusion of titanium into lithium niobate, which forms channel waveguides close to the surface of the substrate material. Assuming that we spatially define titanium stripes of width w_{Ti} and thickness τ_{Ti} in certain technological steps

(see Sec. 4.2.2, we can anticipate the local Ti-concentration after thermal diffusion. For finite thickness τ_{Ti} (along y) and width w_{Ti} (along x), and an infinite length of the Ti-strip along z we can state that we have formed a finite particle reservoir in the x- and y-direction. According to Fick's laws and the continuity equation, the two-dimensional diffusion equation can be written as [102]

$$\frac{\partial c_{\mathrm{Ti}}(x,y,t)}{\partial t} = \mathbf{D}_x \frac{\partial^2 c_{\mathrm{Ti}}(x,y,t)}{\partial x^2} + \mathbf{D}_y \frac{\partial^2 c_{\mathrm{Ti}}(x,y,t)}{\partial y^2}, \tag{3.24}$$

where $\mathbf{D}_i = \mathcal{D}_{i,0} \cdot \exp(-T_0/T)$ [103] with $i = x, y$ denotes the diffusion coefficients with $\mathcal{D}_{i,0}$ being the diffusion constant and T_0 is the temperature related to the activation energy of the diffusion process. The term $c_{\mathrm{Ti}}(x,y,t)$ describes the time- and space-dependent titanium concentration inside the lithium niobate substrate. As an important prerequisite for the following considerations we assume that $c_{\mathrm{Ti}}(x,y,t)$ is separable. This means that the diffusion processes along the x- and y-axes are independent of each other. We write

$$c_{\mathrm{Ti}}(x,y,t) = c_0 \cdot a(x,t) \cdot b(y,t), \tag{3.25}$$

where $c_0 = c(x = 0, y = 0, t)$ shall be the surface concentration after the diffusion time t. The separation of variables yields the diffusion equation along x:

$$\frac{\partial a(x,t)}{\partial t} = \mathbf{D}_x \frac{\partial^2 a(x,t)}{\partial x^2}, \tag{3.26}$$

with the solution for sufficiently long diffusion times t [102, 103]:

$$a(x,t) = \frac{1}{2}\left[\mathrm{erf}\left(\frac{2x + w_{\mathrm{Ti}}}{2D_x}\right) - \mathrm{erf}\left(\frac{2x - w_{\mathrm{Ti}}}{2D_x}\right)\right]. \tag{3.27}$$

Here, we accounted for the finite width of the initial titanium stripe at $t = 0$. We also defined that the Ti-strip is distributed between $-w_{\mathrm{Ti}}/2 < x < w_{\mathrm{Ti}}/2$. The term $D_x = \sqrt{4\mathbf{D}_x t}$ denotes the diffusion distance along the x-axis and $\mathrm{erf}(\tilde{x})$ is the error function defined as

$$\mathrm{erf}(\tilde{x}) = \frac{2}{\sqrt{\pi}} \int_0^{\tilde{x}} \exp\left(-\xi^2\right) \mathrm{d}\xi. \tag{3.28}$$

For the diffusion along the y-direction we can write

$$\frac{\partial b(y,t)}{\partial t} = \mathbf{D}_y \frac{\partial^2 b(y,t)}{\partial y^2}. \tag{3.29}$$

The solution to this equation can be yielded by integration and is given by

$$b(x,t) = \exp\left(-\frac{y^2}{D_y^2}\right), \tag{3.30}$$

when a sufficiently long diffusion time lead to the condition that the initial Ti-layer thickness is much smaller than the $1/e$-diffusion depth along y, i. e. $\tau_{\mathrm{Ti}} \ll D_y =$

$\sqrt{4\mathbf{D}_y t}$. For Eq. 3.30, we defined $y = 0$ to be at the interface between the Ti-reservoir and the lithium niobate substrate, and the diffused region occupies $y > 0$. The total amount of titanium ions per unit length along the z-direction must be preserved during the diffusion processes, which reads [104]

$$\int\int c_{\mathrm{Ti}}(x, y, t)\ \mathrm{d}y\,\mathrm{d}x = \frac{\sqrt{\pi} D_y c_0}{2} \cdot w_{\mathrm{Ti}}. \tag{3.31}$$

Taking the bulk titanium particle density of titanium, $\rho_{\mathrm{Ti}} = 5.67 \cdot 10^{22}\,\mathrm{cm}^{-3}$, into account, we get for the concentration at $y = 0$ and $x = 0$:

$$c_0 = \frac{2\rho_{\mathrm{Ti}} \cdot \tau_{\mathrm{Ti}}}{\sqrt{\pi} D_y}, \tag{3.32}$$

where $D_y = \sqrt{4\mathbf{D}_y t}$ is the $1/e$-depth of the concentration profile along the y direction. We see that, from a technological point of view, we can manipulate c_0 by changing the initial thickness of the titanium stripe. Likewise, the diffusion depths D_x and D_y can be manipulated by setting the temperature T and the duration t of the diffusion process accordingly.

With the aforementioned considerations we calculate the local Ti-concentration in width (x) and depth (y) as [98, 102, 103, 105]

$$c_{\mathrm{Ti}}(x, y) = \frac{\tau_{\mathrm{Ti}} \cdot \rho_{\mathrm{Ti}}}{\sqrt{\pi} \cdot D_{\mathrm{y}}} \cdot \exp\left(-\frac{y^2}{D_{\mathrm{y}}^2}\right) \cdot \left[\mathrm{erf}\left(\frac{2x + w_{\mathrm{Ti}}}{2D_{\mathrm{x}}}\right) - \mathrm{erf}\left(\frac{2x - w_{\mathrm{Ti}}}{2D_{\mathrm{x}}}\right)\right]. \tag{3.33}$$

Note that Equation 3.33 is only valid if the deposited titanium reservoir gets fully depleted by the diffusion process into a semi-infinite substrate, leading to $\tau_{\mathrm{Ti}} \ll D_y$.

The diffusion of titanium locally increases the refractive index of the material and forms, thus, a waveguide. The local refractive index increase $\delta n_i(\lambda, c)$, compared to the dispersive bulk index $n_{\mathrm{B},i}(\lambda)$, can be expressed as a concentration dependent function $f_i(c)$ in conjunction with a function $d_i(\lambda)$, which takes the waveguide dispersion into account. We write

$$\begin{aligned} n_i(\lambda, c) &= n_{\mathrm{B},i}(\lambda) + \delta n_i(\lambda, c) \\ &= n_{\mathrm{B},i}(\lambda) + d_i(\lambda) \cdot f_i(c), \end{aligned} \tag{3.34}$$

where $i = \mathrm{e}, \mathrm{o}$ stands for the extraordinary and ordinary refractive index of the birefringent material. We restrict the index increase to occur only inside the nonlinear material, which means $n_i(\lambda, c) = 1$ for $y > 0$.

It has been found experimentally that the relation between the extraordinary refractive index increase and the Ti-concentration is linear, while for the ordinary index increase it follows a power law [104, 106, 107]:

$$f_e(c) = E \cdot c, \tag{3.35}$$

$$f_o(c) = (F \cdot c)^{\gamma}, \tag{3.36}$$

with the parameters $E = 1.2 \times 10^{-23}\,\mathrm{cm}^3$, $F = 1.3 \times 10^{-25}\,\mathrm{cm}^3$ and $\gamma = 0.55$. The dispersion relations of the waveguides have also been found experimentally and are given by [107]

$$d_e(c) = \frac{0.839 \cdot \lambda^2}{\lambda^2 - 0.0645}, \tag{3.37}$$

$$e_o(c) = \frac{0.67 \cdot \lambda^2}{\lambda^2 - 0.13}, \tag{3.38}$$

where λ is the wavelength in [μm]. Note that the validity of Eq. 3.34 to Eq. 3.38 is provided for surface titanium concentration values $c_0 < 0.9 \cdot 10^{21}\,\mathrm{cm}^3$ and using simple oscillator model for the description of the dispersion in the infrared [107]. For the technological parameter set used in this work the former condition is fulfilled. However, the latter precision restriction to the infrared region means that our model for the refractive index increase is not as precise in the visible wavelength range. We expect the errors between the experiment and theoretical prediction for the relative refractive index increase in the visible region to be less than 10%.

We can calculate the local refractive indices, $n_e(\lambda, c)$ and $n_o(\lambda, c)$ by inserting Eq. 3.35 to 3.38 into Eq. 3.33 and the outcome into Eq. 3.34. We infer from the formulas that, independent of the light polarization, the largest vertical index increase is always given at the interface of the diffused area and surrounding air, i. e. $y = 0$. The lateral maximum of the index increase is achieved in the center of the original Ti-stripe, i. e. $x = 0$. We also notice that the refractive index increase is positive for both polarizations, which provides Ti-diffused waveguides in lithium niobate with the capability to guide light beams of orthogonal polarization directions.

3.2.2. Guided modes in Ti-diffused waveguides

Waveguides are per definition structures which direct light to an intended propagation direction. Typically this is achieved by local increase of the refractive index in a transparent medium. In our case of Ti-diffused waveguides we can manipulate the refractive index distribution $n_i(\lambda, c)$ by choosing the width and the thickness of the initially deposited titanium layer as well as the duration and the temperature of the diffusion process. However, we cannot change the general shape of the index distribution being asymmetric in depth but symmetric in width.

For the description of the guided modes in waveguides we start with Maxwell's equations

$$\vec{\nabla} \cdot \vec{D} = \rho, \tag{3.39}$$

$$\vec{\nabla} \cdot \vec{B} = 0, \tag{3.40}$$

$$\vec{\nabla} \times \vec{H} = \vec{j} + \frac{\partial \vec{D}}{\partial t}, \tag{3.41}$$

$$\vec{\nabla} \times \vec{E} = -\frac{\partial \vec{B}}{\partial t}, \tag{3.42}$$

where $\vec{H}$ is the magnetic intensity, $\vec{B}$ represents the magnetic induction, $\vec{j} = \sigma\vec{E}$ is the free current density within the material, σ represents the electrical conductivity, and $\vec{D}$ is the electric displacement. If we assume that the medium does not contain free charges, i. e. the charge density is $\rho = 0$. Free currents shall also not be contained, which is expressed by $\vec{j} = 0$, and the material is assumed to be non-magnetic, which reads $\vec{B} = \mu_0\vec{H}$. The electric displacement shall be related to the electric field as

$$\vec{D} = \varepsilon_0\vec{E} + \vec{P}, \tag{3.43}$$

with $\vec{P}$ being the nonlinear polarization according to Eq. 3.1. We apply a few mathematic operations and vector calculus on Maxwell's equations. Furthermore, we assume that our nonlinear medium is also isotropic, dispersive and non-dissipative as given in detail Ref. [99], we end up with a general form of the driven 3D wave equation for the n-th frequency component in the three-wave-mixing processes:

$$\vec{\nabla}^2\vec{E}_n - \frac{\varepsilon^{(1)}(\omega_n)}{c^2}\frac{\partial^2\vec{E}_n}{\partial t^2} = \frac{1}{\varepsilon_0 c^2}\frac{\partial^2\vec{P}_n^{\mathrm{NL}}}{\partial t^2}, \tag{3.44}$$

Here, $\varepsilon^{(1)}(\omega_n) = n^2(\omega_n)$ is the linear part of the frequency-dependent permittivity defining the refractive index of the medium at frequency ω_n.

The general notation of an electric field component j, that shall fulfill the wave equation, has already been given in Eq:3.8, where we assumed that the amplitude $A_j(z)$ is only dependent on the propagation direction z:

$$\vec{\tilde{E}}_j(t,\vec{r}) = A_j(z)\,\vec{\mathcal{E}}_j(x,y)\cdot e^{i\vec{k}_j\cdot\vec{r}}\cdot e^{-i\omega_j t} + c.c.. \tag{3.45}$$

Here, we concentrate on the mode profile in the x-y-plane, $\vec{\mathcal{E}}_j(x,y)$, which is closely related to the refractive index distribution of the titanium-diffused waveguides provided in Sec. 3.2.1. According to our diffusion model and waveguide geometry, we can allow for the injection of electromagnetic waves in the z-direction with the time-invariant electric field [10, 98],

$$\vec{E}(x,y,z) = \vec{\mathcal{E}}(x,y)\cdot e^{-i\beta_{j,z}\cdot z} + c.c., \tag{3.46}$$

where we introduced $\beta_{j,z}$ as the propagation constant of the optical modes inside the medium along the propagation direction z, which is identical to the wave number $k_{j,z} = 2\pi n_j/\lambda_j$. Similarly, the magnetic field is given by

$$\vec{H}(x,y,z) = \vec{\mathcal{H}}(x,y)\cdot e^{-i\beta_{j,z}\cdot z} + c.c.. \tag{3.47}$$

We assume lossless propagation, which is fairly well approximated in Ti-diffused waveguides [84]. Furthermore, the Ti-diffused profile of our waveguides shall not change along propagation direction, i. e. $\partial\vec{\mathcal{E}}(x,y)/\partial z = \partial\vec{\mathcal{H}}(x,y)/\partial z = 0$. By inserting Eq. 3.46 and Eq. 3.47 to Maxwell's equations we end up with the general vectorial wave equation [107] for both fields:

$$\left[\alpha_x^{-2}\frac{\partial^2}{\partial x^2} + \alpha_y^{-2}\frac{\partial^2}{\partial y^2} + k_0^2 n^2(x,y) - \beta_{\mathrm{eff},i}^2\right]\phi(x,y) = 0. \tag{3.48}$$

Here, $\phi(x,y)$ represents the transverse field distributions $\vec{\mathcal{E}}(x,y)$ or $\vec{\mathcal{H}}(x,y)$, while the parameters α_x and α_y account for the birefringence of the substrate material dependent on the crystal cut. The solutions to this eigenvalue problem are given by a continuous spectrum of radiation modes on the one hand. These are not of particular interest in this thesis, since they propagate not only in the waveguides and can be interpreted as loss. On the other hand, guided modes at discrete values of the propagation constant are what we aim for in our work. We dedicate the discrete propagation constants,

$$\begin{aligned} \beta_{\mathrm{eff},i} &= \frac{2\pi}{\lambda} \cdot n_{\mathrm{eff},i} \\ &= k_0 \cdot n_{\mathrm{eff},i}, \end{aligned} \tag{3.49}$$

to the guided modes, where k_0 is the vacuum propagation constant, related to the free-space momentum by $p_0 = \hbar k_0$. The propagation constants are associated with the effective refractive indices, and they must have values in the range $n_{\mathrm{B},i} \cdot k_0 < \beta_{\mathrm{eff}} < n_{\mathrm{S},i} \cdot k_0$. Furthermore, the effective refractive indices must fulfill the condition $n_{\mathrm{eff},i}$ with $n_{\mathrm{B},i} < n_{\mathrm{eff},i} < n_{\mathrm{S},i}$. Note that $n_{\mathrm{S},i} = \max\left[n_i(\lambda, c)\right]$ represents the polarization-dependent refractive index at the surface of the Ti-diffused region, where the titanium concentration is maximized. The term $n_{\mathrm{B},i}$ is the polarization-dependent refractive index of the underlying substrate material. Note that in the wave equations 3.48 do not comprise a driving nonlinear polarization term, which means that the solutions have to describe standing waves. This description is very similar to bound electronic states in a 2-D quantum-mechanical potential.

By contrast to planar waveguides, we do not observe translational invariance along the x-direction in our channel waveguides. Additionally we have a discontinuity of the vertical refractive index profile at $y = 0$. Thus, the solutions to the vectorial equation 3.48 cannot be decoupled to transverse-electric (TE) and transverse-magnetic modes (TM), which are linearly independent. Instead, we have to deal also with small field components in the z-direction. We rely on the fact that Ti-diffused waveguides are weakly guiding structures with refractive index increases of the order of $\delta n_i / n_{\mathrm{B},i} \approx 10^{-3}$. This means that only the $\mathcal{E}_{\mathrm{x}}$ and the $\mathcal{H}_{\mathrm{x}}$ components are predominant in our system in terms of quasi-transverse electric (QTE) and quasi-transverse magnetic (QTM) modes, respectively. This allows us to write the wave equations in approximated scalar forms [98, 107–109]:

$$\textbf{QTE}: \qquad \left[\frac{\partial^2}{\partial x^2} + \frac{\partial^2}{\partial y^2} + k_0^2\left(n_o^2 - n_{\mathrm{eff,o}}^2\right)\right]\mathcal{E}_{\mathrm{x}} = 0, \tag{3.50}$$

$$\textbf{QTM}: \qquad \left[\frac{\partial^2}{\partial x^2} + \frac{n_{\mathrm{e}}^2}{n_{\mathrm{o}}^2}\frac{\partial^2}{\partial y^2} + k_0^2\left(n_e^2 - n_{\mathrm{eff,e}}^2\right)\right]\mathcal{H}_{\mathrm{x}} = 0, \tag{3.51}$$

where we accounted for the Z-cut configuration of lithium niobate as our considered crystal orientation [107]. Note that, despite of the approximations and the consequent classification as QTM and QTE modes, we refer to as TM and TE modes throughout this thesis.

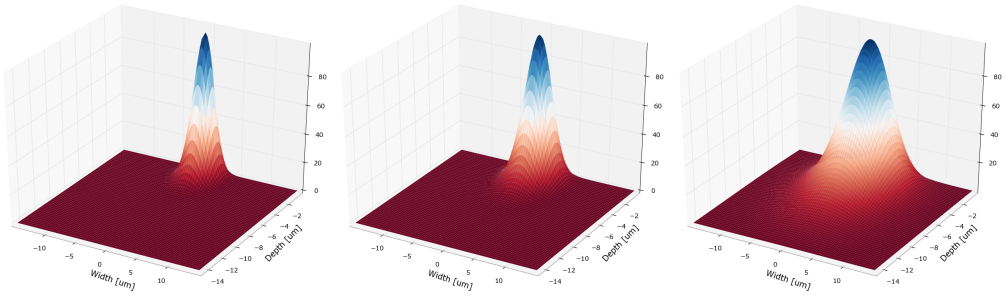

Figure 3.3.: Typical fundamental mode intensities of TM-polarized light are shown for wavelengths of 532 nm (left), 790 nm (middle) and 1625 nm (right). We see that the mode size increases with the wavelength, as the modes are guided weaker and weaker. Likewise, we identify a significant asymmetry in the vertical direction, which is related to the Ti-diffusion process.

The scalar wave-equations are typically not analytically solvable. Besides methods like the Gauss-Hermite-Gauss approximation [109–111], the effective-index method (EIM) offers easy-to-compute approximations and reliable information about the guided modes. Within the framework of the EIM [105, 112], a normalized mode index or normalized propagation constant,

$$b_i = \frac{n_{\mathrm{eff},i}^2 - n_{\mathrm{B},i}^2}{n_{\mathrm{S},i}^2 - n_{\mathrm{B},i}^2}, \tag{3.52}$$

as well as a normalized diffusion depth or normalized mode volume,

$$V_i = k_0 \cdot D_{\mathrm{y}} \cdot \sqrt{n_{\mathrm{S},i}^2 - n_{\mathrm{B},i}^2}, \tag{3.53}$$

have been introduced. Here, D_{y} is the $1/e$-diffusion depth used in Eq. 3.33, and $i = \mathrm{e}, \mathrm{o}$. For weakly guided modes typical values around $0.05 \leq b_i \leq 0.4$ have to be engineered by appropriate waveguide technology. Below that range, more precisely at $b_i = 0$, the modes tend more and more towards cut-off, which is the transition between guided and radiation modes.

Table 3.1.: Numerical calculations on the effective refractive indices, and the normalized mode parameter of TM modes, performed with the FEM and the effective-index method (EIM) explained in the text.

wavelength	mode order	n'_{eff} (FEM)	b' (FEM)	n'_{eff} (EIM)	$b'(EIM)$
790 nm	TM_{00}	2.18909	0.57204	2.18995	0.56596
790 nm	TM_{10}	2.19109	0.38863	2.18806	0.38152
1625 nm	TM_{00}	2.14445	0.19664	2.14376	0.19085
1625 nm	TM_{10}	2.14200	−0.04678	N.A.	< 0

Besides the effective-index method, which is implemented in a software program, our group also uses a fully numeric finite element method (FEM) for the calculation of the effective refractive indices, relying on the work of Strake et al. [107]. However, we do not discuss this method here, but we restrict ourselves to show in Fig. 3.3 typical mode sizes and shapes of TM-polarized light. We identify the increase of mode size with the wavelength, which is due to the tendency of shallower refractive index distributions for larger wavelengths and, thus, weaker confinement. Additionally the plots show the asymmetry of the modes in depth direction, which is associated with the diffusion process, the relation between local titanium concentration and the resulting mode dispersion.

We summarize the effective indices for TM-polarized light at three different wavelengths, computed with both methods, in Tab. 3.1. The chosen wavelengths represent typical colors of light generated in the fabricated waveguides discussed in this thesis. We see that at $\lambda = 1625\,\mathrm{nm}$ the first higher order mode is predicted to have a negative b-parameter, which indicates that our waveguides will be single mode at this wavelength.

3.2.3. Power evolution in second-harmonic and sum-frequency generation processes

With the considerations about quasi-phase-matched processes and the time-invariant properties of the waveguide modes at hand we can anticipate how $\chi^{(2)}$-nonlinear processes take place. The sum-frequency generation as well as the generation of second harmonic light are of particular interest in this thesis.

As a first assumption we rely on the case that the guided modes, regardless of the individual wavelength, do not change their field distribution in the x-y-plane along the z-axis. This condition is given by $\partial\vec{\mathcal{E}}(x,y)/\partial z = 0$ for waveguides without technological inhomogeneities. We can reduce the vectorial wave equation 3.44 to the one-dimensional case for co-directional propagation along z inside the waveguide, and we end up with

$$\frac{\partial^2 E_j}{\partial z^2} - \frac{n_{\mathrm{eff},j}^2(\omega_j)}{c^2}\frac{\partial^2 E_j}{\partial t^2} = \frac{1}{\varepsilon_0 c^2}\frac{\partial^2 P_j^{\mathrm{NL}}}{\partial t^2}. \tag{3.54}$$

Here, $j \in \{1, 2, \mathrm{SHG}, \mathrm{SFG}, \mathrm{DFG}, \mathrm{p}, \mathrm{s}, \mathrm{i}\}$ labels the respective electric field component depending on which second-order nonlinear process we want to describe. Note that the effective refractive index $n_{\mathrm{eff},j}(\omega_j)$ depends on the polarization of the field component E_j in birefringent media and has to be considered accordingly.

For co-linear propagation along the z-direction we can simplify the expression for the time- and space-dependent electric field given in Eq. 3.8 and Eq. 3.45 such that

$$E_j(t,z) = A_j(z)\,\mathcal{E}_j(x,y)\cdot e^{i(k_{j,z}\cdot z-\omega_j t)} + c.c.. \tag{3.55}$$

In this equation we assume that the field amplitude, $A_j(z)$, varies slowly along z, which is approximately fulfilled for small nonlinear polarization as the driving term of the wave equation.

We derive from Eq. 3.4, in conjunction with Eq. 3.15 for the quasi-phase-matching and together with the wave equation Eq. 3.45, that the second-order nonlinear polarization terms for the j-th field component depend on the field amplitude of the other two fields. Taking the highest nonlinear coefficient in lithium niobate for the quasi-phase-matched case, d_{33}^{eff}, into account, we can write for the three interacting waves $j = 1, 2, 3$ [113, 114]:

$$P_1(t,z) = 2\varepsilon_0 d_{33}^{\text{eff}} A_2(z) A_3(z) \mathcal{E}_2(x,y)\mathcal{E}_3(x,y) \cdot e^{i(\omega_1 t-(k_{2,z}+k_{3,z})z)} + c.c \quad (3.56)$$

$$P_2(t,z) = 2\varepsilon_0 d_{33}^{\text{eff}} A_1(z) A_3^*(z) \mathcal{E}_1(x,y)\mathcal{E}_3(x,y) \cdot e^{i(\omega_2 t-(k_{1,z}-k_{3,z})z)} + c.c \quad (3.57)$$

$$P_3(t,z) = 2\varepsilon_0 d_{33}^{\text{eff}} A_1(z) A_2^*(z) \mathcal{E}_1(x,y)\mathcal{E}_2(x,y) \cdot e^{i(\omega_3 t-(k_{1,z}-k_{2,z})z)} + c.c \quad (3.58)$$

We substitute these equations and also Eq. 3.55 into the z-dependent wave equation 3.54 and leave out the conjugate complex terms. Additionally, we take into account that wave number in z-direction is given by $k_{j,z} = \omega_j/c \cdot n_{\text{eff},j}$, and that the transverse field distribution is space-invariant along z. By abbreviating the transverse mode distributions by $\mathcal{E}_j(x,y) = \mathcal{E}_j$ and accounting for the phase-mismatch Δk we get an expression for the time-independent behavior of the respective field amplitudes:

$$\frac{\partial^2 A_1(z)}{\partial z^2} + 2ik_1 \frac{\partial A_1(z)}{\partial z} = -2\frac{\varepsilon_0 d_{33}^{\text{eff}} \omega_1^2}{c^2} A_2(z) A_3(z) \mathcal{E}_2\mathcal{E}_3 \cdot e^{i\Delta kz}, \quad (3.59)$$

$$\frac{\partial^2 A_2(z)}{\partial z^2} + 2ik_2 \frac{\partial A_2(z)}{\partial z} = -2\frac{\varepsilon_0 d_{33}^{\text{eff}} \omega_1^2}{c^2} A_1(z) A_3(z) \mathcal{E}_1\mathcal{E}_3 \cdot e^{i\Delta kz}, \quad (3.60)$$

$$\frac{\partial^2 A_3(z)}{\partial z^2} + 2ik_3 \frac{\partial A_3(z)}{\partial z} = -2\frac{\varepsilon_0 d_{33}^{\text{eff}} \omega_1^2}{c^2} A_1(z) A_2(z) \mathcal{E}_1\mathcal{E}_2 \cdot e^{i\Delta kz}. \quad (3.61)$$

The following derivation of the coupled mode equations for second-order nonlinear conversion processes has been given in full detail by Bortz [113] for arbitrary waveguide structures. We closely follow this theoretical model, but restrict ourselves to the most important calculations for the classical conversion processes applied in this thesis. As a first step and for convenience we normalize the mode field distributions $\mathcal{E}_j(x,y)$ such that

$$\int_{-\infty}^{\infty}\int_{-\infty}^{\infty} \tilde{\mathcal{E}}_j^2(x,y)\,\mathrm{d}x\,\mathrm{d}y = 1, \quad (3.62)$$

which basically reflects normalization of the intensity distribution. This leads to the relation between the actual field modes and the normalized field modes $\mathcal{E}_j = \gamma_j \tilde{\mathcal{E}}$, where the factor of proportionality is given by [99]

$$\gamma_j = \sqrt{\frac{2}{n_j c \varepsilon_0}}. \quad (3.63)$$

These normalizations refer to the conservation of the photon flux, thus, to the Manley-Rowe relations. We furthermore assume that the envelopes of the propagating light waves vary only slowly along z, i. e. $|\frac{\partial^2 \tilde{E}_j}{\partial z^2}| \ll |k_j \frac{\partial \tilde{E}_j}{\partial z}|$. Thus, we can

neglect the leftmost terms in Eq. 3.59 to Eq. 3.61. We also define the transverse mode overlap of the interacting normalized field modes as

$$\nu_k = \int_{-\infty}^{\infty}\int_{-\infty}^{\infty} \tilde{\mathcal{E}}_1(x,y)\tilde{\mathcal{E}}_2(x,y)\tilde{\mathcal{E}}_3^*(x,y)\,\mathrm{d}x\,\mathrm{d}y, \tag{3.64}$$

where $k = SFG, SHG, DFG$ accounts for the respective nonlinear conversion process. In practice, for our asymmetric and dispersive Ti-diffused waveguides, ν_k is typically lower than unity for the three-wave-mixing of only fundamental spatial modes. Additionally, we incorporate the constants and the angular frequencies of the waves in equations 3.59 to 3.61, as well as the normalization constants resulting from Eq. 3.63, to a coupling factor κ_j, which can be written as

$$\begin{aligned} \kappa_j &= \sqrt{\frac{2\omega_j^2 \cdot d_{33}^{\mathrm{eff}}}{n_1 \cdot n_2 \cdot n_{\mathrm{SFG}} \cdot c^3 \cdot \varepsilon_0}} \\ &= \frac{2\pi \cdot d_{33}^{\mathrm{eff}}}{\lambda_j}\sqrt{\frac{2}{n_1 \cdot n_2 \cdot n_{\mathrm{SFG}} \cdot c \cdot \varepsilon_0}}. \end{aligned} \tag{3.65}$$

By inserting the aforementioned simplifications as well as the slowly varying envelope approximation to the set of equations 3.59 to 3.61 we end up with the system of coupled differential equations of first order [113]:

$$\frac{\partial A_1(z)}{\partial z} + i \cdot \kappa_1 \cdot \nu_k^* \cdot A_2^*(z) \cdot A_3(z) \cdot e^{-i\Delta k z} = 0, \tag{3.66}$$

$$\frac{\partial A_2(z)}{\partial z} + i \cdot \kappa_2 \cdot \nu_k^* \cdot A_1^*(z) \cdot A_3(z) \cdot e^{-i\Delta k z} = 0, \tag{3.67}$$

$$\frac{\partial A_3(z)}{\partial z} + i \cdot \kappa_3 \cdot \nu_k \cdot A_1(z) \cdot A_2(z) \cdot e^{i\Delta k z} = 0, \tag{3.68}$$

where lossless propagation is assumed. For titanium-diffused waveguides in lithium niobate this is fairly well given [84].

As an example we compute the field propagation for a sum-frequency process, where the for the output field $\omega_3 = \omega_{\mathrm{SFG}}$. We assume that the input field at ω_1 is much stronger than the input at ω_2. The latter assumption corresponds to frequency up-conversion as performed in Sec. 7.1.3, where the field at ω_1 does not deplete in the conversion process. Note, however, that our description at this point is still relying on classical theory. For a quantum mechanical treatment of frequency up-conversion at the single photon level we refer the kind reader to the literature given, for example, by Brecht (Ref. [10] and references therein).

The negligible variation of the strong pump field along the propagation direction z leads to the expression

$$\frac{\partial A_1(z)}{\partial z} = -i \cdot \kappa_1 \cdot \nu_{\mathrm{SFG}}^* \cdot A_2(z)^* \cdot A_{\mathrm{SFG}}(z) \cdot e^{-i\Delta k_{\mathrm{SFG}} \cdot z} = 0. \tag{3.69}$$

By contrast, the amplitude variations of the weak input and the output field can be written as

$$\frac{\partial A_2(z)}{\partial z} = -i \cdot \kappa_2 \cdot \nu^*_{\mathrm{SFG}} \cdot A_1(z)^* \cdot A_3(z) \cdot e^{-i\Delta k_{\mathrm{SFG}} \cdot z}, \tag{3.70}$$

$$\frac{\partial A_{\mathrm{SFG}}(z)}{\partial z} = -i \cdot \kappa_{\mathrm{SFG}} \cdot \nu_{\mathrm{SFG}} \cdot A_1(z) \cdot A_2(z) \cdot e^{i\Delta k_{\mathrm{SFG}} \cdot z}. \tag{3.71}$$

We consider the boundary conditions $A_1(0) = \sqrt{P_1}$, $A_2(0) = \sqrt{P_2(0)}$ and $A_{\mathrm{SFG}}(0) = 0$, while the total interaction length is $z_{\max} = L$. The solution to the coupled differential equations 3.69 to 3.71 in terms of the generated sum frequency power for arbitrary phase mismatch Δk_{SFG} is given as

$$\mathbf{P}'_{\mathrm{SFG}}(L) = \frac{\lambda_{\mathrm{SFG}}}{\lambda_2} \mathbf{P}_2(0) \sin^2\left(\sqrt{|\nu_{\mathrm{SFG}}|^2 \kappa_2 \kappa_{\mathrm{SFG}} \mathbf{P}_1} \cdot L\right) \cdot \mathrm{sinc}^2\left(\frac{\Delta k_{\mathrm{SHG}} L}{2}\right), \tag{3.72}$$

where $\mathrm{sinc}(x)$ is the sinus cardinalis function. For perfect quasi-phase-matching, $\Delta k_{\mathrm{SFG}} = 0$, the rightmost term is unity, and we get

$$\mathbf{P}_{\mathrm{SFG}}(L) = \frac{\lambda_{\mathrm{SFG}}}{\lambda_2} \mathbf{P}_2(0) \sin^2\left(\sqrt{|\nu_{\mathrm{SFG}}|^2 \kappa_2 \kappa_{\mathrm{SFG}} \mathbf{P}_1} \cdot L\right), \tag{3.73}$$

where $\mathbf{P}_i$ are the powers of the mixing waves. We identify a linear dependence of the output SFG power on the input signal power $\mathbf{P}_2(0)$, but an oscillating behavior with respect to the strong input field, i. e. $\mathbf{P}_{\mathrm{SFG}} \propto \sin^2\left(\sqrt{\mathbf{P}_1} L\right)$. Furthermore, we can compute the normalized conversion efficiency as

$$\begin{aligned} \eta^{\mathrm{norm}}_{\mathrm{SFG}} &= \nu_{\mathrm{SFG}} \cdot \kappa_2 \cdot \kappa_{\mathrm{SFG}} \\ &= \nu_{\mathrm{SFG}} \cdot \frac{4\pi^2 \cdot (d^{\mathrm{eff}}_{33})^2}{n_1^2 \cdot n_2^2 \cdot n^2_{\mathrm{SFG}} \cdot c^2 \cdot \varepsilon_0^2 \cdot \lambda_2 \cdot \lambda_{\mathrm{SFG}}}. \end{aligned} \tag{3.74}$$

Taking into account that the photon number per unit time is given by $n_i \propto \mathbf{P}_i / \hbar\omega_i$ we can derive the photon number conversion efficiency for the lossless nonlinear medium:

$$\eta_{\mathrm{SFG}} = \sin^2\left(\sqrt{\eta^{\mathrm{norm}}_{\mathrm{SFG}} \cdot \mathbf{P}_1} \cdot L\right). \tag{3.75}$$

This means that for $\mathbf{P}_1 = \pi^4 / \left(4 \cdot \eta^{\mathrm{norm}}_{\mathrm{SFG}} \cdot L^2\right)$ we can theoretically achieve complete conversion of the input photons into up-converted photons, which is attractive for addressing wavelength regions in the visible and near-infrared (NIR) which would otherwise not be accessible [85, 114].

For the generation of second-harmonic light we can proceed with similar considerations. We remember that SHG is the special case of SFG, where the two fundamental input fields share the same frequency $\omega_1 = \omega_2 = \omega_{\mathrm{f}}$, wavelength $\lambda_1 = \lambda_2 = \lambda_{\mathrm{f}}$ and refractive index $n_1 = n_2 = n_{\mathrm{f}}$. For the second-harmonic wave we write $\lambda_{\mathrm{SHG}} = \lambda_{\mathrm{f}}/2$ and n_{SHG}. Under the assumptions that neither the pump field is depleted nor that

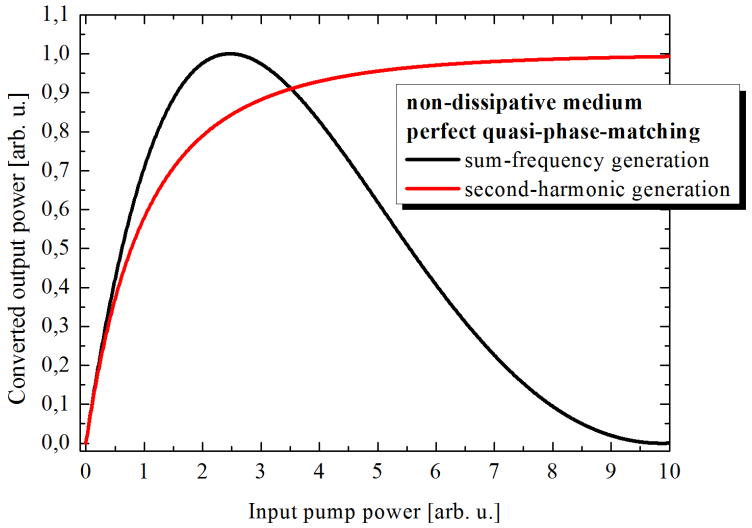

Figure 3.4.: The general dependencies of the SFG and the SHG output powers on the input power are shown for visualization purposes. We identify oscillating conversion in case of the sum-frequency generation or frequency up-conversion, while the maximum achievable second-harmonic power saturates for high fundamental powers due to depletion of the input light.

the nonlinear medium exhibits loss nor that perfect quasi-phase-matching is given, we can write for the output second-harmonic power, according to Ref. [98]:

$$\mathbf{P}'_{\mathrm{SHG}} = \frac{8\pi^2 \cdot (\mathrm{d}_{33}^{\mathrm{eff}})^2}{n_{\mathrm{f}}^2 \cdot n_{\mathrm{SHG}} \cdot c \cdot \varepsilon_0 \cdot \lambda_{\mathrm{f}}^2} \cdot \nu_{\mathrm{SHG}} \cdot \mathbf{P}_{\mathrm{f}}^2 \cdot L^2 \cdot \mathrm{sinc}^2\left(\frac{\Delta k_{\mathrm{SHG}} \cdot L}{2}\right). \tag{3.76}$$

We see that the SHG output power depends on the quasi-phase-matching condition, given by the phase mismatch Δk_{SHG}, which follows a squared sinus cardinalis curve (sinc^2). This function is maximized for $\Delta k_{\mathrm{SHG}} = 0$. Likewise, we infer that the spectral bandwidth of the SHG output depends on the interaction length L, along which the nonlinear susceptibility is inverted with period $\Lambda_{\mathrm{G},1}$. Here, we assume ideal quasi-phase-matching, i. e. $\Delta k_{\mathrm{SHG}} = 0$, which leads to the simplification of Eq. 3.76:

$$\mathbf{P}_{\mathrm{SHG}} = \frac{8\pi^2 \cdot (\mathrm{d}_{33}^{\mathrm{eff}})^2}{n_{\mathrm{f}}^2 \cdot n_{\mathrm{SHG}} \cdot c \cdot \varepsilon_0 \cdot \lambda_{\mathrm{f}}^2} \cdot \nu_{\mathrm{SHG}} \cdot \mathbf{P}_{\mathrm{f}}^2 \cdot L^2. \tag{3.77}$$

We also infer that the output power of the SHG process exhibits quadratic dependencies on the fundamental input power, $\mathbf{P}_{\mathrm{SHG}} \propto \mathbf{P}_{\mathrm{f}}^2$, as well as on the interaction length, $\mathbf{P}_{\mathrm{SHG}} \propto L^2$. The maximal overall conversion efficiency is, thus, commonly defined as

$$\eta_{\mathrm{SHG}} = \frac{\mathbf{P}_{\mathrm{SHG}}}{\mathbf{P}_{\mathrm{f}}^2 \cdot L^2} \cdot 100\%, \tag{3.78}$$

and it is given in units of $[\%\,\mathrm{W}^{-1}\,\mathrm{cm}^{-2}]$. Note that these considerations hold true for the case of an undepleted fundamental wave. For large input powers the con-

version takes place by depleting the fundamental light. A dependency $\mathbf{P}_{\mathrm{SHG}} = \mathbf{P}_{\mathrm{f}} \cdot \tanh^2\left(\sqrt{\eta_{\mathrm{SHG}} \cdot \mathbf{P}_{\mathrm{f}}} \cdot L\right)$ can be found [101, 115], where $\eta_{\mathrm{SHG}}^{\mathrm{norm}}$ is the normalized efficiency of the SHG process. In this depletion regime the absolute conversion efficiency, $\eta_{\mathrm{SHG}} = \mathbf{P}_{\mathrm{SHG}}/\mathbf{P}_{\mathrm{f}}$, tends asymptotically to unity and can cause narrowing of the phase-matching curve due to competing conversion effects [115].

In Fig. 3.4 we summarize our findings and show the theoretical behavior for the conversion efficiencies of SFG andSHG dependent on the pump power.

3.2.4. Directional couplers in the local normal mode description

Integrated devices for quantum optics are intended to carry multiple passive and active functionalities on the very same chip. An important basic element, which is capable of separating light of different colors [21], is given by a wavelength division multiplexer (WDM). Similar elements are also capable of combining or separating light of different polarization [116]. In the following, we also refer to WDMs as directional couplers.

Our findings regarding the effective refractive index of guided light in Ti-diffused strip waveguides allow us to model the behavior of light in a WDM structure, where two identical waveguides are close to each other. The symmetric configuration shown in Fig. 3.5 comprises S-shaped arc elements, also referred to as S-bends, which transform adiabatically to a straight dual-waveguide region with a center-to-center separation $d(z)$. After certain propagation length L_{C}, the straight waveguides end also in S-bends of identical shape. In that manner we have designed a passive directional coupler, the theoretical parameter estimation of which will be explained in this section.

In principle the considered coupled waveguide system can be described by the coupled-mode theory (see, for example, [20, 117, 118]), where the light propagation in one waveguide perturbs the properties in the neighboring waveguide. But in order to apply that theoretical approach, the perturbations have to be very small. This precondition is not fulfilled by Ti-diffused waveguides in lithium niobate (LN), where the relative effective-refractive-index changes are typically of the order of $10^{-4} \leq \delta n_{\mathrm{eff}}/n_{\mathrm{sub}} \leq 10^{-2}$ with respect to the underlying substrate. The most accurate way to treat a waveguide directional coupler is, thus, to describe the properties of the whole system in terms of local normal modes of the dual channel structure [21, 116, 119] with additional input and output ports.

In our considered coupler structure, the local normal modes comprise a symmetric TM_{00} and an anti-symmetric TM_{10} mode, as shown in Fig. 3.5. For sufficiently large channel separation $d(z)$, compared to the mode size, the propagation constants of the two modes are degenerate, $\lim_{z\to\infty} \Delta\beta\left(d(z)\right) = \lim_{z\to\infty} \beta_{00}\left(d(z)\right) - \beta_{10}\left(d(z)\right) = 0$.

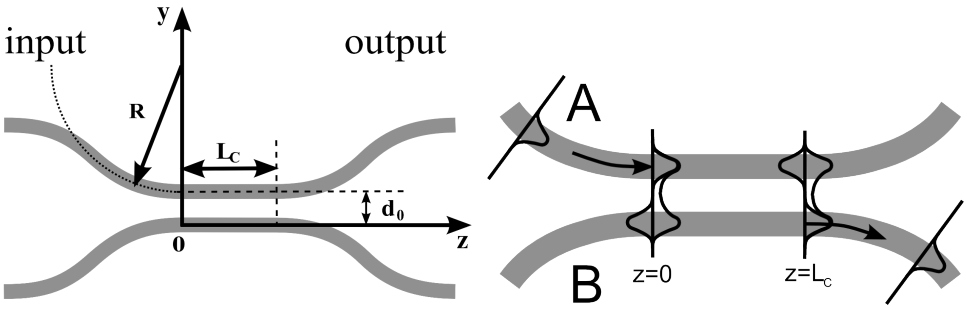

Figure 3.5.: Details of the directional coupler (left) and local normal mode evolution scheme (right) are shown. The symmetry of the considered structure is supported by the S-bend input and output ports.

Here, the propagation constants are given by

$$\beta_{00}\left(d\left(z\right)\right) = \frac{2\pi}{\lambda} \cdot n_{\mathrm{eff},00}\left(d\left(z\right)\right), \tag{3.79}$$

$$\beta_{01}\left(d\left(z\right)\right) = \frac{2\pi}{\lambda} \cdot n_{\mathrm{eff},01}\left(d\left(z\right)\right). \tag{3.80}$$

The launching of light into one input channel is described by constructive interference of the local normal modes in the launching channel and a destructive interference in the adjacent channel. Upon approaching of the two channels towards the homogeneous central section of the directional coupler, the degeneracy of the propagation constants of the two modes is gradually removed, as the propagation constants depend on $d\left(z\right)$. For the dependence of the center-to-center separation on the propagation distance along z-direction we calculate

$$d\left(z \leq 0\right) = d\left(z=0\right) + 2 \cdot \left(R_{\mathrm{Bend}} - \sqrt{R_{\mathrm{Bend}}^2 - |z|^2}\right), \tag{3.81}$$

$$d\left(z \geq L_{\mathrm{C}}\right) = d\left(z=L_{\mathrm{C}}\right) + 2 \cdot \left(R_{\mathrm{Bend}} - \sqrt{R_{\mathrm{Bend}}^2 - |z-L_{\mathrm{C}}|^2}\right), \tag{3.82}$$

where R is the radius of the bent waveguide sections, and $d\left(z=0\right) = d\left(z=L_{\mathrm{C}}\right)$ denotes the waveguide separation of the straight waveguides in the central section. We define the z-axis to have its origin at the interface of the input S-bend and the straight waveguide section. For all further calculations we set $R_{\mathrm{Bend}} = 0.16\,\mathrm{m}$, since it has been shown that large radii prevent additional bending loss in the arc elements and S-bends [21, 24, 120, 121].

In Fig. 3.6 we plot $\Delta\beta\left(d\left(z\right)\right)$ for TM and TE polarization and dependent on the operating wavelength. The calculations are performed according to a similar FEM model for the effective refractive indices as described nore in detail by Strake et al. in Ref. [107]. We use the model in conjunction with the fabrication parameters explained in Chap. 4 and summarized in Appendix C. For the operating temperature

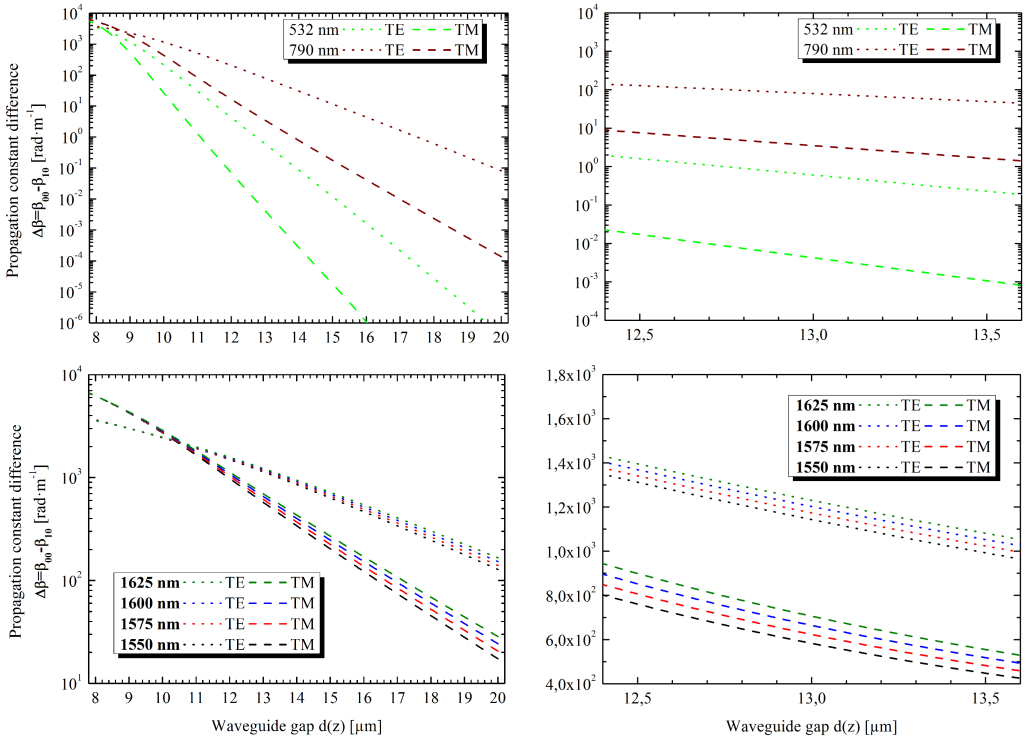

Figure 3.6.: The calculated differences of the propagation constants are plotted dependent on the center-to-center waveguide separation and for TM polarization (dashed lines) and TE polarization (dotted lines). The upper graphs show the behavior for visible and NIR wavelengths, whereas the lower two graphs show the behavior at telecom wavelengths. We identify strong dependencies not only on the waveguide separation, but also on the wavelengths in the left-most graphs, where we plotted with logarithmic scaling of the y-axis. In the right-most graphs we identify reasonable differences of the propagation constants for both polarizations in the telecom C- and L-bands, whereas the visible and NIR light does not exhibit significant non-degeneracy of $\Delta\beta_{00}$ and $\Delta\beta_{01}$.

we choose $140°\mathrm{C} \leq \theta \leq 200°\mathrm{C}$ in steps of $\Delta\theta = 30°\mathrm{C}$, since the effective refractive indices are expected to be temperature dependent. We see that the difference in the phase difference strongly depends on the chosen center-to-center separation. For $11\,\mu\mathrm{m} \leq d(z) \leq 20\,\mu\mathrm{m}$ we identify exponential dependencies for both polarizations (see D.1), where the degree of non-degeneracy of the propagation constants is larger for TE modes. This lets us expect stronger coupling for this polarization in the described model system, where the waveguide separation is larger than the waveguides' designed widths, i. e. $d(z) > w$. The graphs in Fig. 3.6 also exhibit a strong wavelength dependence, which is a result of the waveguide dispersion: since light at shorter wavelengths is much more confined than light at telecom wavelengths,

the former does not show significant differences in the propagation constants of the local normal modes. This feature allows us to design wavelength-selective integrated beam-splitters and -combiners.

In the plots on the right-hand side of Fig. 3.6 we identify comparatively shallow slopes of the model curves with respect to the chosen waveguide separation around $d = 13\,\mu$m. This is very important for the latter fabrication process, since it indicates a high $\Delta\beta$-tolerance to variations in the waveguide separation. Another detail in the lower right graph is of importance for the experiments pursued in this thesis: the $\Delta\beta$ for light at C- and L-band telecom wavelengths between $1550\,\text{nm} \leq \lambda \leq 1625\,\text{nm}$ differ for both polarizations, which allows us to design polarization beam splitters using non-zero-gap waveguide structures on the one hand. On the other hand, it also means that the coupling behavior for the considered wavelength range might not be optimal for a specific operation wavelength. A summary of parameters for the exponential dependencies of $\Delta\beta$ on the waveguide separation is provided in Appendix D.

The propagation of the along the z-direction causes an increasing amount of phase difference between the two local normal modes,

$$\Delta\phi = \int_{z_1}^{z_2} \left(\beta_{00}\left(d\left(z\right)\right) - \beta_{10}\left(d\left(z\right)\right)\right) dz \neq 0, \tag{3.83}$$

and the corresponding interference changes between the two modes. We can separate the integral in Eq. 3.83 into three parts, where the first part,

$$\Delta\phi_{\text{in}} = \int_{z<0}^{z=0} \left(\beta_{00}\left(d\left(z\right)\right) - \beta_{10}\left(d\left(z\right)\right)\right) dz, \tag{3.84}$$

describes the phase difference caused by the input S-bend. The second part,

$$\Delta\phi_{\text{C}} = \left[\beta_{00}\left(d\left(z=0\right)\right) - \beta_{10}\left(d\left(z=0\right)\right)\right] \cdot L_{\text{C}}, \tag{3.85}$$

is caused by the parallel straight waveguide section, whereas the third part,

$$\Delta\phi_{\text{out}} = \int_{z=L_{\text{C}}}^{z>L_{\text{C}}} \left(\beta_{00}\left(d\left(z\right)\right) - \beta_{10}\left(d\left(z\right)\right)\right) dz, \tag{3.86}$$

describes the influence of the output port on the phase difference. Due to the symmetry of the structure we conclude that $\Delta\phi_{\text{in}} = \Delta\phi_{\text{out}} = \Delta\phi_{\text{port}}/2$, and we combine the phase difference caused by the two ports such that we end up with

$$\Delta\phi = \Delta\phi_{\text{C}} + \cdot\Delta\phi_{\text{port}}. \tag{3.87}$$

As a result the injected power transfers gradually from the input channel to the adjacent one. Complete coupling to the neighboring channel is achieved when the accumulated phase difference is $\Delta\phi = (2 \cdot m - 1) \cdot \pi$ with $m \in \mathbb{N}$. From this we can deduce that the power flux will oscillate with a squared sinusoidal behavior dependent on the coupler stem length L_{C}. Note that the intrinsic and mutual

symmetries of the S-shaped input and output ports provide us with phase-jump-free structures, because the arc elements as well as the straight waveguides merge into each other without discontinuities.

We choose a waveguide separation of $d = 13\,\mu\text{m}$ in order to anticipate the power coupling behavior of our considered WDM structure, and we calculate the impact of the input and output ports on the power transfer. Independent of the central stem length, this influence should be constant, but depends on the wavelength. We find from our calculations above that $\Delta\beta \approx 0$ is valid for propagation distances $|z| > 3\,\text{mm}$, because $d\,(z)$ becomes too large for a significant amount of non-degeneracy of the propagation constant difference. Thus, we combine Eq. 3.84 and Eq. 3.86 and approximate with the trapezoidal rule for numerical integration

$$\Delta\phi_{\text{port}} \approx 2 \cdot \sum_{i=1}^{3000} \frac{\Delta\beta\,(d\,(z_i)) + \Delta\beta\,(d\,(z_{i-1}))}{2} \cdot (z_i - z_{i-1})\,, \tag{3.88}$$

where i is an integer value accounting for the step width along the z-axis such that $\Delta z_i = z_i - z_{i-1} = 1\,\mu\text{m}$. Note that the factor of two in front of the sum accounts for the fact that we have two port segments, i. e. input and output.

Since we assume negligible loss in our calculations we can anticipate the power evolution in the adjacent port, $\mathbf{P}_{\text{cross}}\,(L_{\text{C}})$, by combining our calculation results of Eq. 3.85 and Eq. 3.88. Dependent on the stem length L_{C}, which influences only the value of $\Delta\phi_{\text{C}}$, we calculate for the cross-coupled power

$$\mathbf{P}_{\text{cross}}\,(L_{\text{C}}) = \mathbf{P}_{\text{in}} \cdot \sin^2\left(\frac{\Delta\phi_{\text{C}} + \Delta\phi_{\text{port}}}{2}\right). \tag{3.89}$$

In figure 3.7 we plot the expected coupling behavior to the adjacent waveguide for wavelengths in the telecom wavelength regime (left) as well as for $\lambda = 532\,\text{nm}$ and $\lambda = 790\,\text{nm}$. We see that the telecom light requires stem lengths between $3.5\,\text{mm} \leq L_{\text{C}} \leq 4.5\,\text{mm}$ for complete coupling to the adjacent channel. Since the TM-polarized light is almost fully transferred back to the original channel, we can deduce that integrated polarization beam-splitters for telecom light can be fabricated with these stem lengths. The TM-polarized light at the visible and NIR wavelengths couples by $\mathbf{P}_{\text{cross}}/\mathbf{P}_{\text{in}} < 10^{-4}$ to the cross channel for the considered stem lengths, where optimal telecom cross-coupling is provided. Thus, we can fabricate a wavelength demultiplexer with high extinction ratios in the respective other channel, e. g. for the wavelength combination $790\,\text{nm}/1575\,\text{nm}$.

In summary we have applied the local normal mode theory in conjunction with the FEM method for modeling the effective refractive indices of a symmetric passive directional coupler based on titanium-diffused lithium niobate (Ti:LN) waveguide structures. We find that, according to our model, the TE-polarized light exhibits stronger cross-coupling behavior. For center-to-center separation of $d = 13\,\mu\text{m}$ and stem lengths of around $L_{\text{C}} \sim 4\,\text{mm}$ this structure should exhibit excellent properties in terms of demultiplexing TM-polarized light at NIR wavelengths of $\lambda \sim 790\,\text{nm}$ and telecom TM-polarized light light at $\lambda \sim 1575\,\text{nm}$.

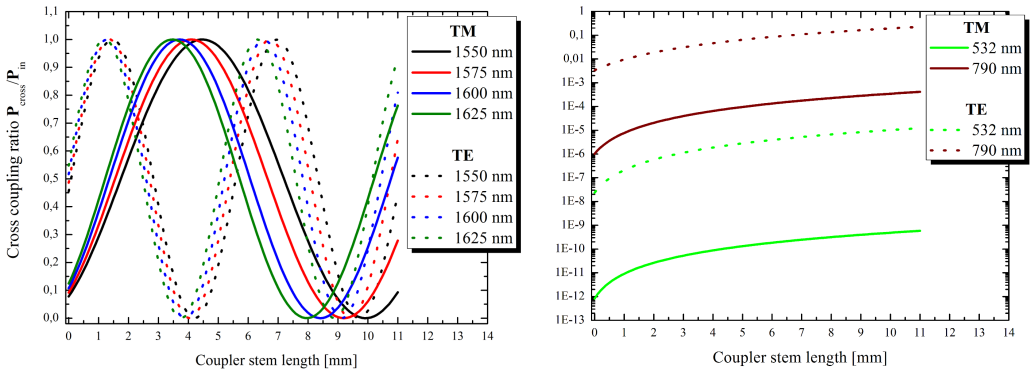

Figure 3.7.: The modeled behavior of the directional coupler is shown for telecom wavelengths (left) as well as for visible and NIR wavelengths (right). We identify stronger coupling for TE modes (dotted lines) compared to the TM modes (solid lines) in general. At stem lengths of around $3.5\,\mathrm{mm} \leq L_C \leq 4.5\,\mathrm{mm}$ we identify full cross-coupling for the TM modes, whereas the power of the TE modes has been transferred back to the input waveguide. Light at the visible and NIR wavelengths does not transfer significant amounts of incoupled power to the adjacent channel for identical stem lengths except for the TE mode at $\lambda = 790\,\mathrm{nm}$. Note that the right plot is scaled logarithmically in order to visualize the large differences in cross-coupled power.

3.3. Quantum-theoretical description of (cascaded) parametric down-conversion

Parametric down-conversion, already introduced in Sec. 3.1.1, requires the change of view from the classical description of light to its quantum co-part. Doing so is equivalent to treat light in terms of photons, which show different behavior for different types of light. In the following section we will give some insight on the different types of ligth.

3.3.1. Types of light and photon number states

Statistical considerations on the ideal measurement of photons in a well-defined temporal durations let us distinguish between bunched light, coherent light and anti-bunched light. The differences become clearer, when the we look at the probability distributions and their variances. While bunched light at an average photon number $\langle n \rangle$ shows a Planck probability distribution for an n-photon state per unit time with variance $(\Delta n)^2_{\mathrm{th}} = \langle n \rangle^2 + \langle n \rangle$, coherent light exhibits Poisson-distributed photon-number statistics with smaller variance $(\Delta n)^2_{\mathrm{coh}} = \langle n \rangle$. By contrast, anti-bunched light in terms of a single photon, being ideally measured per unit time, would require a variance of zero. However, as soon as the detected light shows variances smaller than that of coherent light, it is considered to be genuine quantum light, because

$0 \leq (\Delta n)^2_{\text{quant}} < \langle n \rangle$ cannot be explained with classical theories [122].

Photons can be described as the quantized energy states of the 1D harmonic oscillator. Defining creation and annihilation operators,

$$\hat{a} = \frac{1}{\sqrt{2m\hbar\omega}} \left(m\omega\hat{x} + i\hat{p}_{\text{x}} \right) \tag{3.90}$$

$$\hat{a}^\dagger = \frac{1}{\sqrt{2m\hbar\omega}} \left(m\omega\hat{x} - i\hat{p}_{\text{x}} \right), \tag{3.91}$$

with $\hat{x}$ and $\hat{p}_{\text{x}}$ being the position and the momentum operators, we can show that the photon number operator

$$\hat{n} = \hat{a}^\dagger \hat{a}, \tag{3.92}$$

$$\hat{n}|n\rangle = n|n\rangle \tag{3.93}$$

is the representative of the number of excited energy quanta of the quantum harmonic oscillator, while the photon number states

$$|n\rangle = \frac{1}{\sqrt{n!}} \left(\hat{a}^\dagger \right)^n |0\rangle \tag{3.94}$$

correspond to the energy eigenvalues at angular frequency ω of the 1D quantum harmonic oscillator. The creation and annihilation operators act on photon number states as follows:

$$\hat{a}^\dagger|n\rangle = \sqrt{n+1}|n+1\rangle \tag{3.95}$$

$$\hat{a}|n\rangle = \sqrt{n}|n-1\rangle \tag{3.96}$$

$$\hat{a}|0\rangle = 0. \tag{3.97}$$

With these definitions we defined what is referred to as the photon-number base in the Fock space, and we are able to represent, e. g., a coherent state $|\alpha\rangle$ in the photon-number representation as

$$|\alpha\rangle = e^{-|\alpha|^2} \cdot \sum_{n=0}^{\infty} \frac{\alpha^2}{\sqrt{n!}} |n\rangle. \tag{3.98}$$

The photon number statistics of coherent states results from projecting them on the photon number states:

$$\langle n|\alpha\rangle = e^{-\frac{|\alpha|^2}{2}} \cdot \frac{\alpha^n}{\sqrt{n!}}, \tag{3.99}$$

and we identify the equivalence to Poisson statistics, because $P(n) \equiv |\langle n|\alpha\rangle|^2$. The expectation value of a coherent state's photon number operator is proportional to the intensity of the classical field:

$$\langle \alpha|\hat{n}|\alpha\rangle = \alpha^*\alpha, \tag{3.100}$$

and the mean photon number is given by $\langle n \rangle = |\alpha|^2$.

A versatile figure of merit for distinguishing quantum from classical light is to measure the degree of second-order coherence [122,123]. To verify anti-bunching we might implement a balanced beam splitter with two input mode fields, $\mathcal{E}_1$ and $\mathcal{E}_2$, and two output mode fields, $\mathcal{E}_3$ and $\mathcal{E}_4$. The individual outputs are connected with photon detectors. The electric signals of the detection events, being proportional to the light intensities $I(t)$, are fed to a coincidence counter and analyzed for different times of arrival $t + \tau$. The experimental configuration is commonly called Hanbury Brown-Twiss (HBT) setup [124]. By scanning for different delays τ we can compute the second-order correlation function [122, 125], which quantifies intensity fluctuations in time

$$g^{(2)}(\tau) = \frac{\langle I(t) \cdot I(t+\tau) \rangle}{\langle I(t) \rangle \langle I(t+\tau) \rangle}. \tag{3.101}$$

In the case of single photons we represent the fields by the annihilation operator such that $\mathcal{E}_i \rightarrow \hat{a}_i$, which we use to write for the output modes

$$\hat{a}_3 = \frac{1}{\sqrt{2}} (\hat{a}_1 - \hat{a}_2), \tag{3.102}$$

$$\hat{a}_4 = \frac{1}{\sqrt{2}} (\hat{a}_1 + \hat{a}_2). \tag{3.103}$$

By analogy to Eq. 3.101 we can calculate the second-order correlation functions for τ and $\tau = 0$ as

$$g^{(2)}(\tau) = \frac{\langle \hat{a}_3^\dagger(t) \cdot \hat{a}_4^\dagger(t+\tau) \langle \hat{a}_4^\dagger(t) \cdot \hat{a}_3^\dagger(t+\tau) \rangle}{\langle \hat{a}_3^\dagger(t) \hat{a}_3(t) \rangle \langle \hat{a}_4^\dagger(t+\tau) \hat{a}_4(t+\tau) \rangle}, \tag{3.104}$$

$$g^{(2)}(0) = \frac{\langle \hat{a}_3^\dagger \cdot \hat{a}_4^\dagger \hat{a}_4 \hat{a}_3 \rangle}{\langle \hat{a}_3^\dagger \hat{a}_3 \rangle \langle \hat{a}_4^\dagger \hat{a}_4 \rangle} = \frac{\langle \hat{n}(\hat{n}-1) \rangle}{\langle \hat{n} \rangle^2}. \tag{3.105}$$

The latter equation holds true, if the second input mode is blocked, i. e. $\hat{a}_2 = |0\rangle$ is the vacuum state. We see directly that for genuine single photons, which means that one photon per time bin impinges the HBT setup, the second-order correlation function at zero delay must be $g^{(2)}(0) = 0$, a fact that cannot be explained by classical theories. Thus, it indicates the quantum nature of single photons. For

Table 3.2.: The values of the second-order correlation function for different types of light are provided. While values of $g^{(2)}(0) \geq 1$ can be explained by classical theory, anti-bunching in a stream of photons exhibits $g^{(2)}(0) < 1$ and is a genuine quantum feature [122].

Classical description	Photon stream	$g^{(2)}(\tau)$	$g^{(2)}(0)$
Chaotic	bunched	≥ 1	$\geq g^{(2)}(\tau)$ and > 1
Perfect coherent	random	1	$= g^{(2)}(\tau)$
not available	anti-bunched	< 1	$< g^{(2)}(\tau)$

coherent light we have $g^{(2)}(\tau) = g^{(2)}(0) = 1$ for any temporal dependence of $I(t)$. It has been found that for the different types of light the second-order correlation function exhibits values as given in Tab. 3.2. A custom version of the HBT setup will be employed in Sec. 6.1.1.

3.3.2. Theory of parametric down-conversion

So-called type-0 parametric down-conversion in nonlinear waveguides as a special case of $\chi^{(2)}$-nonlinear interactions requires the quantum mechanical notation of the three-wave-mixing Hamiltonian. This operator describes the interaction of the quantized electric field operator $\hat{\boldsymbol{E}}(z,t) = \hat{E}^{+}(z,t) + \hat{E}^{-}(z,t)$ with the induced second-order nonlinear polarization operator $\hat{\boldsymbol{P}}^{(2)} = 2\varepsilon_0 \cdot d_{33}^{\text{eff}} \cdot \hat{\boldsymbol{E}}\hat{\boldsymbol{E}}$ along the propagation direction z of our second-order nonlinear waveguide. The description of the second-order polarization is given by analogy to Eq. 3.6 and already includes the highest nonlinear optical tensor element in our lithium niobate waveguides, d_{33}^{eff}. The field operators $\hat{E}^{+}(z,t)$ and $\hat{E}^{-}(z,t)$ are defined by

$$\hat{E}^{+}(z,t) = C' \int \exp\left[-i\left(\omega t + k(\omega) z\right)\right] \hat{a}(\omega)\ \mathrm{d}\omega, \tag{3.106}$$

$$\hat{E}^{-}(z,t) = \hat{E}^{+\dagger}(z,t) = C \int \exp\left[-i\left(\omega t + k(\omega) z\right)\right] \hat{a}^{\dagger}(\omega)\ \mathrm{d}\omega, \tag{3.107}$$

and describe the output and the input fields, respectively. Note that we included all constants in C' and C, respectively and assume slowly varying envelopes as in Sec. 3.2.3. Now, we can write for the general tree-wave-mixing Hamiltonian:

$$\hat{H}^{\text{3wm}}(t) = \int_{\text{Z}} \hat{\boldsymbol{P}}^{(2)}(z,t)\, \hat{\boldsymbol{E}}(z,t)\ \mathrm{dz} + \text{h.c.}, \tag{3.108}$$

which can be analyzed for the individual $\chi^{(2)}$-nonlinear process components by analogy to Sec. 3.1.1, Eq. 3.6 (see, for example, Ref. [10]). Additionally, the Manley-Rowe relations [100] have to be considered in order to rule out unphysical solutions, which otherwise would not obey the energy conservation rule. We identify the term that describes the parametric down-conversion interaction as expressed by

$$\hat{H}^{\text{PDC}}(t) = 2\varepsilon_0 d_{33}^{\text{eff}} \int_{\text{Z}} \hat{E}_{\text{p}}^{+}(z,t) \cdot \hat{E}_{\text{s}}^{-}(z,t) \cdot \hat{E}_{\text{i}}^{-}(z,t)\ \mathrm{dz} + \text{h.c.}, \tag{3.109}$$

where the indices p, s and i stand for the pump, signal and idler wave, respectively. The time evolution of an initial quantum state, $|\Psi(0)\rangle$, can be described by

$$|\Psi(T)\rangle = \hat{\mathcal{T}} \exp\left[-\frac{i}{\hbar} \int_{0}^{\text{T}} \hat{H}^{\text{PDC}}(t)\, \mathrm{dt}\right] |\Psi(0)\rangle, \tag{3.110}$$

where $\hat{\mathcal{T}}$ represents a time-ordering operator, which we assume to play no significant role in our considerations for the low gain regime [126,127]. Note also that Eq. 3.109

represents a tri-linear Hamiltonian, the time evolution cannot be solved analytically. Instead, we make use of the fact that PDC is typically pumped by strong classical fields, which allows us to redefine the pump field as

$$\hat{E}^{+}(z,t) \rightarrow E^{+}(z,t) = \int \alpha_{\mathrm{p}}(\omega_{\mathrm{p}}) \cdot \exp\left[i\left(\omega_{\mathrm{p}} t + k(\omega_{\mathrm{p}}) z\right)\right] \, \mathrm{d}\omega_{\mathrm{p}}, \tag{3.111}$$

where a Gaussian pump envelope $\alpha_{\mathrm{p}}(\omega_{\mathrm{p}}) = A_{\mathrm{p}} \exp\left[(\omega_{\mathrm{p}} - \mu_{\mathrm{p}})^2 / (2\sigma_{\mathrm{p}}^2)\right]$ comprises the complex field amplitude A_{p}, the central pump frequency μ_{p} and the pump bandwidth σ_{p} [128]. Note that this notation explicitly covers ultrafast pumps with broad spectral distributions.

The Hamiltonian describing the PDC process generates the unity transformation

$$\hat{U} = \exp\left[-\frac{i}{\hbar} \int \hat{H}^{\mathrm{PDC}}(t) \, \mathrm{d}t\right], \tag{3.112}$$

of an input vacuum state. Neglecting the time-ordering effects and performing the time-integration directly provides us with the delta-distribution $2\pi\delta(\omega_{\mathrm{s}} + \omega_{\mathrm{i}} - \omega_{\mathrm{p}})$, which, in turn, allows for the integration over the pump frequency ω_{p}. Equation 3.112 transforms to

$$\hat{U}' = \exp\left[-\frac{i}{\hbar}\left(A' \int_{-\mathrm{L}/2}^{\mathrm{L}/2} \int\int \alpha_{\mathrm{p}}(\omega_{\mathrm{s}} + \omega_{\mathrm{i}}) \exp\left[i\Delta k z\right] \hat{a}_{\mathrm{s}}^{\dagger}(\omega_{\mathrm{s}}) \, \hat{a}_{\mathrm{i}}^{\dagger}(\omega_{\mathrm{i}}) \, \mathrm{d}\omega_{\mathrm{i}} \, \mathrm{d}\omega_{\mathrm{s}} \, \mathrm{d}z\right)\right]. \tag{3.113}$$

Here A' includes the constants, and $\Delta k = k_{\mathrm{p}}(\omega_{\mathrm{s}} + \omega_{\mathrm{i}}) - k_{\mathrm{s}}(\omega_{\mathrm{s}}) - k_{\mathrm{i}}\omega_{\mathrm{i}})$ is the phase-mismatch according to Eq. 3.13. Performing the integration also over the nonlinear interaction length $Z = L$ we can rewrite the unitary operator that describes the conventional guided-wave PDC process in the low gain regime, as pursued in parts of this thesis:

$$\hat{U} = \exp\left[-\frac{i}{\hbar}\left(A \int\int \alpha_{\mathrm{p}}(\omega_{\mathrm{s}} + \omega_{\mathrm{i}}) \, \phi(\omega_{\mathrm{s}}, \omega_{\mathrm{i}}) \, \hat{a}_{\mathrm{s}}^{\dagger}(\omega_{\mathrm{s}}) \, \hat{a}_{\mathrm{i}}^{\dagger}(\omega_{\mathrm{i}}) \, \mathrm{d}\omega_{\mathrm{i}} \, \mathrm{d}\omega_{\mathrm{s}}\right)\right], \tag{3.114}$$

where A comprises the constants. The corresponding quasi-phase-matching function $\phi(\omega_{\mathrm{s}}, \omega_{\mathrm{i}}) = \mathrm{sinc}(\Delta k L/2)$, including the phase mismatch Δk, can be combined with the pump distribution $\alpha_{\mathrm{p}}(\omega_{\mathrm{s}} + \omega_{\mathrm{i}})$ in order to describe the joint spectral amplitude function of the PDC:

$$f(\omega_{\mathrm{s}}, \omega_{\mathrm{i}}) = \alpha_{\mathrm{p}}(\omega_{\mathrm{s}} + \omega_{\mathrm{i}}) \, \phi(\omega_{\mathrm{s}}, \omega_{\mathrm{i}}). \tag{3.115}$$

We note that the pump distribution in conjunction with the quasi-phase-matching function both determine the spectral correlations of the PDC process. The unitary operation $\hat{U}|\Psi\rangle(0) = \hat{U}|0,0\rangle$ provides us with the output state

$$|\Psi\rangle(T) = \left(1 - \frac{|\kappa|^2}{2}\right)|0\rangle + \kappa|1_{\mathrm{s}}, 1_{\mathrm{i}}\rangle + \kappa^2|2_{\mathrm{s}}, 2_{\mathrm{i}}\rangle + \ldots. \tag{3.116}$$

Here, the parameter κ is the coupling strength of the process defined by the nonlinear optical tensor element, the field overlap integral, the dispersive properties of the nonlinear material, and the length of the periodically inverted grating structure inside the waveguide. The parameter κ is specifically dependent on how well the quasi-phase-matching condition is met. Note that the subscripts s and i label the signal and the idler mode, respectively. We see that the generation of higher-order photon pairs is intrinsic to the PDC process and requires careful treatment of the term *single* photon generation.

While spectrally narrow pump beams usually lead to strictly correlated PDC states in lithium niobate, broad pump beams in conjunction with engineered quasi-phase-matching functions in potassium titanyl phosphate can yield pure single-mode PDC states, which are spectrally decorrelated [50, 129].

The theoretical description of cascaded parametric down-conversion, where the signal photons of a primary PDC process are exploited in order to pump a secondary PDC process in order to generate photon-triplet states, is non-trivial. This is due to the necessity to describe the secondary PDC process in terms of the tri-linear Hamiltonian similar to Eq. 3.110. However, we can write for the overall unitary operation [91]

$$\hat{U} = \hat{U}_2\hat{U}_1, \tag{3.117}$$

$$= \exp\left(-\frac{i}{\hbar}\int_0^{\mathrm{T}_2}\hat{H}_{\mathrm{PDC},2}\left(t\right)\,\mathrm{dt}\right)\exp\left(-\frac{i}{\hbar}\int_0^{\mathrm{T}_1}\hat{H}_{\mathrm{PDC},1}\left(t\right)\,\mathrm{dt}\right), \tag{3.118}$$

$$= \exp\left[-\frac{i}{\hbar}\left(A_2\int\int\hat{a}_{\mathrm{p}}\left(\omega_{\mathrm{s}2}+\omega_{\mathrm{i}2}\right)\phi_2\left(\omega_{\mathrm{s}2},\omega_{\mathrm{i}2}\right)\hat{a}^{\dagger}_{\mathrm{s}2}\left(\omega_{\mathrm{s}2}\right)\hat{a}^{\dagger}_{\mathrm{i}2}\left(\omega_{\mathrm{i}2}\right)\mathrm{d}\omega_{\mathrm{i}2}\mathrm{d}\omega_{\mathrm{s}2}\right)\right]$$
$$\times\exp\left[-\frac{i}{\hbar}\left(A_1\int\int\alpha_{\mathrm{p}}\left(\omega_{\mathrm{s}1}+\omega_{\mathrm{i}1}\right)\phi_1\left(\omega_{\mathrm{s}1},\omega_{\mathrm{i}1}\right)\hat{a}^{\dagger}_{\mathrm{s}1}\left(\omega_{\mathrm{s}1}\right)\hat{a}^{\dagger}_{\mathrm{i}1}\left(\omega_{\mathrm{i}1}\right)\mathrm{d}\omega_{\mathrm{i}1}\mathrm{d}\omega_{\mathrm{s}1}\right)\right], \tag{3.119}$$

where $\omega_{\mathrm{s}1}=\omega_{\mathrm{s}2}+\omega_{\mathrm{i}2}$, and $\hat{U}_1$ is given by a re-labeled version of Eq. 3.114. The pre-factors A_1 and A_2 include the constants for the individual conversion processes, and $\phi_i\left(\omega_{\mathrm{s}i},\omega_{\mathrm{i}i}\right),\ i=1,2$ describe the quasi-phase-matching conditions of the PDC processes. The solution to Eq. 3.119 is highly non-trivial, but treating it by means of first-order perturbation theory allows for an approximation of the generated state:

$$|\Psi\left(T\right)\rangle = \hat{U}_2\hat{U}_1|0_{\mathrm{s}1},0_{\mathrm{i}1},0_{\mathrm{s}2},0_{\mathrm{i}2}\rangle, \tag{3.120}$$

$$\approx -i\kappa_1|1_{\mathrm{s}1},1_{\mathrm{i}1},0_{\mathrm{s}2},0_{\mathrm{i}2}\rangle-\kappa_2\kappa_1|0_{\mathrm{s}1},1_{\mathrm{i}1},1_{\mathrm{s}2},1_{\mathrm{i}2}\rangle \tag{3.121}$$

where the vacuum output state is ignored. The first term in Eq. 3.121 describes the generation of a photon pair in the primary PDC stage, whereas the second term represents the generation of a photon triplet [91]. The latter is what we aim for to generate and to characterize in this thesis in Sec. 7.2. Note that the approximation made here is not taking higher-order photon contributions of the first PDC process

into account, but we will see that for pulsed cascaded parametric down-conversion we have to take these effects into account. At this point we want to emphasize that more theoretical and numerical effort is necessary in the future in order to describe the cascaded PDC process such that higher-order photon contributions are taken into account. It would also be interesting to know, how the individual quasi-phase-matching conditions have to be engineered in order to maximize the efficiency of the overall photon triplet generation process.

Conclusion

In this theoretical section we explained the optical effects caused by the second-order nonlinear polarization in dielectric materials like lithium niobate. We found that $\chi^{(2)}$-nonlinear processes like second-harmonic generation, sum-frequency generation and parametric down-conversion require quasi-phase-matching in order to generate non-negligible output, when the propagation of the three mixing fields propagate co-linearly as in the waveguides we use in this thesis. The quasi-phase-matching condition can be achieved technologically by periodically inverting the sign of the the second-order nonlinear susceptibility inside the medium as we will explain more detailed in Chapter 4.

For sum-frequency processes we inferred a $\sin^2\left(\sqrt{\mathbf{P}_1}\right)$-proportionality of the output power on the stronger of the two input fields, which means that in principle unit conversion of the weaker input field can be achieved. By contrast, the second-harmonic generation output power has been found to respond quadratically on the fundamental input power in the regime of a non-depleted pump field on the one hand. On the other hand, in a depleted-pump scenario, the SHG power asymptotically reaches a maximum, which corresponds to quasi-unit conversion efficiency.

Modeling the diffusion of titanium into a lithium niobate substrate provided us with predictable local refractive index changes, which lead to the formation of channel waveguides. We explained the effective-index method in more detail, because it will be exploited to model the required modes in the next chapters. As a specific type of waveguide structure, we modeled a directional coupler in the local normal mode description in conjunction with the FEM model developed by Strake et al. [107]. We also anticipated the behavior of the coupler implemented to the integrated device in order to compare with the experimental results in Sec. 5.3.

Furthermore, we gave a theoretical description of parametric down-conversion in its conventional and in a cascaded manner. We found for cascaded PDC that more theoretical and numerical work is necessary in the future in order to solve the trilinear Hamiltonian describing the second PDC process in the cascade.

CHAPTER 4

Technology in lithium niobate - A toolbox for integrated quantum optical devices

An overview of the broad range of properties of lithium niobate beneficial for nonlinear optics is given. We briefly discuss different methods for the fabrication of passive wave-guiding structures and focus on the diffusion of titanium to the congruent Z-cut material with X-propagation. Furthermore, a technological recipe as well as typical outcomes for periodically poled structures are described in detail. Finally, we explain the design considerations, the layout parameters and the optical coatings for the multi-functional device with active and passive components on-chip, which all together form the physical basis for the experimental data provided in this thesis.

Contents

4.1. Lithium niobate - an outstanding material for integrated quantum optics

Ever since the intentional development of chemical agents had been pursued, their applicability in order to improve human lifestyle has been at the heart of scientific research. Materials with multi-purpose properties - artificially created, purified or

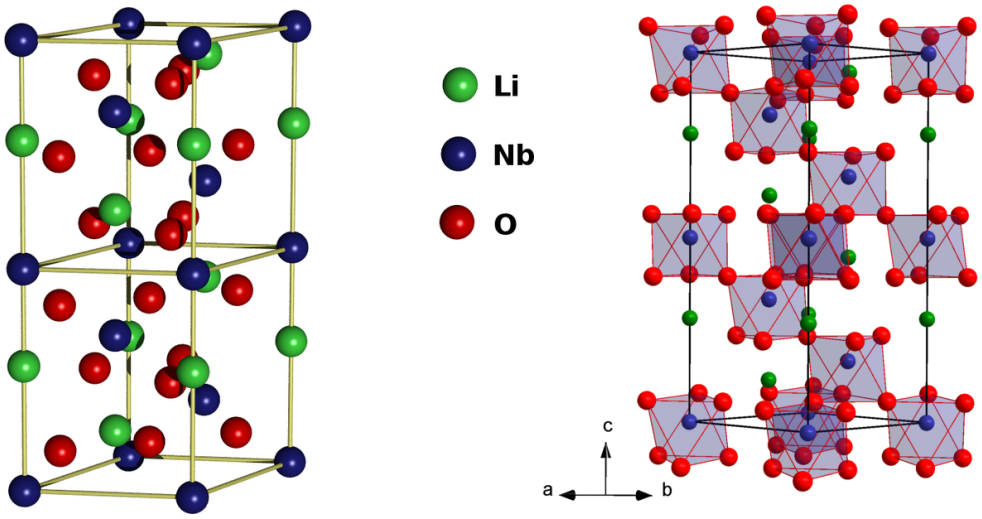

Figure 4.1.: The unit cell of lithium niobate: simple schematic (left [132]) and schematic highlighting oxygenic octahedra (right [133]).

modified elements - gained overwhelming importance to our everyday life, such as steel, silicon, lithium, or fossil fuel.

In a series of outstanding solids, one artificial crystalline material has been playing a predominant role for acousto-optical and nonlinear-optical applications over the last 50 years due to its unique mixture of material properties: lithium niobate ($LiNbO_3$). It was reported on first by Zachariasen [130] and recognized to be ferroelectric by Matthias and Remeika [131].

While structurally belonging to the trigonal crystal class, $LiNbO_3$ shows rotational symmetry around its crystallographic Z-axis, which is commonly labeled as the optical c-axis. Therefore, the point group $3m$ and the space group $R3c$ can be attributed. Two different schematics of the unit cell are depicted in Fig. 4.1. We see in both that each niobium cation Nb^{5+} is surrounded by 6 oxygen atoms arranged as a slightly deformed octahedron. The $[NbO_6]$ substructures share oxygen atoms at their corners diagonally, such that one hexagonal unit cell contains 16 oxygenic octahedra. The oxygen sub-lattice forms gaps along the c-axis, which are filled by niobium cations, vacancies and lithium cations in series of Nb^{5+} - vacancy - Li^{+} - Nb^{5+} - vacancy - Li^{+}... . Hence, each lithium cation is surrounded by 12 oxygen atoms with different distances.

The diagonal interconnection of oxygen octahedra, different Li-O distances and the alternating occupation of octahedral gaps lead to a non-inversion symmetry and to spontaneous polarisation of the crystal - two features, which all favorable properties of $LiNbO_3$ are directly related to. We can deduce its optical $\chi^{(2)}$-nonlinearity and ferroelectricity, its piezo-electric, pyro-electric, photo-refractive properties and optical anisotropy from the crystallographic structure. The following subsections will

emphasize the benefits of these $LiNbO_3$ properties for nonlinear (quantum-) optics in more detail. In this thesis, we concentrate only on the so called congruent lithium niobate (CLN) in the crystal Z-cut and X-propagation configuration, which is the most common and cheapest modification of $LiNbO_3$ under Czochalski growth [134] conditions. It shows a slight lithium deficiency with a Li/Nb ratio of 0.94553 compared to the stoichiometric material (=1).

4.1.1. Birefringence and dispersion

The rotational symmetry of the $LiNbO_3$ crystals around its optical c-axis determines its uniaxial birefringence, which means that the refractive indices of the material depend on the polarization of incident light fields on the one hand and on the angle of incidence relative to the crystallographic axes on the other hand. The grade of birefringence is usually given by the difference of the ordinary refractive (n_o) and the extraordinary refractive indices (n_e). Both are considered to be dependent on the wavelength, i. e., they show dispersion, and also on temperature. Among other mathematical forms [135, 136] the following expression is used for the calculation of the extraordinary refractive index (RI) [137]:

$$n_e^2(\lambda) = A_{1,e} + B_{1,e}\cdot f + \frac{A_{2,e} + B_{2,e}\cdot f}{\lambda^2 - (A_{3,e} + B_{3,e}\cdot f)^2} + \frac{A_{4,e} + B_{4,e}\cdot f}{\lambda^2 - A_{5,e}^2} - A_{6,e}\lambda^2, \quad (4.1)$$

where $f = (T - 24.5)(T + 570.82)$ is a unit-less temperature correction term with T being the temperature in the Celsius scale. The coefficients $A_{k,e}$ and $B_{l,e}$ account for oscillatory properties of the involved ion species and for the temperature dependence, respectively.

By contrast, the ordinary refractive index for congruent, undoped lithium niobate can be described with a different mathematical expression [138]:

$$n_o^2(\lambda) = A_{1,o} + \frac{A_{2,o} + B_{1,o}\cdot F}{\lambda^2 - (A_{3,o} + B_{2,o}\cdot F)^2} + B_{3,o}\cdot F - A_{4,o}\lambda^2, \quad (4.2)$$

where $F = (T - 24.5)(T + 546)$ accounts for the temperature. Note that this dispersion relation has been derived and optimized for type-I noncritical phase-matching processes in bulk congruent lithium niobate by difference-frequency generation in the range of $2159\,\mathrm{nm} \leq \lambda_\mathrm{DFG} \leq 3235\,\mathrm{nm}$. The relative uncertainty in the visible and near-infrared range is around 1.8×10^{-4}. Lacking a more precise temperature dependent Sellmeier expression in the literature for QPM processes in undoped LN, we use equation 4.2 for our refractive index calculations.

In the Appendix A the coefficients and RI dispersion curves for the wavelength range from 350 nm to 2500 nm at room temperature and at 170° C are given, respectively. We note that not only the ordinary refractive index is in general larger than the extraordinary refractive index, but also that with higher temperature both

RIs have slightly increased values. Immediately, we conclude that a tuning of the temperature will change the optical properties of CLN, which is beneficial not only for linear optical applications, but it will also play a significant role for the nonlinear applications pursued in this thesis, as we will show in more detail in subsequent chapters.

4.1.2. Second-order nonlinearity and electro-optic Pockels effect

The most prominent feature of CLN is connected to the lacking inversion symmetry of the crystallographic system. This finds its expression in the second-order nonlinear susceptibility tensor $\chi^{(2)}_{ijk}$, which is related to the nonlinear optical tensor, $d_{ijk} = \frac{1}{2}\chi^{(2)}_{ijk}$ as mentioned already in Sec. 3.1.2. A brief derivation of the nonlinear optical tensor with respect to symmetry considerations of lithium niobate is given in the Appendix B.

For the different crystal geometries commonly applied in research and industry, i. e. Z-cut X-propagation and X-cut Z-propagation, only the d_{33} and d_{31} elements are of significant relevance. At a wavelength of 1064 nm the values of reported nonlinear optical tensor elements range from $25.2 \leq d_{33} \leq 34\,\mathrm{pm\,V^{-1}}$ and from $6.5 \leq d_{31} \leq 10.9\,\mathrm{pm\,V^{-1}}$, respectively [95]. The former is important for applications, since it allows for most efficient nonlinear three-wave mixing-processes.

Additionally, every crystallographic system with a non-inversion symmetry also exhibits changes of the refractive indices, when static or low-frequency electric fields are applied. This effect is commonly referred to as the linear electro-optic or Pockels effect, since the index changes show linear dependencies on the external field strength [99]. Without deriving the mathematical formalism thoroughly (see for example Ref. [101]), we can state that the linear electro-optic tensor elements r_{ijk} are related to the elements of the nonlinear optical tensor via

$$d_{ijk} = \frac{\epsilon_i \epsilon_j}{2} r_{ijk}, \tag{4.3}$$

where the ϵ represent the dielectric functions of the material, and are related to the complex refractive indices, $\sqrt{\Re\{\epsilon\} + \imath\Im\{\epsilon\}} = n + \imath k$. If we assume no absorption of the material, the imaginary parts of the refractive indices vanish and we get the individual $\epsilon = n^2$. The precondition of no absorption is fulfilled very well over a broad spectral range ($350 \leq \lambda \leq 4500\,\mathrm{nm}$) for congruent lithium niobate, especially in the visible and the telecom wavelength region. For this reason and due to the large electro-optical coefficients, the different configurations of lithium niobate are excellent material bases for commercial and scientific electro-optic modulator (EOM) [139]. In integrated nonlinear optics, phase-shifters [140–142], polarization-controllers [143, 144], Mach-Zehnder-interferometers [145–147] and directional couplers [148, 149] are used for a multitude of applications.

Besides its second-order nonlinear properties, lithium niobate also exhibits third-order nonlinear characteristics like the electro-optic Kerr effect, self-focusing, self-phase- modulation, and it provides four-wave-mixing processes. Since $\chi^{(3)}$-processes

are much more inefficient than $\chi^{(2)}$-processes, they require much larger intensities of incident light fields to become significant. We note but discard them for further application considerations.

4.1.3. Piezo-electric, acousto-optic and photorefractive effects

In the field of classical integrated optics, other properties in lithium niobate have been successfully applied, such as the generation of surface acoustic wave (SAW) via strain-induced changes of the refractive indices. These acousto-optic properties found a variety of applications, most prominently in acousto-optic modulator (AOM) [150–152], which allow for frequency tuning of laser light, for switching of the quality factors or for active mode-locking of lithium niobate-based pulsed lasers.

Acousto-optical applications would not work in lithium niobate if the material was not also exhibiting photo-elastic and piezo-electric properties, which are directly related to the symmetry of the unit cell and its ferroelectric spontaneous polarization. Piezo-electricity is based on the generation of electric fields under the influence of stress or strain: if the unit cell with lack of inversion-symmetry is stretched or compressed, the distances of the involved ions and sub-lattices change, and electric dipole moments are induced. Macroscopically, the accumulation of the dipole moments or - per unit volume - polarization leads to the build-up of electric fields, which may change the refractive index of the material locally via the electro-optic effect. Likewise, acousto-optically induced stress and strain can change the birefringence of lithium niobate via the photo-elastic effect (see, for example, Ref. [101]). Depending on the crystal cut of the material and the involved tensor elements, the acousto-optical properties in lithium niobate are often an overlap of both, photo-elasticity and the piezo-electric/electro-optic effect.

Another phenomenon is the photo-refractive effect [153], which is often referred to as optical damage. Large intensities of incident light in the range of visible and near-infrared (IR) wavelengths, can induce electric fields that change the refractive index of the material locally via the electro-optic effect, especially in waveguide (WG) structures. As the waveguide's confinement for optical modes depends on the effective refractive index, these local changes cause local fluctuations in the confinement, i. e. the intensity changes dynamically. For visible light, this effect can be visualized by mapping the near field of the WG mode to a screen, and is characterized by uncontrolled blurring of the mode structure. Since this effect depends on the atomic species that build the waveguide, much effort has been taken to decrease the photo-refractive damage for high-power continuous-wave applications [154, 155]. On the other hand, photo-refraction can be employed to inscribe holograms to the material system and, thus, to store information [156].

In this work, we are aware of the general properties of lithium niobate, but restrict ourselves on the congruent material in the Z-cut with X-propagation. Except for the outlook, we do not take electro-optically active elements or applications into

account. Instead, we base this thesis and our device design on the combination of passive guided wave structures with active wavelength conversion regions, the latter of which rely on the largest $\chi^{(2)}$-nonlinear coefficient (i. e. d_{33}) in order to provide the most efficient type-0 quasi-phase-matched processes possible.

4.2. Waveguide Fabrication Techniques

In the last four decades a variety of different techniques has been developed and pushed to the limits in order to fabricate waveguides in lithium niobate. We can find several ways of waveguide classification, be it on a structural or a material-related basis. The former classification divides the waveguides into planar slabs [157], two-dimensional ridges [23,158], slots [159], strips [25] or buried channels [160–163] being either metal-diffused [25], ion-exchanged [164], laser-written [165] or sawed [166]. The latter classification refers to the chemical agents brought into the bulk LN. Among others, the most common agents for diffusion-based waveguide fabrication are hydrogen, zinc [167] and titanium [25]. However, all of the techniques aim for a well-defined local increase of the refractive index with respect to the substrate in order to enable modal confinement of light.

For comparison, we restrict ourselves to the description of two common technologies. Firstly, the creation of buried waveguides by reverse proton exchange (RPE) is briefly explained. Secondly, we provide a deeper insight to the titanium-diffusion technique, which our nonlinear quantum-optical device is fabricated of.

We describe first the technological preparation of the LN substrates prior to any waveguide fabrication. Several steps are necessary to provide an optimized photolithographic processing. As shown schematically in Fig. 4.2, we start with a 12 mm wide, 0.5 mm thick and up to 100 mm long sample, which is cut from a 10-inch Z-cut wafer such that its length direction is parallel to the crystallographic X-axis.

Along the X-direction, we carefully grind the edges of the surface in an angle of 2◦ in order to provide homogeneous layers of spin-coated photo-resist structures in later technology steps. After this, we clean the substrates carefully in a three-step procedure, which removes organic and inorganic residues on the polished +Z-surface. Hereafter, the samples are ready-to-use for any further technological processing steps.

4.2.1. Proton exchange, annealing and burying of waveguides

The probably most commonly applied technique to fabricate low-loss waveguides with good resistance to photo-refractive damage effects is the so called proton exchange (PE). Among other chemical agents, benzoic acid [164] represents the standard material for PE, since it is easy to handle in clean-room facilities, it offers low melting temperatures, comparably large diffusion constants and, thus, requires acceptable technological effort for preparing the waveguides.

The proton exchange technique leads to an increase only of the extraordinary refractive index of lithium niobate, whereas the ordinary index is reduced. This means, that with this type of waveguides, only one polarization of light can be guided: in Z-Cut congruent LN, we lose the degree of freedom of having access to type-II QPM nonlinear processes, which involve transverse electric (TE) polarized light. It also restricts applications, which include integrated electro-optical polarization controllers or the generation of polarization-entangled photons, to other technological approaches. Another drawback of pure PE processing is its tendency to destroy the nonlinear properties of lithium niobate, since large amounts of incorporated hydrogen lead to phase changes [168] and significantly deform the crystallographic unit cell towards an inversion-symmetric lattice [169]. By heat treatment of the material in the so-called annealed proton exchange (APE) technique [170] or with a direct fabrication method, the so-called soft proton exchange (SPE) [171], it is possible to restore the nonlinear coefficient or even keep the beneficial α-phase of the material.

Nevertheless, proton exchanged waveguides offer two striking arguments in terms of applicability in quantum optics: by burying the waveguides after the annealing step, a symmetrization of the incorporated proton concentration profile is possible [114]. If we assume - for simplicity - a linear dependence of the local refractive index increase, this means that the index profile can be made symmetric, too. Taking normal mode dispersion into account, the centers of mass of modes at different wavelengths overlap better than for APE waveguides, which are strongly asymmetric. The immediate benefit is a higher nonlinear conversion efficiency on the one hand, while on the other hand also the coupling to modes in optical fibers can be significantly increased. The group of Fejer and co-workers reported the world record in terms of conversion efficiency for second harmonic generation [172], being a manifold higher than for PE or APE waveguides.

4.2.2. Titanium diffusion for ultra-low loss waveguide structures

Applied quantum optics requires devices with extremely low loss. Promising approaches include the integration of multiple quantum optical functionalities to monolithic chips [63,65,66,68,70,71,74,173–177]. We chose to pursue the path of fabricating integrated devices in LN waveguide structures by titanium-diffusion, since it is known from classical nonlinear optics to provide the lowest scattering loss [84]. The technological basis also allows for all of the aforementioned benefits of the substrate material.

In order to generate waveguides structures in Ti:LN, we start with the edge-grinded and cleaned chips - as discussed in the introduction of this section -, and we deposit highly pure titanium on the -Z-face via electron-beam evaporation in an evacuated chamber with rotary calotte. This yields a uniform titanium thickness of 76 nm over the whole sample surface. The titanium layer thickness was chosen such that eventually our waveguides show single-mode operation at telecom wavelengths from 1500 nm up to around 1650 nm.

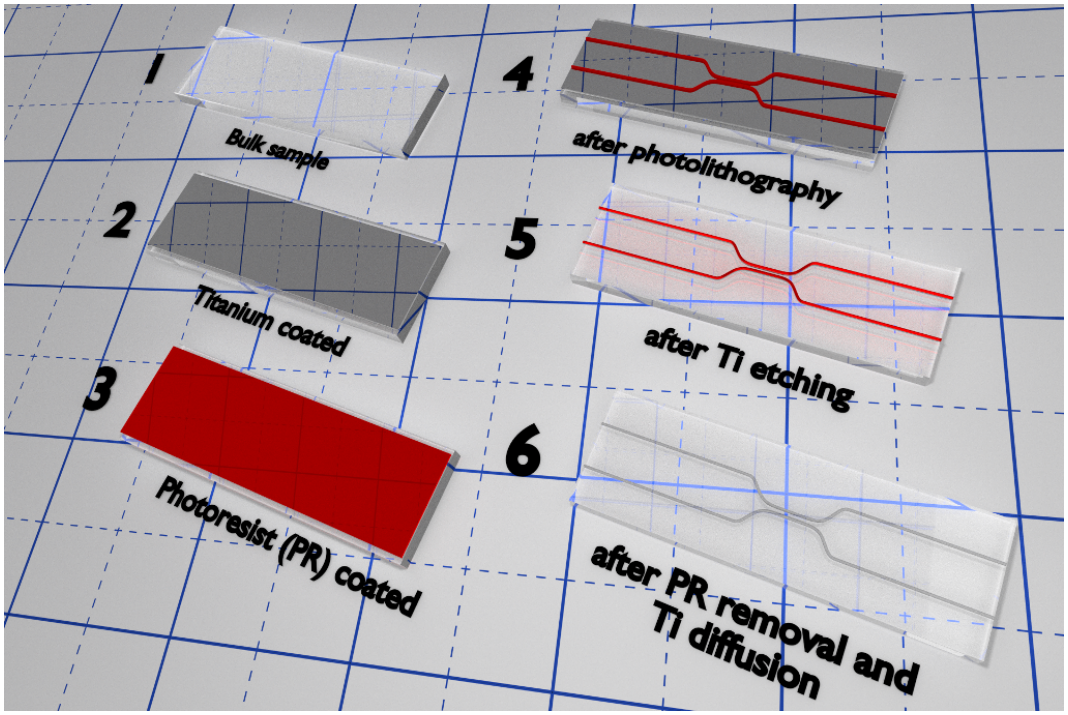

Figure 4.2.: Overview of fabrication steps for titanium-diffused waveguides.

As depicted in Fig. 4.2, we subsequently deposit a homogeneous layer of positive photo-resist (PR) onto the titanium with a spin-coater, resulting in a PR thickness of few micrometers. Since it still contains a certain amount of solvents, we put the sample in an oven at elevated temperature for several minutes minutes in order to solidify the PR. After gently cooling back to room temperature, the resist is ready for temporally limited exposure with ultra-violet (UV) light through a contact mask, which contains the desired structural information of the waveguides. The positive resist allows for the generation of structures as written on the mask, i.e. stripes on the mask will yield stripes in the PR after development, since the UV light breaks the molecular structure of the resist and increases its solubility in a developing agent.

After the development for a few seconds, the photo-resist requires a second heat treatment above the temperature, where the resist becomes liquid again, for several minutes in order to stabilize the edges of the developed structures.

Once the waveguide structures are situated on top of the titanium, we etch the latter without temporal delays in order to prevent oxidization. At slightly above room temperature, the sample is immersed into a mixture of water, hydrogen peroxide and ammonium for a few minutes. Hereafter, the uncovered titanium layer vanished and we remain with PR-covered Ti stripes of the desired nominal width. A short-term bath in acetone removes the residual PR and we are left with the wanted titanium structures.

In general, the thickness and the width of the Ti-structures define the reservoir of material to diffuse fully into the substrate [107]. Thus, we check the optical quality control of these two parameters via UV-filtered bright field light microscopy combined with appropriate analysis software tools.

In the next step, we put the sample in a platinum box and into a three-zone tube oven with calibrated temperature profile along its symmetry axis. The diffusion of the titanium takes place at 1060°C, where the oven is heated up within 1.5 hours, kept there for 8.5 hours in an oxygen atmosphere in order to prevent reduced states of incorporated photorefractive centers. During diffusion of titanium into the lithium niobate bulk material, lithium oxide diffuses out of the substrate, and it builds an amorphous structure of around 30 microns in thickness especially on the -Z face of the substrate. After slow cooling down to room temperature, we carefully grind the backside of our waveguide device in a planar manner, since the Li_2O layer would prevent the electric field poling as described in the next section.

4.3. Periodic domain inversion

The conversion efficiency of co-linear three-wave-mixing processes in waveguide structures usually suffers from mismatched phases of the involved fields, since material dispersion at different wavelengths leads to different phase velocities. Field amplitudes generated at different positions inside a waveguide will on average not add up (or interfere constructively) to significant strengths and, thus, output powers due to different phase relations will remain negligible in all types of waveguided three-wave-mixing processes.

A well-understood method to overcome this issue is to introduce an artificial compensation mechanism for the accumulated phase difference. In ferroelectric LN, we can achieve the QPM condition by periodic inversion of the spontaneous polarization. To do so, it is recommended to apply an electric field, which is larger than the coercive field strength of the crystal, to specially masked (periodic) areas. Due to the hysteresis of the internal polarization with respect to electric fields, we locally change the spontaneous polarization of ferroelectric LN by moving the lithium ions with respect to the oxygen octahedra sub-lattice.

According to the rules of energy and momentum conservation, the period of such a grating is strongly dependent on the chosen wavelength combination of the $\chi^{(2)}$-nonlinear process as well as on the type of process in terms of field polarizations.

Table 4.1 shows a brief overview over different PDC processes and the required periodicities of the poled gratings in titanium-diffused periodically poled lithium niobate (Ti:PPLN) waveguides. Note that we applied the waveguide model of Strake et al. [107, 116]. We recognize that shorter wavelengths involved will require smaller structures, and type-II nonlinear processes need smaller periodicities than type-0 processes. Also very interesting, but technologically most challenging are processes based on counter-propagating fields inside waveguides [73, 178–180]. Here, the necessary periodicities reach the sub-micron region, which has not been achieved in

Table 4.1.: Calculated poling periods for typical parametric down-conversion processes in Ti-diffused waveguides in lithium niobate.

$\chi^{(2)}$**process**	**polarizations**	**wavelengths** $[nm]$	Λ_G $[\mu m]$
PDC type 0	$e \to e + e$	$532(p) \to 803(s) + 1575(i)$	6.74
PDC type II	$o \to o + e$	$532(p) \to 803(s) + 1575(i)$	4.83
PDC type II	$o \to e + o$	$532(p) \to 803(s) + 1575(i)$	3.97
PDC type 0	$e \to e + e$	$775(p) \to 1550(s) + 1550(i)$	16.63
PDC type II	$o \to o + e$	$775(p) \to 1550(s) + 1550(i)$	9.29
PDC type 0 (idler counter prop.)	$e \to e + e$	$532(p) \to 803(s) + 1575(i)$	~ 0.348
PDC type 0 (signal counter prop.)	$e \to e + e$	$532(p) \to 803(s) + 1575(i)$	~ 0.178
PDC type II (idler counter prop.)	$o \to o + e$	$775(p) \to 1550(s) + 1550(i)$	~ 0.337
PDC type II (signal counter prop.)	$o \to o + e$	$532(p) \to 803(s) + 1575(i)$	~ 0.171

lithium niobate with state-of-the-art poling techniques over considerably large device length scales.

For the devices considered and characterized in this thesis, we concentrate on a standard and reliable method for periodic domain inversion: the pulsed electric field poling [181–184]. This technique has the benefit, that it can be employed using optical lithographic preparation steps. Since the poling pattern is imprinted to a photo-resist via vacuum contact lithography through masks of extremely high period accuracy (written with electron beam lithographic methods), practically no errors occur in the otherwise exponentially dependent phase-matching conditions [179]. Besides, pulsed electric field poling does not necessitate sample thicknesses below 0.5 mm in order to achieve periodicities larger than 6.5 μm homogeneously over several millimeters of length due the difference of vertical and lateral domain growth [185]. For poling duty-cycles close to the perfect 50/50 ratio, we can compensate this difference by off-equilibrium duty-cycles on the lithography mask and, subsequently, the photo-resist [98].

In detail, the photo-resist for poling patterns acts as an insulator, which generates a contrast in the applied electric field between regions covered with PR (smaller field strength) and areas without PR (higher field strength, to be poled). This contrast, although of the order of only $\sim$ 0.5% for half millimeter thick samples and the respective PR thicknesses, suffices to allow the nucleation of inverted domains only in uncovered regions, where the liquid electrode contacts the LN surface. Once the nucleation has taken place, the domains grow spike-like through the crystal until they reach its backside [185]. Simultaneously, lateral growth accompanies the vertical growth, but with around 2 orders of magnitude lower velocities. Thus, a

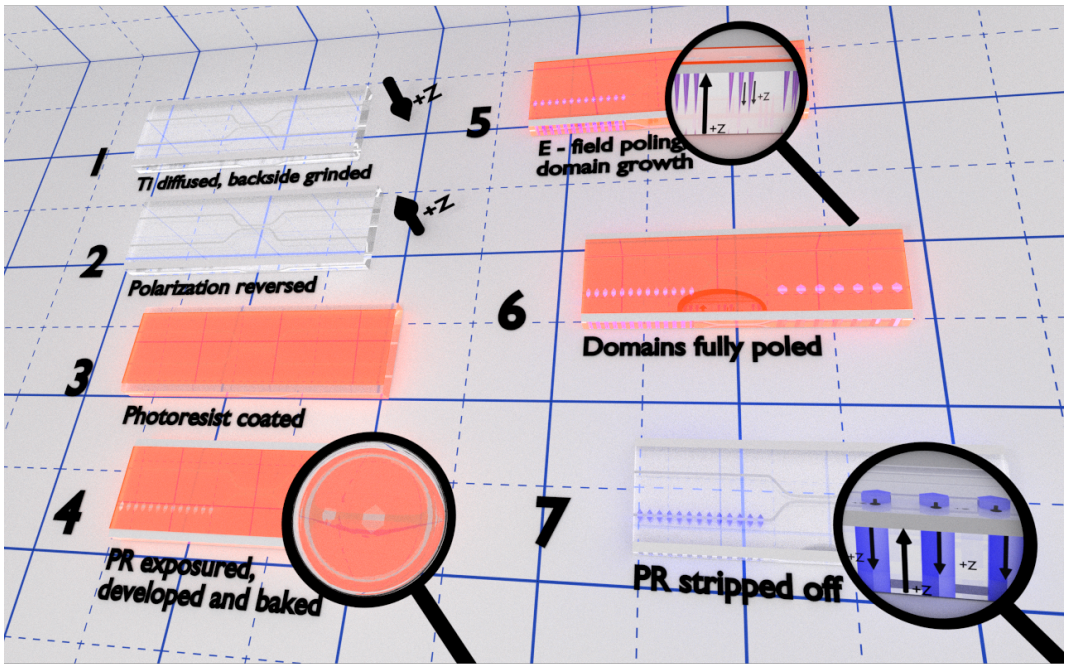

Figure 4.3.: Schematic overview of technological steps for the fabrication of periodically inverted domains in lithium niobate.

comparably well controlled duty-cycle can be achieved by monitoring the poling current and the accumulated charge during the application f the electric field.

As shown in Fig. 4.3, we start our technological procedure for periodic poling with the backside-grinded samples with the titanium-diffused waveguides on the -Z face, which the vendor provided with better surface polishing quality. It is known that a uniform nucleation and growth of inverted domains starts from the +Z-face, instead. Therefore, we invert the polarization of almost the whole chip area by applying the high electric field in a special sample holder. Herein, the two ±Z-faces are contacted by a liquid electrode consisting of 2-propanol and a dissolved salt as the electrolyte. We apply a single ramped pulse of 12 kV and few seconds of duration, and we monitor the voltage as well as the current and conducted charge. We stop the pulse abruptly and clean the sample after removing from the special holder, when the amount of charge for complete areal inversion has flown. Since the liquid electrodes do not cover the full ±Z-faces and the poling process induces a fair bit of stress/strain to our samples, we can visualize the domain walls by transmitted-light polarization microscopy. A short annealing step at several hundred degree Celsius in an oxygenic atmosphere relaxes the induced stress/strain of the domain walls and further processing of the sample is possible.

We spin-coat the sample homogeneously with a viscous positive photo-resist, bake it for several minutes at elevated temperatures in order to remove the solvents, and

we remain with a hardened resist of several micrometers in thickness. The process of vacuum contact imprinting of the poling structures is similar to the waveguide fabrication steps, while the illumination duration is longer due to the thicker resist layer, and the mask alignment is done with respect to the underlying waveguides. Our poling patterns on the lithography mask consist of segments which are as broad as the waveguides and show a hexagonal shape. This is adapted to the crystallographic unit cell Z-cut and prevents additional distortions due to angeled domain walls with respect to the natural crystal structure. The limited width of the poling structures also prevents domain growth in the non-waveguide region, where the nucleation and growth has been found to start at significantly lower electric field strengths compared with titanium-diffused areas.

After illumination through the photo mask, we immediately develop the PR with a basic developer for several tens of seconds and remain with hexagonally shaped open areas on the new +Z face right above our waveguides (see Fig. 4.3, step #4). At this point, the resist structure shows steep edges without pedestals just as desired, but it will not chemically withstand the immersion to our electrolyte solution. Therefore, we bake the structures in a three-step procedure above 100∘C, each for one hour. This procedure overcomes the temperature region, where the resist plastically flows and deforms in terms of rounding of formerly sharp edges. Therefore we heat up through this temperature region as fast as possible. Temperatures above 150°C also lead to chemically less sensitive resist layers, which will survive the direct contact with our electrolytes dissolved in classical solvents like 2-propanol. A typical hard-baked structure is shown in Fig. 4.4 (left).

In the next step we again use the special sample holder and perform the pulsed electric field poling. Depending on the area to be poled, we apply between two and sixty pulses of around 15 ms duration and 12 kV voltage amplitude. During pulse application, nucleation spots of inverted domains form on the +Z-face, where the waveguide resides and where the liquid electrode has direct contact to the LN surface. The inverted domains grow spike-like in depth, tend to merge and grow also in width, and finally they stabilize according to the superstrating resist structure, if the required accumulated charge per area has been reached. Afterwards, we remove the photo-resist structure by either stripping it with 1-Methyl-2-pyrrolidone (NMP) or ashing it in oxygen plasma.

Since the poling process again induces stress to the sample, we can conveniently visualize the inverted domains under the transmitted-light polarization microscope as shown schematically in Fig. 4.3 (step #7). It is likely that these stressed structures induce high optical scattering loss to the waveguide transmission. In order to prevent this, we repeat the short annealing step at several hundred degree Celsius for stress-removal. After this, the domains can be visualized only by selective etching of the LN surface, the outcome of which is shown as an example in Fig. 4.4 (right).

With this quality check of periodicity, duty-cycle and homogeneity, we finished the periodic domain inversion procedure, but still have to polish the X-faces in a perpendicular manner with respect to the waveguide propagation direction. This will

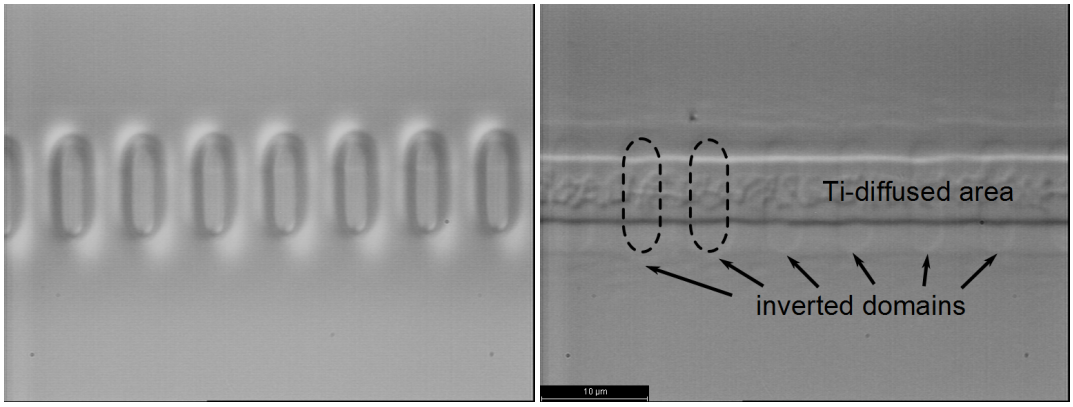

Figure 4.4.: Typical 6.75 μm poling structure in the photo-resist after hard-bake (left) and on the sample after selective domain etching (right).

ensure optimal coupling of light into and out of the device, since angular distortions of the wave fronts can be minimized. The number of scratches in the waveguide cross-sections, which lead to interference patterns in the near-field and to low overall device efficiencies, is likewise reduced.

4.4. Device design for cascaded conversion processes

With the technological procedures described in the previous sections at hand, we are able to design a large variety of devices for classical and quantum optical applications as mentioned above in this chapter. For the device that is considered in this thesis, we rely on the reproducibility of our technological toolbox, the robustness of the device with respect to environmental variations (temperature etc.), and - most importantly - on an increased number functionalities combined with a simple and compact design. The main goal of this work in terms of functionality is a single chip, which is capable of generating photonic triplet states in a cascade of parametric down-conversion sources, paired with on-chip spatial demultiplexing and low loss.

In particular, we have chosen the structures as shown in Fig. 4.5: pairs of waveguides with 127 microns of distance and a nominal width of seven micrometer are directed along the X-axis of our samples. The distance between the two waveguides is adapted to the center-to-center-distance of paired single-mode fiber (SMF) in dual-core ferrules for future fiber-integration of our device.

The waveguide coupling ports at the inputs are equipped with linear tapers from seven micron down to three micron in width towards the device's end-facet. This shall reduce the number of guided modes at 532 nm wavelength. In the middle of the individual structure, we included a symmetric directional coupler, which is fed by S-shaped ports. The center-to-center distance of the couplers' stem length region

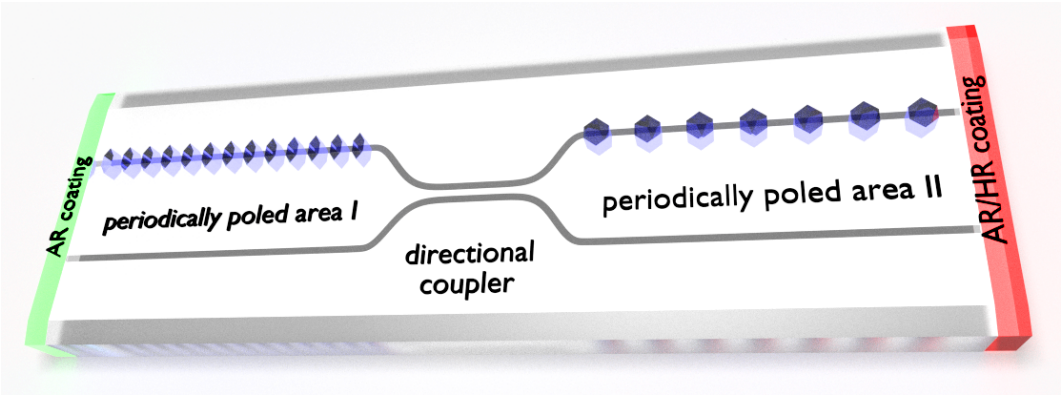

Figure 4.5.: Schematic device design for a cascaded wavelength conversion device. Coupled waveguide structures are surrounded by two differently poled areas, in which the wavelength conversion processes take place. End-face coatings serve to improve the overall device efficiency.

is 13 micron. This has been found to be a trade-off between high coupling strengths for transverse magnetic (TM)-polarized telecom light in the fundamental mode, the suppression of coupling for fundamental TM-modes at 532 nm and $\sim$ 800 nm, and the compactness of the structure. Across the 12 mm width of our device we vary the stem length of the directional couplers from 2750 to 4250 micrometers in 250 micron steps in order to provide optimized coupling for different telecom wavelengths of our future cascaded wavelength conversion processes. These values have been estimated by finite element calculations for the interferometric local normal mode approach according to section 3.2.4. Each paired-waveguide coupler structure has been repeated three times within a group, which exhibits the same coupler stem length, i.e., we have seven groups with three waveguide pairs or 42 waveguides in total.

Prior to and behind an individual coupler structure, we leave the waveguides straight, and the periodic domain inversion is done in two separate lithography steps, as described in section 4.3. We vary the poling periods of the first poling pattern (input side) from 6.71 μm to 6.91 μm within each group, and we parameterize the second poling period from 17.45 μm to 18.27 μm across the whole device width. This strategy allows us not only to optimize our device for (cascaded) wavelength conversion processes from 532 nm to IR wavelengths at $\sim$ 800 nm and $\sim$ 1600 nm, but it also provides us with a variety of other feasible classical and quantum application options, where coarse wavelength tuning of independent three-wave-mixing processes is necessary. In Appendix C we show an overview of the necessary design parameters. We emphasize that the device shown in Fig. 4.5 is not only capable of generating photon triplet states, but we demonstrate in Sec. 7.1 that frequency up-conversion to the visible range is also possible for classical telecom light.

In order to provide the best possible coupling in and out of the waveguide struc-

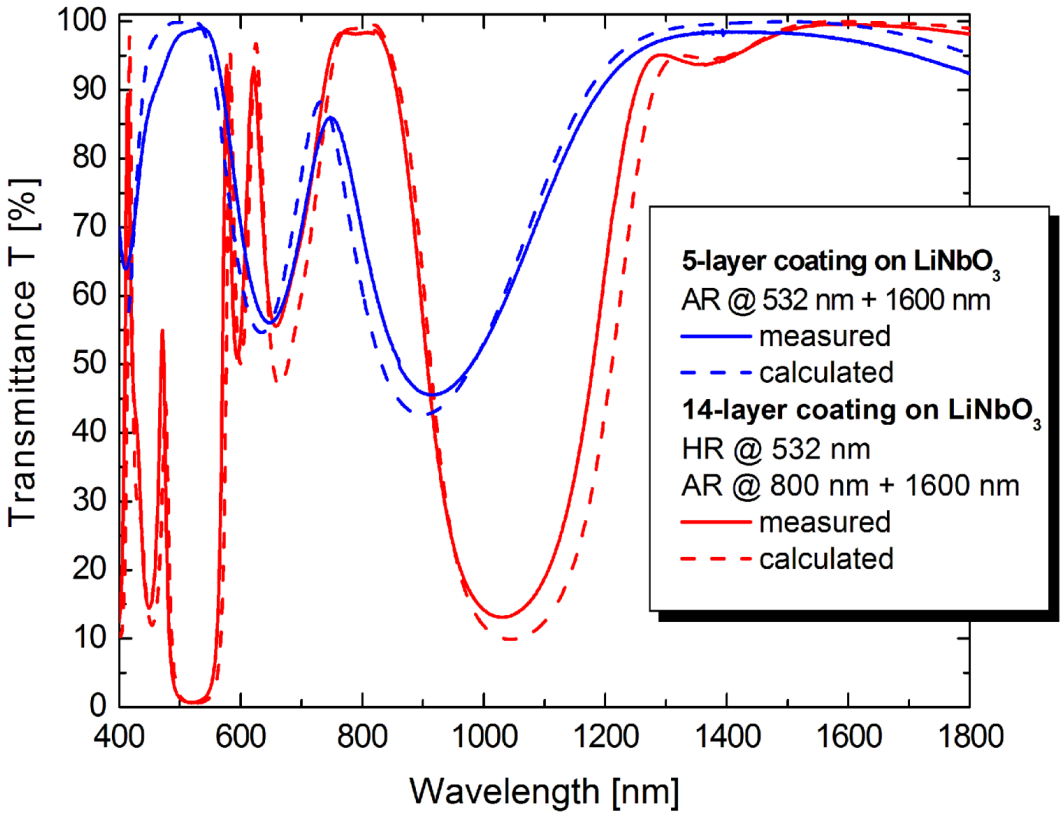

Figure 4.6.: Comparison of designed and measured end-face coating transmittances. we achieve high reflection and anti-reflection characteristics for the desired wavelengths, respectively. The spectra are in very good agreement with the design.

tures at the desired wavelengths, we designed and deposited dielectric optical coatings onto the end-facets of our waveguides. For the calculations, we use commercially available design software with the capability for reverse-engineering and optimization of individual layer deposition processes (OptiLayer, OptiRE and OptiChar).

For the input ports of our device, where we want to couple green light and telecom wavelengths into the waveguides without significant Fresnel losses, we chose a simple 5-layer coating stack, which is anti-reflective (AR) for 532 nm and at 1600 ± 75 nm. We decided for titanium dioxide as the high-index material, whereas silicon dioxide served as the low-index material.

On the output side of the chip we aim for blocking the green light in the best possible way, while NIR light at ~ 800 nm and telecom light at ~ 1600 nm should be transmitted optimally. Since we have to control three different wavelength regions with different transmittance options, a more sophisticated layer stack has been designed and deposited by electron-beam evaporation. We coated 14 alternating layers of high- and low-index material. Although optically indifferent, we always

start with the titanium oxide, because its adhesion properties on lithium niobate substrates outperform silicon oxide.

In Fig. 4.6, the calculated and measured coating spectra is shown for the device's input (blue lines) and the output facet (red lines). We recognize the high quality of the deposited stacks in terms of wavelength accuracy and transmittance/reflectance. Compared to the natural reflectance of around 14 % to 16 % per facet - stemming from Fresnel reflections between uncoated lithium niobate and the surrounding air - we could drastically increase the transmittances up to over 98% for IR wavelengths at the output. Likewise, we have a high-reflective (HR) mirror for green light with over $R > 99\%$.

As a closing remark for this chapter we emphasize that, with both coatings at hand, we increase the overall device efficiency significantly. As an example, the pair emission efficiency from a parametric down-conversion process with respect to the number of input pump photons is increased by $\sim (58.0 \pm 0.3)\,\%$ compared to an uncoated device. In this rough estimation we took only into account the measured input transmittance for 532 nm photons of $(98.9 \pm 0.1)\,\%$ and the output transmittances for individual IR photons of $(98.4 \pm 0.1)\,\%$ and $(99.6 \pm 0.1)\,\%$ at 803 nm and 1575 nm, respectively.

Conclusion

In conclusion, we have pointed out the outstanding properties of lithium niobate as a versatile $\chi^{(2)}$-nonlinear optical material for integrated classical and quantum optics. In the technological sections we described the general procedures for fabricating waveguide and directional coupler structures as well as the periodic domain inversion of the crystal.

With the mature technology of titanium-diffused waveguide structures in periodically poled lithium niobate at hand, we were able to design and fabricate an integrated device with multiple functionalities on-chip for applications in quantum optics, which is characterized and tested as described in the following chapters.

CHAPTER 5

General linear and nonlinear optical properties of the integrated device

Contents

With the technological procedures and proper design parameters at hand, we fabricated an integrated nonlinear waveguide chip, which is utilized in the quantum optical applications of the next chapters. But for now, we characterize it in terms of basic linear and nonlinear optical behavior. Individual measurements were carried out in order to determine the properties of the individual integrated building blocks, and we compare the outcomes with our theoretical model. We determine the typical near field pattern of telecom modes and check for the scattering loss in the waveguide structures. Additionally, we investigate the coupling behavior of the integrated wavelength division multiplexer. A special focus of this chapter has been put on fundamental nonlinear optical experiments, in which we address the two periodically poled waveguide regions independently and describe the tuning of the quasi-phase-matching (QPM) conditions.

5.1. Linear optical waveguide properties

5.1.1. Near-field pattern and mode size

With the main content of this thesis related to nonlinear and quantum optical applications of our fabricated integrated chip, we have to characterize its linear optical properties very carefully. As a first fundamental benchmark, we investigate the near field pattern of the guided optical modes at different wavelengths. Measuring the shape and size of the fundamental TM_{00} modes at involved telecom wavelengths of our planned three-wave-mixing processes provides not only valuable information for the calculation of mode overlaps with centro-symmetric optical fiber-modes, but it also offers a calculation basis for the approximation of nonlinear conversion efficiencies.

We implement a simple setup, which lets us transmit telecom light from a tunable laser source or - more reliably - a source of amplified spontaneous emission (ASE) through our waveguides. The out-coupled radiation is collected and projected onto a camera, beam profiler or video camera tube (Vidicon) with a microscope objective under high numerical aperture of 0.95, which offers a resolution (Rayleigh-criterion) of approximately 1.00 μm at wavelengths of 1550 nm and a hundred-fold magnification. Customized analysis software provides the correct calibration and offers reliable estimation of the full width at half maximum (FWHM) of the mode.

Fig. 5.1 shows typical mode profiles of fundamental TM_{00} and TE_{00} modes at 1550 nm wavelength. We see that for both polarizations the shape of the mode is asymmetric in depth (Z-direction) with the center of mass being shifted towards the device surface. The asymmetry can be quantified by the ratio of the vertical and horizontal FWHMs, i. e. the ellipticity e, on the one hand. For the TM_{00} modes we get $e_{\mathrm{TM}} = 0.75$ and for the TE_{00} modes we get $e_{\mathrm{TE}} = 0.73$ on average. On the other hand, the vertical asymmetry can be defined as the ratio of the intensity's half-width at half maximum (HWHM) a. For the TM_{00} modes we get $a_{\mathrm{TM}} = 0.62$ and for the TE_{00} modes we get $a_{\mathrm{TE}} = 0.68$ on average. Both asymmetry parameters are ideally 1. This means that TM_{00} modes show not only smaller mode areas, but also slightly more symmetric mode shapes for our waveguide structures for both, ellipticity and vertical asymmetry. This is in acceptable agreement with our waveguide model (see Chap. 3), because the anticipated mode sizes are smaller than for the measured profiles.

We can calculate the fiber-waveguide coupling efficiency according to Murphy et al. [186] as the overlap integral of the modal field distribution of the measured waveguide $\phi(y,z)$ with the modal field distribution of a single mode fiber $\psi(y,z)$:

$$\eta_{\mathrm{WG-F}} = \frac{|\int\int \phi(y,z)\cdot\psi(y,z)\,\mathrm{d}y\,\mathrm{d}z|^2}{\int\int \phi^2(y,z)\,\mathrm{d}y\,\mathrm{d}z\cdot\int\int \psi^2(y,z)\,\mathrm{d}y\,\mathrm{d}z}. \tag{5.1}$$

Since our experimental data access is restricted only to mode intensities and Gaussian fitted HWHM for the different directions, $a_{\mathrm{i}}^{\mathrm{HWHM}}$, we have to translate these

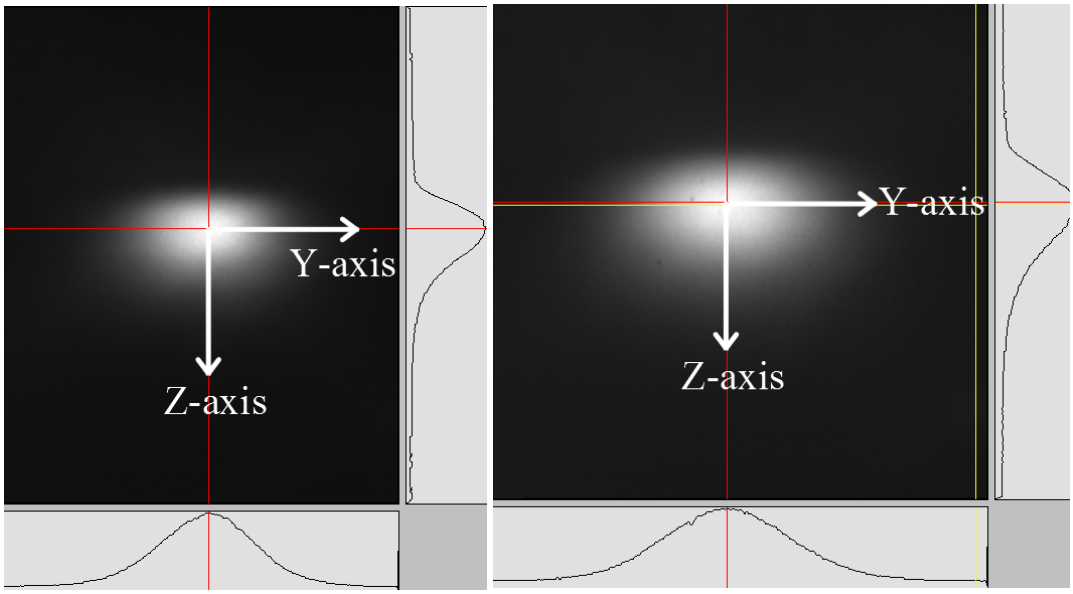

Figure 5.1.: The typical mode size pattern of TM-polarized fundamental modes at 1550 nm (left) and of TE-polarized light (right). We notice that the TE modes are larger than the TM modes, which impacts the butt-coupling efficiencies to single mode fibers.

dimensions into $1/e$ - radii of the mode fields. Assuming the validity of Gaussian beam approximation in our case, we write for the $1/e$ - radii of the mode field:

$$a_{\mathrm{y}} = \sqrt{\frac{2}{\ln 2}} \cdot a_{\mathrm{y}}^{\mathrm{HWHM}}, \tag{5.2}$$

$$a_{\mathrm{z1}} = \sqrt{\frac{2}{\ln 2}} \cdot a_{\mathrm{z1}}^{\mathrm{pos.HWHM}}, \tag{5.3}$$

$$a_{\mathrm{z2}} = \sqrt{\frac{2}{\ln 2}} \cdot a_{\mathrm{z2}}^{\mathrm{neg.HWHM}}. \tag{5.4}$$

Herein, a_{y} denotes the radius symmetrically in the $\pm Y$ direction, whereas a_{z1} and a_{z2} label the $1/e$ - radii in the surface- and the substrate Z direction, respectively.

We take the symmetry of fiber modes and our horizontal waveguide intensity distributions into account and modify Eq. 5.1 [187]. Thus, we get for the coupling efficiencies for both polarizations

$$\eta^{*}_{\mathrm{WG-F}} = \frac{2a_{\mathrm{y}} \cdot w^2}{(a_{\mathrm{z1}} + a_{\mathrm{z2}})\left(a_{\mathrm{y}}^2 + w^2\right)} \left(I_1 + I_2\right)^2, \tag{5.5}$$

with

$$I_1 = \frac{a_{\mathrm{z1}}}{\sqrt{a_{\mathrm{z1}}^2 + w^2}} \cdot \exp\left(-\frac{(c-b)^2}{(a_{\mathrm{z1}}^2 + w^2)}\right) \cdot \left[1 - \mathrm{erf}\left(\frac{a_{\mathrm{z1}}(c-b)}{w\sqrt{a_{\mathrm{z1}}^2 + w^2}}\right)\right] \tag{5.6}$$

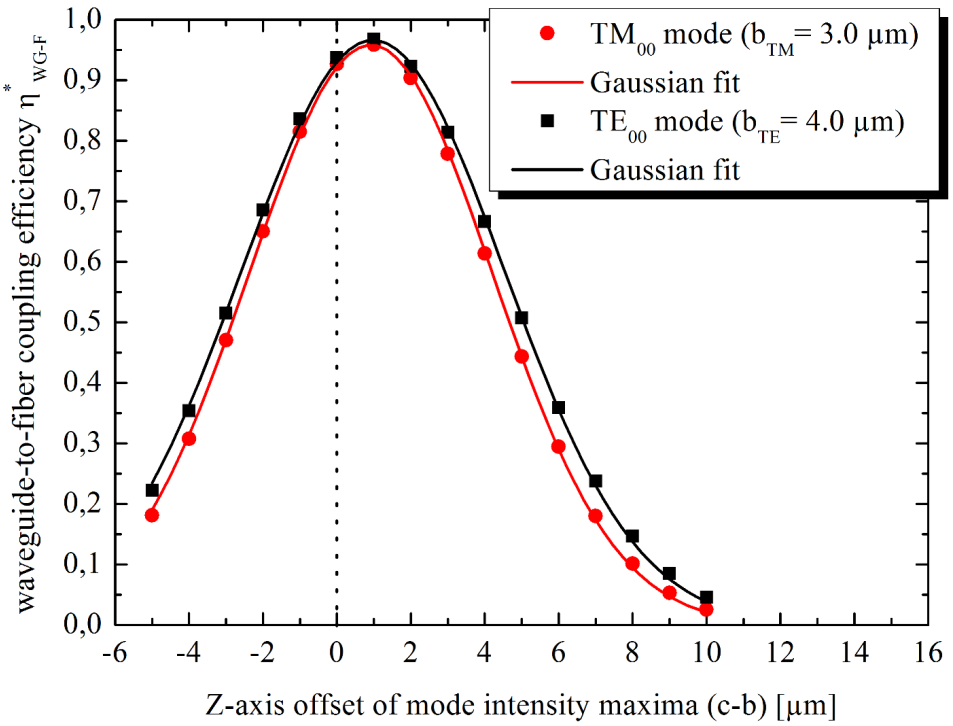

Figure 5.2.: Calculated mode overlap dependence on the vertical offset between fiber and waveguide mode intensity maxima. We conclude that the different modal overlap maxima and axis offsets for TE_{00} and TM_{00} can cause efficiency issues for type-II wavelength conversion processes in fiber-pigtailed devices.

and

$$I_2 = \frac{a_{z2}}{\sqrt{a_{z2}^2 + w^2}} \cdot \exp\left(-\frac{(c-b)^2}{(a_{z2}^2 + w^2)}\right) \cdot \left[1 + \mathrm{erf}\left(\frac{a_{z2}(c-b)}{w\sqrt{a_{z2}^2 + w^2}}\right)\right]. \tag{5.7}$$

The parameter b describes the vertical distance of the waveguide's maximum intensity from the -Z surface. Likewise, c is the vertical mismatch of the fiber symmetry point with respect to the device top surface. Thus, the parameter $(c-b)$ labels the vertical offset of the mode intensities of fiber and waveguide. The fixed parameter $w = 5.2\,\mu\mathrm{m}$ is the specified $1/e^2$ mode intensity radius of a standard SMF28e+ fiber [188], which equals its $1/e$ mode field radius.

In practice, it is non-trivial to determine the exact vertical position of the waveguide mode's center of mass with respect to the physical boundary at the top. Therefore we approximate b using our waveguide modeling program and yield $b_{\mathrm{TM}} = 3.00\,\mu\mathrm{m}$ and $b_{\mathrm{TE}} = 4.00\,\mu\mathrm{m}$ for the two polarizations. As shown in Fig. 5.2, we find

that the maximum waveguide-to-fiber-overlap is not given at $(c - b) = 0\,\mu$m, but shifted towards the substrate by $(c - b)_{\text{opt}} \approx 0.95\,\mu$m for both polarizations.

We notice a maximum theoretical waveguide-to-fiber overlap for TM_{00} modes of $(95.8 \pm 4.0)\,\%$, whereas TE modes overlap by $(96.6 \pm 4.0)\,\%$. Likewise, we infer different widths of the Gaussian fit curves in Fig. 5.2, which means slightly different overlap robustness against vertical misalignment of the fiber. The TE_{00} modes can benefit more from this effect than the TM_{00} modes.

Note that these calculations strongly depend on the resolution of the mode size measurements as well as on the validity of Gaussian approximations, and the given error bars are rough estimates based on the measurement uncertainties. Especially a_{z1}, i. e. the vertical mode width towards the top surface, is a critical parameter that could warp the maximum theoretical coupling efficiency. We expect the different modal overlap maxima and axis offsets for TE_{00} and TM_{00} to cause coupling efficiency differences for example in type-II wavelength conversion processes in conjunction with fiber-pigtailed devices.

Additionally, the use of coherent sources for the mode size measurements will usually lead to interference patterns, which disturb the Gaussian fitting of the mode profiles. Thus, incoherent sources are preferred for this task.

5.1.2. Loss measurements

In a second characterization method, we estimate the overall scattering loss of our straight control waveguides interleaving the coupler structures. It must be stressed that loss has a critical impact on the performance of quantum optical devices and, thus, has to be determined with the most accurate characterization method.

Our loss measurements have to be done prior to any end-face coating, since the method relies on the natural Fresnel reflections of the input and output facets. According to the expression for weakly guiding structures [189]

$$R = \left(\frac{n_{\text{eff}} - 1}{n_{\text{eff}} + 1}\right)^2, \tag{5.8}$$

we get reflectances of individual facets of $R_{\text{TM}} \sim 0.133$ for TM_{00} modes and $R_{\text{TE}} \sim 0.145$ for TE_{00} modes with the effective refractive indices n_{eff} at $\lambda = 1590$nm and at device temperatures of $\theta = 25°$C. In that manner, our waveguide chip forms a low-finesse Fabry-Perot resonator, the transmitted power of which depends on its length and on the addressing wavelength. We chose to change the length L of the resonator by tuning its temperature. This method leads to oscillatory transmitted powers P of the excited fundamental modes, the contrast of which is related to the overall loss D (in dB) as [84]

$$\alpha = \frac{10}{L_{\text{WG}}} \cdot \log\left[R \cdot \frac{1 + \sqrt{P_{\text{min}}/P_{\text{max}}}}{1 - \sqrt{P_{\text{min}}/P_{\text{max}}}}\right], \tag{5.9}$$

where L_{WG} is the length of the waveguide.

Table 5.1.: Summary of the measured linear optical waveguide properties and calculated quantities for fundamental waveguide modes.

Parameter	**measured value**	**numerical value**
TM_{00} horizontal FWHM at 1590 nm	$(6.29 \pm 0.15)\ \mu$m	$5.33\,\mu$m
TM_{00} vertical FWHM at 1590 nm	$(4.68 \pm 0.14)\ \mu$m	$3.68\,\mu$m
TM_{00} pos. vertical HWHM at 1590 nm	$(1.78 \pm 0.10)\ \mu$m	
TM_{00} neg. vertical HWHM at 1590 nm	$(2.90 \pm 0.10)\ \mu$m	
TE_{00} horizontal FWHM at 1590 nm	$(7.61 \pm 0.20)\ \mu$m	$7.18\,\mu$m
TE_{00} vertical FWHM at 1590 nm	$(5.63 \pm 0.15)\ \mu$m	$5.20\,\mu$m
TE_{00} pos. vertical HWHM at 1590 nm	$(2.18 \pm 0.10)\ \mu$m	
TE_{00} neg. vertical HWHM at 1590 nm	$(3.45 \pm 0.10)\ \mu$m	
max. TM_{00} coupling efficiency		$(95.8 \pm 4.0)\,\%$
max. TE_{00} coupling efficiency		$(96.6 \pm 4.0)\,\%$
expected TM_{00} loss at 532 nm	$\sim (0.3 \pm 0.1)$ dB/cm	
expected TM_{00} loss at 800 nm	$\sim (0.2 \pm 0.1)$ dB/cm	
average TM_{00} loss at 1590 nm	(0.08 ± 0.03) dB/cm	

We find, by analyzing the transmitted power with an IR-sensitive PIN-diode, average loss values as low as (0.08 ± 0.02) dB/cm for the straight test waveguides. Since this method is only reliable for single-mode excitation, it tends to fail at lower wavelengths, where our waveguides are multi-mode. Especially in the visible and NIR regime, we cannot reliably determine the exact waveguide loss by this measurement technique. Instead, we assume that at 532 nm we have around 0.3 dB/cm of loss, whereas at around 800 nm we have to deal with ~ 0.2 dB/cm loss. We mainly expect Rayleigh-scattering to cause qualitatively higher loss at shorter wavelengths, whereas the quantities are guessed.

We also have in mind that, due to our bent coupler structures, additional loss might occur for all involved wavelengths. This could become significant especially for weakly guiding structures, i. e. single-mode waveguides at telecom wavelengths. It has been shown, e.g. in Refs. [21, 120], that for increasing radii of curvature, the additional bending losses decay exponentially, and at $R_{\mathrm{Bend}} \geq 160$ mm they become negligible compared to the straight waveguide scattering loss [24, 121].

In Tab. 5.1 we summarize the experimentally determined and theoretical mode sizes, the measured loss values and the coupling coefficients to fiber modes, the latter of which being deduced from the near-field measurements. We see that the numerical results for the mode size parameters differ significantly from the measured values. This appears to be related to the assumed volumetric mass density of the titanium, which is deposited in the electron beam evaporation process prior to diffusion. Here, we assumed identical volumetric mass density as bulk titanium. When we reduce the titanium thickness in our diffusion model by $\sim 25\,\%$, we achieve around the same vertical and lateral FWHM as in the experiment. Seemingly, the deposited

titanium mass is significantly lower than assumed in our model. In other words, the mass density of the evaporated and deposited titanium is apparently lower than for bulk material. More in-depth investigation is necessary in the future in order to compensate this discrepancy to our model.

5.2. Emission characteristics of the primary parametric down-conversion source

Parametric down-conversion (PDC) [17] is the work horse for the generation of single photons in this thesis and in a wide spectrum of theoretical and experimental quantum optical work. We characterize the properties of our implemented PDC sources in this section. In particular, we focus on the tuning behavior of the primary source's photon pair emission with respect to the phase-matching condition, which is influenced by the periodically poled structures and by the temperature.

We intend to convert photons from wavelengths around 532 nm into daughter photons at around 800 nm and around 1600 nm within the integrated primary photon pair source, using the setup shown in Fig. 5.3. We control the temperature as well as the position of our device using high precision three-axis stages in combination with a properly designed oven, which allows for mechanical and thermal stabilization. The green pump light is coupled to our waveguide structures in TM polarization using a 10-MHz pulsed laser system (Katana-05, Onefive GmbH) offering 43 ps pulse duration and up to 23 mW continuous-wave-equivalent power in conjunction with a home-built variable attenuator, standard mirrors and a half-wave plate. For focusing the pump light down to the size of the waveguide modes we use a microscope objective with long working distance ($\sim$ 12 mm), a 20$\times$ magnification factor and a numerical aperture of 0.4.

The temperature stabilization of our source is provided by an oven, which is matched to the length of the device and driven by a home-made temperature controller. The latter offers stabilization of $\Delta\theta = \pm 0.1°\mathrm{C}$, which is sufficient for the characterization methods throughout this thesis.

At the exit of our waveguides, we magnify the waveguide modes with an anti-reflex coated aspherical lens, transmitting infrared light with more than 97%. The two output beams are further split up by D-shaped mirrors after passing a customized color-glass filter (RG715) with high-reflector for the pump. This is intended to reduce the possibility for non-converted high energetic pump photons to generate fluorescence in the color glass absorber, but it still allows for transmission of the expected signal and idler wavelengths of our primary and secondary PDC sources at $(\sim 790 \pm 30)$ nm and (1590 ± 75) nm with more than 95%, respectively.

In order to be able to address different measurement apparatuses in the visible and NIR wavelength region, we implement a high-precision fiber coupling stage equipped with a high-transmittance aspheric lens in combination with a multi-mode optical fiber.

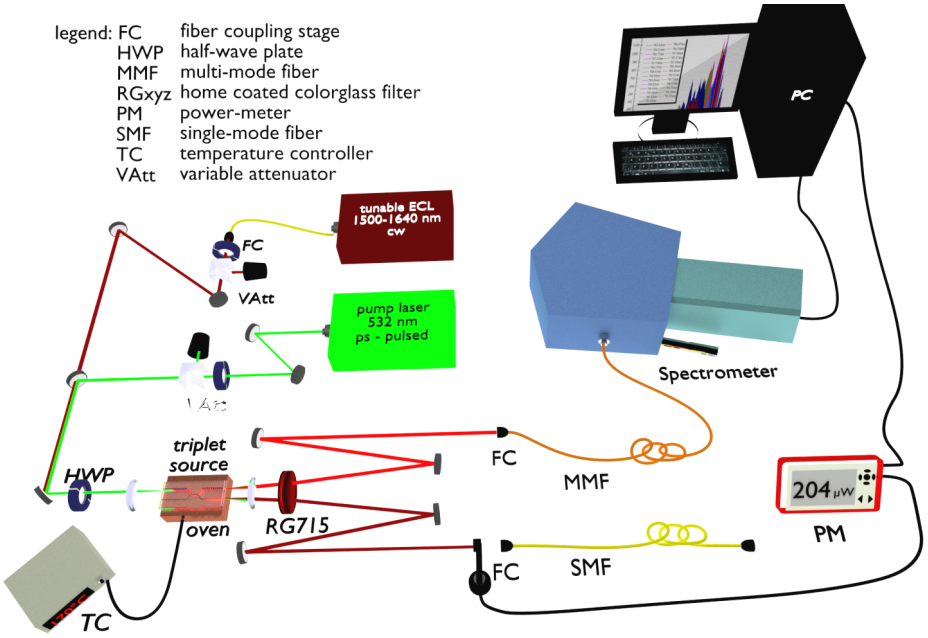

Figure 5.3.: Schematic of the basic setup for the characterization of the primary PDC emission and for the on-chip WDM. Our chip is pumped by a green pulsed laser, which generates PDC photon pairs in the periodically poled area. Addressing the spectrometer with the individual output arms offers information about the PDC signal spectra and coupling behavior. With the external cavity laser, we have access to the power ratio at the idler wavelengths in the respective output arm via standard power-meters. This method is deployed in Sec. 5.3 for characterizing the integrated coupler. Additional single mode fiber coupling servers as an extension for later experiments.

The beam that corresponds to the pumped waveguide is directed to a single-photon sensitive spectrometer system (Andor Shamrock 163i, Andor Newton CCD camera, grating: 600 lines per mm) via standard dielectric mirrors, the latter of which operates with a spectral resolution of around 0.23 nm and in the region between 400 nm and 1080 nm. The device's accuracy is influenced by the efficiency and the dispersion of the built-in grating, which has a blaze-wavelength of 500 nm. However, we concentrate on the wavelength region at around (800 ± 50) nm, and we assume a constant quantum efficiency as well as negligible grating dispersion.

For the adjacent output beam, we implement additional standard mirrors and a coupling stage to single-mode fibers in order to connect the measurement equipment necessary for the experiments provided in the next chapters. Intermediately, we can put a standard power-meter into the beamline in order to get information about the transmitted light at telecom wavelengths. The latter are provided by an external cavity laser (ECL), which is tunable from 1500 nm to 1640 nm.

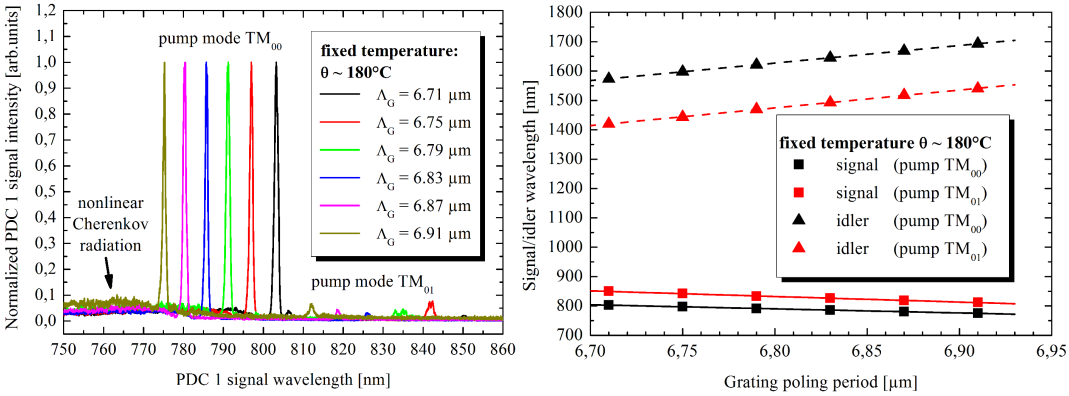

Figure 5.4.: Signal wavelength tuning by changes in the primary grating dimension. **Left**: Tuning spectra of the PDC signal stemming from the TM_{00} and the TM_{01} pump mode. **Right**: The tuning curves of signal (squares, solid-line linear fits) and idler (triangles, dashed-line linear fits) in the addressable wavelength region show linear behavior in the considered range of poling periods. Note that the error bars are smaller than the markers. Larger poling periods lead to a higher degree of non-degeneracy at constant operating temperatures.

5.2.1. Coarse parametric down-conversion tuning by poling period

For the first nonlinear characterization of our chip, we set the temperature of our device to $\theta \approx 180°C$. It has been found in previous work (see, for example, Nouroozi (2010) [190]) that temperatures above $\theta \geq 140°C$ are sufficiently high in order to minimize photorefractive damage due to the strongly confined incident pump light at wavelengths in the visible and NIR regime. Since our source has been designed such that we can address a variety of waveguide structures on-chip with different poling structures, this design allows us to determine coarse tuning curves of the primary PDC source conveniently. In Fig. 5.4 (left), the signal emission spectra for poling periods from 6.71 μm to 6.91 μm are shown, whereas the rightmost graph in Fig. 5.4 shows the tuning curve of the signal and idler peak wavelengths as dependent on the poling periods at fixed temperature. Note that we also include the characteristic behavior of the signal TM_{00} mode being partially excited by the TM_{01} mode of the pump. We could not prevent this by high precision alignment of our device.

For the type-0 parametric down-conversion process we deduce from the graphs that the signal wavelength of the TM_{00} mode shifts towards shorter wavelengths with increasing poling periods. Essentially, the slope of the PDC signal tuning curve can be described accurately by a linear fit function in the reported range of poling periods, $6.71\,\mu m \leq \Lambda_{G1} \leq 6.91\,\mu m$. The slope of the fit curve reflects the step-wise tuning behavior of the signal TM_{00} mode. We deduce the grating-related tuning capability of our source to be $\Delta\lambda_{s1}^{TM_{00}} = -(5.573 \pm 0.098)$ nm per poling

period interval of $\Delta\Lambda_{G1} = \pm 0.04\,\mu$m. This underlines general tuning opportunities of our primary PDC source for later experiments by choosing a proper poling period. The absolute wavelength errors of $\delta\lambda_{s1} = \pm 0.23$ nm are given by the accuracy and grating dispersion of the measurement apparatus.

Similarly, we recognize the presence of the TM_{00} signal mode stemming from the TM_{01} pump mode in our spectra. Its tuning curve appears to be steeper than of the fundamental mode combination. Fitting the measured peak wavelengths linearly, we derive a grating-related tuning capability $\Delta\lambda_{s1}^{TM_{01}} = -(7.636 \pm 0.189)$ nm per poling period interval of $\Delta\Lambda_{G1} = \pm 0.04\,\mu$m.

Furthermore, we infer the spectral FWHM of the primary signal photons to be $\lambda_{s1}^{FWHM} = (0.752 \pm 0.072)$ nm on average. The FWHM error bars are determined mainly by the wavelength resolution of the spectrometer system and the quality of the effective poling length. Note that the spectral width plays an important role for cascaded nonlinear conversion experiments in Chap. 7, since it determines the spectral overlap between two individual processes and, in turn, the overall conversion efficiency.

Another feature of the spectra is the broad spectral distribution in the lower wavelength region next to the fundamental signal mode. This nonlinear Cherenkov radiation [191] arises due to the weakly guiding structures and the scattering of pump light into the substrate. Since our device is periodically poled through it's whole Z-dimension, pump photons can cause non-colinear PDC, when they scatter at variable angles into the substrate and, thus, give rise to different other phase-matched processes than the designed one. The generated Cherenkov signals could couple back at variable wavelengths to the bar channel simultaneously, and they overlap with the guided-wave PDC emission as a broad spectrum.

In the graph in Fig. 5.4 (right), we include the corresponding idler wavelengths, which we calculate with the law of energy conservation. For the fundamental idler mode being generated together with the TM_{00} signal mode, we find the tuning range $1693 \geq \lambda_{i1} \geq 1573$ nm for a fixed temperature of $\theta \approx 180°$C. We deduce a tuning characteristics of $\Delta\lambda_{i1}^{TM_{00}} = (24.219 \pm 1.682)$ nm per period step of our inscribed poling grating.

Although not performed explicitly in the experiment, we can also conclude from our findings that the conversion of green pump photons to daughter photon pairs at degenerate wavelengths requires shorter poling periods than non-degenerate PDC, which is an important information in terms of the technological effort for possible future work.

5.2.2. Fine-tuning by temperature manipulation

In order to provide optimal primary PDC wavelength tuning, we have to be able to change the phase-matching conditions very accurately. Here, we achieve convenient signal and idler wavelength tuning by changing the device temperature in conjunction with the temperature-dependent effective refractive indices of the involved fields. We must not underestimate this effect, since for the experiments on

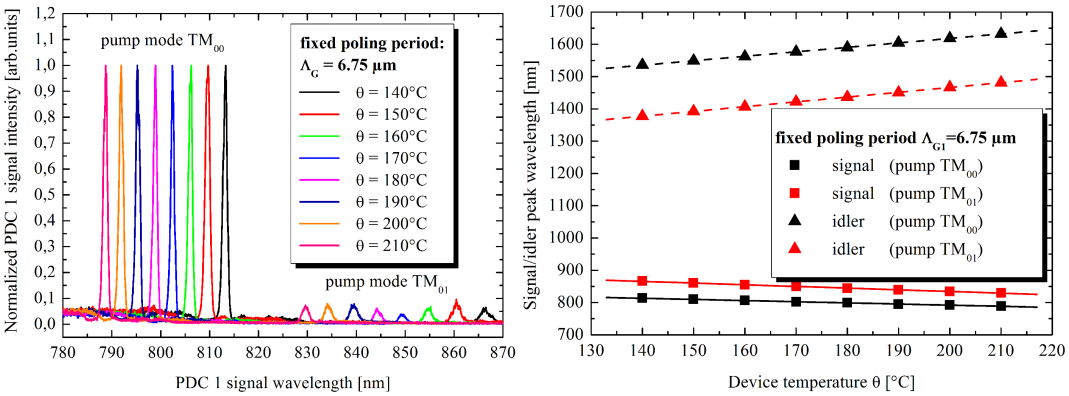

Figure 5.5.: Signal wavelength fine-tuning by changing the device temperature. **Left**: Tuning spectra of the PDC signal including nonlinear Cherenkov radiation and the higher order mode combination originating from the TM_{01} pump mode. **Right**: The tuning curve of signal and idler in the addressable wavelength region exhibits linear dependencies for signal (squares, solid-line linear fits) and the corresponding idler (triangles, dashed-line linear fits). Note that the error bars are smaller than the markers. Larger temperatures lead to a higher degree of non-degeneracy at a fixed nominal poling period.

cascaded wavelength conversion described in Chap. 7, it is essential to match two individually phase-matched processes with only one free parameter on our single chip device.

Due to the fact that the geometric properties of our device change only by around $\left[3 \leq \frac{\Delta(\mathrm{X,Y,Z})}{(\mathrm{X,Y,Z})} \leq 14\right] 10^{-6}\ \mathrm{K}^{-1}$ in the considered temperature range [192], we can neglect the gratings' thermal expansion influences compared to changes in the waveguide dispersion.

As shown in Fig. 5.5 (left), we vary the device temperature between $140°\mathrm{C} \leq \theta \leq 210°\mathrm{C}$ for one of the fixed poling periods at $\Lambda_{\mathrm{G1}} = 6.75\,\mu\mathrm{m}$. The error of the set temperature is estimated to be $\delta\theta = \pm 0.1°\mathrm{C}$. We acquire the spectral characteristics of the PDC signal photons, while the chosen temperature range suffices for the suppression of photorefractive damage due to the green pump light. Additionally, we plot the fine-tuning curves of the fundamental signal and idler peak wavelengths dependent on the waveguide temperature in Fig. 5.5 (right).

From the spectra we deduce very convenient fine-tuning capabilities, covering PDC emission wavelengths of $788\,\mathrm{nm} \leq \lambda_{\mathrm{s1}} \leq 813\,\mathrm{nm}$ for the signal center wavelength and for the chosen periodically inverted structure. Applying the law of energy conservation, we calculate the spectral tuning range of the corresponding idler photons to be in the range of $1635\,\mathrm{nm} \geq \lambda_{\mathrm{i,1}} \geq 1537\,\mathrm{nm}$ and include our findings in Fig. 5.5 (right). Analyzing the temperature tuning curve for signal photons in the TM_{00} by linear regression, we deduce the thermal fine-tuning capability from the slope of the fit. We get for the considered temperature range $\Delta\lambda_{\mathrm{s1}}^{\mathrm{TM00}}(\theta) = -(0.354 \pm 0.003)^{\circ}\,\mathrm{C}^{-1}$.

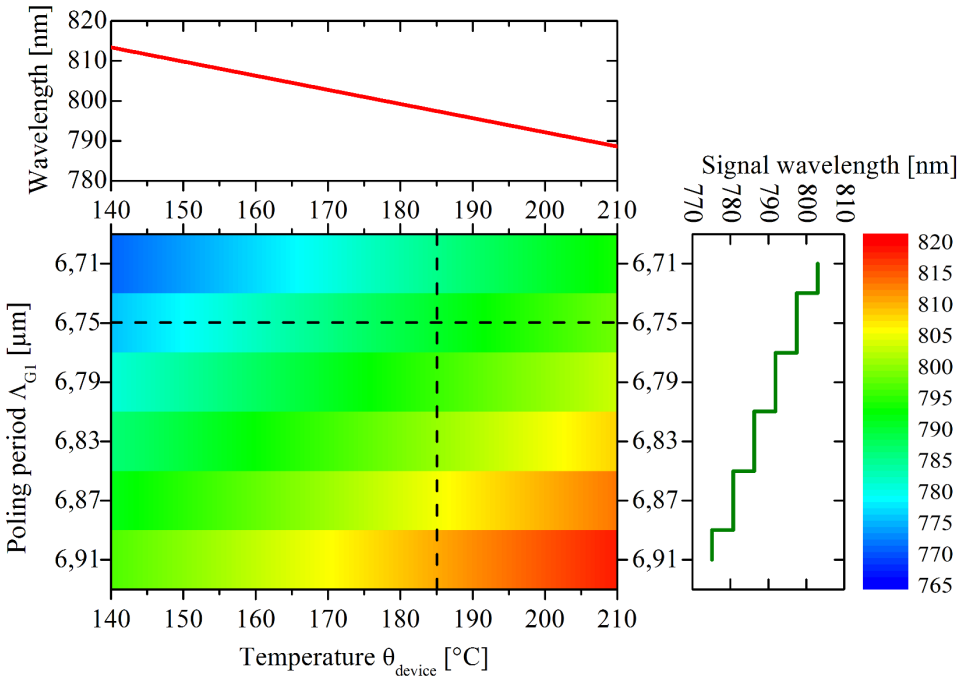

Figure 5.6.: Signal wavelength tuning with two parameters: Wavelength gaps stemming from fixed poling periods (horizontal bands, color-coded) can be bridged by quasi-continuous temperature changes. The top graph visualizes the temperature tuning at $\Lambda_{G1} = 6.75\,\mu$m (dashed horizontal line), whereas the side graph shows the coarse tuning by grating period at $\theta \approx 180°$C (dashed vertical line) for comparison with the measured data.

The shallow slope defines not only the fine-tuning opportunities in general, but together with the temperature accuracy it also expresses that, for thermal fluctuations of $\delta\theta = \pm 0.1°$C, we are able to stabilize the center signal wavelength with an accuracy of $\delta\lambda_{s1} = \mp 0.035\,$nm. This experimental result is essential for the cascaded nonlinear conversion processes described in Chap. 7. It defines the long-term stability and efficiency of the device and experiments (see Sec. 7.2.3.1), when we take possible environmental thermal fluctuations into account possibly acting against the temperature controller.

Correspondingly, we can fine-tune the idler emission according to the rules of energy conservation. From the linear fit of the calculated data, we derive the temperature-related fine-tuning capability for the idler TM_{00} mode as $\lambda_{i1}^{TM_{00}}(\theta) = (1.384 \pm 0.010)°\,C^{-1}$, and we recognize the stronger impact of the temperature on the idler emission wavelength compared to the signal.

With our temperature tuning at hand, we are able to fully bridge the gap of addressable signal wavelengths arising from the fixed grating periods in different periodically poled waveguides. If a specific primary signal (and idler) wavelength

combination is sought, but not directly accessible by changing the poled waveguide structures, we can achieve the wanted spectral emission by modifying the device temperature carefully.

Under the assumption that the slope of the temperature tuning curve is the same for all periodically poled structures available on our chip, we can combine the results of the previous paragraphs. This provides us with the empirical grating- and temperature-dependent dependence for the wavelength in [nm] of TM_{00} signal modes:

$$\lambda_{s1}^{TM_{00}}(\theta, \Lambda_{G1}) \approx \frac{(139.3 \cdot \Lambda_{G1} - 1737.5) \cdot (0.354 \cdot \theta - 862.8)}{\lambda_{s1,meas}^{TM_{00}}}. \tag{5.10}$$

Here $\lambda_{s1,meas}^{TM_{00}} = 797.0\,\text{nm}$ is the reference wavelength measured at $\theta \approx 180°\text{C}$ and $\Lambda_{G1} = 6.75\,\mu\text{m}$. We can faithfully claim a wavelength accuracy of $\delta\lambda_{s1}^{TM_{00}} = \pm 0.5\,\text{nm}$ for the calculated 2D curve. The overall tuning behavior is depicted in Fig. 5.6. We notice again that arbitrary primary signal wavelengths in the considered range are accessible by proper temperature tuning, although the tuning by poling period is rather coarse.

5.3. Properties of the integrated directional coupler

Another important building block on our integrated device is given by the directional coupler or wavelength division multiplexer (WDM), which has been designed to work in the demultiplexing operation mode and for photons being generated in the first parametric down-conversion process. This shall allow for on-chip spatio-spectral splitting of the photon pairs.

As modeled in Sec. 3.2.4 and decided in Sec. 4.4, we vary the coupler geometry according to our theoretical predictions such that the stem length changes in the range $2750\,\mu\text{m} \leq L_C \leq 4250\,\mu\text{m}$ in seven different structures. Other technological and design parameters (diffusion time, diffusion duration, waveguide width, waveguide center-to-center-distance, S-bend radius) have been kept constant. This strongly reduces the experimental characterization effort. We check for the WDM de-multiplexing behavior using the setups shown in Fig. 5.3.

5.3.1. Signal wavelength coupling

While at signal wavelengths our waveguides are multi-mode and the exclusive excitation of the fundamental guided mode with laser light is experimentally not trivial, the most convenient way to analyze the coupling properties is to make direct use of the generated PDC signal. With the setup shown above in Sec. 5.2 in Fig. 5.3, we acquire the spectra of generated signal photons over 10 seconds at the two output ports and integrate both over their full peak width after subtraction of electronic background contributions from the measurement device. The pump power was set

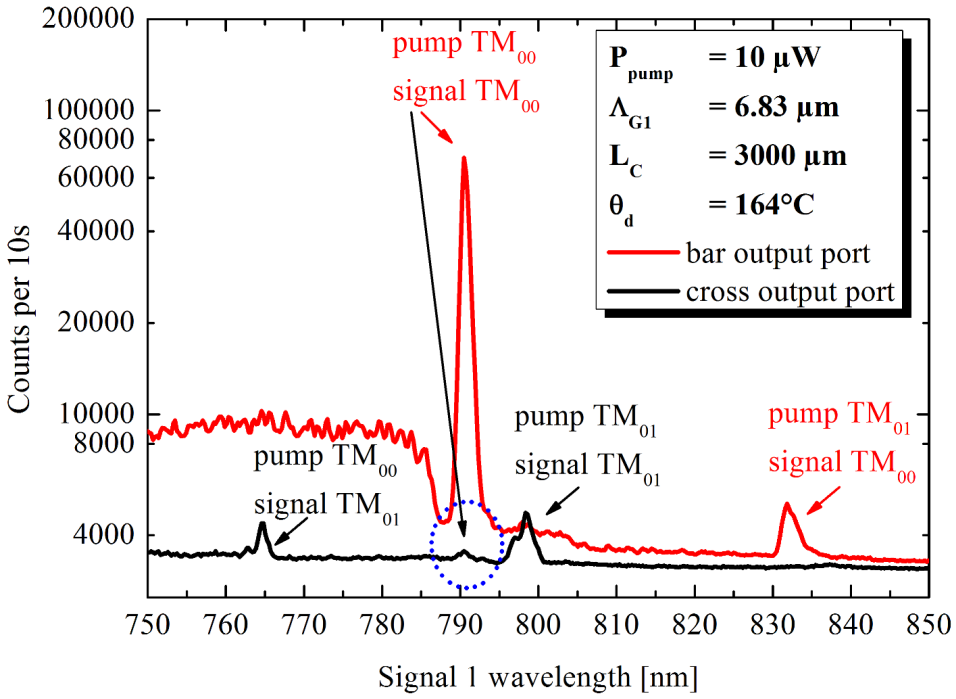

Figure 5.7.: The coupling behavior at signal wavelengths is shown. While the fundamental signal modes remain in the original arm as designed (red curve), the TM_{01} modes couple predominantly to the adjacent waveguide (black curve). Only a small fraction of the TM_{01} signal stemming from the TM_{01} pump mode remains in the original arm. The blue circle is a guide to the eye in order to identify the falsely coupled TM_{00} signal mode in the cross arm. Note that nonlinear Cherenkov radiation is prominently present in the bar output port, whereas this is not the case for the adjacent channel.

to $P_{\mathrm{pump}} = 10\,\mu\mathrm{W}$ in front of the incoupling objective. The relation

$$S_{\mathrm{s1}}^{\mathrm{TM_{00}}} = 10 \cdot \log\left(\frac{N_{\mathrm{s1,cross}}^{\mathrm{TM_{00}}}}{N_{\mathrm{s1,cross}}^{\mathrm{TM_{00}}} + N_{\mathrm{s1,bar}}^{\mathrm{TM_{00}}}}\right) = 10 \cdot \log\left(CR_{\mathrm{s1}}^{\mathrm{cross}}\right) \tag{5.11}$$

describes then the suppression of the fundamental signal mode in the adjacent output port, where $N_{\mathrm{s1,bar}}^{\mathrm{TM_{00}}}$ and $N_{\mathrm{s1,cross}}^{\mathrm{TM_{00}}}$ are the transmitted photon counts in the original (bar) and the adjacent (cross) arm, respectively. For the example shown in Fig. 5.7, we calculate the fundamental signal mode suppression to be $S_{\mathrm{s1}}^{\mathrm{TM_{00}}} \geq 15\,\mathrm{dB}$. This relates to cross-coupled power fraction of around 3%, which is higher than what we theoretically predicted in Sec. 3.2.4, where we anticipated only around 0.1% of cross-coupled NIR light. Nevertheless, the experimatal results meet our requirements reasonably.

Interestingly, this direct measurement method offers also valuable information

about the coupling of higher-order signal modes. Together with the effective refractive index model described in Sec. 3.2 we identify signal modes in the bar output port at $\theta \approx 163.5°\mathrm{C}$ mainly TM_{00}. These stem from the TM_{00} and TM_{01} pump modes, which is shown in the spectra in Fig. 5.7. However, a small fraction of the TM_{01} signal at $\lambda_{\mathrm{s1}}^{\mathrm{TM}_{01}} = 798.4\,\mathrm{nm}$ stemming from the TM_{01} pump mode remains also in the original arm and causes a TM_{00} idler mode at $\lambda_{\mathrm{i1}}^{\mathrm{TM}_{00}} = 1592\,\mathrm{nm}$, which is spectrally close to our preferred fundamental process.

The cross channel exhibits a different picture: the TM_{01} signal modes at $\lambda_{\mathrm{s1}}^{\mathrm{TM}_{01}} = 764.8\,\mathrm{nm}$ and $\lambda_{\mathrm{s1}}^{\mathrm{TM}_{01}} = 798.4\,\mathrm{nm}$ are simultaneously excited by the TM_{00} and the TM_{01} pump modes, respectively. Both higher-order signals were only predominant in the adjacent output port. This behavior offers opportunities for future projects, where spatial mode-splitting at around the same wavelengths might be of interest. Also interestingly, the non-existent broad spectral emission in the cross output below $\lambda_{\mathrm{s1}} \leq 788.0\,\mathrm{nm}$ indicates that our explanation of its origin seems to be correct: the nonlinear Cherenkov radiation is generated right below our input waveguide, only where the periodically poled structures exist. A significant coupling of this radiation - back into the spatially separated *adjacent* output port - is not given, because the spectrum of the adjacent channel, at wavelengths lower than the signal 1 wavelength, shows significantly less counts than the spectrum of the original waveguide. Generally speaking, the fundamental signal photons almost fully remain in the original arm, which is an important feature for all following experiments on the single quantum level.

5.3.2. Power transfer at idler wavelengths

For the primary idler photon coupling behavior, we rely on the fact that telecom light is guided only in the fundamental spatial mode. Therefore, we include the tunable external cavity laser (NetTest Tunics Plus) in our setup as the characterization light source, which emits in the range of $1500 \leq \lambda_{\mathrm{char}} \leq 1640\,\mathrm{nm}$. The output power of this device was kept constant to $P_{\mathrm{set}} = 2$ mW over the gain spectrum of interest by internal adjustment of the driving current. We implement a standard power-meter as the measurement device. This allows for automated wavelength tuning of the laser and data acquisition from the two coupler outputs. While $P_{\mathrm{i1,bar}}$ and $P_{\mathrm{i1,cross}}$ are the measured optical powers in the original and the adjacent output arm, respectively, the coupling ratios are calculated as

$$CR_{\mathrm{i1}}^{\mathrm{cross}}\left(\lambda_{\mathrm{i1}}\right) = \frac{P_{\mathrm{i1,cross}}\left(\lambda_{\mathrm{i1}}\right)}{P_{\mathrm{i1,cross}}\left(\lambda_{\mathrm{i1}}\right) + P_{\mathrm{i1,bar}}\left(\lambda_{\mathrm{i1}}\right)} \tag{5.12}$$

and

$$CR_{\mathrm{i1}}^{\mathrm{bar}}\left(\lambda_{\mathrm{i1}}\right) = \frac{P_{\mathrm{i1,bar}}\left(\lambda_{\mathrm{i1}}\right)}{P_{\mathrm{i1,cross}}\left(\lambda_{\mathrm{i1}}\right) + P_{\mathrm{i1,bar}}\left(\lambda_{\mathrm{i1}}\right)}. \tag{5.13}$$

Note that the wavelength-dependent measurements were taken for seven different structures, where the stem length is the changing parameter. For the calculations

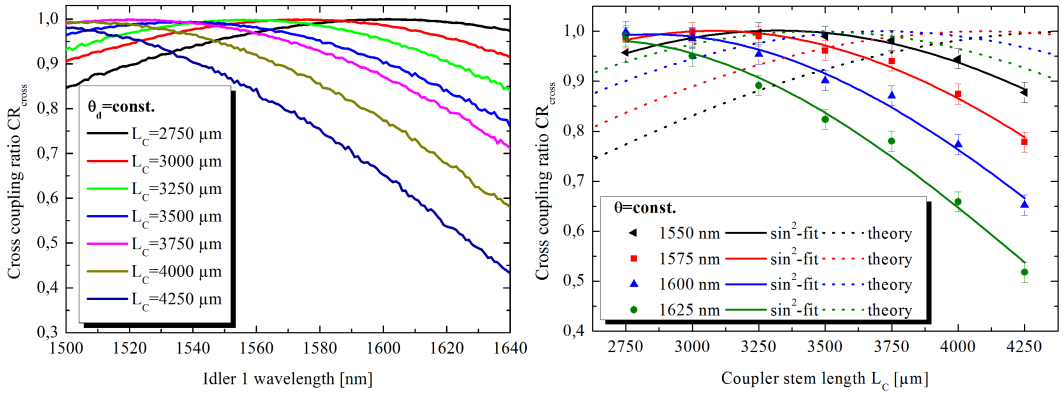

Figure 5.8.: Idler cross coupling behavior. **Left**: We identify a $\sin^2$-like dependency on the idler wavelength with peak coupling ratios over 98.5% for all of our coupler structures. **Right**: The stem-length-dependent cross power transfer exhibits also a $\sin^2$-behavior at fixed wavelengths. Both dependencies underline the validity of the underlying local normal mode interference theory.

we assume also that the output ports do not suffer from optical loss at all. Any distortion in, e.g. a bar output arm, would artificially increase the corresponding cross coupling ratio and vice versa.

From our underlying interference model (see Sec. 3.2.4), we expect the power cross-transfer to follow a $\sin^2$-function with the argument being approximately a linear function. The latter consists of the (wavelength-dependent) difference in propagation constants of the symmetric and anti-symmetric WDM system mode, $\Delta\beta_{\mathrm{s,as}}(\lambda_{\mathrm{i1}})$, as the slope and a wavelength-dependent offset $\phi_{\mathrm{bend}}(\lambda_{\mathrm{i1}})$, which describes the amount of power being transfered only by the input and output S-bends.

We plot the measured wavelength-dependent cross-coupling ratios for the different on-chip WDM structures in Fig. 5.8 (left). From these measurements, we derive the stem-length-dependent ratios simply by re-ordering the data at fixed wavelengths for the different WDM geometries, which is depicted in Fig. 5.8 (right). From the left graph we infer $\sin^2$-dependencies of $CR_{\mathrm{i1}}^{\mathrm{cross}}(\lambda_{\mathrm{i1}})$ at fixed stem lengths, which is in reasonable agreement with FEM model. Apparently, the couplers provide slightly stronger coupling due to more weakly confined modes, a fact that is also covered by our findings concerning the differences in mode sizes between effective index method (EIM) theory and measurement (see Sec. 5.1.1). The analysis of the argument functions of the $\sin^2$-behavior, however, provides us with the wavelength-dependent mismatch of the propagation constants between the symmetric and anti-symmetric eigenmodes. We see that the propagation constant mismatch and, thus, the difference of the effective refractive indices increase linearly with wavelength in the telecom regime.

We also extract information about the wavelength-dependent influence of the

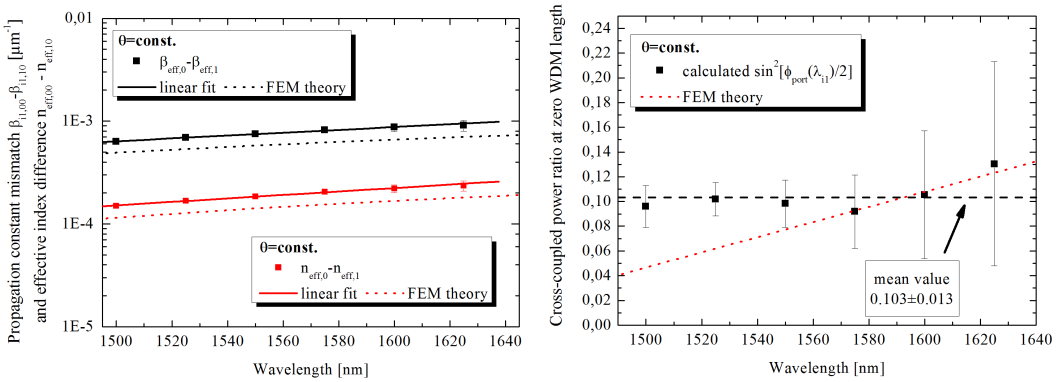

Figure 5.9.: Measurement-deduced coupler properties. **Left**: The difference of propagations constants as well as the effective refractive index difference between the symmetric and the anti-symmetric system mode both increase linearly with the idler wavelength. **Right**: The coupler's S-bend input and output ports have an almost constant influence on the amount of cross-coupled power at different wavelengths. Note the slight increase when approaching the waveguide cut-off wavelength.

WDM input and output ports on the overall power transfer, i. e. the cross-coupling amount at $L_C = 0\,\mu$m. This information is extractable from the y-axis offset of the $\sin^2$-fit curves, and it is plotted in the right graph of Fig. 5.9. We find that the influence of the S-bend ports on the amount of cross-coupled power is almost constant for the whole idler wavelength range of interest. A zero-length S-bend WDM potentially couples around $CR_{i1}^{cross}\,(L_C = 0\,\mu\text{m}) = (0.103 \pm 0.013)$ with the technological treatment applied in our case. Our experimental results are in good agreement with the FEM model, which predicts between 4% and 13% of cross-coupled power increasing almost linearly within the range of $1490\,\text{nm} \leq \lambda_{i1} \leq 1640\,\text{nm}$. The small remaining discrepancies are expected to stem from the limited number of different coupler stem lengths and, thus, data points. This leads to uncertainties in the y-axis offset of the $\sin^2$-curves, which might be higher than what we calculated.

Additionally, we calculate the suppression of the idler light for the bar output arm, similarly to Eq. 5.11:

$$S_{i1}\,(\lambda_{i1}) = 10 \cdot \log\left(\frac{P_{i1,\text{bar}}\,(\lambda_{i1})}{P_{i1,\text{cross}}\,(\lambda_{i1}) + P_{i1,\text{bar}}\,(\lambda_{i1})}\right). \tag{5.14}$$

In Fig. 5.10, the dependency of the bar output suppression on the stem length L_C and on the wavelength is illustrated. We identify shifts in the optimum suppression towards higher wavelengths, when choosing WDM structures with shorter stem length. This means that idler photons at higher wavelengths have to propagate shorter distances in order to fully transfer to the adjacent channel due to the larger difference in propagation constants. We find that a following parabolic curve

$$\lambda_{i1}^{peak}\,(L_C) = a \cdot L_C^2 + b \cdot L_C + \lambda_0$$

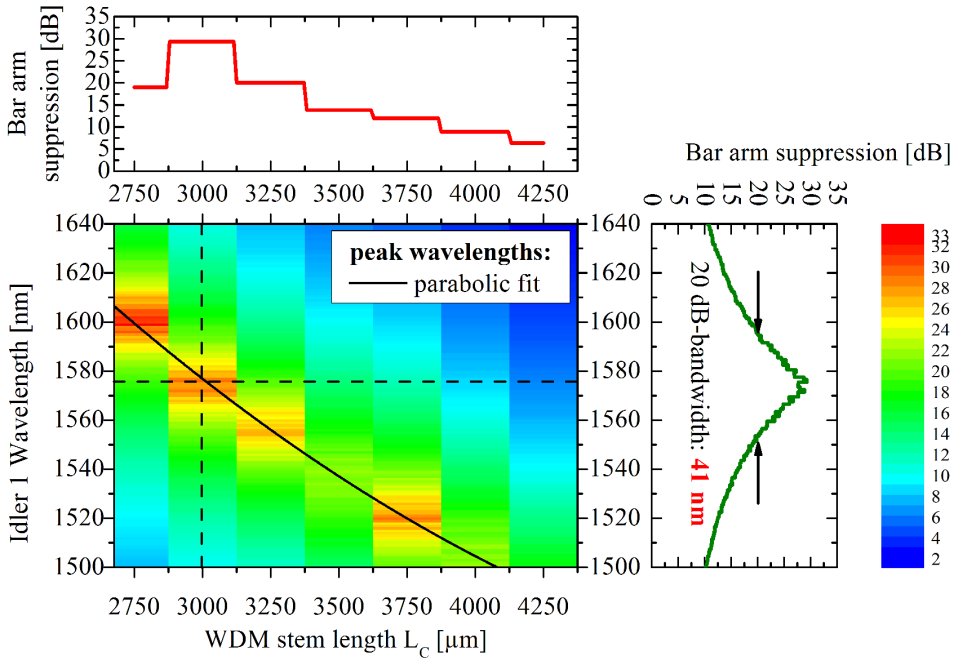

Figure 5.10.: Idler suppression calculated from the measured data: with the fixed coupler stem lengths on our chip (vertical bands, color-coded), we can address distinct idler wavelengths. We achieve bandwidths of $\Delta\lambda_{\mathrm{i1}}^{20\mathrm{dB}} = (40 \pm 4)\,\mathrm{nm}$ with more than $S_{\mathrm{i1}} \geq 20\,\mathrm{dB}$ of suppression for all structures. Note that at $L_{\mathrm{C}} = 3500\,\mu\mathrm{m}$ the bar suppression is still larger than 99%, despite the color-coding.

predicts the wavelength in [nm] of maximum idler cross-coupling in the considered range of stem lengths in [μm]. The best-matching set of parameters is given by $a = 1.44 \cdot 10^{-5}\,\mathrm{nm} \cdot \mu\mathrm{m}^{-2}$ and $b = -0.1731\,\mathrm{nm} \cdot \mu\mathrm{m}^{-1}$, which jointly determine the negative slope of the peak wavelength, and $\lambda_0 = 1966.576\,\mathrm{nm}$ being the y-axis wavelength offset.

Another feature of the integrated WDMs is their high suppression over considerably large bandwidth. From the side graph in Fig. 5.10, we deduce that at least 20 dB suppression for wavelengths ranges of $\Delta\lambda_{\mathrm{i1}}^{20\mathrm{dB}} = 40 \pm 4\,\mathrm{nm}$ around the peaks with $S_{\mathrm{i1}}\,(\lambda_{\mathrm{i1}}) \geq 30\,\mathrm{dB}$ is possible to achieve. Likewise, we note that the chosen power measurement method still leaves space for improvements, since we use large-area sensors, which inevitably collect light from scattered substrate modes. Especially the peak suppressions can be estimated to reach higher values, when spatial restrictions to only the guided modes (e. g. by pinholes or irides) are considered.

Our findings make also clear the necessity of future technological effort on adiabatic mode converters and improved waveguide tapers. In order to address only the fundamental signal mode by proper pump injection, the tailoring of the input

waveguide appears reasonable. Alternatively, it is also worth exploring the inclusion of taper structures behind the integrated directional coupler. This approach could reduce the guided signal mode number to only the fundamental one in the bar output port. This also leads to the benefit that non-properly coupled idler photons do not remain in the original output arm. Instead, these photons scatter to the substrate due to the changed cut-off condition of the waveguide. Thus, improperly coupled idler photons will have significantly decreased impact on high-sensitive measurements for telecom wavelengths in the bar output arm.

5.4. Secondary parametric down-conversion source conversion characterics

As mentioned above, it is important for cascaded wavelength conversion processes that the intermediate wavelengths match. If we want, for example, signal photons of our primary PDC source to act as pump photons for the secondary PDC stage, the emission wavelength must range within the acceptance bandwidth of the secondary phase-matched process. This makes the careful analysis of the tunability of the secondary conversion stage in terms of reasonable free parameters absolutely necessary. In this section, the description is given of how we analyzed the secondary PDC stage emission.

Specifically, we employ second harmonic generation as a basic characterization method. Direct spectral measurements of down-converted photon pairs at the telecom wavelength regime with the fiber spectrometer method are also presented.

5.4.1. Indirect characterization method by second-harmonic generation

For the experimentally most convenient PDC characterization method at the infrared wavelengths, we make use of the fact that second-harmonic generation (SHG) labels the reverse process of degenerate parametric down-conversion. Thus, the injection of TM-polarized coherent light from a tunable external cavity laser at wavelengths $1570\,\mathrm{nm} \leq \lambda_\mathrm{F} \leq 1610\,\mathrm{nm}$ to our waveguide structures allows us to measure second harmonic classical light with a photodiode. Since the secondary periodic grating is situated at the output of our chip, the launching of the fundamental telecom light is done from the backward direction.

In the measurement, we benefit from several design properties of the integrated device. The end-face anti-reflective coating allows for optimized pump coupling at telecom wavelengths. The on-chip directional coupler, on the other hand, provides the generated second harmonic light to be transferred to the nominal bar input port without significant loss, whereas the fundamental pump light is coupled to the nominal cross input. Thus, we can easily separate the pump from the generated SHG.

Due to the non-optimized end-face for $\sim 790\,\mathrm{nm}$ at the output, around 30% of the SHG light gets reflected and might exit the sample at the optimized input. However,

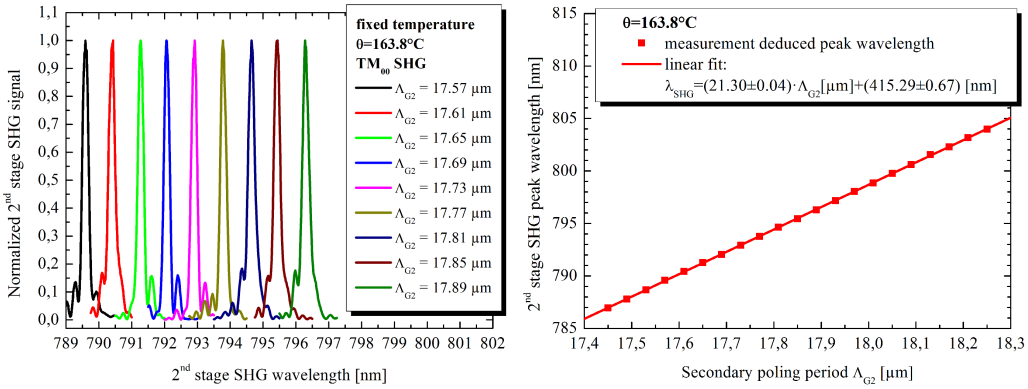

Figure 5.11.: We generate second harmonic with a tunable laser at telecom wavelengths. **Left:** The normalized data shows a shift towards longer SHG wavelengths with larger poling periods Λ_{G2} at a temperature of $\theta = 163.8°C$. The full set of available poling periods is not shown. **Right:** Tuning curve of the secondary phase-matching condition. The generated second harmonic depends linearly on the poling period and shifts by $\Delta\lambda_{SHG}^{peak} = \pm 0.43\,nm$ per $\Delta\Lambda_{G2} = \pm 0.02\,\mu m$ grating period step.

we cannot expect any significant fringing in the generated second harmonic signal, since no intrinsic Fabry-Perot-resonator is formed by the coatings for wavelengths of $\sim 1580\,nm$ and $\sim 790\,nm$.

In Fig. 5.11, we visualize the dependence of the normalized SHG spectra on the poling period. Obviously, the second harmonic peak shifts linearly towards longer wavelengths with increasing grating periods. We deduce from the linear regression curve that the slope defines the step-wise tuning capability for the fixed device temperature of $\theta = (163.8 \pm 0.1)°C$. We calculate the SHG wavelength tuning to be $\Delta\lambda_{SHG}^{peak} = \pm(0.426 \pm 0.001)\,nm$ per on-chip poling period step of $\Delta\Lambda_{G2} = \pm 0.02\,\mu m$. We notice that the tuning by changing the grating periods can only act as a coarse adjustment for the sought NIR wavelength.

For fine-tuning the secondary QPM condition, we focus on the temperature-dependent behavior of the second harmonic peak. Supported by Fig. 5.12 we derive a linear relationship between the SHG peak wavelength and the temperature. The SHG peak wavelength fine-tuning is deduced from the slope as $\Delta\lambda_{SHG}^{peak}(\theta) = (0.1015 \pm 0.001)$ in the range of $140°C \leq \theta \leq 200°C$. This means that the wavelength shifts by $\Delta\lambda_{SHG}^{peak} = \pm(10.15 \pm 0.02)\,pm$ per $\Delta\theta = \pm 0.1°C$ change in temperature. The data is provided for the poling period $\Lambda_{G2} = 17.61\,\mu m$. The shallow slope has a positive impact on the source stability at changing thermal conditions: despite the tuning range is limited over a broad temperature range, wavelength drifts are limited as well for changing ambient temperatures. This makes our secondary PDC/SHG source thermally and temporally stable. From the normalized spectra, we also estimate the bandwidth of the generated second harmonic to be $\lambda_{SHG}^{FWHM} = (0.45 \pm 0.03)\,nm$.

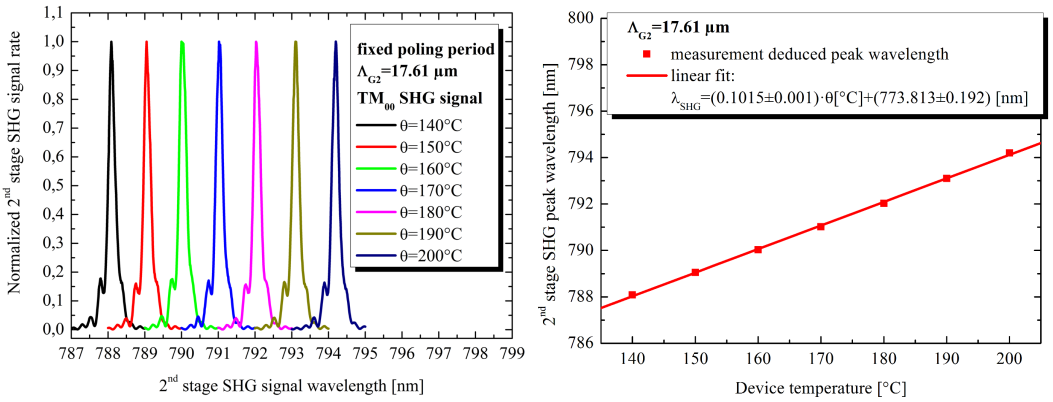

Figure 5.12.: Fine-tuning of the secondary phase-matching condition by device temperature. **Left:** The generated second harmonic shifts towards longer wavelength at higher temperatures **Right:** For a fixed poling period of $\Lambda_{\mathrm{G2}} = 17.61\,\mu\mathrm{m}$ we derive a linear dependency of the SHG peak wavelength on temperature such that thermal fluctuations of $\Delta\theta = \pm 0.1°\mathrm{C}$ lead to SHG wavelength deviations of only $\Delta\lambda_{\mathrm{SHG}}^{\mathrm{peak}} = \pm 10.2\,\mathrm{pm}$.

5.4.2. Direct parametric down-conversion emission characterization using dispersive fibers

The direct measurements of secondary PDC emission requires some experimental effort, but yields valuable information for cascaded parametric down-conversion experiments. The content of this section denotes the main prerequisite for the experimental work in section 7.2

We implement the setup shown in Fig. 5.13 and stabilize our source at $\theta = (163.8 \pm 0.1)°\mathrm{C}$. The secondary PDC stage is pumped with picosecond laser pulses at a repetition rate of $f = 1\,\mathrm{MHz}$ in the range of $785.84\,\mathrm{nm} \leq \lambda_{\mathrm{p2}} \leq 791.88\,\mathrm{nm}$ and in steps of $\Delta\lambda_{\mathrm{p2}} = 0.23\,\mathrm{nm}$. The phase-matching condition does not change for thermal reasons, but with the pump wavelength due to energy and momentum conservation. Note that the chosen step width equals the spectral resolution of the pump-monitoring spectrometer device, which has been used also for the PDC characterization in Sec. 5.2.

The analysis is performed using a highly dispersive fiber of around 5 km length in combination with a superconducting nanowire detector and a time-tagging module. This experimental configuration builds a fiber-spectrometer system, that stretches the generated signal/idler pulses in time, according to their spectral components [193]. The wavelength calibration of the fiber-spectrometer has been performed only for the range of $1500\,\mathrm{nm} \leq \lambda \leq 1600\,\mathrm{nm}$ [194], where a linear dependence of the delay on the wavelength is sufficiently accurate. However, we expect that driving our PDC source at strongly degenerate wavelengths will exceed the calibrated wavelength

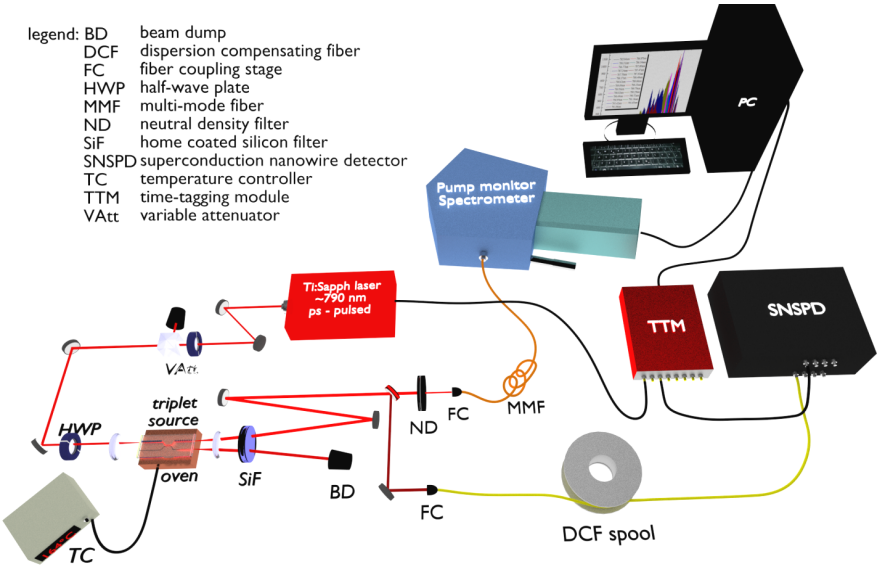

Figure 5.13.: Schematic setup for alternative 2nd PDC stage characterization: We pump the secondary PDC source with ps-pulsed NIR light variably at around $790 \pm 5\,\mathrm{nm}$ and $\sim 1\,\mathrm{MHz}$. After spectral broadening in a calibrated highly dispersive fiber, we collect the emitted photons in a temporally delayed manner according to their spectral contributions with a superconducting nanowire detector. For the synchronization, we feed the electronic laser trigger into the time-tagging module.

range to around $1400\,\mathrm{nm} \leq \lambda_{\mathrm{PDC},2} \leq 1750\,\mathrm{nm}$. Therefore, we perform a parabolic fit to our calibration data in order to achieve lower χ^2 values and, thus, smaller confidence intervals for the expected signal and idler wavelengths. For a reference wavelength of $\lambda_{\mathrm{ref}} = (1570 \pm 0.5)\,\mathrm{nm}$, measured with a well-known narrow-band filter characteristics and the generated PDC at $f_{\mathrm{rep}} = 1\,\mathrm{MHz}$ repetition rate, we register an arrival time of $\tau_{1570} = (217.35 \pm 0.11)\,\mathrm{ns}$. Here, the ultimate resolution of the spectrometer is technically given by the temporal resolution of the time-tagging module of $\Delta\tau_{\mathrm{TTM}} = \pm 0.0823\,\mathrm{ns}$, but this uncertainty convolutes with the error in the central wavelength of the calibration filter. Solving the calibration fit equation for the reference wavelength provides us with the time, which the reference light took for traveling along the fiber spool. We subtract this time from the y-axis offset of the calibration curve and get the reduced timing offset $\tau_0 = -1346.987\,\mathrm{ns}$. In that manner, we have shifted the calibration curve towards earlier arrival times in order to accommodate for the pump laser repetition time. In other words: we perform an operation of the total fiber delay modulo the repetition time.

By re-arranging the modified fit curve we can deduce the actual wavelengths in [nm] from the relative arrival times τ_{delay} in [ns] with respect to the electronic trigger of our pulsed laser system. Doing so, we get the following formula of square-root

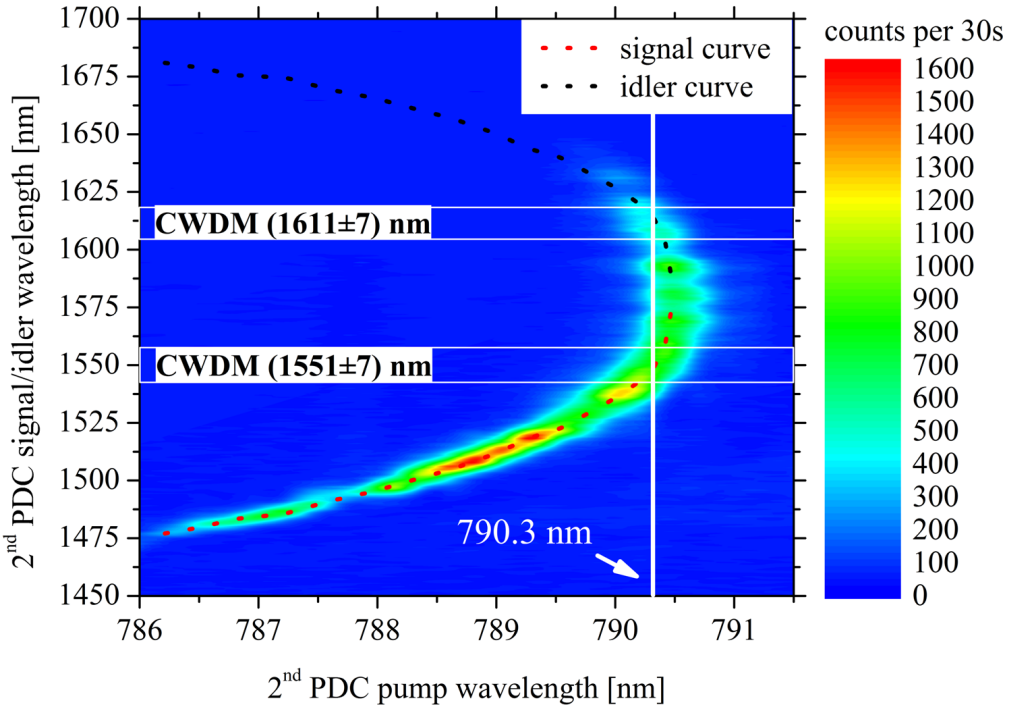

Figure 5.14.: The spectral splitting of signal and idler wavelengths can be tuned such that addressing of suitable fiber-based CWDM filters can be achieved (horizontal bands). The operation of the secondary PDC with primary signal photons at $\lambda_{s1} = \lambda_{p2} \leq 790.3\,\mathrm{nm}$ improves the spectral separability by dielectric edge-filters with finite slope. The idler photons tend to be guided more and more weakly at wavelengths above $1635\,\mathrm{nm}$, and dashed lines serve as a guide to the eye for the spectral signal/idler splitting.

type:

$$\lambda_{s2/i2}\left(\tau_{\mathrm{delay}}\right) = \lambda_0 + \sqrt{\lambda_0^2 - \left(\frac{\tau_0 + \tau_{\mathrm{delay}}}{d_{\mathrm{F}}}\right)}. \tag{5.15}$$

For the cut-on wavelength $\lambda_0 = 1200.146\,\mathrm{nm}$ the calibration formula shows real values. The parameter $d_{\mathrm{F}} = 0.0012\,\mathrm{ns}\cdot\mathrm{nm}^{-2}$ is an expression for the fiber dispersion.

The definition range for the calibration is given by $0\,\mathrm{ns} \leq \tau_{\mathrm{delay}} \leq 382\,\mathrm{ns}$. Note that we do not pre-compensate optical and electronic delays, but we benefit from the low repetition rate of the pulsed laser, which prevents photons from consecutive pulses to overlap temporally. In other words, the temporal width of a stretched pulse is significantly smaller than the laser repetition time window.

We acquire the number of click events of the secondary PDC outcome over 30 seconds for different pump wavelengths. A color-coded and pump-wavelength-dependent graph is shown in Fig. 5.14. Signal and idler are at degenerate wavelengths and

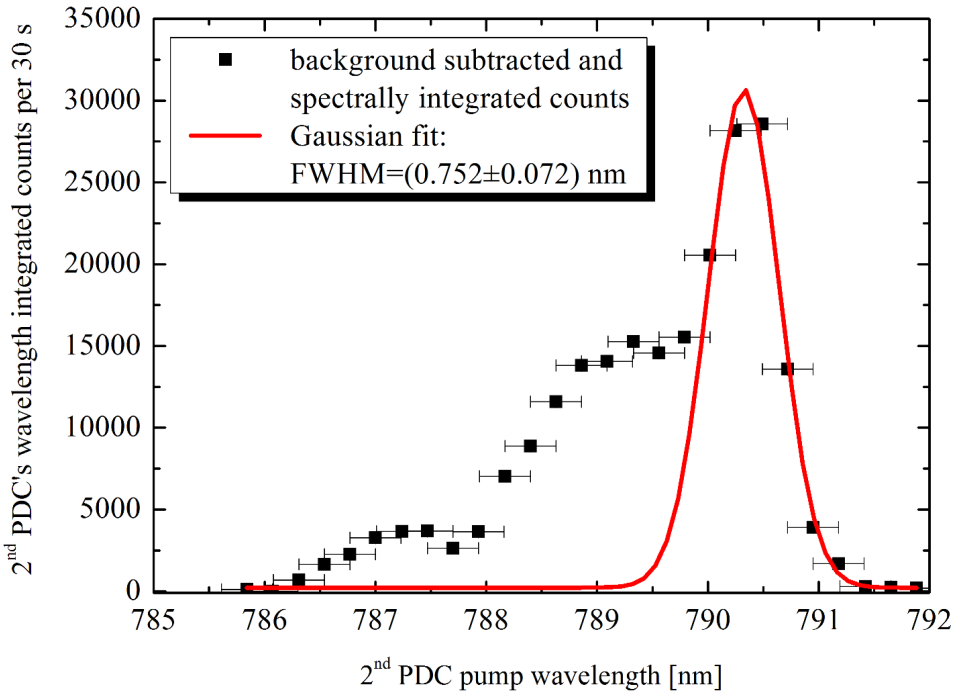

Figure 5.15.: We integrate the spectrally resolved PDC outcome dependent on the pump wavelength. The peak at $\lambda_{p2} = 790.5\,\mathrm{nm}$ labels the principle wavelength operation point for a fixed temperature, while the width of our Gaussian fit curve indicates the acceptance bandwidth of the secondary PDC process and, thus, defines the good spectral overlap to the first PDC process.

with broad spectral distribution at $\lambda_{s2} = \lambda_{i2} = (1581 \pm 35)\,\mathrm{nm}$, while pumping at $\lambda_{p2} = (791.49 \pm 0.23)\,\mathrm{nm}$. Likewise, we infer that decreasing the pump wavelengths leads to splitting of the PDC emission into two spectral arms, i. e. non-degenerate signal and idler photons. The two parts of the spectrum narrow down with higher degrees of non-degeneracy. The graph also exhibits the tendency of our waveguides to guide idler photons at wavelengths higher than $\lambda_{i2} > 1635\,\mathrm{nm}$ only weakly. This effect can be reduced in the future by increasing the initial titanium layer thickness to be deposited. This dispersion engineering task increases the effective refractive indices of our waveguide and, in turn, their mode confinement.

From the emission characteristics, we also infer the acceptance bandwidth of our secondary PDC stage. The necessity of this estimation evolves from the need for spectral overlap of primary PDC signal photons serving as the pump for the secondary PDC process in cascaded PDC processes. We sum over the number of acquired counts per 30 s for individual 2^{nd}-stage PDC emission spectra and plot the outcomes dependent on the pump wavelength. This yields the graph depicted in Fig. 5.15, which is nothing else than a summation over the count rates of the y-axis

in Fig. 5.14 for discrete pump powers. We include a Gaussian fit curve of the form

$$g_{\mathrm{p2}}\left(\lambda_{\mathrm{p2}}\right) = \frac{A_{\mathrm{PDC,2}}}{\sqrt{2 \cdot \pi \cdot \sigma_{\mathrm{PDC,2}}^2}} \cdot \exp\left[-\frac{\left(\lambda - \lambda_{\mathrm{PDC,2}}^{\mathrm{deg}}\right)^2}{2 \cdot \sigma_{\mathrm{PDC,2}}^2}\right] \tag{5.16}$$

to the peak data points. Here, $A_{\mathrm{PDC,2}}$ is a scaling parameter, $\lambda_{\mathrm{PDC,2}}^{\mathrm{deg}}$ denotes the central wavelength of the peak, i. e. the wavelength, where degenerate PDC occurs. The fit parameter $\sigma_{\mathrm{PDC,2}}$ is the $1/e$-decay width, from which we deduce the FWHM of the spectral acceptance bandwidth. By normalizing the fit curve, which is indicated by the primed scaling parameter $A'_{\mathrm{PDC,2}} = 0.8079$, we get $\sigma_{\mathrm{PDC,2}} = 0.32217\,\mathrm{nm}$, from which we calculate the spectral acceptance bandwidth to be $\Delta\lambda_{\mathrm{p2}}^{\mathrm{FWHM}} = (0.759 \pm 0.031)\,\mathrm{nm}$. The accumulated emission shows a maximum at the third fit parameter, i. e. the degeneracy pump wavelength $\lambda_{\mathrm{PDC,2}}^{\mathrm{deg}} = (790.324 \pm 0.130)\,\mathrm{nm}$.

The acceptance bandwidth of the secondary PDC process is narrower than the emission bandwidth of our primary PDC signal photons. Note that the data points at short pump wavelengths reflect non-degenerate phase-matched PDC in the graph in Fig. 5.15. The two seeming side peaks in the integrated count rates at $\lambda_{\mathrm{p2}} = 787.2\,\mathrm{nm}$ and $\lambda_{\mathrm{p2}} = 789.3\,\mathrm{nm}$ pump wavelengths are suspected to be caused by variations in the transmittance of the end-face coating of our device for different signal 2. By contrast, the steep drop above the degeneracy pump wavelength indicates the emission tendency towards non-phase-matched cases. We estimate the emission bandwidth of the primary PDC signal from the spectrum in Fig. 5.7, where thermal stabilization at $\theta \approx 163.5°\mathrm{C}$ is given. We perform a Gaussian fit of the form

$$f_{\mathrm{s1}}\left(\lambda\right) = \frac{A_{\mathrm{s1}}}{\sqrt{2 \cdot \pi \cdot \sigma_{\mathrm{s1}}^2}} \cdot \exp\left[-\frac{\left(\lambda - \lambda_{\mathrm{s1}}^{\mathrm{peak}}\right)^2}{2 \cdot \sigma_{\mathrm{s1}}^2}\right] \tag{5.17}$$

to our acquired data. Similar to the case above, we derive the individual parameters after normalization. We get for the scaling factor $A'_{\mathrm{s1}} = 1.2351$ and for the $1/e$-decay width of the PDC signal $\sigma_{\mathrm{s1}} = 0.53969\,\mathrm{nm}$. From the latter, we derive the FWHM $\Delta\lambda_{\mathrm{s1}}^{\mathrm{FWHM}} = (1.27 \pm 0.28)\,\mathrm{nm}$. The center wavelength is well-approximated by $\lambda_{\mathrm{s1}}^{\mathrm{peak}} = (790.633 \pm 0.261)\,\mathrm{nm}$.

Consequently, we calculate the spectral overlap of the two nonlinear processes as

$$\eta_{\mathrm{s1-p2}} = \frac{|\int f_{\mathrm{s1}}(\lambda) \cdot g_{\mathrm{p2}}(\lambda)\,\mathrm{d}\lambda|^2}{\int f_{\mathrm{s1}}^2(\lambda)\,\mathrm{d}\lambda \cdot \int g_{\mathrm{p2}}^2(\lambda)\,\mathrm{d}\lambda}. \tag{5.18}$$

For the thermally not yet optimized case discussed here, we only get a spectral overlap of around $\eta_{\mathrm{s1-p2}} = 0.69$. After perfect alignment of the center wavelengths of the primary PDC signal and secondary PDC acceptance curve, we achieve $\eta_{\mathrm{s1-p2}} = 0.88$ at maximum, limited by the different spectral widths, for the optimum temperature $\theta = (163.8 \pm 0.1)°\mathrm{C}$.

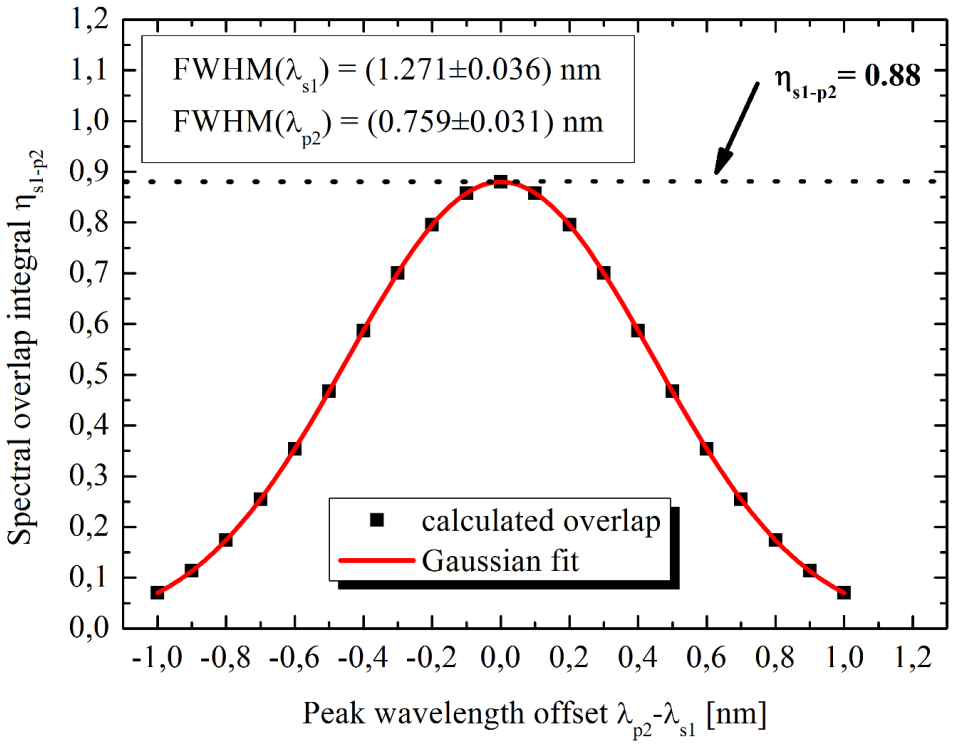

Figure 5.16.: The spectral mode overlap integral is shown dependent on the peak wavelength offset and does not only depend on the (fixed) spectral bandwidths of primary signal emission and the secondary pump acceptance wavelength. By contrast, the matching of the peak wavelengths has a strong impact on the mode overlap integral. For variations of the center wavelengths by less than $\pm 0.15\,\mathrm{nm}$, we do no suffer from overlap fluctuations by more than $5\,\%$. This requirement is met with our temperature tuning and stabilization apparatus.

In Fig. 5.16 we plot the dependency of the spectral overlap integral on the center wavelength mismatch $\Delta\lambda_{\mathrm{s1-p2}} = \lambda_{\mathrm{p2}} - \lambda_{\mathrm{s1}}$, the latter of which can be set to zero by temperature tuning. The graph shows that we can afford spectral mismatch between the two PDC sources of around $\Delta\lambda_{\mathrm{s1-p2}} = \pm 0.15\,\mathrm{nm}$, without losing more than $5\,\%$ of spectral overlap efficiency.

Remembering the temperature dependencies of the two sources (see Sec. 5.2 and this section above), we can conclude that in a cascaded PDC process our secondary stage will be pumped by primary PDC signal photons with perfect intrinsic spatial mode matching and very good spectral overlap. Accurate thermal stabilization to $\theta = (163.8 \pm 0.1)^{\circ}\mathrm{C}$ is the essential requirement, but can be achieved with low effort using standard temperature controllers. Our findings in this section underline that we can expect a long-term stable and reliable source for the photon-triplet generation by cascaded parametric down-conversion as described in Sec. 7.2. However, with

further technological work, we can achieve unit spectral compatibility of the two PDC processes. Tailoring the effective periodic poling lengths, such that the first PDC's effective poling length is enhanced, will narrow down the emission bandwidth of the primary PDC signal photons. In addition, this will also increase the internal conversion efficiency. If the effective poling length for the second PDC stage is reduced simultaneously, we can broaden its pump acceptance bandwidth, but at the cost of interaction length.

Conclusion

In this chapter we performed basic linear characterization measurements, which yielded information not only about the low waveguide losses in our integrated device, but also on the mode shape and size of telecom light. The latter characteristics has been used to propose a good mode overlap of both polarizations to standard single-mode fibers, which could be used for packaging of the device in the future.

Additionally, we characterized the integrated directional coupler thoroughly, and we proved that quasi-deterministic spatio-spectral splitting (demultiplexing) of TM-polarized light at around 800 nm and 1600 nm can be conveniently achieved on-chip. We also inferred from our data that further optimization of the coupling behavior at C- and L-band telecom wavelengths can be pursued by adapting the coupler stem length.

We characterized the periodically poled waveguide structures in terms of nonlinear wavelength conversion processes, most importantly parametric down-conversion. Our findings show that our device's spectral conversion characteristics can be manipulated conveniently by temperature tuning and stabilization. We also found that our waveguides exhibit the tendency to run into cut-off for wavelengths above 1635 nm, which could limit the nonlinear emission tuning capabilities.

However, we were able to anticipate several combinations of periodically poled waveguide structures, which are mutually compatible in terms of their emission spectra. With this information we will be able to perform cascaded wavelength conversion processes, as will be described in Chap. 7.

CHAPTER 6

Device application in selected quantum information tasks

Contents

Having characterized our integrated device in the previous sections enables us to perform selected quantum optical application tasks as will be described in this chapter. As a first experiment, the heralded preparation of single photons at telecom wavelengths is presented, which underlines the high brightness and low noise properties of our primary parametric down-conversion source on-chip. We achieve heralding efficiencies of $\eta_{\mathrm{H}} \geq 60\,\%$ and high coincidences-to-accidentals ratios (CAR) of higher order photon contributions up to values of $CAR_{\mathrm{HOP}} \geq 7400$. The second-order auto-correlation function around $g^{(2)} = 3.8 \cdot 10^{-3}$ not only proves the single photon character of the generated light quanta, but it is also among the lowest values measured so far. Additionally, the applicability of the chip as a source for passive decoy state quantum key distribution (QKD) is examined experimentally and discussed. We prove the heralding of higher order n-photon states up to $n = 4$, while the inferred photon click statistics exhibit excellent agreement with theoretical predictions. Our source meets the requirements to avert photon-number-splitting attacks in passive decoy state quantum key distribution (QKD).

6.1. Heralding single photons with high brightness and low noise

The preparation of single photons is a fundamental prerequisite for quantum information processing tasks like quantum key distribution [53] and linear optical quantum computing [51, 195–198]. The deterministic availability, i. e. photonic quantum states on-demand, can be called the "holy grail" of quantum optics. Among several promising technologies like trapped ions [35–37], cold atoms [41, 42], vacancies in diamond [45–47], and quantum dots [43, 44], the generation of single photons via parametric down-conversion (PDC) is the work horse for preparing photons with high purity and brightness. Although PDC is a probabilistic single photon generation process, it can offer pseudo-deterministic single photon sources by making use of the fact that the generated photons are always created as correlated pairs. If one of the photons is detected, it allows us to announce or herald the presence of its twin, dependent on the loss in its detection channel. The combination of PDC and quantum memories can also provide pseudo-on-demand single photons [199].

In all the single-photon-generation techniques, the probability to detect single photons is crucial for judging the on-demand character: the higher the chance to detect a single photon, the closer the source is to a genuine on-demand single-photon source. This means for PDC-based photon-pair sources the probability to herald one single photon by the detection of its twin has to be as close to unity as possible. As long as there are no detectors with almost unit quantum efficiency available, we can determine the so-called Klyshko efficiency [200] by relating the number of coincident photon detection events to the number of single events for the heralding or heralded photons. At the same time, the generated single photons must exhibit true quantum characteristics, for example self-interference and interference with identical single photons in an interferometer or at beam splitters. This anti-bunching phenomenon is typically proven by Hong-Ou-Mandel interference [27]. In 1977 Kimble et al. [26] demonstrated the first photon anti-bunching phenomena with sodium atomic emission. Later on, in 1986 Grangier et al. [201] applied the concept of Clauser [202] in a Hanbury Brown-Twiss (HBT) geometry [124] to characterize anti-correlation effects by conditioned preparation of single photon states (see description in the next section 6.1.1). A well-established method to estimate the mean photon number of a PDC source is the anti-correlation parameter α, the value of which can be determined by relating the count rates and coincidence rates of binary detectors [203] in conditioned correlation measurements (see Sec. 6.1.2). This parameter is similar to the second-order auto-correlation function $g^{(2)}(0)$ (see Sec. 3.3), which is different for the types of light. While for bunched light $g^{(2)}(0) > 1$, coherent light sources like lasers show values of $g^{(2)}(0) = 1$. By contrast, the second-order auto-correlation function for genuine single photons is $g^{(2)}(0) = 0$. This means that conditioned $g^{(2)}(0)$ measurements providing values below one indicate the quantumness of the considered light source. In practice, the upper bound convention for defining the photons' single quantum character is commonly $g^{(2)}(0) < 0.5$ [47].

In this part of the thesis, the generation of heralded single photons at telecom wavelengths with the fabricated integrated device is pursued. For the testing, the full number of on-chip functionalities is not employed, but we restrict ourselves to the application of the primary guided-wave PDC stage in conjunction with the integrated directional coupler. The deposited end-face coatings support our aims for the device application in terms of an expected overall efficiency increase. In our experiments we aim for highest possible Klyshko- and heralding efficiencies, while the single-photon character must be given by $g^{(2)}(0)$-values close to zero. If the second-order auto-correlation function differs from zero, this indicates the generation of higher-order photon-number contributions. The rates, by which the single photons are generated and detected, should be as high as possible for proving applicability in quantum optical tasks like QKD or linear optical quantum computing. At the same time, the purity of the heralded single photons over spurious noise contributions must be given by the highest possible coincidences-to-accidentals ratio (CAR).

The investigation of the different periodic poling structures in Sec. 5.2 as well as the telecom coupling behavior (see Sec. 5.3) allows us to determine a combination of both integrated elements, where the best possible spectro-spatial demultiplexing of the generated photon pairs is achieved. More specifically, a poling period of $\Lambda_{\mathrm{G1}} = 6.75\,\mu\mathrm{m}$ in conjunction with a coupler stem length of $L_{\mathrm{C}} = 3000\,\mu\mathrm{m}$ is chosen for the experiments described in this section.

At temperatures around $\theta = 175°\mathrm{C}$ we benefit from the stability of the device such that the emission wavelengths of $\lambda_{\mathrm{s1}} = 803\,\mathrm{nm}$ for signal photons and $\lambda_{\mathrm{i1}} = 1573\,\mathrm{nm}$ for the idler photons are set by temperature tuning. This wavelength combination allows for the quasi-deterministic on-chip spectro-spatial splitting of the photon pairs. While the signal photons remain in the original waveguide with the bar-coupling ratio $1 - CR_{\mathrm{s1}}^{\mathrm{cross}} = (99.2 \pm 0.1)\,\%$, the idler photons are transferred to the adjacent channel with the cross-coupling ratio $CR_{\mathrm{i1}}^{\mathrm{cross}} \geq (99.5 \pm 0.1)\,\%$ defined in Sec. 5.3.1. The chosen wavelength combination of the photon pairs has a high relevance to applications in quantum network applications: The signal photons can be detected very efficiently with off-the-shelf components, while the idler photons have a high transmittance (low propagation loss) in optical fibers.

6.1.1. Hanbury Brown-Twiss setup

With the setup depicted in Fig. 6.1 we implement a HBT-type measurement apparatus for the characterization of the pump-power-dependent brightness and the single photon character of the primary PDC source. This kind of experimental configuration makes use of the photon-splitting capabilities of a balanced beam-splitter: if higher-order photon contributions are present, spatial splitting will occur with specific probabilities. For example, a two-photon state will be split with 50% chance, where either one of the photons ends up in one output arm of the beam-splitter. Likewise, the probability of having both photons in the same arm is only 25% for each arm. Stochastic calculations on even higher-order n-photon contributions can

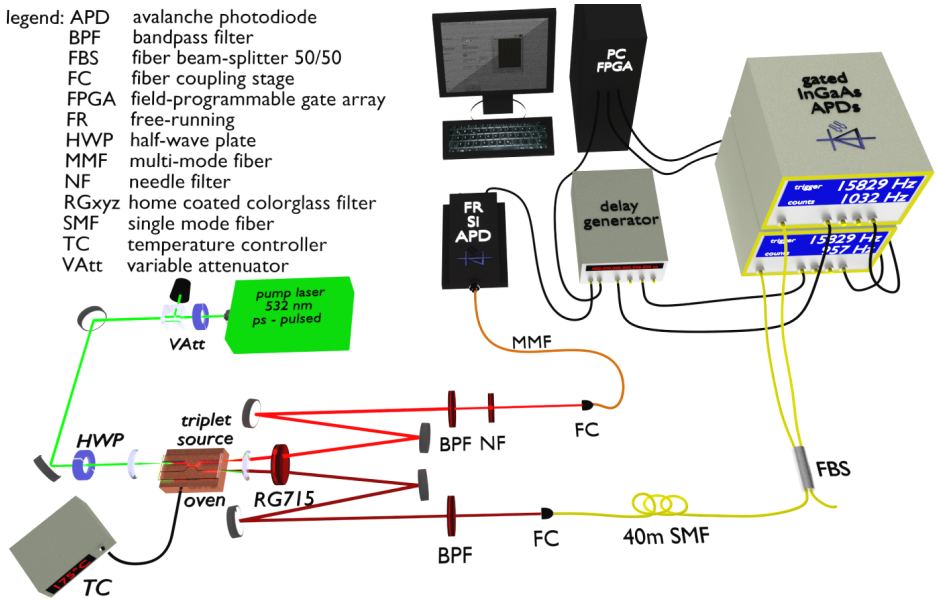

Figure 6.1.: Experimental setup for conditioned measurements. The detection of signal photons at the silicon avalanche photodiode announces the presence of its twin photon. If higher order photon pairs are involved, their simultaneous appearance is detected as a coincidence at the gated InGaAs-APDs. For the count and coincidence analysis, a field-programmable gate array is employed.

bring to light that the chance of having a detection event in only one of the output arms decreases with n. This means, in turn, that the probability of detection coincidences between both output arms increases and provides us with the opportunity to prove directly the non-single-photon character of the generated PDC light. In other words: we have to prove a low the impact of higher-order photons in order to verify the heralding of single photons.

Compared to the described PDC characterization experiments in the previous chapter we modified neither the temperature and input polarization control nor the coupling stage for the picosecond pulsed pump light at 10 MHz repetition rate and $\lambda_p = 532\,\mathrm{nm}$. While the pump is suppressed by around two orders of magnitude at the high-reflecting end-face coating of the device, an additional customized absorptive filter (RG715) with high reflection for 532 nm and $T_{\mathrm{RG715}} \geq 97\,\%$ transmission at signal and idler wavelengths is placed behind the anti-reflection-coated output objective. Two D-shaped mirrors split up the on-chip separated output beams to a signal and an idler arm.

In order to reduce the impact of spurious noise contributions stemming from either the heated device or residual pump photons we include a bandpass-filter with the

characteristics of $FWHM = 12\,\mathrm{nm}$ and $T_{\mathrm{peak}} \geq 99.5\%$ as well as a needle filter with $FWHM = 0.5\,\mathrm{nm}$ and $T_{\mathrm{peak}} = 78\%$ in the signal beam path. Both filters suppress the nonlinear Cherenkov radiation optimally.

Additionally, the analysis part of the setup was extended such that coupling of signal photons into a multi-mode fiber (MMF) can be achieved. The MMF is connected to a free-running silicon avalanche photo-diode (Si-APD) (Perkin Elmer SPCM-AQRH-13) with specified detection efficiency of $\eta_{\mathrm{Si}} = 0.55$ at around 800 nm and an average dark count rate of $R_{\mathrm{T,dark}} = (238 \pm 16)\,\mathrm{s}^{-1}$. The specified dead time of $\tau_{\mathrm{Si}}^{\mathrm{dead}} = 50\,\mathrm{ns}$ is smaller than the temporal pulse-to-pulse-distance of our pump laser. This means that dead time effects should not play a role for the measurement of signal photons.

The idler beam, after free-space spectral filtering, is fed to a 40 m long anti-reflexion-coated single-mode fiber by a high-precision coupling stage. A fiber-based 50/50 beam-splitter allows for the individual addressing of two gated InGaAs-APDs (ID Quantique ID201) for $g^{(2)}(0)$ measurements. The detectors operate in the Geiger mode and are specified to yield detection efficiencies of $\eta_{\mathrm{InGaAs}} = 0.24$ at the expected idler wavelength. The acquisition time gates for idler detection events have been set to 2.5 ns with zero internal dead time.

When generated signal photons are detected by the Si-APD, the corresponding electronic pulse is sent through a delay generator (Stanford Research DG645), which compensates for optical path differences between signal and idler photons. The variably delayed electrical pulses have been employed to trigger the two InGaAs-APDs for (measured) gate widths of $\tau_{\mathrm{gate}} = (1.16 \pm 0.32)\,\mathrm{ns}$, mainly determined by the timing jitter of the detectors.

The single signal photon detection rate R_{Si}, as well as the *conditioned* detection rates $R_{\mathrm{i1,1}}$ and $R_{\mathrm{i1,2}}$ have been recorded using a field-programmable gate array (FPGA) with 25 ns temporal resolution, which suffices to resolve subsequent pulses of our 10 MHz-pulsed system. Likewise, the FPGA is capable of registering coincidences of the three detector signals within its temporal precision.

The classical characterization of the overall idler transmission loss from the device's endface to the InGaAs-APDs input results in a transmission factor of $T_{\mathrm{i1}} = 0.663 \pm 0.030$. Thus, the maximum achievable Klyshko efficiency [200] of our experimental setup is limited by the overall transmission in the idler arm, by the respective detector efficiency and by the coupling efficiency of the on-chip integrated directional coupler to

$$\eta_{\mathrm{K,System}} = T_{\mathrm{i1}} \cdot \eta_{\mathrm{InGaAs}} \cdot CR_{\mathrm{i1}}^{\mathrm{cross}} = 0.151. \tag{6.1}$$

This upper experimental boundary only holds for low pump power levels, where higher order photon pair contributions can be neglected.

6.1.2. Heralded single photons, conditioned $g^{(2)}(0)$-measurements and coincidences-to-accidentals-ratios - theoretical considerations

Before the experimental results are presented, let us briefly concentrate on the derivation of suitable benchmarking properties in order to be able to compare with

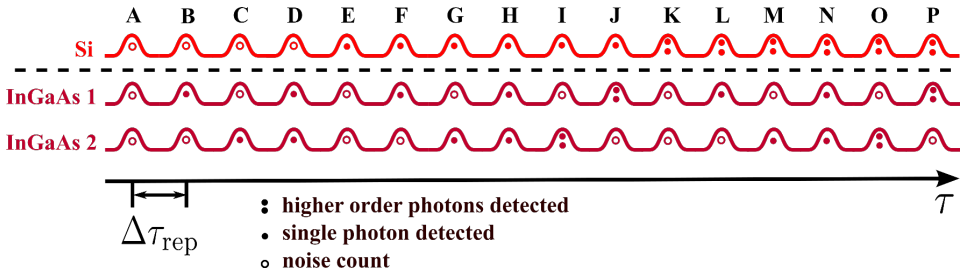

Figure 6.2.: Possible measurement outcome schematic for the HBT configuration. The cases A - D represent the conditioning on noise events especially at very low pump powers, whereas in E - J single detected photons herald the presence of either noise (E), genuine single photons (F and G) or higher order photon contributions (H - J). Higher order photon contributions may also act as the herald at the signal binary detector, and the possible distributions of corresponding idler photons are depicted in cases K - P. Note that every single shown event option has an impact on the coincidence measurements, but only the single photon cases F and G are of interest.

similar work of other groups. The schematic in Fig. 6.2 illustrates the possible measurement results in a Hanbury Brown-Twiss-type experimental configuration. Therein, we assume that generated PDC photon number per pulse follows Poisson distribution for the spectrally multi-mode case [204, 205].

At very low pump powers, where the zero-photon contributions are predominantly present in the optical pulses, the influence of noise counts in any of the detectors on the measurements outcomes is crucial. For moderate pumping, genuine single signal photons dominate the heralding events as well as the conditioned detection of idler photons. The impact of higher order photon contributions in the signal and the idler beam path can be determined by careful analysis of the experimental data.

The generated idler photons are sent through a 50/50 beam-splitter in front of the detection apparatus. Thus, the rates $R_{\mathrm{i1,1}}$ and $R_{\mathrm{i1,2}}$ and their sum, $R_{\mathrm{c,double}} = R_{\mathrm{i1,1}} + R_{\mathrm{i1,2}}$, reflect genuine photon pair events, as long as both InGaAs-detectors do *not* fire coincidently. Otherwise, the generation of at least two photon pairs in the PDC process is indicated by the coincidence rate R_{c}, which labels simultaneous detection events in all three involved detectors.

In this conditioned setting, the anti-correlation parameter α is given by [201, 203]

$$\alpha = \frac{R_{\mathrm{Si}} \cdot R_{\mathrm{c}}}{R_{\mathrm{i1,1}} \cdot R_{\mathrm{i1,2}}}. \tag{6.2}$$

For judging the amount of higher order photon components within the PDC pulses we also utilize the second-order auto-correlation or Glauber function $g^{(2)}(0)$. It has

been shown (see, for example, [206]) that $g^{(2)}(0)$ can be calculated as

$$g^{(2)}(0) \simeq 4\frac{R_{\mathrm{Si}} \cdot R_{\mathrm{c}}}{\left(R_{\mathrm{i1,1}} + R_{\mathrm{i1,2}}\right)^2} \tag{6.3}$$

for conditioned measurements, if we assume higher order photon components being generated with much lower probabilities than single photon pairs. The two values α and $g^{(2)}(0)$ are both measures for the ratio between single photon pairs and higher order components, although they have been derived from different conceptual approaches. However, for conditioned genuine single photon detection, both will approach zero, if experimental imperfections like noise counts are neglected.

The joint Klyshko efficiency η_{K} represents the transmittance and detection in the idler arm. It depends also on the measurable rates and is determined by the formula

$$\eta_{\mathrm{K}} = \frac{R_{\mathrm{i1,1}} + R_{\mathrm{i1,2}}}{R_{\mathrm{Si}}} = \frac{R_{\mathrm{c,double}}}{R_{\mathrm{Si}}}. \tag{6.4}$$

Thus, at low pump powers, where higher-order photon contributions do not play a significant role, it serves as a general measure for the generation of single photon pairs. Since our deployed InGaAs-APDs have been operated at efficiencies below unity we also calculate the heralding efficiency

$$\eta_{\mathrm{H}} = \frac{\eta_{\mathrm{K}}}{\eta_{\mathrm{InGaAs}}} \approx T_{\mathrm{i1}} \cdot CR_{\mathrm{i1}}^{\mathrm{cross}}, \tag{6.5}$$

which describes the performance of the single photon preparation, when noise contributions are neglected. The heralding efficiency denotes one of the most important figures of merit for PDC-based single photon sources as discussed above.

Similar to continuous-wave (cw) experiments, the coincidences-to-accidentals ratio (CAR) provides information about the performance of the implemented parametric down-conversion source. However, the fact that our measurements have been performed with pulsed light requires suitable definitions. We notice that the CAR is dependent on the relative time delay between signal and idler detection. Shifting the relative delay of the trigger pulse and the correlated idler gradually to a timing between two consecutive idler pulses we expect decreasing Klyshko- and heralding efficiencies. Relating the maximum Klyshko efficiency at perfect pulse overlap to the minimum Klyshko efficiency we get

$$CAR_{\Delta\tau} = \frac{\eta_{\mathrm{K}}(\mathbf{P}_{\mathrm{p}}, \Delta\tau = 0)}{\eta_{\mathrm{K}}(\mathbf{P}_{\mathrm{p}}, \Delta\tau = T)}, \tag{6.6}$$

where $|T|$ must be larger than the gating time window width but smaller than the repetition time τ_{rep} of our pump. Whenever parasitic fluorescence with long lifetimes is induced, $CAR_{\Delta\tau}$ will drop significantly due to artificial coincidences outside the region of perfect temporal pulse overlap. This definition of $CAR_{\Delta\tau}$ is similar to the one of a signal-to-noise-ratio (SNR), and it is equivalent to the inverse optical noise factor (ONF), provided in Ref. [207] for cw heralded single photon sources [208].

Another CAR_{rep} definition, on the other hand, provides indirect information about two-photon-pair contributions. We shift the relative time delay such that a correlated pulse overlaps with a neighboring pulse at integer multiples of the repetition time τ_{rep}. The detected coincidences originate from non-correlated PDC events. From the expression

$$CAR_{\mathrm{rep}} = \frac{R_{\mathrm{c,double}}(\mathbf{P}_{\mathrm{p}}, \Delta\tau = 0)}{R_{\mathrm{c,double}}(\mathbf{P}_{\mathrm{p}}, \Delta\tau = m \cdot \tau_{\mathrm{rep}})}, \quad m \in \mathbb{N}. \tag{6.7}$$

we deduce the photon pair generation probability p, which is closely linked to the mean photon number per pulse and hence to the brightness of our source. The value of CAR_{rep} for different neighboring pulses has to be the same, regardless of the number of skipped pulses.

The third useful definition of CAR evolves as a general measure of higher order photon contributions, if we relate the rate of all two-fold coincidences, $R_{\mathrm{c,double}}$, to the rate of unwanted three-fold coincidences R_{c} at perfect temporal pulse overlap (i.e. $\Delta\tau = 0$). The purity of the single photon preparation, in addition to the $g^{(2)}(0)$ value, is characterized by

$$CAR_{\mathrm{HOP}} = \frac{R_{\mathrm{c,double}}(\mathbf{P}_{\mathrm{p}}, \Delta\tau = 0)}{R_{\mathrm{c}}(\mathbf{P}_{\mathrm{p}}, \Delta\tau = 0)}. \tag{6.8}$$

The value of CAR_{HOP} is expected to drop drastically with higher pump powers according to the increasing probability of generating higher order photon pairs. Note that, for the case of perfect detectors, CAR_{rep} and CAR_{HOP} result in exactly the same values, whereas deviations of this equality can be solely contributed to imperfect detectors.

6.1.3. Experimental verification and discussion of high-fidelity heralded single photons

6.1.3.1. State preparation rates

The power-dependent $g^{(2)}(0)$-measurements yield heralding rates R_{Si}, overall two-fold coincidence rates $R_{\mathrm{c,double}}$ and triple coincidence rates R_{c} for 1 s of measurement time. We repeat the measurement hundred-fold and analyze the statistics of our data. Additionally, we perform the same number of measurements with blocked idler detectors in order to get information about the uncorrelated noise counts. For the evaluations below we subtract the noise count rates from the measured rates in order to estimate the performance of the source best. Thus, we rule out the measurement outcome A - E in Fig. 6.2 for our data analysis in general.

Figure 6.3 depicts the recorded, noise-corrected count rates in double-logarithmic scaling, which exhibits the expected behavior: the signal photon count rate, which acts as the herald, depends linearly on the increasing pump power up to around $\mathbf{P}_{\mathrm{p}} = 20\,\mu\mathrm{W}$. The slope of the linear fit curve

$$R_{\mathrm{Si}}^{\mathrm{meas}}(\mathbf{P}_{\mathrm{p}}) = a_{\mathrm{Si}} \cdot \mathbf{P}_{\mathrm{p}} + b_{\mathrm{Si}}, \tag{6.9}$$

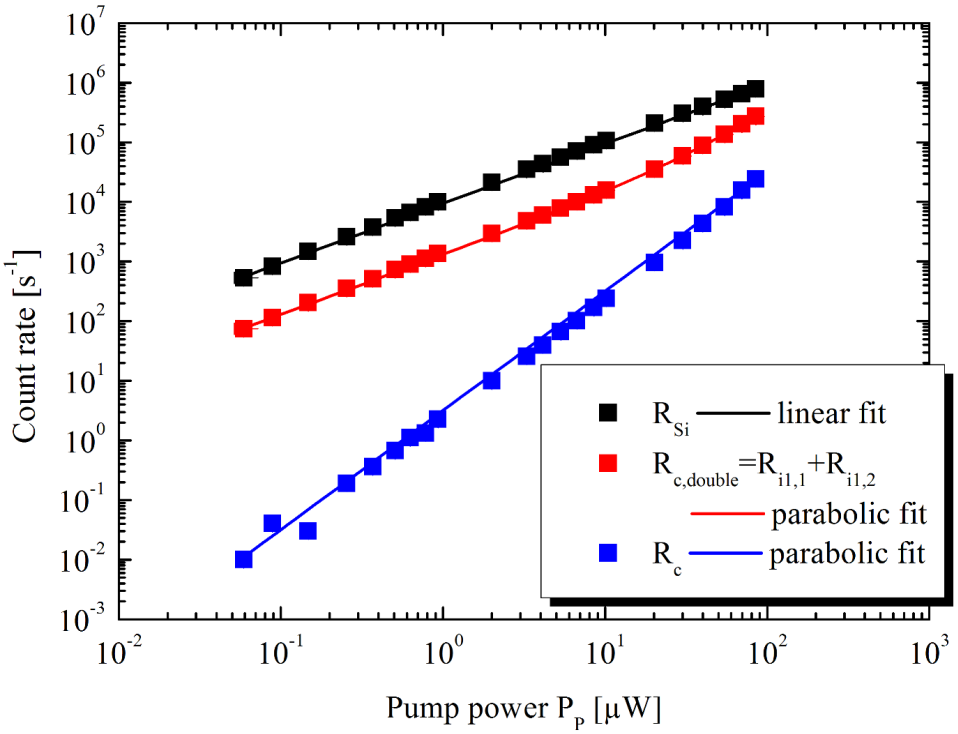

Figure 6.3.: The plot shows the pump-dependent count rates of the trigger (black), the sum of the two-fold coincidences (red) and the three-fold coincidences (blue) in conditioned measurements. We notice a linear behavior of the count rate in the Si-APD, whereas the coincidence rates are fitted best by quadratic functions (see main text).

which is related to the PDC conversion probability in conjunction with beam path and detection efficiencies in the signal arm, has been determined as $a_{\mathrm{Si}} = (10339 \pm 33)\,\mu\mathrm{W}^{-1}\,s^{-1} \approx 10^7\,\mathrm{mW}^{-1}\,s^{-1}$ for the considered pump power range. We can also label this term as the brightness of the heralding photons. By taking the detector efficiency of the Si-APD, $\eta_{\mathrm{Si}} = 0.55$, and the arm signal transmittance, $\eta_{\mathrm{s1}} = (0.59 \pm 0.05)$, into account we get a conversion efficiency of $P_{\mathrm{PDC,1}} = (1.16 \pm 0.10) \cdot 10^{-8}$ pairs per pump photon, where the pump coupling efficiency to the waveguide is not included. The y-axis offset, $b_{\mathrm{Si}} = (357 \pm 206)\,\mathrm{s}^{-1}$, represents the noise count rate of the Si-APD at zero pump power and matches the specified dark count rate very well.

At higher power levels, the Si-APD tends to saturate, which we could blame on dead time effects of this detector type. The more intuitive explanation for the gap between the linear behavior and the measured one arises from the expected influence of higher order photon contributions: while the detector is not photon-number-resolving, all higher order signal photon contributions have inevitably been counted only as one event. Together with the suspected Poisson-distributed photon-

number characteristics of the PDC at elevated pump powers (i. e. generated mean photon numbers per pulse), the avalanche photo-diodes detects less photons than expected for a linear behavior [209].

By contrast, the conditioned detection rates $R_{\mathrm{i1},1}$ and $R_{\mathrm{i1},2}$ can be described best by quadratic curves. For the single count rates of both idler detectors we get

$$R^{\mathrm{meas}}_{\mathrm{i1},1/2}\left(\mathbf{P}_{\mathrm{p}}\right) = a_{\mathrm{i1},1/2} \cdot \mathbf{P}_{\mathrm{p}}^2 + b_{\mathrm{i1},1/2} \cdot \mathbf{P}_{\mathrm{p}}, \tag{6.10}$$

where the quadratic parameters $a_{\mathrm{i1},1} = (11.3 \pm 0.2)\,\mu\mathrm{W}^{-2}\,\mathrm{s}^{-1}$ and $a_{\mathrm{i1},2} = (10.8 \pm 0.2)\,\mu\mathrm{W}^{-2}\,\mathrm{s}^{-1}$ per heralding photon are related to the impact of higher-order photon-number contributions to the respective unconditioned count rates. Those contributions are present at higher pump powers because the more photons a pump pulse contains, the higher is the probability that more than one conversion process into signal and idler occurs, while the pump pulse propagates along the periodically poled waveguide. Additionally, self-seeding effects in the PDC process can take place, a process which is equivalent to optical parametric amplification or difference-frequency generation in classical nonlinear optics. We notice almost identical absolute values of $R^{\mathrm{meas}}_{\mathrm{i1},1}\left(\mathbf{P}_{\mathrm{p}}\right)$ and $R^{\mathrm{meas}}_{\mathrm{i1},2}\left(\mathbf{P}_{\mathrm{p}}\right)$, which indicates balanced splitting at the beam splitter in front of the two idler detectors. The linear parameters $b_{\mathrm{i1},1} = (675.4 \pm 12.1)\,\mu\mathrm{W}^{-1}\,\mathrm{s}^{-1}$ and $b_{\mathrm{i1},2} = (619.7 \pm 11.3)\,\mu\mathrm{W}^{-1}\,\mathrm{s}^{-1}$ per heralding photon are connected to the unconditioned noise count probabilities at the individual InGaAs-APDs.

The sum of both rates, $R^{\mathrm{meas}}_{\mathrm{c,double}}\left(\mathbf{P}_{\mathrm{p}}\right) = R^{\mathrm{meas}}_{\mathrm{i1},1}\left(\mathbf{P}_{\mathrm{p}}\right) + R^{\mathrm{meas}}_{\mathrm{i1},2}\left(\mathbf{P}_{\mathrm{p}}\right)$, expresses the overall heralded photon rate according to a logical OR operation, and it is fitted also by a quadratic curve very well:

$$R^{\mathrm{meas}}_{\mathrm{c,double}}\left(\mathbf{P}_{\mathrm{p}}\right) = a_{\mathrm{c,double}} \cdot \mathbf{P}_{\mathrm{p}}^2 + b_{\mathrm{c,double}} \cdot \mathbf{P}_{\mathrm{p}}. \tag{6.11}$$

The parameters $a_{\mathrm{c,double}} = (22.1 \pm 0.3)\,\mu\mathrm{W}^{-2}\,\mathrm{s}^{-1}$ and $b_{\mathrm{c,double}} = (1295.1 \pm 23.4)\,\mu\mathrm{W}^{-1}\,\mathrm{s}^{-1}$ both correspond simply to the sums of the individual parameters in Eq. 6.10. The slope of the fit function, i. e. the derivative of $R^{\mathrm{meas}}_{\mathrm{c,double}}\left(\mathbf{P}_{\mathrm{p}}\right)$ with respect to the pump power, is an expression for the overall brightness gain of our source due to the inevitable higher-order m-photon contributions, because these increase with higher pump powers and yield clicks around m times more often than one-photon states. As an example, we scale up our result to the common unit of one milliwatt of pump power and assuming the validity of this extrapolation, we deduce a source brightness of $R_{\mathrm{c,double}}\left(\mathbf{P}_{\mathrm{p}} = 1\,\mathrm{mW}\right) = (2.21 \pm 0.03) \cdot 10^7$ pairs per second, which is significantly higher than the value deduces from just the signal count rates above.

Since we have not set an additional dead time to the InGaAs-APDs we neglect an impact thereof. The non-linear heralding rate at the silicon detector mimics a lower mean photon number than the linear ideal case. Together with the fact that m-photon states lead to detection events around m times more often than one-photon events we deduce that the well-fitting parabolic curves stem mainly from one- and two-photon contributions.

Three-fold coincidences between the detectors occur very rarely at the lowest pump powers and, thus, must be attributed with the largest error bars. For increasing powers, the following quadratic curve with only one free parameter fits our measurement data best:

$$R_{\mathrm{c}}^{\mathrm{meas}}\left(\mathbf{P}_{\mathrm{p}}\right) = a_{\mathrm{c}} \cdot \mathbf{P}_{\mathrm{p}}^{2}. \tag{6.12}$$

The fit parameter $a_{\mathrm{c}} = (3.188 \pm 0.046)\,\mu\mathrm{W}^{-2}\,\mathrm{s}^{-1}$ defines the increase of the slope of the fit curve, which again relates to the increase of the impact of higher-order photon contributions. The good agreement between the fit curve and the measured data, in conjunction with negligible linear and zero-order parameters, indicates the expected behavior of the measurement data in a conditioned setup: if the heralding rate is close to zero, the heralded coincidence count rate in an HBT setup must be zero. Another reasonable explanation for the quadratic behavior is given by the fact that for the chosen pump powers, the mean output photon number per pulse comprises mainly higher-order photon states $m = 2$ besides the zero- and one-photon states. The two-photon components can split up in the HBT setup with 50 % probability. After splitting, the individual detection probability for these photons grows almost linearly with increasing pump power. Since the detection of split two-photon states represents stochastically independent events, the resulting coincidence probability as well as the coincidence rate comprises the product of the individual, linearly growing click probabilities. Thus, the coincidence rate, $R_{\mathrm{c}}^{\mathrm{meas}}\left(\mathbf{P}_{\mathrm{p}}\right)$, shows quadratic behavior dominantly.

From the results in this section we infer that the criterion for single photon sources is fulfilled by the verification of the high heralding rate of $R_{\mathrm{c,double}}\left(\mathbf{P}_{\mathrm{p}} = 1\,\mathrm{mW}\right) = (2.21 \pm 0.03) \cdot 10^{7}\,\mathrm{pairs/s}$. This is of the order of up-to-date photon sources based on type-I PDC [210].

6.1.3.2. Heralded single photon preparation

From the count rates we calculate the Klyshko efficiencies according to Eq. 6.4 as well as the heralding efficiencies with Eq. 6.5, and we plot both in Fig. 6.4.

We identify a constant heralding efficiency as high as $\eta_{\mathrm{H}} \geq 60\,\%$ for pump powers $\mathbf{P}_{\mathrm{p}} \leq 10\,\mu\mathrm{W}$, where seemingly only first order photon pairs contribute to the measurement outcome. The signal photon rate is up to $R_{\mathrm{Si}} = 1.05 \cdot 10^{5}\,\mathrm{s}^{-1}$ (compare with plot in Fig. 6.3). In Ti:PPLN based type-0 PDC devices, this labels the highest heralding efficiency reported to date. Other sources using comparable detection schemes (see for example [211–213]) rely on bulk nonlinear materials or optical fibers and do not offer more than one integrated functionality.

The limitations of our lab system are given mainly by free-space-to-fiber coupling efficiencies. They can be overcome in the future if a fiber-pigtailed architecture is connected with our PDC source. This measure can further improve the heralding efficiencies to around $\eta_{\mathrm{H}} \geq 80\%$, which is the current benchmark [50,62,212,214,215]. However, the symmetry of our guided modes and the spatial overlap to fiber modes is a limiting factor. In Sec. 5.1.1 we calculated the maximum overlap to be around 96%,

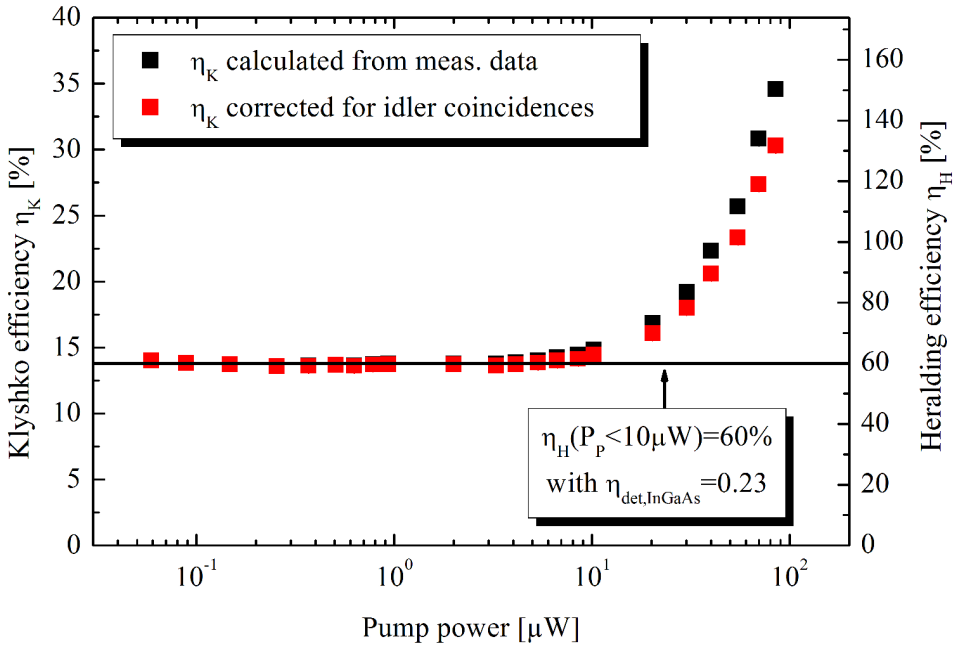

Figure 6.4.: Pump-dependent Klyshko efficiency and heralding efficiency. For pump powers below $10\,\mu$W, an almost constant heralding efficiency of $\eta_{\mathrm{H}} \geq 60\,\%$ has been achieved. We notice a super-linear increase for higher pump powers due to higher order photon contributions.

which denotes the fundamental limit for the heralding efficiency in fiber-pigtailed devices in Ti:PPLN.

The $g^{(2)}(0)$ values and the anti-correlation parameter α have been calculated using Eq. 6.3 and Eq. 6.2, respectively. As shown in Fig. 6.5, the second-order auto-correlation function at very low power levels ($\mathbf{P}_{\mathrm{p}} \leq 1\mu$W) reaches a minimum value of $g^{(2)}(0) = 0.0038$. This is one of the best results for heralded single photon sources in general [79, 206, 208], while it is the lowest obtained value in Ti:PPLN waveguide PDC sources to date. Our source, in that manner, typically outperforms other technological approaches, which provide GHz-rate single photons from quantum dots [216] or which make use of color-centers in diamond [47, 217]. The presented auto-correlation function can be pushed to even lower values at the cost of the heralded single photon rate. However, for applications in quantum key distribution low trigger rates are always related to only low secret key transmission rates. Thus, a proper trade-off between high rates and the genuine single photon character has to be found. Alternatively, the increase of the pump pulse repetition rates can improve the generated pair rates of our source [79].

From our results we also conclude that the approximation for the conditioned second-order auto-correlation function $g^{(2)}(0)$, made in Eq. 6.3 and in Ref. [203,206],

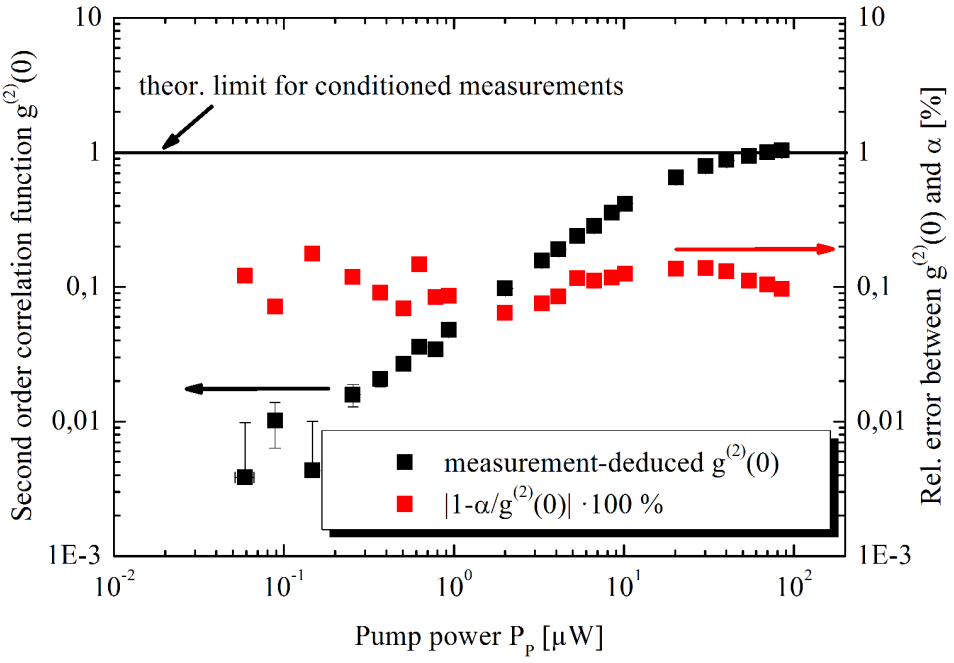

Figure 6.5.: Second-order auto-correlation function and its relative difference to the anti-correlation parameter α (right). For low pump powers, $g^{(2)}(0)$ tends to zero as expected, whereas for the highest applied pump powers, it approaches one. Note that the almost negligible relative difference of the two defined correlation parameters proves the equivalence of the derived Eq. 6.2 and Eq. 6.3. Note that values $g^{(2)}(0) < 1$ cannot be explained using classical assumptions about the light field.

is only valid and suitable for the low pump power regime. At the upper end of power scale used in these experiments we notice that $g^{(2)}(0)$ approaches one, which corresponds to an infinite mean photon number of the PDC output. Additionally, the uncorrelated noise which we did not treat separately and which follows thermal statistics increases the $g^{(2)}(0)$ artificially. Our assumption that the probability of generating higher order photon pairs is much smaller than the probability of single photon pairs, does not remain valid at high pump powers. Figure 6.5 additionally shows that the relative differences between the calculated values of $g^{(2)}(0)$ and the anti-correlation parameter α are very small, which is a proof of the equivalence of Eq. 6.2 and Eq. 6.3 for our measurements.

The triple coincidence rate R_c tends to be overestimated due to higher order photon contributions. Internal dead time effects of the InGaAs-APDs individually limit the rate of the detection of two-fold coincidences. We derive from the graph in Fig. 6.3 in conjunction with Fig.6.5, that heralding rates higher than $R_{\mathrm{Si}} \approx 3.1 \cdot 10^5\,\mathrm{s}^{-1}$ should be avoided for this kind of detectors in combination with the presented measurement scheme.

In order to overcome the limitations previously discussed, detectors with higher efficiencies, low noise rates and timing jitter, without intrinsic dead times as well as with the general capability to tell different photon numbers apart [218–220] should be used in the future. These detectors also allow for the conditioned detection of signal photons by employing the idler photons as heralds. However, addressing low-loss optical networks with the heralded single photons in the telecom wavelength regime would also require different wavelength combinations in the PDC process. The gap between the Klyshko efficiencies and the heralding efficiencies could also be minimized by the latest detector technology. As a result, the Klyshko efficiency could be a more direct benchmark for the *preparation* performance of genuine single PDC photons.

In summary we have achieved high heralding efficiencies of around 60% as the second prerequisite for an ideal single photon source. This is still significantly lower than what has been reported by other groups [50, 62, 214, 215], but we are confident to improve our results with additional efforts on loss reduction in the detection arms or by fiber-packaging of our device. Additionally, the measured $g^{(2)}(0)$-values are among the lowest reported so far and indicate the heralding of genuine single photons at low input powers.

6.1.3.3. Measurement of CARs

For the analysis of detrimental noise photon events we determine the source's heralding efficiency around the optimum time delay between the heralding signal photons and the heralded idler photons. For two different pump powers we measure the individual count rates in step widths of $\Delta\tau = 0.2\,\mathrm{ns}$, each for 5 seconds.

From the results, shown in Fig.6.6 we deduce a Gaussian-like envelope of the Klyshko efficiency with a temporal width of $\tau_{\mathrm{gate}} = (1.16 \pm 0.32)\,\mathrm{ns}$, which mainly reflects the intrinsic gate shape of the InGaAs-APDs. The error includes the combined timing jitter of the InGaAs-APD, the Si-APD and the delay generator. The graph also visualizes the slight increase of η_{K} at higher pump powers. This is due to the stronger impact of higher order photon pair contributions on the two-fold coincidence rates as well as on $R_{\mathrm{c,double}}$. At $\mathbf{P}_{\mathrm{p}} = 500\,\mathrm{nW}$ and $\mathbf{P}_{\mathrm{p}} = 5\,\mu\mathrm{W}$, the values $CAR_{\Delta\tau}$ have been calculated to be 1383 and 1165, respectively and do not decrease significantly. Please note, that in Fig. 6.6 this feature cannot to be identified intuitively due to the scaling. However, the (almost) constant $CAR_{\Delta\tau}$ for different pump powers is a strong indicator that the pump laser does not induce long-life fluorescence in any of the implemented optical elements.

Inverting the $CAR_{\Delta\tau}$ values provides us with ONF of 0.072% and 0.086%, respectively, which are both a factor of 3 smaller than the best ONFs in comparable continuous-wave experiments [208]. Together with the facts, that we still operate our source in the single photon regime ($0.027 \leq g^{(2)}(0) \leq 0.24$) and that we achieve high heralding rates of $5.3 \cdot 10^3\,\mathrm{s}^{-1} \leq R_{\mathrm{Si}} \leq 5.6 \cdot 10^4\,\mathrm{s}^{-1}$, this points out the benefits

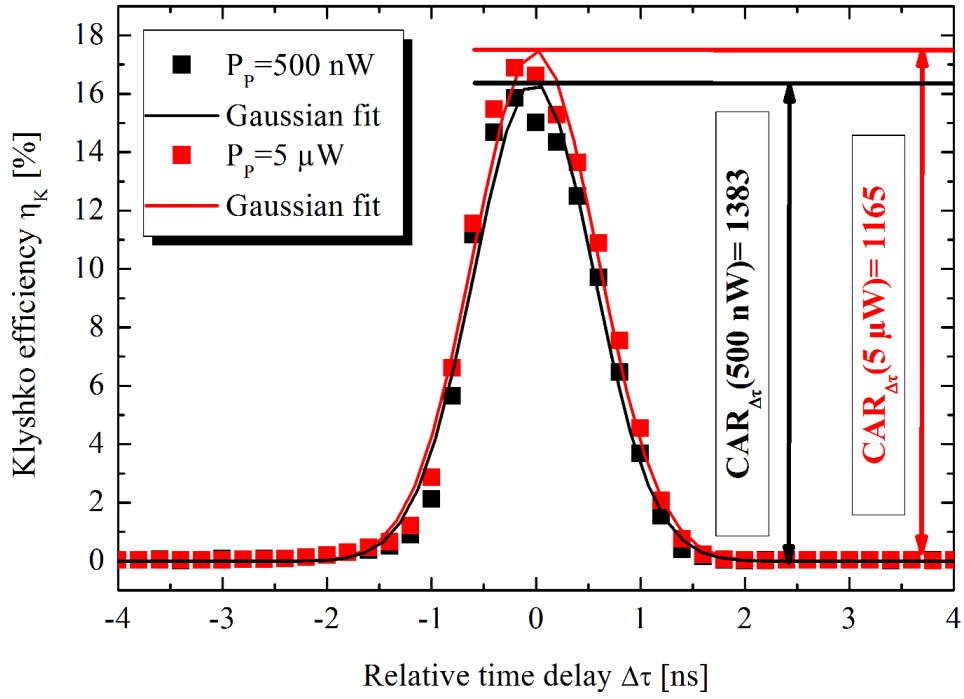

Figure 6.6.: Dependency of the Klyshko efficiency on the temporal overlap between signal and idler detection. We notice an increase of η_K at the higher pump power, but also an almost constant $CAR_{\Delta\tau}$. This behavior allows us to rule out the influence of pump-induced long-life fluorescence processes on our measurements.

of heralding single photons in the pulsed regime.

Figure 6.7 shows that the CAR_{rep} for two adjacent pulses asymptotically approaches 1 at the highest suitable pump power, while the CAR_{HOP} drops from 7440 to around 10 . This behavior proves the impact of higher order photon contributions and indicates, again, the usefulness of a trade-off between high heralding rates and a low $g^{(2)}(0)$.

One of the most important figures of merit of our source is its high brightness. Besides the high output photon pair rate per milliwatt we have determined the pump dependent mean photon number per pulse of the generated photons. The heralding rate R_{Si} has been divided by the transmission factors of all optical components in the signal arm and by the repetition rate $R_{\text{rep}} = 10\,\text{MHz}$. The graphical result is shown in Fig. 6.8. We identify a maximum achievable mean photon number per pulse of $\langle n_{\text{pulse,max}} \rangle = (0.24 \pm 0.02)$ at the highest applied pump power of $85.14\,\mu\text{W}$. The slope of the linear fit, $m = (3.14 \pm 0.06) \cdot 10^{-3}\,\text{pairs} \cdot \mu\text{W}^{-1}$, allows us to evaluate the lower bound for the PDC conversion efficiency of $\P_{\text{PDC}} = (1.172 \pm 0.093) \cdot 10^{-8}$ pairs per pump photon, where the coupling efficiency of the green pump laser to

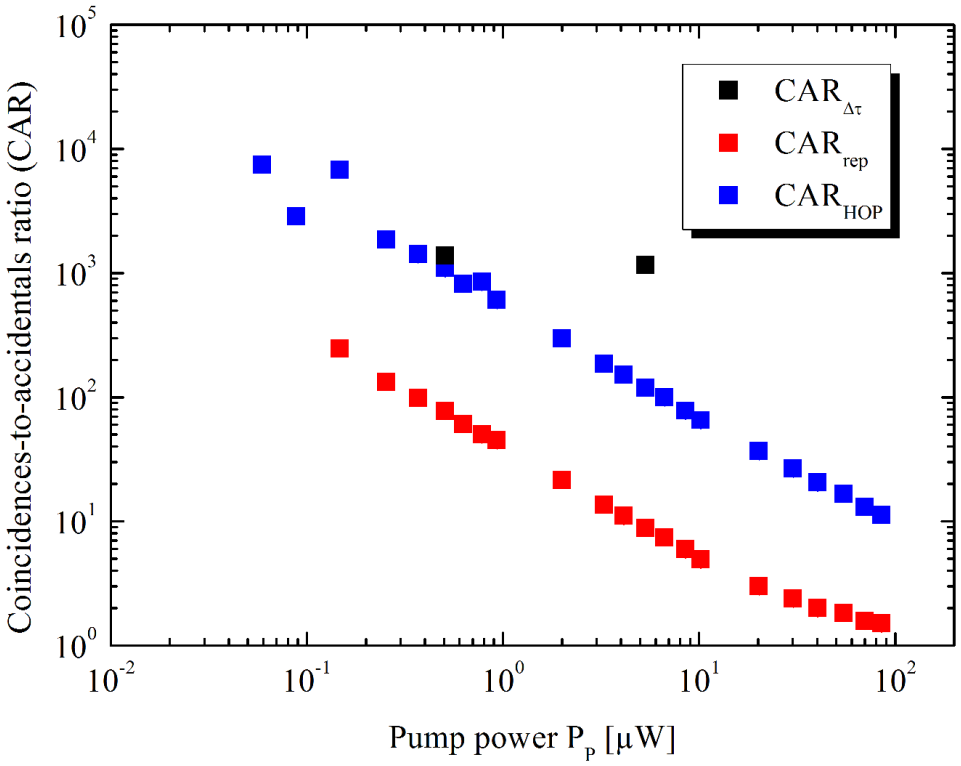

Figure 6.7.: Pump dependency of the three calculated coincidence-to-accidentals ratios. While $CAR_{\Delta\tau}$ does not change significantly at higher pump powers, the other two coincidences-to-accidentals-ratios drop rapidly to values close to one.

the waveguide structure is not included. It also allows for extrapolating an average photon number per pulse of $\langle n_{\mathrm{pulse,th}} \rangle \approx (34 \pm 2.7)$ at $\mathbf{P}_{\mathrm{p}} = 10$ mW of cw-equivalent pump power. This could be easily achieved with the employed pump laser. However, care must be taken of optical damage effects on the phase-matching conditions at high power levels.

As a closing remark for this section we conclude that the primary PDC stage of the presented device, in conjunction with the on-chip demultiplexer, acts as a versatile and efficient source for heralded single photons. It exhibits very high brightness in terms of pair generation rates even at low pump powers $\mathbf{P}_{\mathrm{p}} \leq 10\,\mu$W. The low impact of noise contributions on the single photon heralding, the high preparation efficiency as well as the pulsed excitation all underline the prospects of our integrated approach for applications in quantum information tasks. Additional functionalities can be integrated in future work in order to manipulate the generated photons on-chip, e.g. by electro-optic elements. However, in our measurements we did not take care of the spectral purity of the generated single photon pairs. Due to the dispersion properties of LN it is technologically hard to provide de-correlated pairs in terms of

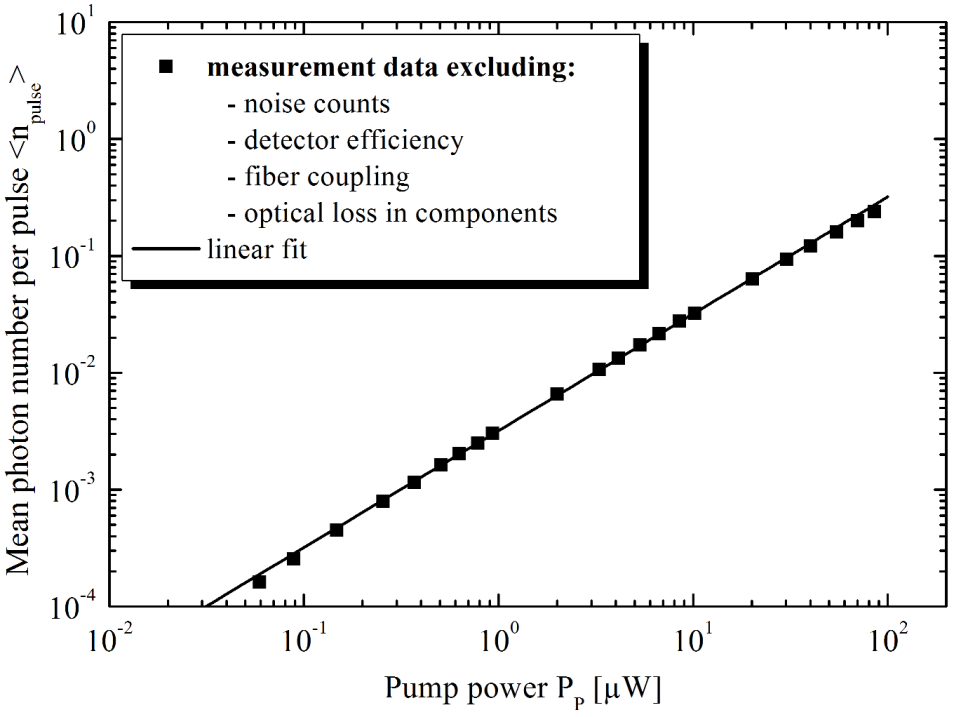

Figure 6.8.: The generated mean photon number per pulse is linearly depending on the pump power. From the linear fit curve we inferred that mean photon numbers up to $\langle n_{\mathrm{pulse}} \rangle \approx 34$ at pump powers of only $\mathbf{P}_{\mathrm{p}} = 10\,\mathrm{mW}$ could be achieved.

spectral indistinguishability. For this task it has been shown that periodically poled potassium titanyl phosphate waveguide structures offers spectrally pure states, the power-dependent mean photon number per pulse of which increases super-linear [50]. We also infer clear evidence for the scalability to higher order photon contributions, which are beneficial for the application of our device in passive decoy state quantum key distribution. This will be examined in more detail in the next section. However, we also note the current limitations of the presented experimental realization, which could be overcome by latest developments in detector technology, by pump lasers with high repetition rates [79] as well as by complete fiber-integrated solutions with our device. It has also been found that temporal multiplexing schemes could reduce the required pump pulse energy such that the impact of higher-order photons is significantly reduced, while the source brightness in terms of heralded single photons does not decrease [221].

6.2. Source applicability in passive decoy-state quantum key distribution

Quantum key distribution is one of the feasible applications in quantum information science and has been a field of high interest for the last three decades. It allows two trustworthy parties, Alice and Bob, to communicate with unconditional security in principle [53]. The main idea behind QKD is to generate a secret key, which consists of a series of light quanta in a specific encoding degree of freedom and which is shared by only the two trustworthy parties, similar to the one-time-pad [222], in order to decode secret information. Any interception and resending of the key must be either circumvented or at least recognized, when an arbitrarily powerful third party, Eve, who is only bound to the laws of nature, intends to get information about the key and the encrypted message.

Realistic implementations of QKD schemes can suffer from various security loopholes [223–240] due to technical imperfections of the implemented photon sources, quantum channels and measurement devices. The eavesdropper Eve could make use of any of these loopholes in order to break the security of the QKD system.

The so called photon-number-splitting attack (PNS) attack [241], in particular, allows Eve to make use of non-ideal properties of real-world photon sources. As shown in the previous section, photon-pair sources based on PDC can emit signal pulses with higher-order photon contributions. In the following we describe briefly the PNS attack together with the decoy state method, which aims for the removal of the PNS security loophole.

6.2.1. Photon-number-splitting attacks and the decoy state countermeasure

The idea to implement decoy states to QKD protocols has been proposed by Hwang in 2003, and first experimental demonstrations have been presented simultaneously by Lo et al. [242] and Wang in 2005 [243].

The photon-number-splitting attack arises from the fact that in QKD the yield Y_n of an n-photon state, i. e. the conditional probability that Bob detects a signal, given that an n-photon signal is emitted by Alice [242], depends strongly on the optical loss in the quantum channel. Assuming Alice prepares her key string using a photon source with Poissonian photon-number distribution (weak coherent pulses or multi-mode PDC sources), will lead to a specific yield for Bob due to optical loss. An eavesdropper could tap Alice's key string in order to analyze it for n-photon events. Whenever she detects a single photon, she blocks the transmission towards Bob's detector. For higher order photon states, she splits them such that only one photon is sent to Bob via an assumed lossless channel. Eventually, Bob will measure the same yield as if the quantum channel was not disturbed by Eve.

The decoy method intends to detect Eves activities in terms of the photon-number-splitting attack, and it basically relies on the following assumptions. On the one hand, the decoy scheme makes use of the fact that a weak coherent state with

average photon number $\langle n \rangle \ll 1$ is equivalent to a mixed Fock state in terms of Poissonian photon statistics, if the phases ϕ are totally randomized [244]:

$$|\langle n \rangle^{\imath\phi}\rangle \equiv \sum_n p_n(\langle n \rangle)|n\rangle\langle n| \tag{6.13}$$

with the probabilities of an n-photon state

$$p_n(\langle n \rangle) = \rho_n = \frac{e^{-\langle n \rangle} \cdot \langle n \rangle^n}{n!}. \tag{6.14}$$

Note that the generation of random phases is not necessarily an easy task for weak coherent pulses. On the other hand, we assume that Alice is able to replace her signal source randomly by a decoy source with average photon number $\langle n' \rangle \geq 1$, which means that the decoy source emission is dominated by higher order photon contributions. Achieving genuine randomness for the manipulation of the amplitudes of weak coherent states is highly non-trivial, and the required modulators must be able to be operated in a random manner. This leads to the conclusion that the active generation of applicable decoy states is technologically hard.

Furthermore, we require the general properties, e. g. the wavelength, of signals and decoy states to be identical. Likewise, the loss for higher order photons stemming from the signal source is assumed to be equal to the loss of the decoy source. In addition, the weighted average of the quantum bit error rates (QBER) e_n of various photon-number eigenstates is expected to depend on the photon number n.

Under these conditions, the eavesdropper cannot tell apart the photons of the secret key from decoy photons. The only information that Eve can get is the number of photons per optical pulse, but not the source emitting it. Since Alice and Bob can extract the yields Y_n and the QBERs e_n simultaneously for all n with high statistical precision from their measurements [245], Eve's PNS attack will inevitably change the values of the yields and quantum bit error rates. Thus, she can be detected with high probability using the decoy method.

Besides the robustness of the decoy state method against PNS attacks, it also offers, in combination, higher key generation rates and longer transmission distances [242, 246] than, for example, the standard Gottesman-Lo-Lütkenhaus-Preskill QKD protocol [223].

6.2.2. The passive decoy state method

In 2007, Mauerer and Silberhorn proposed the passive decoy-state QKD protocol [94] and theoretically showed the possible detection of photon-number-splitting attacks, even in the presence of imperfect PDC sources [247, 248]. It was also proven that the unconditionally secure transmission distance is on par with perfect single-photon sources [94, 249].

The passive decoy scheme is based on the idea of Hwang, but in contrast to active decoy schemes discussed above, which usually rely on strongly attenuated laser pulses (see, for example Yin et al. (2012) [250]), it turns the unavoidable

higher photon-number components of a parametric down-conversion source into a benefit by tagging them as *intrinsic* decoys. Importantly, this does not require any active amplitude modulation or phase randomization of the photon source's emission, since the probabilistic nature of PDC emission inherently exhibits neither phase reference information nor fixed optical pulse-to-pulse amplitudes.

The key feature of passive decoy QKD using PDC sources is that the system itself does not open any side channels with distinguishing information for different intensities, because all required decoy states are post-selected *after* transmission of a sufficiently large number of signals. This prevents Eve from distinguishing decoys from the intended signal key string during the transmission of the key.

Additionally, we make use of the fact that Alice can keep an exact copy of the generated pulse string for characterization purposes, given by the correlated twin photons of the PDC source. If Alice utilizes a photon-number-resolving detector [251, 252], she can convert the measured click statistics into the photon-number statistics [245] in order to separate signal states from decoy states during post-processing [94].

6.2.3. Experimental verification of the device applicability in passive decoy state quantum key distribution

In this section we characterize our integrated source in terms of its applicability in passive decoy-state quantum key distribution. We present the photon-number-resolved analysis of the photon click statistics over a broad range of pump powers, and we prove heralded n-photon states up to $n = 4$, which can be employed as post-selectable decoys. The measured photon click statistics exhibit excellent agreement with the theoretical predictions. We also conclude that our source meets the requirements to avert photon-number-splitting attacks.

In analogy to the previous section, our source is intended to generate signal photons at around 803 nm and idler photons around 1573 nm efficiently. The reasons for this choice can be found again in the efficient detection at the shorter wavelength, whereas the idler photons at telecom wavelengths allow for low-loss transmission in fiber-based QKD systems.

The capability of our device, to split the generated photons on-chip in a spatio-spectral manner, will conveniently allow Alice to keep one half (signal) of the strictly correlated pairs for thorough photon-number analysis using the time-multiplexed detector (TMD) described in [251]. The other half (idler) can be transmitted to her trusted counterpart Bob. Note that our nomenclature is the opposite of the one in Ref. [94], since our labeling is based on the common wavelength dependent notation of signal and idler.

6.2.3.1. Theoretical description of Alice's photon-number-resolving detector

In order to realize photon-number resolution with Alice's detection apparatus we implemented a time-multiplexer for signal wavelengths of 803 nm . The delay between

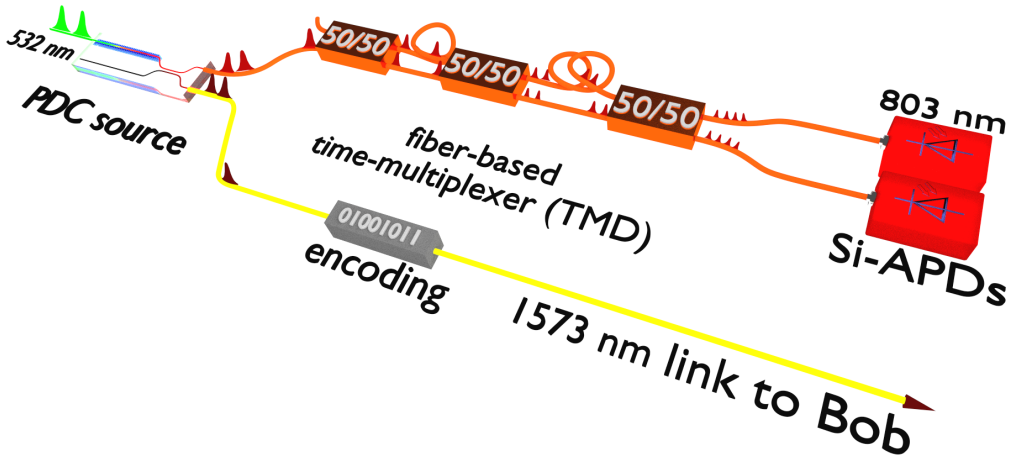

Figure 6.9.: Alice's source configuration for passive decoy-state QKD: PDC signal photons ($803\,\mathrm{nm}$) are separated on chip from idler photons ($1573\,\mathrm{nm}$), fed into a multi-mode fiber and subsequently to the eight-bin TMD. The TMD consists of three multi-mode fiber-based balanced beam splitters and two different intermittent fiber loops of fixed lengths. Two binarySi-APDs are employed for photon detection. The idler photons are transmitted to Bob after encoding via the single-mode fiber quantum channel.

individual time bins has been designed for $\tau_{\mathrm{delay}}^{\mathrm{TMD}} \approx 127\,\mathrm{ns}$ by appropriate choice of the multi-mode fiber lengths, and it is larger than the dead time of standard silicon avalanche photodiodes used for signal photon detection. The TMD architecture provides eight temporal output modes, $N = 8$, addressing two APDs and, thus, photon numbers of $n \leq 8$ without losing optical pulses due to dead-time effects. Our chosen temporal mode separation is also appropriate for repetition rates of our PDC pump laser of $f_{\mathrm{rep}} = 1\,\mathrm{MHz}$, since the four output mode timings per APD do not add up to the inverse repetition time, $\tau_{\mathrm{rep}} > \frac{N}{2} \cdot \tau_{\mathrm{delay}}^{\mathrm{TMD}}$.

Because of the bin number limitation, only pseudo-photon-number-resolution can be achieved, and we have to take convolution effects [245, 251] of higher-order photon contributions for the data analysis method [253] as well as for the theoretical predictions into account.

Figure 6.9 shows the schematic of Alice's side in one possible passive decoy state QKD implementation. The sender's system consists of the PDC source and the includes the TMD, as proposed by Mauerer and Silberhorn in 2007. For the reconstruction of the photon-number statistics from the measured click statistics we model the TMD according to Achilles et al. [245, 251]. We consider its implementation in our setup for eight output modes with the temporal delay given above. Additionally, we treat convolution effects and optical loss in the TMD independently such that the convolution matrix $\mathbf{C}^{\mathrm{TMD}}$ describes the bin occupation distribution inside the TMD, whereas the loss matrix $\mathbf{L}^{\mathrm{TMD}}$ represents the overall loss of TMD and addi-

tional optical elements as well as the efficiencies of the Si-APDs. The convolution matrix comprises of the individual elements

$$C_{\mathrm{kn}}^{\mathrm{TMD}} = p\left(k|n\right), \tag{6.15}$$

which describe the probabilities that k photons are detected, given n photons at the TMD input. Thus, we can write for the probability of detecting k photons, contributing to the TMD output photon-number distribution vector $\vec{p}_k$:

$$p_k = \sum_n p\left(k|n\right) \cdot \rho_n. \tag{6.16}$$

In other words, the convolution matrix converts the emitted Poissonian photon-number distribution vector $\vec{\rho}$ of the PDC source, which consists of individual probabilities ρ_n, into a click number distribution vector at the output of the TMD:

$$\vec{p}_k = \mathbf{C}_{\mathrm{TMD}} \cdot \vec{\rho}. \tag{6.17}$$

Inversely, we can reconstruct the photon-number distribution from the acquired click statistics for the lossless case:

$$\vec{\rho} = \mathbf{C}_{\mathrm{TMD}}^{-1} \cdot \vec{p}_k. \tag{6.18}$$

We emphasize that the individual matrix elements $C_{\mathrm{kn}}^{\mathrm{TMD}}$ ideally have values of the inverse of the overall number of possible temporal modes (here: eight). Due to imbalanced beam-splitters in our real-world implementation, the matrix elements can vary from 0.125. Additionally, the robustness of this method, i. e. using the inverted convolution matrix for photon-number probability reconstruction, strongly requires the number of photons to be lower than the number of temporal modes, $k < N$. It has been found that for an eight-mode-TMD, the mean photon number of the impinging states should be $\langle n \rangle \leq 3$. Otherwise the inverse convolution matrix is singular [245].

Taking also the overall TMD loss into account, which inevitably occurs in real-world scenarios, the different n-photon states can lose their photon-number content partially or fully. An emitted photon-number distribution, represented by $\vec{\rho}$, will be converted by the losses into a photon-number distribution represented by vector $\vec{\rho}_l$ at the TMD *input*:

$$\vec{\rho}_l = \mathbf{L}_{\mathrm{TMD}} \cdot \vec{\rho} \tag{6.19}$$

with the matrix elements

$$L_{\mathrm{ln}}^{\mathrm{TMD}}\left(\eta_{\mathrm{T}}\right) = \binom{n}{l} \eta_{\mathrm{T}}^{l} \left(1 - \eta_{\mathrm{T}}\right)^{n-l}, \; n \geq l, \tag{6.20}$$

where η_{T} is the overall efficiency (including detectors) of the TMD. Subsequently, the TMD is assumed to deconvolute the photon-number states, $\vec{\rho}_l$, into the different

temporal modes. Consequently, the complete photon-number reconstruction from a measured click statistics must be written as in the following order:

$$\vec{\rho} = \mathbf{L}_{\mathrm{TMD}}^{-1}\left(\eta_{\mathrm{T}}\right) \cdot \mathbf{C}_{\mathrm{TMD}}^{-1} \cdot \vec{p}. \tag{6.21}$$

Note that this calculation includes a re-notation of the respective variables and indices in the aforementioned Eq. 6.18 and Eq. 6.19.

6.2.3.2. Experimental considerations and setup

As a first step towards the experimental implementation we write down the probability that Bob's binary detector generates a click from an arbitrary m-photon state:

$$p(\mathrm{click}) = 1 - (1 - \eta_{\mathrm{B}})^m, \tag{6.22}$$

where Bob's transmission and detection efficiency is given by $\eta_{\mathrm{B}} = \eta_{\mathrm{C}} \cdot \eta_{\mathrm{Det,i1}}$. Here η_{C} denotes the length-dependent quantum channel efficiency, including supplementary optical components, and η_{InGaAs} labels Bob's detector efficiency. Note that Eq. 6.22 already implies different click probabilities for different m-photon states. It also describes the probability, that at least one photon out of m arrives at Bob's detector.

Second, we assume that Alice's uses a photon-number-resolving detector, which is capable of delivering n detection events from an m-photon state with $m \geq n$. The conditioned probability that Bob's detector fires due to a generated m photon state, is described by

$$p(\mathrm{click}|n) = \frac{p(\mathrm{click} \cap n)}{p(n)} \tag{6.23}$$

$$= \frac{\sum_{m=n}^{\infty} \binom{m}{n} \eta_{\mathrm{T}}^n \left(1 - \eta_{\mathrm{T}}\right)^{m-n} \left(1 - (1 - \eta_{\mathrm{B}})^m\right) \rho_m}{\sum_{m=n}^{\infty} \binom{m}{n} \eta_{\mathrm{T}}^n \left(1 - \eta_{\mathrm{T}}\right)^{m-n} \rho_m}, \tag{6.24}$$

where $p(\mathrm{click} \cap n)$ is the cumulative joint probability of a click event in Bob's detector from a generated m-photon state, while n out of m photons impinge on Alice's photon-number-resolving detector. The coefficients ρ_{m} describe the occupation probabilities of the Poissonian m-photon state in our spectrally multi-mode PDC device (see Eq. 7.19 and also [205, 254]). The term η_{T} is experimentally accessible according to Eq.6.28, and it describes, again, the overall efficiency of the photon-number-resolving detector and includes losses as well as the detection efficiency.

In the limit of a low transmission and detection efficiency at Bob's side, $\eta_{\mathrm{B}} \ll 1$ we can calculate the conditioned probabilities $p(\mathrm{click}|n)$ for different n-photon states from Eq. (6.23), and we find that the approximation

$$r\left(n\right) = \frac{p\left(\mathrm{click}|n\right)}{p\left(\mathrm{click}|1\right)} \approx \frac{n \cdot \eta_{\mathrm{B}}}{\eta_{\mathrm{B}}} = n \tag{6.25}$$

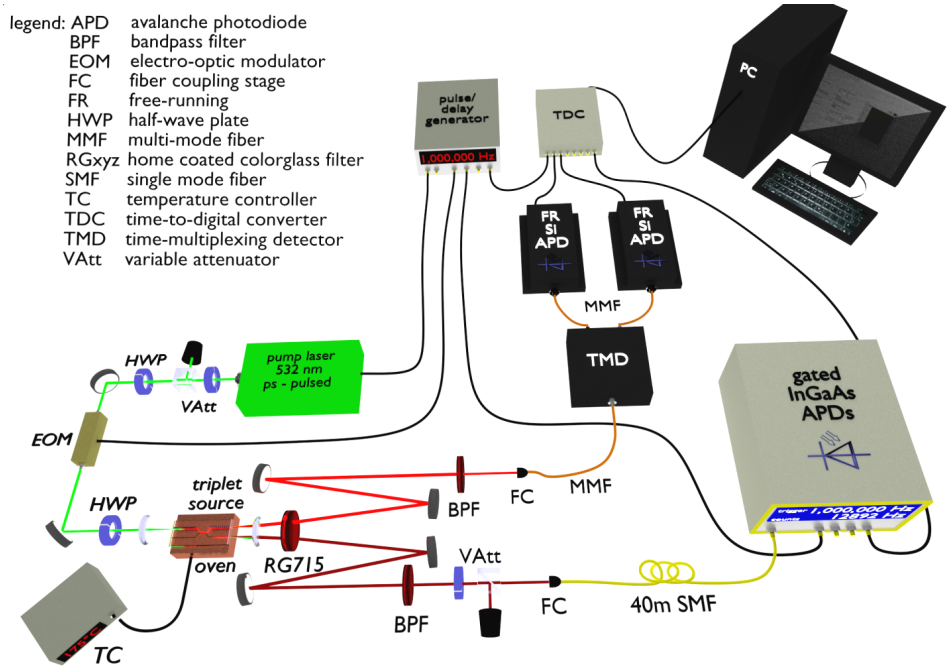

Figure 6.10.: Experimental implementation of photon-number-resolving PDC analysis. See text for a detailed description.

is valid. This basically means that Bob's detector clicks about m times more often for an n-photon state than for a one-photon state. At higher efficiencies η_{B} the values of $r(n)$ will decrease. Thus, at elevated pump power levels the impact of higher-order photon contributions as well as non-ideal photon-number-resolving capabilities of the TMD must be taken into account.

For the analysis of the experimental data we derive the conditioned click probabilities $p(\mathrm{click}|n)$ as the fraction of measured click events in Bob's detector, given that an n-photon state is detected by Alice's non-ideal TMD, and the total number of events:

$$p(\mathrm{click}|n) = \frac{N(\mathrm{click}|n)}{N(\mathrm{click}|n) + N(\mathrm{no\,click}|n)}. \tag{6.26}$$

Note, that the probabilities $p(\mathrm{click}|n)$ still have to be corrected for convolution effects in order to reconstruct the photon-number statistics.

We carry out pump-power-dependent measurements with the setup shown in Fig. 6.10, since the mean photon number of PDC states is related to the power of the pump pulse (see Sec. 6.1 above). Behind the waveguide chip we clean up PDC photons from background and residual pump light using a customized absorber and narrow-band dielectric filters. In the signal arm we address the TMD and, subsequently, the two free-running silicon APDs, both with $\eta_{\mathrm{Si}} = 0.55$ detection

efficiency and dark count rates of ~ 250 per second. The idler arm consists of a variable attenuator, which mimics an arbitrary channel loss η_{C}. Behind this device we address a gated InGaAs-APD, which offers 2.5 ns detection windows, a detection efficiency of $\eta_{\mathrm{Det,i1}} = 0.24$ and 1 μs dead time. It exhibits a dark count probability of $p_{\mathrm{dc}} = 1.75 \times 10^{-4}$ per gate.

For the data acquisition, all APDs are connected to a standard time-to-digital converter (TDC) offering 82 ps resolution. A home-programmed software analyzes the impinging signals for coincidences in order to extract the PDC click statistics for a specific pump power, i.e., output mean photon number. The TMD and the InGaAs-APD are synchronized, triggered, and delay compensated in terms of optical path differences by a delay generator running at 1 MHz repetition rate. Furthermore, we implemented an electro-optic amplitude modulator prior to the pump incoupling, which is driven by the delay generator and acts as a pulse picker for our 10 MHz-pulsed pump laser. This technique, in conjunction with the synchronization of the delay generator's and the pump laser's timebase, allows for waveguide-coupled pump pulses also at a repetition rate of 1 MHz.

We analyze the photon-number-resolved click statistics of our PDC process at pump powers that range over two orders of magnitude. A high pump power forces the generation of higher-order photon states. The maximum accessible cw-equivalent pump power of 2 μW corresponds in this experiment to a mean photon number of $\langle n \rangle = 0.84$, and it is determined by the saturation limit of our data acquisition system. At each pump-power level we can set almost arbitrary quantum channel transmission $0 < \eta_{\mathrm{C}} \leq 1$ in the idler arm, mimicking different transmission distances of a real-world QKD system.

The Klyshko efficiencies of the signal and idler arm, η_{T} and η_{B}, are given by the ratio of coincidence counts N_{coinc} and the total number of single counts in the respective opposite arm, N_{B} and $\sum_{n\geq 1} N_{\mathrm{T}}(n)$. In order to correct the Klyshko efficiencies for uncorrelated events we estimate the number of accidentals beforehand as

$$N_{\mathrm{acc}} = \frac{N_{\mathrm{B}} \cdot \sum_{n\geq 1} N_{\mathrm{T}}(n)}{N_{\mathrm{Trig}}}, \tag{6.27}$$

where $\sum_{n\geq 1} N_{\mathrm{T}}(n)$ is the accumulated number of detection events in the TMD. The term N_{B} denotes the number of click events in the InGaAs-APD and N_{Trig} is the number of trigger events within our measurement time. This correction provides us with a lower bound for the actual Klyshko efficiency, because higher-order photon contributions lead to an overestimation of the real values. We also subtract coincidences $N_{\mathrm{noise,B}}$ and $N_{\mathrm{noise,T}}$, caused by noise counts of the respective detector, and we eventually find

$$\eta_{\mathrm{T}} = \frac{N_{\mathrm{coinc}} - N_{\mathrm{acc}} - N_{\mathrm{noise,T}}}{N_{\mathrm{B}}} \tag{6.28}$$

to be the Klyshko efficiency in the signal/TMD arm, and

$$\eta_{\mathrm{B}} = \frac{N_{\mathrm{coinc}} - N_{\mathrm{acc}} - N_{\mathrm{noise,B}}}{\sum_{n\geq 1} N_{\mathrm{T}}(n)} \tag{6.29}$$

Table 6.1.: Power-dependent Klyshko efficiencies at maximum channel transmission. The efficiencies $\eta_{\mathrm{T}}^{\mathrm{A}}$ describe the TMD Klyshko efficiencies not corrected for uncorrelated accidentals.

$\mathbf{P}_{\mathrm{p}}$ [nW]	20	50	100	200	500	1000	2000
$\eta_{\mathrm{B}}[\%]$	10.75	10.72	10.65	10.02	9.97	9.41	8.55
$\eta_{\mathrm{T}}^{\mathrm{A}}[\%]$	14.17	16.44	17.07	17.29	17.06	16.50	15.39
$\eta_{\mathrm{T}}[\%]$	17.76	17.76	17.72	17.66	17.21	16.58	15.47

Table 6.2.: Click-statistics at 2 μW pump power and with channel transmission $\eta_{\mathrm{C}} = 1$.

	0-photon	1-photon	2-photon	3-photon	4-photon
$N(\text{'no click'}|n)$	49244089	6157356	334960	10383	197
$N(\text{click}|n)$	3049176	1092105	102653	4608	112
$N_{\mathrm{T}}(n)$	52293265	7249461	437613	14991	309

is the Klyshko efficiency of the idler arm.

6.2.3.3. Experimental results

The power-dependent Klyshko efficiencies for different pump powers are shown in Tab. 6.1 and indicate that our calculated values are only reliable at low pump powers, since we tend to over-estimate accidentals - according to Eq. (6.27) - for increasing pump powers and, thus, will artificially decrease the Klysko efficiencies. In order to predict the behavior of different n-photon states in the following we base our theoretical calculations on Klyshko efficiencies obtained at the lowest available pump power. Note that this will underestimate the influence of accidentals.

In order to ensure distinct detection probabilities for different n-photon states after transmission through the quantum channel we analyze the click statistics and reconstruct the probabilities $p\,(\text{click}|n)$ therefrom using Eq. (6.26) and the inverse convolution matrix [209, 245, 253] of our TMD. A typical measurement result at the highest accessible pump power of 2 μW and with $\eta_{\mathrm{C}} = 1$ is shown in Tab. 6.2. We can clearly identify click events up to photon numbers $n = 4$ within 60 s of measurement time, which strongly indicates heralded four-photon states.

In Fig. 6.11 we plot $p\,(\text{click}|n)$ versus the channel transmission η_{C}, the latter of which represents an arbitrarily long transmission device between the two QKD parties. The distinct n-photon components clearly follow different slopes and show also higher detection probabilities for higher photon states. This verifies not only the high brightness of our source, but it also agrees excellently with the expected behavior.

Our measurements closely match the theoretical curves calculated with Eq. (6.23), where we considered Poisson distributions ρ_{m} as well as convolution effects. We

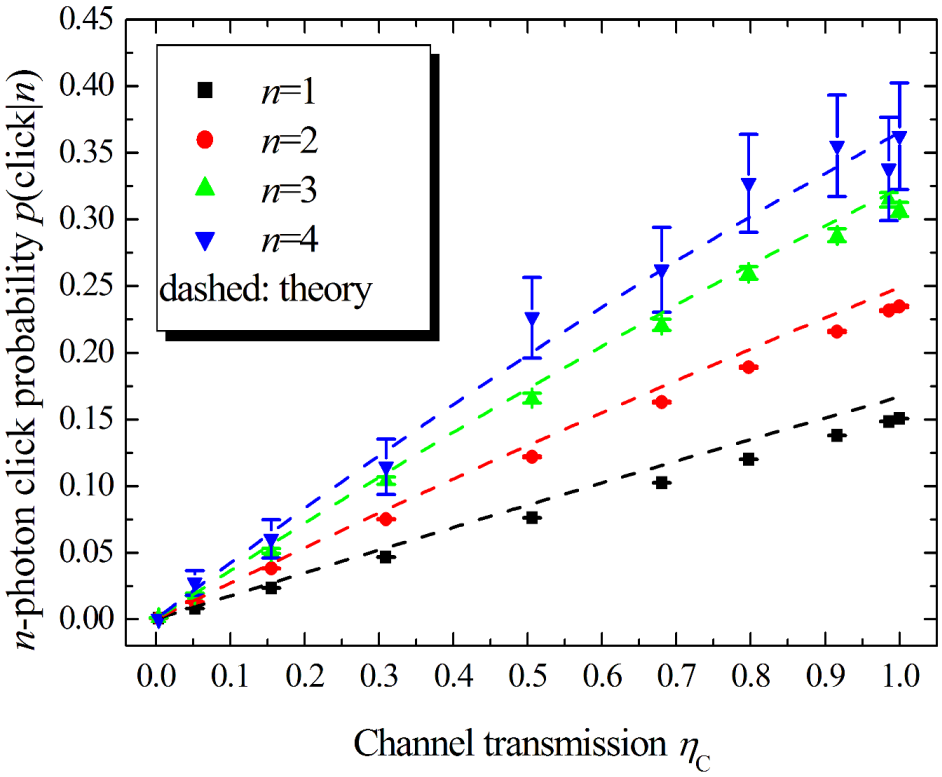

Figure 6.11.: Dependencies of the n-photon click probabilities on the channel transmission at 2 μW cw-equivalent pump power; dashed: theory curves.

have also implied Klyshko efficiencies of the low power regime, $\eta_{\mathrm{T}} = 0.1776$ and $\eta_{\mathrm{B}} = 0.1075$, respectively. Note, that the differences to the detection efficiencies η_{Si} and η_{InGaAs} are caused by losses introduced by the optical components.

With our analysis scheme it is easy for Alice to anticipate, how the click statistics at Bob's side should behave at distinct pump powers. Thus, our PDC source fulfills the necessary requirements for passive decoy-state QKD in terms of predictable photon statistics and accessibility to higher-order n-photon states in general. Our results imply that an eavesdropper, Eve, will be recognized, since her activities on photon-number-splitting activities will change the expected detection behavior at Bob's side.

The seemingly growing mismatch between experimental data and theory curves for small n at large η_{C} can be explained by uncorrelated coincidences, which have an impact on $p\,(\mathrm{click}|n)$. As stated above, by applying only Klyshko efficiencies from the low-power measurement to the theory we underestimate accidentals for higher pump powers.

The applicability of our source over a large range of different brightnesses, as

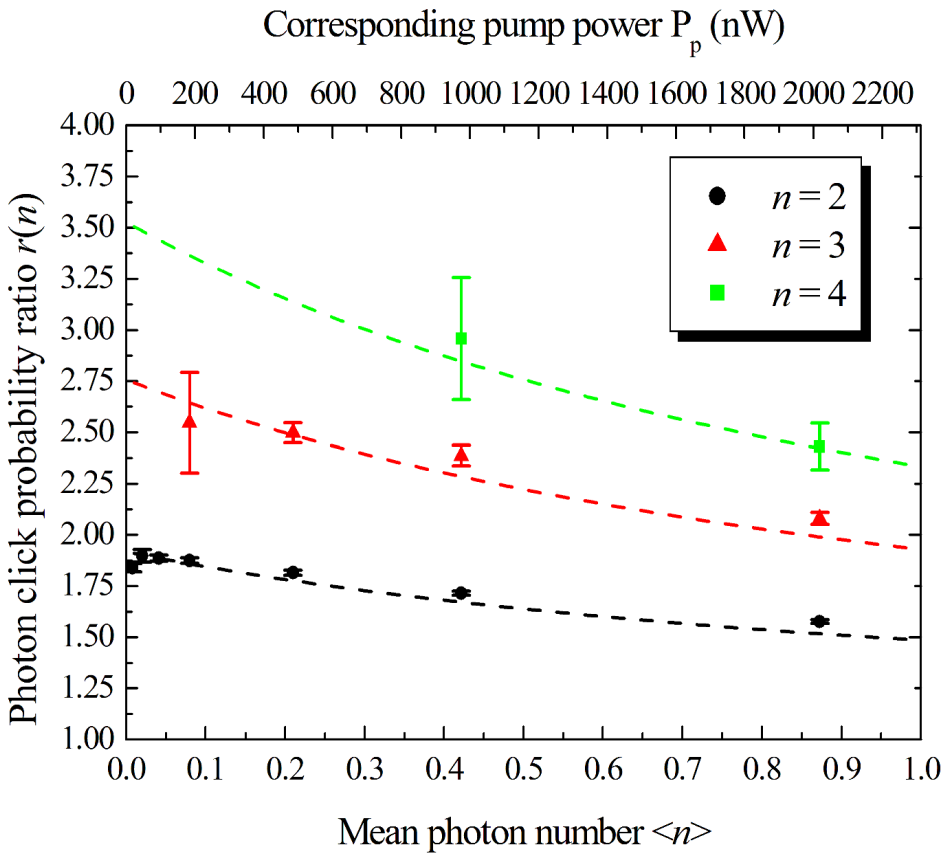

Figure 6.12.: The click-probability ratios $r\,(n)$ follow Poissonian distributions (dashed: theoretical predictions for $\eta_{\mathrm{T}} = 0.1776$ and $\eta_{\mathrm{B}} = 0.1075$).

needed for optimization of the passive decoy scheme, is underlined by the behavior of the PDC states for different mean photon numbers. In particular, we calculated $r\,(n)$ according to Eq. (6.25) from the individual de-convoluted click probabilities at variable channel transmissions. The average ratios are plotted against the mean photon number $\langle n \rangle$ in Fig. 6.12. We did not register significant three- and four-photon components at small mean photon numbers within acceptable measurement durations. However, our measurement data exhibit decreasing ratios $r\,(n)$ at higher pump powers according to Poissonian statistics. This, on the one hand, underlines the photon-number-resolving capabilities of our TMD, while on the other hand the very good agreement to the theory proves that the n-photon PDC states in our spectrally broad source ($FWHM\,(803\,\mathrm{nm}) \sim 0.7\,\mathrm{nm}$) show almost genuine Poisson distributions. Remaining deviations from theory can be explained by the finite number of spectral modes in our source, and again by the impact of uncorrelated accidentals at higher mean photon numbers. By contrast, exact Poisson distribution could be expected only for infinite numbers of spectral modes [126, 255].

The distinct detection probability ratios for different n-photon states are key to

accessing higher-order photons as decoy states reliably. Eve's PNS attack will change the above characteristics in a way that the ratios $r(n)$ decrease artificially due to the increased amount of one-photon contributions during classical PNS attacks. Therefore, Fig. 6.12 proves our source suitable for a broad range of pump powers.

Further activities on the field of passive decoy state QKD could include the implementation of our device in a complete QKD system, which includes also the encoding at Alice's side as well as optical fibers as the lossy quantum channel to Bob's side instead of the variable attenuator implemented in our work. Likewise, the detailed security analysis in terms of yield, quantum bit error rates and secret key rates should be pursued for that specific system in the future.

Conclusion

We have demonstrated that our integrated device can be employed as a probabilistic single photon source for quantum optical tasks. It exhibits a very high brightness in the pulsed excitation in conjunction with high quality of the generated photon pairs in terms of low optical noise figures. The input powers ranged only at $10\,\mathrm{nW} \leq \mathbf{P}_\mathrm{p} \leq 85\,\mu\mathrm{W}$. We used only part of the functionalities available on our chip, namely one PDC stage in combination with the quasi-deterministic demultiplexer, and the second PDC stage did not influence the quality of our results.

More specifically, we performed the generation of heralded single photons and achieved high heralding efficiencies of around 60% in combination with extraordinarily high coincidences-to-accidentals ratios. We also determined one the lowest second-order auto-correlation function reported to date, i. e. $g^{(2)}(0) = 0.0038$. These results have been reported in Ref. [256].

By using pseudo-photon-number-resolving detection techniques we were able to show that our source meet the requirements for averting photon-number-splitting attacks in quantum key distribution. We showed that the high source brightness, i. e. the emission of higher-order photon-number contributions, can be turned into a real benefit, if the passive decoy state method is exploited in future QKD applications. Our results on this topic have been reported in Ref. [257].

CHAPTER 7

Cascaded nonlinear wavelength conversion processes

Contents

In this Chapter we exploit the full functionality of our integrated device for exploring its applicability in cascaded frequency conversion processes. We show that up-conversion of classical telecom light to the visible regime is feasible and provides us with a tunable source of green laser light. It is also demonstrated that our device, in the current state of development, does not meet the requirements for (quasi-)single-photon up-conversion. By contrast, our integrated chip allows for the generation of photon triplets from a single green photon via cascaded parametric down-conversion. We model and analyze the cascaded parametric down-conversion (PDC) process in terms of expected triplet generation rates, signal-to-noise ratios and coincidences-to-accidentals ratios. Additionally, we compare and discuss our predictions with our experimental results, and we verify the on-chip generation of photon triplets from a pulsed cascaded parametric down-conversion.

7.1. Cascaded frequency up-conversion from telecom to visible wavelengths

In classical integrated optics based on $\chi^{(2)}$-nonlinear devices, the wavelength conversion using second-harmonic generation (e. g. [172, 181]), difference-frequency generation (e. g. [258]) and sum-frequency generation (e. g. [259]) have been studied [15] and brought to a manifold of applications in the past 40 years. The reasons for these huge theoretical and technological efforts can be found, for the majority of work, in the necessity to address wavelength regions which are otherwise not accessible. For example, green lasers emitting at 532 nm have been made possible by frequency-doubling (i. e. second-harmonic generation) of neodymium-doped yttrium aluminum garnet (Nd:YAG) laser emission.

In recent years the field of quantum optics explores integrated nonlinear devices in order to translate optical frequencies from one band to others. The reasons for this development can be found in the key ingredient for quantum optics: coherence. For complex systems like quantum optical networks and any other application in quantum information processing (QIP), coherent interactions and processes are absolutely required. It appears to be reasonable that future quantum networks consist of a multitude of subsystems, which have to be mutually compatible in one or the other degree of freedom. Apart from temporal issues like synchronization, the frequency (or wavelength) of the involved quantum states has to match the individual subsystem's characteristics. Otherwise, converter stages, providing coherent frequency up- or down-conversion, are essential building blocks for the interfacing of quantum network nodes. In the following paragraphs we explain briefly, for which related reasons frequency up-conversion is desired: First, the necessity to prevent optical loss, e. g. during transfer of quantum states (flying qubits) in quantum networks, has to be minimized. Since the telecommunication C-band offers the lowest optical loss in fused silica fibers, the aim of quantum key distribution is to exploit this technology basis. Thus, the generation and also the conversion of photon states to the wavelength region around 1550 nm is highly attractive.

Second, the detection of those photons with off-the-shelf components is usually not very efficient. Thus, the conversion of flying qubits to wavelength regions, where detectors are much more efficient, is attractive and can be performed with almost unit conversion efficiency [85, 86] as well as under conservation of the quantum state properties [87–90].

Third, the storage of quantum states in quantum memories usually involves the UV to NIR wavelength regions [260–263] and, thus, requires narrow-band frequency up-conversion to the respective memory absorption bands [264–266].

The techniques of cascaded wavelength/frequency conversion have been employed in classical nonlinear optics, e. g., for optical burst switching [267, 268] and various other telecom applications [269–272], which aim for bridging large wavelength gaps [273]. Relatively few literature about the application of cascaded frequency up-conversion for quantum optical applications exists in the scientific community

[274, 275]. It has been shown experimentally that the single-photon conversion from 1550 nm via intermediate signals at 832 nm to outputs at 570 nm is possible with efficiencies of up 87% [275], which is very close to unit conversion efficiency. However, the design and phase-matching properties of that particular integrated device, employing the very same pump for both up-conversion processes, limits its applicability for broad-band single photon conversion.

The increasing number of functionalities on single devices lies at the heart of Integrated Quantum Optics. As the logical consequence of our findings in the previous chapters, we make use of all active and passive elements in this section in order to perform cascaded frequency up-conversion of classical light and quasi-single photons in terms of weak coherent states.

7.1.1. Cascaded SHG/SFG of classical light at low pump powers

In Fig. 7.1 we show the schematic conversion principle (top) as well as the on-chip functionalities of our device within the intended cascaded SHG/SFG processes (bottom). For the first time in this thesis we will make use of all the integrated functionalities simultaneously, be it the end-face coatings for optimal in- and out-coupling of the involved light, the passive directional coupler for wavelength-selective add-/drop-multiplexing or the two periodically poled areas for the cascaded up-conversion processes.

The purpose of this initial experiment is to learn more about the tuning behavior of the two phase-matched processes by changing the temperature. We aim for only partial conversion of the pump 1 light into green photons and employ low pump 1 input powers for the SHG process. By manipulating the device temperature we detune the phase-matching conditions of the SHG and the cascaded SFG process. The main goal is to understand, which combination of periodically poled structures and directional couplers we will have to use for the optimal inverse process, i. e. cascaded parametric down-conversion, as will be described in detail in Sec. 7.2 below in this chapter.

The conversion of infrared light to the visible wavelength regime in our device by cascading a second-harmonic generation process and a subsequent sum-frequency process has to fulfill the law of energy conservation. We write down in the frequency domain for the SHG process

$$\omega_{\mathrm{SHG}} = 2 \cdot \omega_{\mathrm{p1}}, \tag{7.1}$$

and for the cascaded SFG process

$$\begin{aligned} \omega_{\mathrm{SFG}} &= \omega_{\mathrm{SHG}} + \omega_{\mathrm{p2}} \\ &= 2 \cdot \omega_{\mathrm{p1}} + \omega_{\mathrm{p2}}. \end{aligned} \tag{7.2}$$

This means that one photon at SFG frequencies ω_{SFG} can be generated only if three pump photons (at two different frequencies ω_{p1} and ω_{p2}) are present. Intermediate second harmonic light occurs at frequencies ω_{SHG}. With the relation $\lambda_j = \frac{c}{2\pi \cdot \omega_j}$

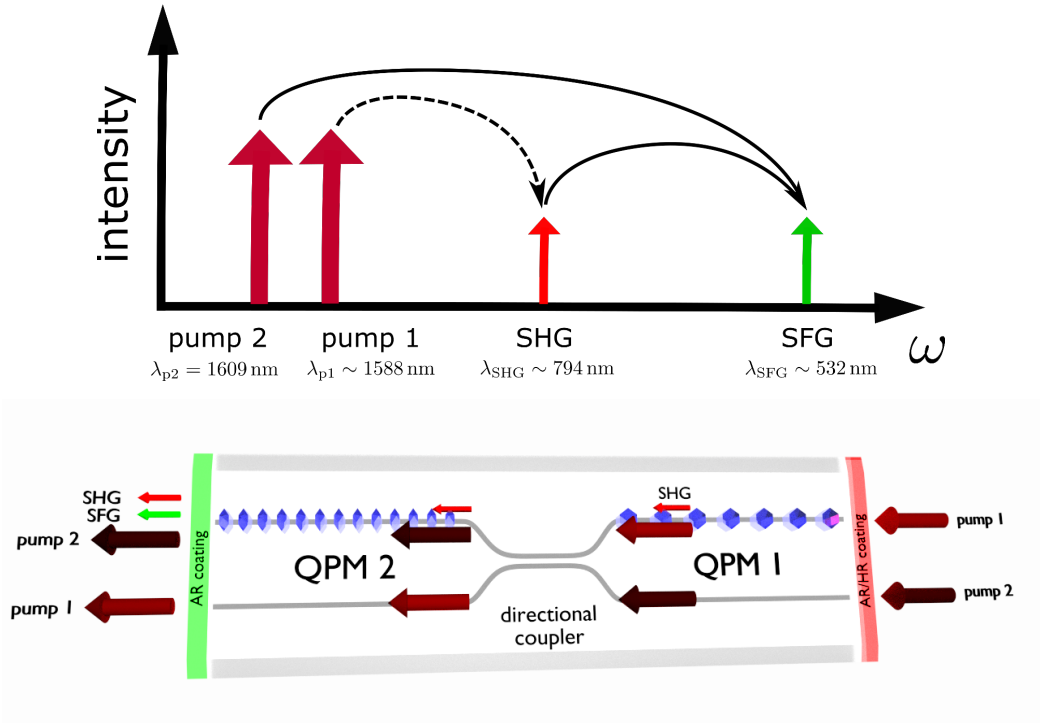

Figure 7.1.: The schematic of the cascaded SHG/SFG process is visualized (top): The first pump generates light at the second-harmonic wavelength $\lambda_{p1}/2 = \lambda_{SHG} \sim 794\,\mathrm{nm}$, which can be converted to green light at $\lambda_{SFG} \sim 532\,\mathrm{nm}$ by adding a secondary pump at $\lambda_{p2} = 1609\,\mathrm{nm}$. While pump 1 is injected to the upper waveguide, the secondary pump is fed into the adjacent channel. After SHG has been generated in the QPM 1 grating structure, both pump beams are transfered to the respective other channel in the integrated directional coupler. The SHG remains in the waveguide, where it has been generated. It sums with the pump 2 in the QPM 2 grating structure, and green SFG light is generated.

and $j = \mathrm{p1}, \mathrm{p2}, \mathrm{SHG}, \mathrm{SFG}$ we can re-write equations 7.1 and 7.2 in the wavelength description. We get for the SHG process

$$\lambda_{SHG} = \frac{\lambda_{p1}}{2}, \tag{7.3}$$

and for the SFG process

$$\lambda_{SFG} = \frac{\lambda_{SHG} \cdot \lambda_{p2}}{\lambda_{SHG} + \lambda_{p2}} = \frac{\lambda_{p1} \cdot \lambda_{p2}}{2 \cdot \lambda_{p2} + \lambda_{p1}}. \tag{7.4}$$

The conservation of momentum has to be obeyed in the two consecutively arranged and periodically poled waveguide structures. The wave numbers (or momenta) of

the propagating light along the waveguides are defined as scalars of the form

$$k_j = \frac{2\pi}{\lambda_j} \cdot n_{\mathrm{eff,j}}, \tag{7.5}$$

with λ_j and $n_{\mathrm{eff,j}}$ being the wavelength and the effective refractive index of the guided modes, respectively. We get for quasi-phase-matched SHG processes in our injection waveguide

$$0 \equiv k_{\mathrm{SHG}} - 2 \cdot k_{\mathrm{p1}} - K_{\mathrm{QPM,1}}, \tag{7.6}$$

and for cascaded SFG light

$$\begin{aligned} 0 &\equiv k_{\mathrm{SFG}} - k_{\mathrm{p2}} - k_{\mathrm{SHG}} - K_{\mathrm{QPM,2}} \\ &= k_{\mathrm{SFG}} - k_{\mathrm{p2}} - 2 \cdot k_{\mathrm{p1}} - K_{\mathrm{QPM,1}} - K_{\mathrm{QPM,2}}, \end{aligned} \tag{7.7}$$

with $K_{\mathrm{QPM,i}} = \frac{2\pi}{\Lambda_{\mathrm{QPM,i}}}$ being the wave numbers of the two periodically inverted domain structures. Individual poling periods are given by $\Lambda_{\mathrm{QPM,i}}$, $i = 1, 2$.

Figure 7.2 shows the experimental setup for cascaded SHG/SFG (cSHG/SFG) of L-band telecom light to the visible. Note that, in comparison to the experiments carried out so far, we reversed the direction of feeding the pump light into our device, i. e. from the right-hand side. A tunable, cw ECL with available pump powers of $\mathbf{P}_{\mathrm{p1}} \leq 8\,\mathrm{mW}$ at $\lambda_{\mathrm{p1}} \sim 1588\,\mathrm{nm}$ serves as the primary pump for the SHG process, the poling period for which is available on-chip at $\Lambda_{\mathrm{QPM,1}} = 18.09\,\mu\mathrm{m}$. Once the second harmonic light is generated in its fundamental mode, it remains in the same waveguide at the integrated directional coupler. The secondary pump at $\lambda_{\mathrm{p2}} \sim 1609\,\mathrm{nm}$, available from a second ECL, is added via the waveguide adjacent to the pump 1 light. Thus, the pump 2 cross-couples to the waveguide, where the SHG resides, and sum-frequency can be generated in the second periodically poled area with $\Lambda_{\mathrm{QPM,2}} = 6.83\,\mu\mathrm{m}$. Note that residual pump 1 light also couples very well to the other waveguide within the directional coupler structure, which is beneficial for the suppression of competing parasitic SFG processes in the secondary conversion stage (see Fig. 7.1 (bottom)).

We collect the generated SHG and cSHG/SFG power with standard power meters after spectral separation and filtering. A computer program controls the emission wavelengths and also the powers of the pump lasers, and registers the measured cSHG/SFG power. In our measurements at low pump powers around $\mathbf{P}_{\mathrm{p1}} \approx \mathbf{P}_{\mathrm{p2}} \sim 2\,\mathrm{mW}$ we vary the temperature in the range $174.1°\mathrm{C} \leq \theta \leq 175.6°\mathrm{C}$ by steps of $\Delta\theta = 0.5°\mathrm{C}$, and we study the shift of the phase-matching conditions. Figure 7.3 shows the normalized power of the generated green light. We see reasonable spectral shifts in the cascaded SHG/SFG light from the upper left to the lower right graph, which indicates once more that the two individual phase-matching conditions depend both on the device temperature. In this configuration we have built a source of green laser light, the emission wavelength of which is tunable by thermal manipulation in

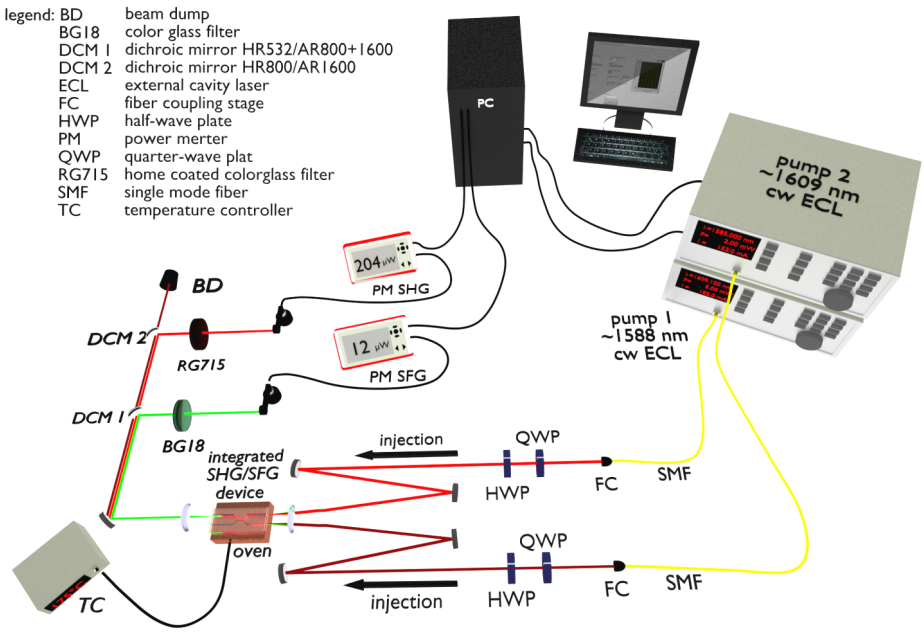

Figure 7.2.: We use two identical, tunable and cw external cavity lasers for pumping our cascaded SHG/SFG process. The temperature of the integrated chip can be tuned via standard temperature controller. While the pump 1 at $\lambda_{\mathrm{p1}} \sim 1588\,\mathrm{nm}$ is injected to the second-harmonic generation stage of our integrated device (upper beam path), the pump 2 at $\lambda_{\mathrm{p2}} = 1609\,\mathrm{nm}$ is fed into the adjacent waveguide (lower beam path). After the generated SHG at $\lambda_{\mathrm{SHG}} \sim 794\,\mathrm{nm}$ and the pump 2 have mixed and light at the sum-frequency at $\lambda_{\mathrm{SFG}} \sim 532\,\mathrm{nm}$ has been generated, we measure the powers of the SFG and the remaining SHG light with standard power meters. The pump lasers' emission wavelengths and output powers are controlled by computer software, which also attributes the measured SHG and SFG powers with the respective spectral information.

conjunction with the adaption of the two pump wavelengths according to the quasi-phase-matching conditions. The parabolic curve

$$\lambda_{\mathrm{SFG},2}(\theta) = a \cdot \theta^2 + b \cdot \theta + \lambda_0 \tag{7.8}$$

describes the peak wavelength of the cSHG/SFG very well with the parameters $a = 0.00885\,\mathrm{nm} \cdot \mathrm{K}^{-2}$ and $b = -3.03715\,\mathrm{nm} \cdot \mathrm{K}^{-1}$ both defining the positive slope in the considered temperature regime. The parameter $\lambda_0 = 792.222\,\mathrm{nm}$ describes the y-axis offset wavelength. The fit is valid for θ in the Celsius scale. We infer the phase-matching bandwidth of the visible emission, $\lambda_{\mathrm{SFG},2}^{\mathrm{FWHM}} = (0.045 \pm 0.005)\,\mathrm{nm}$, by analyzing the normalized power along the direction of the energy-conservation condition. The peak power of the green SFG light has been measured to be around

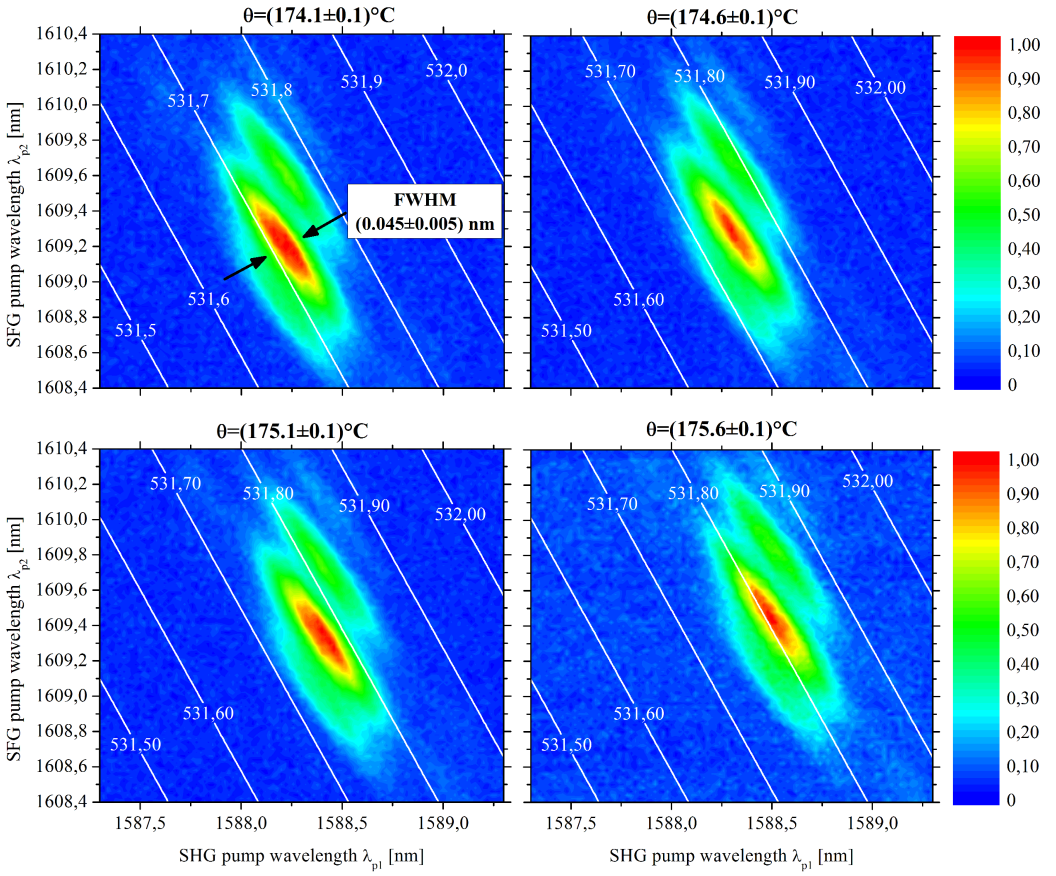

Figure 7.3.: The phase-matching behavior for four different device temperatures is shown color-coded and dependent on the two pump wavelengths. From the graphs we deduce a FWHM phase-matching bandwidth of $\lambda_{\mathrm{SFG}} = (0.045 \pm 0.005)\,\mathrm{nm}$ for the generated green light, while the diagonal white lines represent the conservation of energy. We notice a second (side-) peak at identical pump1/SHG wavelengths at slightly different pump 2 wavelengths.

$P_{\mathrm{SFG},2}^{\mathrm{peak}} = (7.37 \pm 0.52) \cdot 10^{-5}\,\mathrm{mW}$, while the main focus is not on the maximum achievable up-conversion of the intermediate SHG beam.

In the graphs in Fig. 7.3 we also identify neighboring peaks to our quasi-phase-matched power maximum for larger pump 2 wavelengths. This phenomenon cannot be attributed to a competing SFG process, where a higher-order spatial mode of the generated SFG field is involved, because these processes are not phase-matched according to our model. Instead, we suspect that the region of the $\Lambda_{\mathrm{QPM},1} = 6.83\,\mu\mathrm{m}$ domain grating suffers from waveguide inhomogeneities, and the related effective refractive index vary throughout the SFG grating region. Our suspicion is supported by the lack of side-lobes along the pump 1 axis, i. e. the SHG process, but techno-

logical investigation and optimization steps can minimize inhomogeneities in future work.

7.1.2. Cascaded SFG/SFG of classical light

In this section we aim for the cascaded frequency up-conversion from classical telecom light to visible light at around $\lambda_{\mathrm{SFG},2} \sim 532\,\mathrm{nm}$. By contrast to the previous section, where the first conversion process has been SHG, we now perform two sum-frequency generation processes in series. In the following, we demonstrate that cascaded SFG/SFG (cSFG/SFG) can offer the flexibility for broad-band telecom conversion from the L-band. The type-0 quasi-phase-matched process in our case requires poling periods around $\Lambda_{\mathrm{QPM},1} = \Lambda_{\mathrm{G}2} = 18.09\,\mu\mathrm{m}$ and can be driven such that non-degenerate PDC is feasible (compare with Sec. 5.4.2, Fig. 5.14). For this reason, the sum-frequency generation can benefit from the broad spectral range around the degeneracy wavelength, where the quasi-phase-matching condition is fulfilled and, thus, frequency up-conversion is feasible.

In this a proof-of-principle experiment, we drive our first SFG stage with a strong pump in the telecom C-band at $\lambda_{\mathrm{p}1} = 1563\,\mathrm{nm}$, which sums with injected idler light at $\lambda_{\mathrm{i}} = 1615\,\mathrm{nm}$. The generated SFG 1 light at $\lambda_{\mathrm{SFG},1} = 794.29\,\mathrm{nm}$ is spectrally very close to the generated SHG light discussed in the section above. Thus, the secondary sum-frequency process, occurring behind the integrated directional coupler in the cascaded QPM grating, also requires a similar secondary pump wavelength at $\lambda_{\mathrm{p}2} = 1609\,\mathrm{nm}$ as discussed before in order to generate SFG light at $\lambda_{\mathrm{SFG},2} = 531.78\,\mathrm{nm}$.

The schematic of this cascaded up-conversion process as well as the on-chip propagation scheme are depicted in Fig. 7.4. We emphasize that both wavelengths in the first SFG stage could be interchanged or spectrally shifted in principle, according to the energy- and momentum-conservation conditions. We assume, furthermore, that the pump 1 power is much higher that the power of the idler, $\mathbf{P}_{\mathrm{p}1} \gg \mathbf{P}_{\mathrm{i}}$.

Experimentally, we rely on the setup depicted in Fig. 7.5. We employ three tunable ECL lasers in cw operation, which provide us with the necessary wavelength combination for both SFG processes to be quasi-phase-matched. The idler light at $\mathbf{P}_{\mathrm{i}} = 2\,\mathrm{mW}$ of set power is injected to the waveguide structure, after having passed a dichroic mirror, which is transmitting idler wavelengths, but reflecting pump 1 light. The dichroic mirror is a limiting factor in terms of the spectral tunability of the cascaded SFG/SFG process, since it does not provide the required infinite slope at the degeneracy wavelength of the first SFG process, $\lambda_{\mathrm{p}1}^{\mathrm{deg}} = 1588.4\,\mathrm{nm}$. However, the primary pump light is provided by the second ECL laser. We feed the pump 1 into an erbium-doped fiber-amplifier (EDFA), the driving current of which is controllable by a computer program. After free-space coupling, the pump 1 is reflected by the dichroic mirror and, thus, combined and launched into the waveguide together with the idler light.

The third ECL laser is set to the pump 2 emission wavelength and connected to

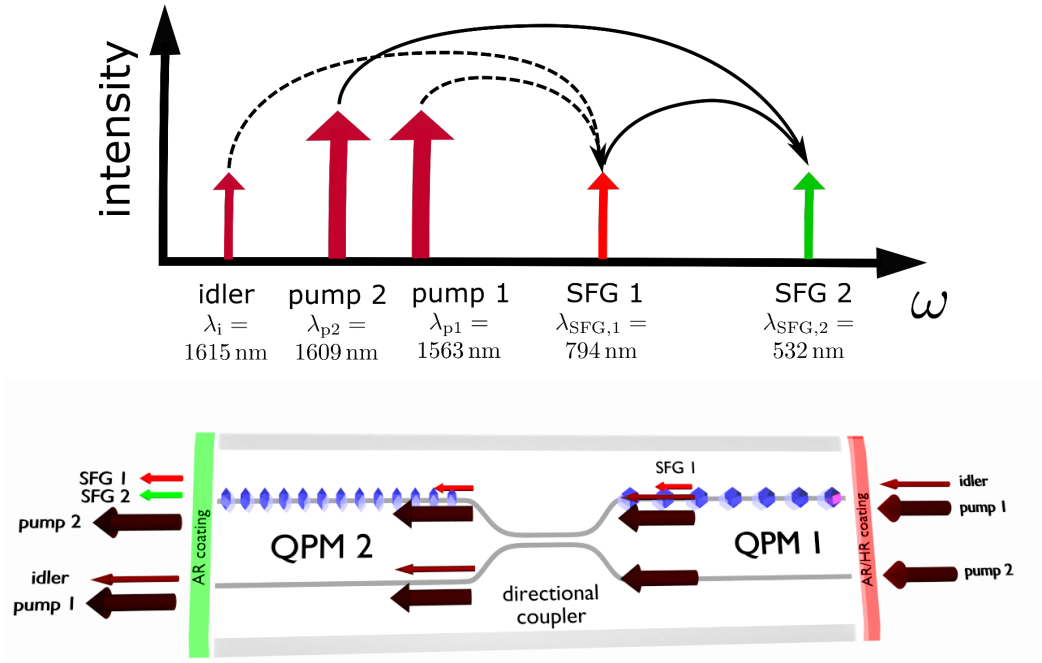

Figure 7.4.: The frequency-mixing schematic of the cascaded SFG/SFG process is shown (top): The strong first pump at $\lambda_{p1} = 1563\,\text{nm}$ up-converts a weaker idler beam at $\lambda_i = 1615\,\text{nm}$, and SFG 1 light is generated at $\lambda_{SFG,1} = 794\,\text{nm}$. Since this wavelength is identical to the SHG mentioned in Sec. 7.1.1, a strong pump also at $\lambda_{p2} = 1609\,\text{nm}$ is necessary for the secondary up-conversion process to $\lambda_{SFG,2} = 532\,\text{nm}$. Note, again, that both pump beams transfer to the respective adjacent waveguide at the integrated directional coupler (bottom).

a second computer-controlled EDFA. The injection of the amplified pump 2 light to our integrated chip is performed to the waveguide adjacent to the pump1/idler waveguide.

For the experiment we stabilize the temperature of our device to $\theta = (175.0 \pm 0.1)°\text{C}$. By setting the EDFA driving currents, we vary the calibrated waveguide input powers for pump 1 in the range $4\,\text{mW} \leq \mathbf{P}_{p1} \leq 496\,\text{mW}$ and for pump 2 in the range $0\,\text{mW} \leq \mathbf{P}_i \leq 608\,\text{mW}$. We measure the two SFG output powers with standard power meters after spectral splitting. The computer program relates the output SFG powers with the actual input current in order to calculate the conversion efficiency.

Figure 7.6 shows the conversion efficiency for the first SFG process dependent on the two pump powers $\mathbf{P}_{p1}$ and $\mathbf{P}_{p2}$, normalized to the idler input power. Note that we scale the conversion efficiency by the wavelength ratio between SFG 1 and

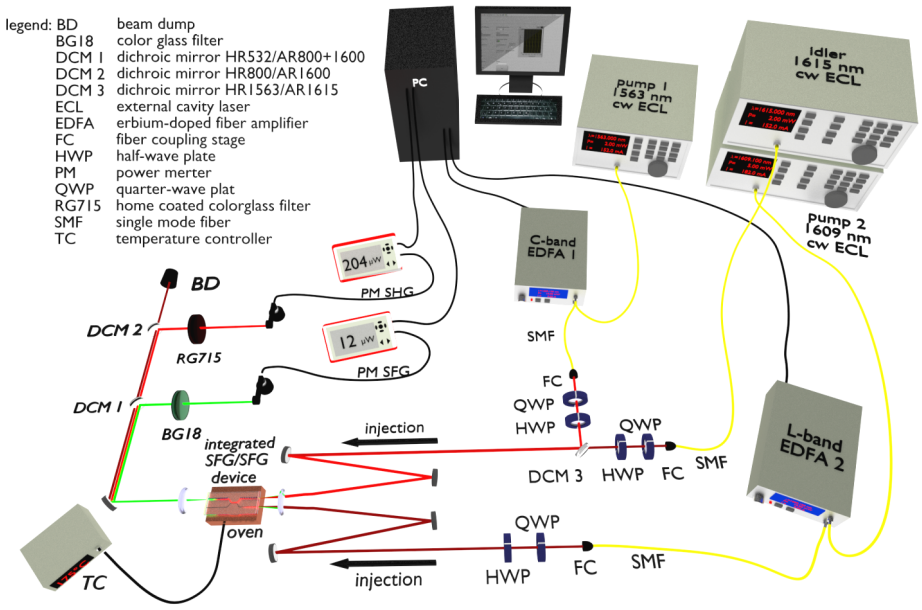

Figure 7.5.: Experimental setup for cascaded SFG/SFG process: A weak idler at powers around $\mathbf{P}_\mathrm{i} = 2\,\mathrm{mW}$ and a wavelength of $\lambda_\mathrm{i} = 1615\,\mathrm{nm}$ are combined with the pump 1 at $\lambda_\mathrm{p1} = 1563\,\mathrm{nm}$ by the DCM 3 and subsequently injected to our integrated device. The pump 2 at $\lambda_\mathrm{p2} = 1609\,\mathrm{nm}$ is fed into the adjacent waveguide using a different beam path prior to the coupling. Both pump beams are variable in power via computer-controlled individual erbium-doped fiber-amplifiers. The generated SFG 1 and SFG 2 signal powers are registered by standard power meters, which are read out by the computer.

the idler, i. e. the photon numbers are assumed to be preserved according to the Manley-Rowe relation [100]. Likewise, we included all transmittances and loss figures for the involved beams for the calculations. At zero power of the secondary EDFA, we identify that the SFG 1 conversion efficiency increases along the y-axis of our color-coded graph. As soon as the pump 2 increases we notice that the maximum conversion efficiency at given pump 1 power decreases, which means that the intermediate SFG 1 signal gets depleted by the secondary SFG process as expected.

The graph in Fig. 7.6 (right) visualizes the $\sin^2\left(\sqrt{\kappa^2_\mathrm{SFG} \cdot \frac{\lambda_\mathrm{SFG}}{\lambda_\mathrm{i}} \cdot \mathbf{P}_\mathrm{p}} \cdot L_\mathrm{QPM}\right)$- dependence of the conversion efficiency of the SFG process on the pump 1 power according to Sec. 3.2.3, Eq. 3.75. For practical reasons we fit the similar curve

$$\eta_{\mathrm{SFG},j} = \eta^{\max}_{\mathrm{SFG},j} \cdot \sin^2\left(\sqrt{\eta^{\mathrm{norm}}_{\mathrm{SFG},j} \cdot P_{\mathrm{p},j}}\right), \tag{7.9}$$

where $j = 1, 2$. We derive a maximum internal conversion efficiency of $\eta^{\max}_{\mathrm{SFG},1} =$

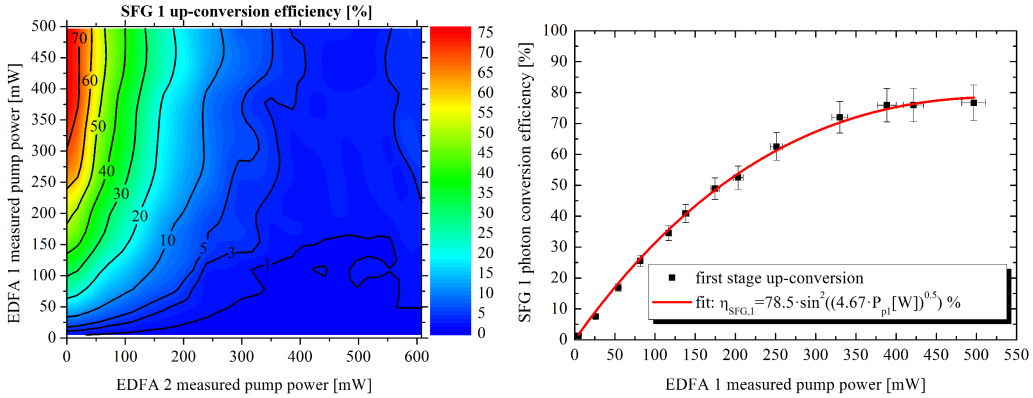

Figure 7.6.: The normalized conversion efficiency (left) for the first SFG process is depicted dependent on the EDFA pump powers (left). It shows an increase with larger EDFA 1 pump powers. This power dependence follows the expected $\sin^2\sqrt{\mathbf{P}_{\mathrm{p1}}}$-curve (right), where we achieve a maximum of $\eta^{\mathrm{max}}_{\mathrm{SFG},1} = 78.5\%$ at around $\mathbf{P}_{\mathrm{p1}} = 500\,\mathrm{mW}$. As the power of the EDFA 2 increases, the intermediate SFG 1 signal gets almost fully depleted at $\mathbf{P}_{\mathrm{p2}} = 450\,\mathrm{mW}$, because the second SFG process converts it into green light.

$(78.5 \pm 1.0)\%$. The normalized SFG efficiency reads $\eta^{\mathrm{norm}}_{\mathrm{SFG},1} = 4.47\%\,\mathrm{W}^{-1}\mathrm{cm}^{-2}$. Knowing that the individual interaction lengths, i. e. the nominal periodically poled lengths, are given by $L_{\mathrm{QPM},1} = L_{\mathrm{QPM},2} = 3\,\mathrm{cm}$, we infer the nonlinear coupling parameter for the primary SFG process by comparison of coefficients. We get $\kappa_{\mathrm{SFG},1} = (1.027 \pm 0.035)\mathrm{W}^{-1/2}\mathrm{cm}^{-1}$.

For the second SFG process we plot the conversion efficiency in a similar manner, which is shown in Fig. 7.7. Our findings from the paragraph above are verified: the increasing pump 2 power leads to a conversion of the intermediate SFG 1 signal into the SFG 2 output. By contrast to Fig. 7.6, where we derived the right graph from a single cut along the y-axis at $\mathbf{P}_{\mathrm{p2}} = \mathbf{0}$ with the respective error bars, we infer the data points for the right graph in Fig. 7.7 as well as the error bars from averaging over the data sets along the x-axis, i. e.for several pump 1 powers in the range $4\,\mathrm{mW} \leq \mathbf{P}_{\mathrm{p1}} \leq 496\,\mathrm{mW}$. A fit analogue to Eq. 7.9 yields a maximum conversion efficiency of only $\eta^{\mathrm{max}}_{\mathrm{SFG},2} = (47.5 \pm 0.2)\%$. The reduction of the maximum conversion efficiency, in comparison with theoretically achievable unit conversion efficiency, cannot be explained in our model with reduced spatial mode overlap factors ν_{SFG} or poor coupling coefficients κ_j (see Eq. 3.73), but solely with higher-than-expected transmission loss of the SFG light [85].

By analogy to the primary SFG process we deduce the internal coupling parameter for the second SFG from the normalized coupling efficiency $\eta^{\mathrm{norm}}_{\mathrm{SFG},2} = 5.57\%\,\mathrm{W}^{-1}\mathrm{cm}^{-2}$. We get for the coupling parameter $\kappa_{\mathrm{SFG},2} = (0.961 \pm 0.035)\mathrm{W}^{-1/2} \cdot \mathrm{cm}^{-1}$, which is

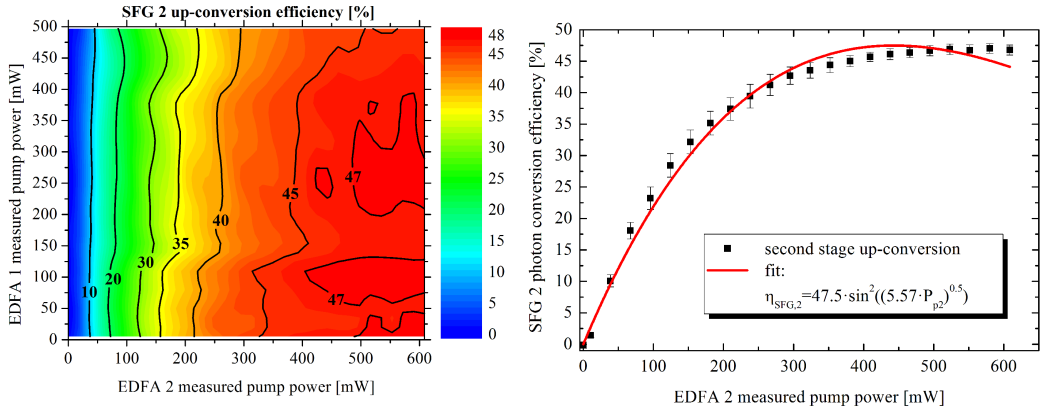

Figure 7.7.: The secondary SFG signal is shown dependent on the EDFA pump powers (left). It increases with higher EDFA 2 pump powers, as expected. The theory-aided fit to the measurement outcome in the right graph shows maximum conversion efficiencies of $\eta^{\max}_{\mathrm{SFG},2} = 47.5\%$ at $\mathbf{P}_{\mathrm{p2}} = 450\,\mathrm{mW}$ independently of the EDFA 1 power, and it shows the expected $\sin^2\sqrt{\mathbf{P}_{\mathrm{p2}}}$-behavior (right). Note that we averaged over the whole set of data at various EDFA 1 powers and derived the error bars accordingly. The curve represents the fit to these averaged values.

slightly lower than for the SFG 1 process. Since we recorded our data in terms of 2D-arrays, it is convenient to perform a matrix multiplication in order to get the joint conversion efficiency for the cascaded SFG/SFG process. This means that the left plot in Fig. 7.8 shows the photon-number normalized conversion efficiency from the input idler at $\lambda_{\mathrm{i}} = 1615\,\mathrm{nm}$ to the SFG 2 output at $\lambda_{\mathrm{SFG},2} \approx 531.8\,\mathrm{nm}$. We identify the maximum conversion efficiency of the cascaded process as $\eta^{\max}_{\mathrm{cSFG/SFG}} = (35.7 \pm 0.5)\%$ for $\mathbf{P}^{\max}_{\mathrm{p1}} = (400 \pm 50)\,\mathrm{mW}$ and $\mathbf{P}^{\max}_{\mathrm{p2}} = (550 \pm 70)\,\mathrm{mW}$.

In the Fig. 7.8 (right) we show the relative internal depletion of the SFG 1 signal, which reaches a maximum of $D^{\max}_{\mathrm{SFG},1} = (100.4 \pm 0.8)\%$. The normalized conversion efficiency of $\eta^{\mathrm{norm}}_{\mathrm{SFG},1} = (6.05 \pm 0.1)\%\,\mathrm{W}^{-1}\mathrm{cm}^{-2}$ is derived from the fit curve

$$D_{\mathrm{SFG},1} = D^{\max}_{\mathrm{SFG},1} \cdot \sin^2\left(\sqrt{\eta^{\mathrm{norm}}_{\mathrm{SFG},1} \cdot \mathbf{P}_{\mathrm{p2}}}\right). \tag{7.10}$$

From the fit we deduce a coupling parameter for the depletion of $\kappa^{\mathrm{D}}_{\mathrm{SFG},1} = (1.004 \pm 0.045)\,\mathrm{W}^{-1/2}\mathrm{cm}^{-1}$, which is nearly identical to the SFG 2 coupling parameter. We conclude that, although an almost perfect depletion of the intermediate SFG 1 signal is achieved by the secondary up-conversion, the overall cascaded up-conversion process shows only comparatively poor internal efficiency of $\eta_{\mathrm{cSFG/SFG}} = (35.7 \pm 0.5)\%$. In the literature even $\eta_{\mathrm{cSFG/SFG}} = 87\%$ have been achieved. For slightly higher output wavelengths the pump used in Ref. [275] was at around $\lambda_{\mathrm{p1}} = \lambda_{\mathrm{p2}} \approx 1.8\,\mu\mathrm{m}$ in wavelength. Taking the technological background of those reverse proton-exchanged waveguides in lithium niobate into account, we suspect the buried waveguides not

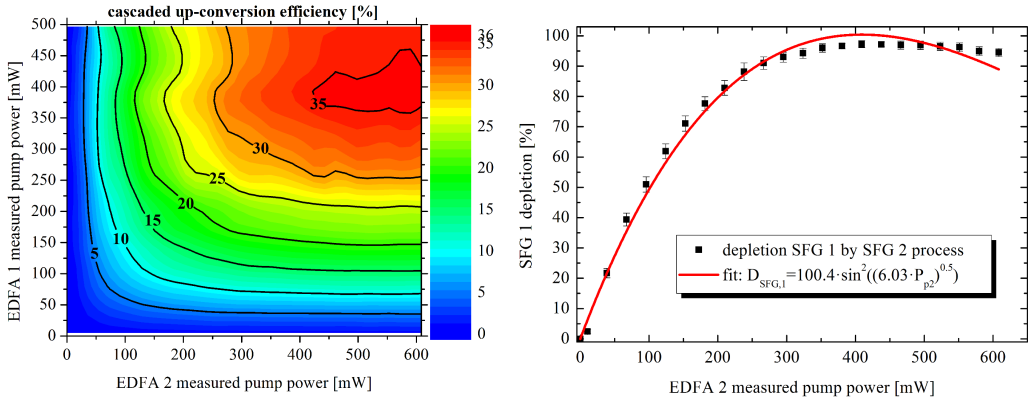

Figure 7.8.: The overall normalized conversion efficiency from $\lambda_\mathrm{i} = 1615\,\mathrm{nm}$ to $\lambda_\mathrm{SFG,2} = 531.8\,\mathrm{nm}$ is shown (left). We calculate the data by matrix multiplication of the data from the individual SFG processes, and we notice a maximum of $\eta^\mathrm{max}_\mathrm{cSFG/SFG} = 35.7\%$ for $\mathbf{P}^\mathrm{max}_\mathrm{p1}(400 \pm 50)\,\mathrm{mW}$ and $\mathbf{P}^\mathrm{max}_\mathrm{p2}(550 \pm 70)\,\mathrm{mW}$. Also the depletion of the intermediate SFG 1 signal is shown (right), the $\sin^2\sqrt{\mathbf{P}_\mathrm{p2}}$-fit curve of which shows-close-to-perfect depletion at EDFA 2 powers, where the overall cSFG/SFG signal conversion to the green wavelength region is maximized. This indicates that the limited overall conversion efficiency is caused predominantly by high waveguide losses at $\lambda_\mathrm{SFG,2}$.

only to be more beneficial for larger coupling parameters κ due to better spatial mode overlap integrals, but also for lower scattering losses at short-wavelength intermediate and output signals. This effect can be attributed to the drastically decreased impact of surface scattering centers to the buried waveguide modes. By contrast, the asymmetric refractive index profiles in our Ti-diffused waveguides lead to more significant mode dispersion, which means that light at shorter wavelengths is guided closer to the waveguide-to-air interface and is, thus, more susceptible to surface scattering loss. However, our results prove that Ti-diffused waveguides in lithium niobate allow for cascaded up-conversion from the telecom L-band to the visible wavelength regime. The comparatively low "photon-number"-normalized conversion efficiency for the cascaded process reduces the feasibility of up-conversion detector applications, because the possible gain in detection efficiency is canceled out by the low on-chip conversion efficiency. Especially, the cascaded frequency up-conversion of single photons from telecom to visible appears to be obsolete in terms of detection efficiency gain, since fast, highly efficient and low-jitter detectors at $\lambda_\mathrm{i} \sim 1600\,\mathrm{nm}$ are already commercially available [276, 277].

In summary, we have demonstrated that cascaded up-conversion can be deployed for the generation of classical light at visible wavelengths. With two independent pump laser wavelengths, the green output light is tunable by temperature and shows line widths of around $(45 \pm 5)\,\mathrm{pm}$.

7.1.3. Single photon frequency up-conversion

In the previous section we have shown that, due to scattering loss effects, the individual up-conversion efficiencies of our cascaded SFG/SFG processes are bound to $\eta^{\max}_{\mathrm{SFG},1} = (78.5 \pm 1.0)\%$ and $\eta^{\max}_{\mathrm{SFG},2} = (47.5 \pm 0.2)\%$, respectively. These figures of merit limit the applicability of our device as a hybrid up-conversion detector. As an example, for the first SFG process we can achieve a combined detection efficiency for up-converted wavelengths around $\lambda_{\mathrm{i}} = 1615\,\mathrm{nm}$ of around $\eta^{\mathrm{det,max}}_{\mathrm{SFG},1} \equiv 53\%$, if we assume negligible transmission loss to Si-based avalanche photodiodes with $\lambda^{\mathrm{det}}_{\mathrm{Si}}(794\,\mathrm{nm}) = 0.68$ detection efficiency at the sum-frequency signal [278]. This value is significantly higher as for typical InGaAs-based avalanche photodiodes, and the hybrid up-conversion detection can offer low timing jitter and dead-times [279–281].

However, the cascaded up-conversion of telecom idler photons at $\lambda_{\mathrm{i}} = 1615\,\mathrm{nm}$ to visible wavelengths can have only $\eta^{\mathrm{det,max}}_{\mathrm{cSFG/SFG}} \equiv 18.2\%$ maximum detection efficiency, if we assume nominal detection efficiencies of $\eta^{\mathrm{det}}_{\mathrm{Si}}(532\,\mathrm{nm}) = 51\%$ [282]. This combined detection efficiency is just on par with with latest InGaAs-APD technology [283], while higher single-photon detection efficiencies are desired.

In this section we show that, apart from the limitations mentioned above, the (cascaded) up-conversion from the telecom wavelength regime to NIR (or visible) wavelengths has even more severe restrictions for single photons and is, thus, not feasible with our integrated device as it is. For this purpose we changed the setup from the previous section such that it allows us to inject the idler at quasi-single-photon levels. In particular, we inserted a fiber-optic variable attenuator and additional neutral-density filters in order to feed our first SFG stage with only $\mathbf{P}_{\mathrm{i}} \sim 300\,\mathrm{fW}$ of idler power. At wavelengths of $\lambda_{\mathrm{i}} = 1615\,\mathrm{nm}$ this corresponds to idler photon rates of $R_{\mathrm{i}} \sim 2.55 \cdot 10^6\,\mathrm{s}^{-1}$. The setup is shown in Fig 7.9 and comprises a silicon-based avalanche photodiode, which collects the converted and spectrally filtered NIR photons via multi-mode fiber-coupling.

We perform power-dependent measurements, where we assume that the pump light is not depleted significantly. Likewise, due to narrow-band spectral filtering at the single-photon up-conversion (SPUC) wavelength of $\lambda_{\mathrm{SPUC},1} = 794.1\,\mathrm{nm}$, we can neglect competing conversion processes with the amplified spontaneous emission (ASE) background of our EDFA. However, we measure nearly quadratic growth of the up-converted photon count rate at $\lambda_{\mathrm{SPUC},1}$ with increasing pump power. Thus, an identical measurement has been performed, where only the pump beam is involved, but the idler input is blocked. We notice almost identical count rates in both measurements, and the results are depicted in the left graph in Fig. 7.10, where we calculated the count rates taking the measured transmittances and efficiencies of the optical components and the detector into account. Only after subtracting the EDFA-induced output from the signal including the idler input, we see the typical $\sin^2\sqrt{\mathbf{P}_{\mathrm{p1}}}$-behavior for the normalized conversion efficiency in Fig. 7.10 (right).

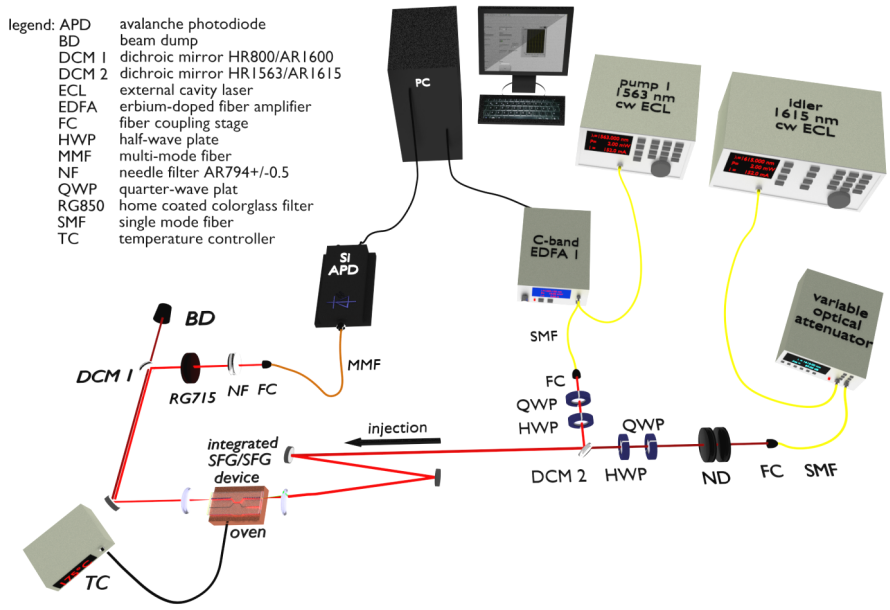

Figure 7.9.: Experimental setup for the single-stage frequency up-conversion: The pump 1 at $\lambda_{\mathrm{p1}} = 1563\,\mathrm{nm}$ is combined with strongly attenuated idler light at $\lambda_{\mathrm{i}} = 1615\,\mathrm{nm}$ prior to the coupling into our waveguide structure. The calibrated variable attenuator provides us with idler power levels corresponding to only $2.55 \cdot 10^6$ photons per second. If the single-photon conversion took place, we collect the up-converted photons with a Si-based avalanche photodiode behind narrow-band spectral filtering and fiber-coupling.

From the post-processed data we infer a maximum of the normalized internal conversion efficiency of

$$\eta_{\mathrm{SPUC},1}^{\mathrm{max}} = (48.9 \pm 0.7)\%$$

at a pump power of $\mathbf{P}_{\mathrm{p}} = (350 \pm 25)\,\mathrm{mW}$. This corresponds to a maximum overall system detection efficiency of only $\eta_{\mathrm{SPUC},1}^{\mathrm{PDE,max}} = (6.00 \pm 0.09)\%$, if all transmittances and the detector efficiency is included. For the coupling parameter, we calculate

$$\kappa_{\mathrm{SPUC},1} = (1.267 \pm 0.045)\frac{1}{\sqrt{\mathrm{W} \cdot \mathrm{cm}}},$$

which is slightly higher than for the analogous bright-light sum-frequency generation process in the previous section. However, the maximum achievable conversion efficiency is significantly lower than for the bright-light sum-frequency process. We suspect the difference for the quasi-single-photon up-conversion to be caused by the fiber-based routing of the photons towards the Si-APD detector and the detection efficiency of the latter. In particular, we assumed a specified detection efficiency of $\eta_{\mathrm{Si}} = 0.55$ at wavelengths of the up-converted light, which might have been lower

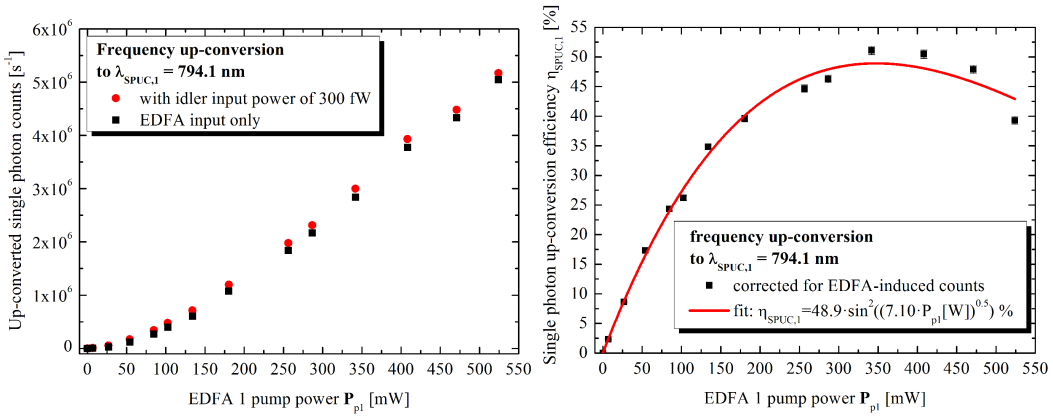

Figure 7.10.: The up-conversion from quasi-single photons from $\lambda_\mathrm{i} = 1615\,\mathrm{nm}$ to $\lambda_\mathrm{SPUC,1} = 794.1\,\mathrm{nm}$ is shown with (red dots) and without (black squares) the idler input (left). We notice almost identical behavior of the two curves. Only after subtraction of the EDFA-based measurement outcome and subsequent normalization we identify the expected $\sin^2\sqrt{\mathbf{P}_\mathrm{p1}}$-curve (right), showing a maximum of $\eta^\mathrm{max}_\mathrm{SPUC,1} = (48.9 \pm 0.7)\%$. Note that the error bars in the left graph are smaller than the markers.

in practice. Additionally, the vendor's specifications do not consider multi-mode fiber-connectors to the detector. Most importantly, we did not take the free-space-to-fiber-coupling efficiency into account, which is mainly responsible for the decrease to around 61.5% of the maximum achievable classical conversion efficiency.

Due to the very low sensitivity of our Si-APD at telecom wavelengths, we neglect the option that residual pump photons, which survived our strong spectral filtering, are responsible for the increasing photon count rate although no idler input is present. Instead, we suspect the pump to induce spontaneous Raman scattering [284] while propagating along our waveguides. It has been reported in the literature [280] that if the pump wavelength is spectrally close to the degeneracy wavelength of the up-conversion process, the Stokes- as well as the anti-Stokes-shifted side band can mix with the strong pump to up-converted signals at the SPUC wavelength. For this reason, long-wavelength pumps, being spectrally far away from Raman side bands have been proposed to induce significantly less noise, if the quasi-phase-matching condition is fulfilled. However, this negative effect can also offer a fast and reliable method for the characterization of the spontaneous Raman scattering inside our waveguides: By scanning the narrow-band pump from the wavelength, where SHG occurs, to lower wavelengths, we would be able to visualize the anti-Stokes-shifted Raman side-band by frequency up-conversion. The Stokes-shift can be visualized with the same method, if the pump wavelength is increased to $\lambda_\mathrm{p1} > 2 \cdot \lambda_\mathrm{SHG}$. For more detailed information, see Refs. [280, 285].

The aforementioned limitations of the first single-photon up-conversion stage lead to the conclusion that the cascaded conversion of quasi-single idler photons to the

visible wavelength range is, although possible, not promising in terms of low noise figures. Thus it would not provide significant benefits compared to other state-of-the-art single-photon detectors [278, 282] or hybrid systems [275, 281], unless one applies more sophisticated noise suppression techniques [286].

As a closing remark we can state that our device is not suitable for single-photon up-conversion from telecom to NIR wavelengths in its actual configuration. Likewise, the cascaded up-conversion to visible wavelengths cannot be performed reliably, unless the quasi-phase-matching condition of first process and the waveguide cut-off condition have been changed such that we are able to pump this process at wavelengths of $\lambda_{\mathrm{p1}} \geq 1750\,\mathrm{nm}$, where Raman scattering does not lead to increased noise levels.

7.2. Photon-triplet generation - stochastic anticipation and experimental verification

The generation of multi-partite entanglement has been studied [33, 287] and experimentally demonstrated (see, for example [288]) the last 25 years. It has been shown that a class of quantum states, which comprise at least three entangled quantum particles, i. e., so called Greenberger-Horne-Zeilinger states (GHZ), can be used to prove the non-locality of quantum physics [34] and the missing of hidden variables in the theory of quantum mechanics [9, 11, 289].

The generation of optical GHZ and heralded Bell states [11] states requires quantum technology, which is capable of producing the more fundamental tripartite photonic states, namely, photon triplets. A few theoretical considerations and experiments relied on the simultaneous generation of higher-order photon states in a single parametric down-conversion source [290,291] in order to produce heralded Bell pairs. Other approaches concentrated on the parallelized generation of photon pairs in two physically independent PDC sources with subsequent sum-frequency generation of one of the generated photons of each source [292, 293].

Cascaded parametric down-conversion sources in an interfacing sequence of a bulk and a guided-wave PDC source have been applied first by Hübel and coworkers in 2010 [91] in order to generate photon-triplet states. The verification of tripartite entanglement in the energy-time regime [92] domain as well as in the polarization degree of freedom [93] have been demonstrated by the same group. The violation of the Clauser-Horne-Shimony-Holt (CHSH) inequality [18] and the Mermin [294–296] inequality, which are derivatives of Bell's inequality [11], by up to ten standard deviations have been shown. The experimental results proved the feasibility of generating heralded Bell states with high visibility and fidelity, but without the need of post-selection. With cascaded PDC sources, also hyper-entangled photon-triplets and also heralded GHZ states become achievable perspectives.

Other approaches to generate tripartite or multi-partite photonic states rely on cascades of either hot atomic vapor cells [297,298] or cascaded non-degenerate optical parametric oscillators [299]. Only very recently, the generation of photonic triplet states in a hybrid cascade of optical nonlinearities, consisting of a $\chi^{(2)}$-nonlinear waveguide and $\chi^{(3)}$-nonlinear atomic vapor, has been shown [300].

In most of the aforementioned experiments on cascaded parametric down-conversion as a photon-triplet generation process, cw lasers have been employed. By contrast, pulsed pump light would provide timing information beneficial for source synchronization and simplifying the analysis of higher photon number contributions. But even more important for quantum technology and quantum network applications is the operation of triplet sources with low loss. Due to the hybrid approach of combining a bulk and a guided-wave PDC, lossy interfaces had to be used in that work in order to provide mutual compatibility of the two cascaded PDC stages.

Monolithically integrated triplet sources have not been shown, yet, neither in the cw nor in the pulsed pump regime. They can offer a significant reduction of interface

losses in between the cascaded conversion stages. Likewise, the full guided-wave approach also allows for higher individual conversion efficiencies [48].

Motivated by the idea to generate photon triplets (and eventually GHZ states) by cascaded PDC, we pursued the fully monolithic integration of photon-triplet source on the basis of titanium-diffused waveguides in lithium niobate. In this section, we present the main results of this thesis.

In Section 4.4 we have described the design and the parameter choice for our device comprising two consecutive wavelength converters, which are interfaced by passive directional coupler as shown in Fig. 4.5. The compact design as well as the number of functionalities, including the high-quality end-face coatings, allows for the generation of photon-triplet states in pulsed cascaded parametric down-conversion, as we will point out in this part of the thesis.

Figure 7.11 shows an abstracted schematic of our device including the important parameters, which will not only help us to design an appropriate experimental setup, but they also allow us to analyze and predict the outcome of our cascaded parametric down-conversion process itself. We pursue a deductive strategy, i. e., we first conceive the experimental setup as described in the next section, from which we derive the triplet-generation theory.We also benefit from the experimental results on the individual PDC emission characteristics described in Sec. 5.2 and 5.4. The theory, however, can be generalized also to bulk and hybrid versions of *pulsed* cascaded parametric down-conversion processes by adapting and re-labeling the respective parameters.

7.2.1. Source settings and experimental setup

As a first step on the route to photon-triplet generation via cascaded parametric down-conversion, we determine the on-chip combinations of poling gratings, where the PDC signal (1^{st} grating) and the SHG (2^{nd} grating) emission are at around the same NIR wavelength. This is absolutely necessary because the two individual PDC stages have to be mutually compatible: the signal from the first PDC process serves as the pump for the second PDC. We identify several of these poling combinations according to the multi-parameter design of our device (see Sec. 4.4). Our findings from the previous section 7.1 not only helped us to find this combination of structures in general, but also taught us that possible non-ideal QPM conditions can be compensated for by temperature tuning.

The on-chip directional coupler behavior changes for the available poling grating combinations, and we have also to select a coupler, that provides the best possible transfer of primarily generated idler photons to the adjacent channel. The corresponding signal photons (referred to as signal 1 in the following) must remain in the bar output waveguide, which is the case for all of our integrated WDMs. Specifically, we identify the second coupler structure of the group 6 with $L_{\text{C}} = 3000\,\mu\text{m}$, where primary idler photons at $\lambda_{\text{i1}} \approx 1625\,\text{nm}$ (idler 1 in the following) get transferred with $CR_{\text{i1}}^{\text{cross}} = (0.94 \pm 0.01)$. This waveguide structure is surrounded by the two

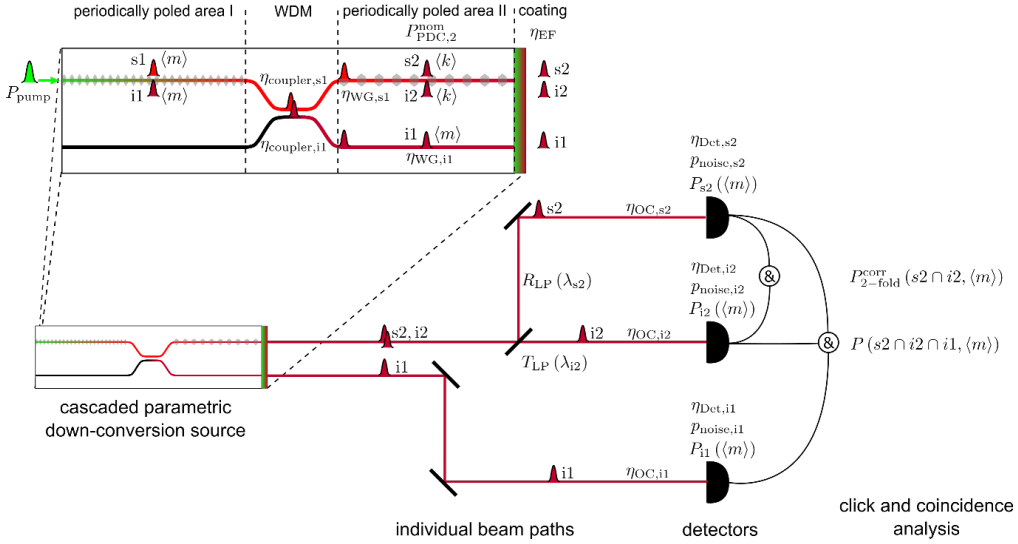

Figure 7.11.: The monolithic source and measurement schematic for cascaded parametric down-conversion is shown. In the periodically poled area I, pulsed pump photons decay to non-degenerate photon pairs, s1 and i1, sharing the same mean photon number per pulse $\langle m\rangle$. The primary photon pair splits up spatio-spectrally at the integrated WDM. Short-wavelength s1 photons remain in the original waveguide and decay to time-correlated secondary photon pairs, s2 and i2 (with common mean photon number per pulse $\langle k\rangle \ll \langle m\rangle$), in the periodically poled area II. Effectively, we convert one pump photon into three telecom photons, which are directed to individual detectors and undergo coincidence measurements, as described in detail in the text.

gratings of $\Lambda_{\mathrm{G1}} = 6.83\,\mu$m and $\Lambda_{\mathrm{G2}} = 17.61\,\mu$m poling periods, respectively.

As shown in Fig. 7.12 for this grating combination, we conveniently extract the principal working point for cascaded parametric down-conversion processes by changing the only free parameter left, i.e. the device temperature. We call this the principal working point, because the secondary PDC process is phase-matched at degenerate wavelengths, which reads $\lambda_{\mathrm{s1}} = \lambda_{\mathrm{p2}} = (790.47 \pm 0.35)\,\mathrm{nm}$ for $\theta^{\mathrm{WP}} = (163.5 \pm 0.1)^{\circ}\mathrm{C}$.

From the secondary PDC emission characteristics given in Fig. 5.14 in Sec. 5.4.2, we learned that a broad spectral distribution of secondarily generated photon pairs is present around the degeneracy wavelength of $\lambda_{\mathrm{s2/i2}} = (1581 \pm 35)\,\mathrm{nm}$. Deterministic splitting of secondary signal and idler photons (signal 2 and idelr 2 in the following) usually fails due to the low dispersion of common dielectric bulk filter materials at telecom wavelengths. Thus, even complicated layer stacks, e. g. in edge- or band-pass dielectric filters, cannot provide the necessary (infinite) slope for deterministic splitting.

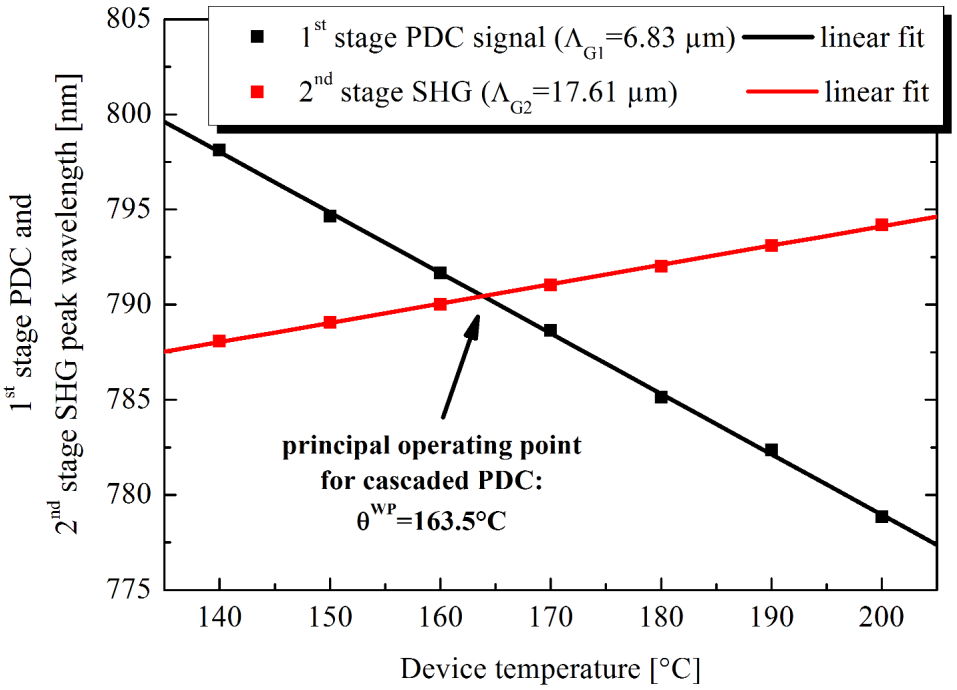

Figure 7.12.: With the two individual temperature tuning curves for fixed poling periods, it is convenient to find the fundamental point of operation at $\theta = 163.5°\mathrm{C}$ and $\lambda_{s1} = 790.5\,\mathrm{nm}$. Note that the error bars are smaller than the square markers.

As explained in Sec. 5.3, we also measure a non-vanishing TM_{01} signal mode at $\lambda_{s1}^{\mathrm{TM}_{01}} \approx 798.4\,\mathrm{nm}$, which appears in combination with the corresponding TM_{00} idler mode at $\lambda_{i1}^{\mathrm{TM}_{00}} \approx 1592\,\mathrm{nm}$. Together with imperfect coupler behavior at telecom wavelengths, this will cause serious complications for cascaded parametric down-conversion processes: The existence of the TM_{00} idler mode, residing spectrally close to the expected degeneracy wavelength of the desired secondary PDC process, requires the secondary PDC stage to be driven in a non-degenerate manner. This rules out spectral superpositions of the emission contributions from two PDC processes. Alternatively, narrow-band optical filtering can prevent false interpretations. The latter option, in turn, reduces the device brightness for cascaded parametric down-conversion.

Likewise we deduce from Fig. 5.14 that the waveguide dispersion properties restrict the low-loss PDC emission to wavelengths below $\lambda_{s2/i2} \leq 1635\,\mathrm{nm}$. In order to prevent waveguide cut-off and substrate mode scattering at idler 2 wavelengths, we determine $\lambda_{s1} = \lambda_{p2} = 790.3\,\mathrm{nm}$ to be the trade-off pump wavelength for the secondary PDC process. Consequently, we extract the working temperature of $\theta_{\mathrm{device}}^{\mathrm{opt}} = 163.8°\mathrm{C}$ for the cascaded PDC process. This also has the advantage, that signal and idler emission wavelengths concentrate at around $\lambda_{s2} = (1551 \pm 25)\,\mathrm{nm}$

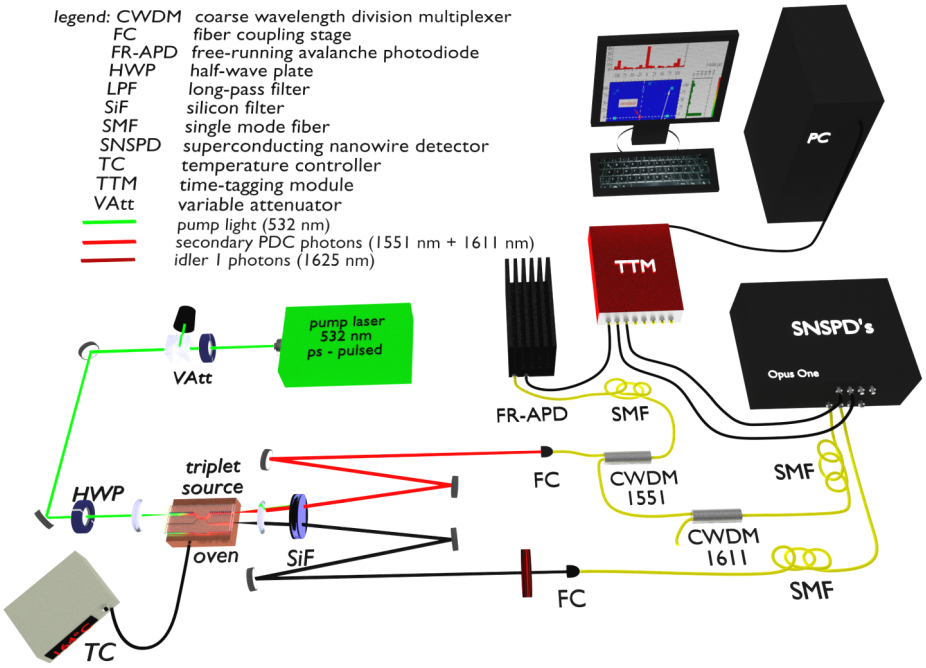

Figure 7.13.: Schematic experimental realization for the generation and measurement of photon triplets, generated in our temperature-stabilized, integrated source for cascaded parametric down-conversion. The output beams are split spatio-spectrally and directed to three free-running detectors after strong spectral filtering. The time-tagging module registers the arrival times of detector click events and provides convenient data analysis. See text for a detailed description.

and $\lambda_{s2} = (1611 \pm 25)\,\mathrm{nm}$, respectively. For these emission wavelengths, it is possible to separate the photon pairs spatially in a quasi-deterministic manner using dielectric edge filters with finite transmission slopes. From our findings in Sec. 5.4.2 we also conclude to achieve the maximum spectral overlap between the two PDC processes of around $\eta_{s1-p2} = 0.88$ at the set temperature.

Taking the impact of higher-order mode combinations and the spectral-splitting issue into account, we chose the alternative option to implement fiber-based CWDM for spectro-spatial splitting. These elements offer excellent filtering properties for unwanted wavelengths around our expected secondary PDC emission (suppression over 35dB). However, we are aware of the fact that the filtering bandwidths of around $\pm 7\,\mathrm{nm}$ limit the measurable brightness of the secondary PDC process and, thus, also of the photon-triplet generation process. These preconditions allow us to conceive and build up the setup for the generation and measurement of photon-triplet states in a cascaded parametric down-conversion process shown in Fig. 7.13.

The incoupling part of the experimental solution is in principle the same as for the nonlinear experiments carried out in the previous chapters. Here, we pay particular attention to the measurement apparatus and the analysis section of the setup.

The spectral cleanliness of the telecom photons is guaranteed by the implementation of a customized silicon filter window, which absorbs perfectly all residual pump photons as well as the intermediate signal 1 at $\lambda_{s1} = 790.3\,\mathrm{nm}$. While the quasi-deterministic spectral splitting of signal 2 and idler 2 photons is realized by a cascade of fiber-coupled CWDMs with $(1551 \pm 7)\,\mathrm{nm}$ and $(1611 \pm 7)\,\mathrm{nm}$ transmission window, the overall output of our integrated chip could be directed to three individual single photon detectors for the telecom wavelength range. The idler 1 photons are detected by a superconducting nanowire single-photon detector (SNSPD), which has around 50% detection efficiency, ~ 600 dark counts per second and allows for saturation- and dead-time-free registering of the primary idler photons. Signal 2 photons, due to their expected wavelength range around $\lambda_{s2} = (1551 \pm 25)\,\mathrm{nm}$, are expected to occur very rarely in cascaded PDC and are, thus, guided to a free-running InGaAs-APD (ID Quantique ID230-FR-SMF) as the detector, which has around 25% detection efficiency and a $20\,\mu\mathrm{m}$ dead-time setting for the suppression of after-pulses and for low dark-count rates around 150 counts per second. The idler 2 photons are detected by a second SNSPD (Quantum Opus OpusONE) with around 60% detection efficiency and ~ 1200 dark counts per second and dead times of around 100 ns. Each detector is connected to a time-tagging module converter, which registers individual detection events and assigns absolute time stamps. This simplifies the post-selection of individual and coincidently occurring events.

As the last remaining preparative step for the theoretical analysis as well as for the experimental verification of photon-triplet generation, we characterized the both PDC stages individually performing the photon pair preparation at variable pump powers for both processes. We register the single counts of the silicon avalanche photodiode (signal 1) and a superconducting nanowire detector (idler 1) as well as the coincidences with the time-tagging module and, by analogy to the method described in Sec. 6.1, we calculate the Klyshko efficiencies for our three measurement arms. Together with the respective repetition rates of the pump lasers, we derive the single count probabilities per optical pulse according to

$$P_\mathrm{s} = \eta_\mathrm{s} \cdot P_\mathrm{PDC}^\mathrm{pulse} = \frac{R_\mathrm{s}}{R_\mathrm{rep}} \tag{7.11}$$

$$P_\mathrm{i} = \eta_\mathrm{i} \cdot P_\mathrm{PDC}^\mathrm{pulse} = \frac{R_\mathrm{i}}{R_\mathrm{rep}}. \tag{7.12}$$

For the coincidence probability of time-correlated events per pulse we get

$$\begin{aligned} P\left(\mathrm{s} \cap \mathrm{i}\right) &= P_\mathrm{i} \cdot P_\mathrm{s}\left(\mathrm{s}|\mathrm{i}\right) = P_\mathrm{s} \cdot P_\mathrm{i}\left(\mathrm{i}|\mathrm{s}\right) \\ &= \eta_\mathrm{s}\eta_\mathrm{i} \cdot P_\mathrm{PDC}^\mathrm{pulse} \\ &= \frac{R_\mathrm{coinc}}{R_\mathrm{rep}}. \end{aligned} \tag{7.13}$$

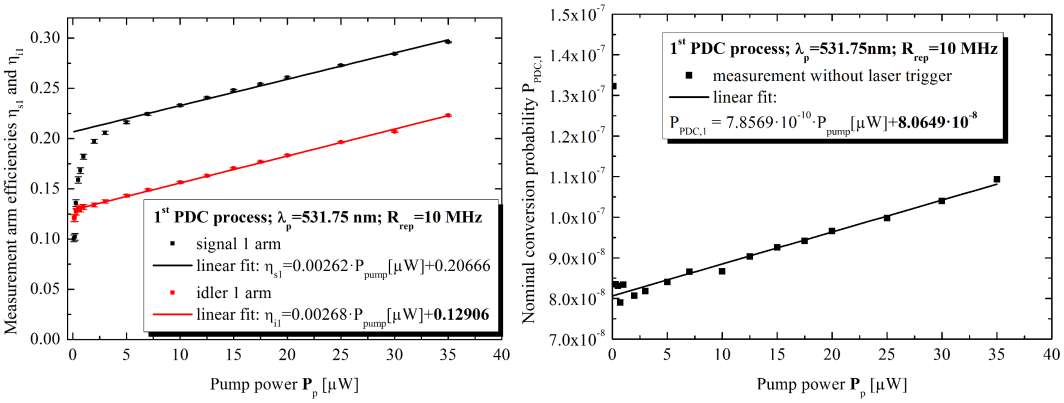

Figure 7.14.: Pump dependent Klyshko efficiencies of the primary PDC process, measured with the setup for photon-triplet generation (**left**). We derive linear dependencies with increasing pump powers, and the arm efficiencies are given as the y-axis offset of the fit curves. At the lowest available pump powers, we notice a significant influence of noise counts to the single count rates and, thus very low Klyshko efficiencies. The calculated PDC conversion probability is depicted also pump power dependent (**right**), and we infer the internal PDC probability per pump photon from the y-axis offset of the linear fit.

Herein, η_s and η_i represent the overall efficiencies in the respective detection arms. Note that $P_\mathrm{PDC}^\mathrm{pulse}$ denotes the nominal generation probability for a PDC photon pair per pump pulse.

The detection probability of one photon, given that the detection of its twin already occurred, is expressed by the conditional probabilities

$$P_\mathrm{s}\left(\mathrm{s}|\mathrm{i}\right) = \frac{P\left(\mathrm{s}\cap\mathrm{i}\right)}{P_\mathrm{i}} = \eta_\mathrm{K,s} = \eta_\mathrm{s} = \frac{R_\mathrm{coinc}}{R_\mathrm{i}} \tag{7.14}$$

$$P_\mathrm{i}\left(\mathrm{i}|\mathrm{s}\right) = \frac{P\left(\mathrm{s}\cap\mathrm{i}\right)}{P_\mathrm{s}} = \eta_\mathrm{K,i} = \eta_\mathrm{i} = \frac{R_\mathrm{coinc}}{R_\mathrm{s}}, \tag{7.15}$$

and we see that they can be extracted conveniently by relating the measurable count rates for signal, idler and coincidences accordingly. Since the generation probabilities of higher-order photon contributions grow with increasing pump powers (see Sec. 6.1.3.2), we rely on the determination of the Klyshko efficiencies by linear regression, i. e., the y-axis offset for the regression curves.

Figure 7.14 (left) shows the pump power dependent Klyshko efficiencies for the first PDC process. We deduce the arm efficiencies as $\eta_\mathrm{K,s1} = 0.207 \pm 0.002$ for the signal 1 arm and, more important for the triplet generation process, $\eta_\mathrm{K,s1} = 0.129 \pm 0.001$ for the idler 1 arm from the fit curves. Note that these values include the respective detection efficiencies, the on-chip waveguide and coupler properties,

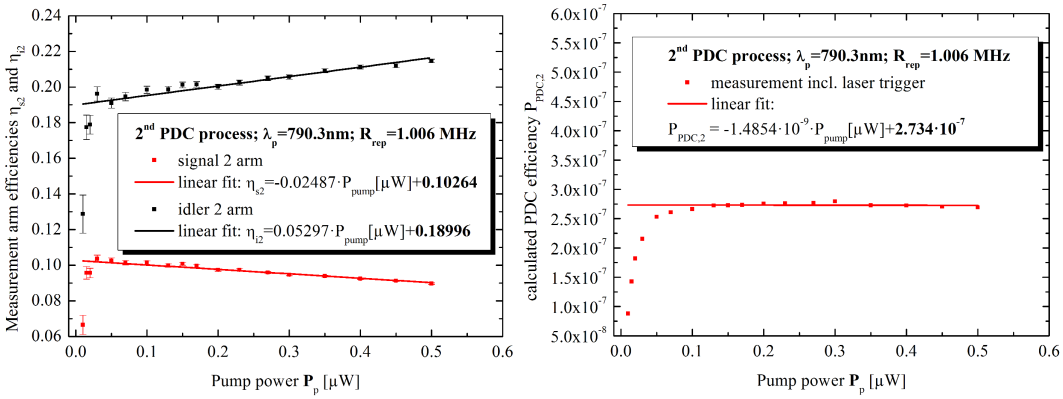

Figure 7.15.: The pump dependent Klyshko efficiencies of the 2nd PDC process are shown (**left**), measured photon-triplet generation setup. We pump with infrared laser light at 1 MHz and$\lambda_{p1} = 790.3\,\mathrm{nm}$, and we synchronize the laser trigger with the time-tagging module.The signal 2 and idler 2 efficiencies are given as the y-axis offset of the linear fit curves. In comparison to the first PDC stage (see Fig. 7.14) we notice a negligible influence of noise on the single count rates at low pump powers. This is due to the laser synchronization with the coincidence measurement, which denotes an additional AND gating. The negative slope of the signal 2 Klyshko efficiency originates from saturation effects in the InGaAs-APDe. The conversion probabilities are plotted in a pump-power-dependent graph (**right**), where the internal PDC generation probability per pump photon is given by the y-axis offset of the linear fit.

as well as individual transmittances of supplementary optical components.

In combination with equation 7.13 we calculate the nominal PDC probabilities

$$P_{\mathrm{PDC}}^{\mathrm{pulse}} = \frac{R_{\mathrm{coinc}}}{R_{\mathrm{rep}} \cdot \eta_{\mathrm{s}} \cdot \eta_{\mathrm{i}}}, \tag{7.16}$$

which include information about the PDC success probability per pump pulse, whereas the pump injection efficiency and pump losses in the waveguide are not taken into account. In order to derive the internal PDC generation probabilities per pump photon, P_{PDC}, we relate $P_{\mathrm{PDC}}^{\mathrm{pulse}}$ to the number of pump photons per pulse, $n_{\mathrm{ph}}(\lambda_{\mathrm{p}})$:

$$P_{\mathrm{PDC}} = \frac{P_{\mathrm{PDC}}^{\mathrm{pulse}}}{n_{\mathrm{ph}}(\lambda_{\mathrm{p}})} = P_{\mathrm{PDC}}^{\mathrm{pulse}} \cdot \frac{h \cdot c}{\lambda_{\mathrm{p}}} \cdot \frac{R_{\mathrm{rep}}}{\mathbf{P}_{\mathrm{p}}}. \tag{7.17}$$

Here, $\mathbf{P}_{\mathrm{p}}$ denotes the measured pump power prior to coupling into our waveguide structures.

For the first process we infer the internal PDC generation probability of $P_{\mathrm{PDC},1} = (8.065 \pm 0.4) \cdot 10^{-8}$ photon pairs per pump photon by fitting the pump-dependent nominal PDC probabilities linearly as shown in Fig. 7.14. The achieved y-axis offset

Table 7.1.: Experimental conditions for triplet analysis and measurements

characteristics	**symbol**	**value**
pump pulse width	τ_{pulse}	$4.4 \cdot 10^{-11}$ s
pump repetition rate	R_{rep}	10^7 Hz
waveguide end-face transmittance	$\eta_{\text{EF}}(\text{C}+\text{L}-\text{band})$	0.995
waveguide loss	$\alpha_{\text{WG}}(\text{C}+\text{L}-\text{band})$	0.08 dB/cm
waveguide loss	$\alpha_{\text{WG}}(790.5)$	~ 0.2 dB/cm
s1 waveguide transmittance	$\eta_{\text{WG,s1}}(790.5\,\text{nm})$	0.813
s1 coupler efficiency	$\eta_{\text{coupler,s1}}(790.5\,\text{nm})$	0.995
s1 waveguide transmittance	$\eta_{\text{WG,s1}}(790.5\,\text{nm})$	0.81
s1 channel efficiency	η_{s1}	0.207
i1 waveguide transmittance	$\eta_{\text{WG,i1}}(1625\,\text{nm})$	0.895
i1 noise count probability per ns	$p_{\text{noise,i1}}$	$7 \cdot 10^{-6}$
i1 detection efficiency	$\eta_{\text{Det,i1}}(1625\,\text{nm})$	~ 0.5
i1 coupler efficiency	$\eta_{\text{coupler,i1}}(1625\,\text{nm})$	0.94
i1 channel efficiency	η_{i1}	0.129
1^{st} **PDC gen. probability**	$P_{\text{PDC,1}}$	$8.1 \cdot 10^{-8}$
s2 waveguide transmittance	$\eta_{\text{WG,s2}}(1551\,\text{nm})$	0.973
s2 detection efficiency	$\eta_{\text{Det,s2}}$	~ 0.25
s2 noise count probability per ns	$p_{\text{noise,s2}}$	$6.5 \cdot 10^{-7}$
s2 channel efficiency	$\eta_{\text{s2}}^{\text{tot}}$	0.103
i2 waveguide transmittance	$\eta_{\text{WG,i2}}(1611\,\text{nm})$	0.973
i2 detection efficiency	$\eta_{\text{Det,i2}}$	~ 0.6
i2 noise count probability per ns	$p_{\text{noise,i2}}$	$1.8 \cdot 10^{-6}$
i2 channel efficiency	$\eta_{\text{i2}}^{\text{tot}}$	0.190
2^{nd} **PDC gen. probability**	$P_{\text{PDC,2}}$	$2.73 \cdot 10^{-7}$

value denotes $P_{\text{PDC,1}}$ and is around two orders of magnitude lower than the best values achieved to date [48]. However, we do not take loss effects of the pump injection into account in our calculations. The nominal internal conversion probability is certainly higher by the amount of coupling loss of the pump. We estimate around $30-50\%$ higher values for $P_{\text{PDC,1}}$, when the pump loss is excluded.

The secondary PDC process is characterized in a similar manner, but we include the electronic pump laser trigger in our singles and coincidences measurements. For appropriate post-processing in very small coincidence windows, this technique significantly reduces the impact of noise-related detection events. Additionally, we use an InGaAs-APD (signal 2) and a superconducting nanowire detector (idler 2). From the graphs in Figure 7.15 and our findings summarized in Appendix E we conclude that, especially at low pump powers, the detected single counts coincide with the laser trigger at lower rates. This leads to increased Klyshko efficiencies as compared to the non-triggered case.

The resulting values for $\eta_{\mathrm{K,s2}}$ and $\eta_{\mathrm{K,i2}}$ are deduced from the y-axis offset in the power dependent measurements. We get $\eta_{\mathrm{K,s2}} = 0.10264 \pm 0.00087$ and $\eta_{\mathrm{K,i2}} = 0.18996 \pm 0.00171$. The error bars represent the uncertainties of the fit. We calculate the internal PDC generation probabilities for the different pump powers, apply a linear regression to the data points in Fig. 7.15 (right) and get $P_{\mathrm{PDC,2}} = (2.7342 \pm 0.0252) \cdot 10^{-7}$ per pump photon. This internal PDC generation probability is also reduced by the amount of loss due to coupling and propagation loss of the pump light prior to the genuine PDC process. However, we expect $P_{\mathrm{PDC,2}} > P_{\mathrm{PDC,1}}$. On the one hand, the secondary conversion involves wavelengths, which do not suffer from mode dispersion in the waveguides as much as in the first PDC process. On the other hand, the required poling periods are significantly larger and, thus, can be fabricated more homogeneously and with less errors in the duty-cycle. This provides longer effective poling and interaction lengths for the nonlinear processes in the second PDC stage. Detailed mode distribution studies as well as a technological analysis of the effective poling lengths should be performed in the future in order to verify these assumptions.

In summary, we have collected the parameters necessary for the theoretical studies and experimental verification of photon-triplet generation. Table 7.1 shows the important values, and we proceed with the theoretical analysis and estimation in the following.

7.2.2. Stochastic analysis of photon-triplet-generation process in pulsed cascaded parametric down-conversion sources

In this section, we study the photon-triplet generation performance for the pulsed regime in order to anticipate and compare later experimental results. In detail, we make reasonable assumptions concerning design parameters and measurement conditions deduced from the aforementioned experiments. We calculate not only the achievable rates of three-fold coincidences, but also estimate the influence of higher-order photon contributions on the measurement outcome. Furthermore, the analysis of the signal-to-noise behavior with real-world components is provided.

7.2.2.1. Description of the model system

Our theoretical and experimental considerations are inspired by the idea to generate photon triplets with cascaded PDC processes, as shown by Hübel et al. [91]. By contrast to their cw experiment involving two different PDC sources in a spatially separated cascade, we consider our fabricated monolithic device in combination with the experimental setup as shown in Fig. 7.11 and Fig. 7.13. We exclusively assume pulsed excitation, which we expect to be more power-efficient on the one hand, while it allows for convenient synchronization with other components of complex hybrid quantum networks in possible future applications.

The input waveguide is periodically poled with two different grating periods in consecutive areas. In the first poled region, non-degenerate (primary) photon pairs

at around $\lambda_{s1} \approx 790.5\,\text{nm}$ (signal 1) and $\lambda_{i1} \approx 1625\,\text{nm}$ (idler 1) are generated in type-0 parametric down-conversion (PDC) from a pulsed pump at 531.78 nm.

The passive directional coupler between the two poled regions separates signal 1 and idler 1 photons as discussed in Sec. 5.3. Idler 1 photons at the longer wavelength are transferred to an adjacent waveguide by evanescent field coupling with efficiency $\eta_{\text{coupler,i1}}$, and they pass on-chip optical losses with efficiency $\eta_{\text{WG,i1}}$. The coupler is wavelength selective in the telecom region for transverse magnetic (TM) polarization.

The short-wavelength signal 1 photons, generated in the fundamental spatial mode, remain in the pump channel with efficiency $\eta_{\text{coupler,s1}}$ due to strong mode confinement, and they pass optical loss along the directional coupler and the straight waveguide with efficiency $\eta_{\text{WG,s1}}$.

In the secondary periodic poling, primary signal photons are predominantly present and decay with the nominal internal conversion probability per pump photon, $P'_{\text{PDC,2}}$, into signal 2 and idler 2 photons, which are distributed around the degeneracy wavelength of $\lambda_{s,2} = \lambda_{i,2} = 1581\,\text{nm}$. This is in accordance to the rules of energy and momentum conservation (phase-matching) for the secondary type-0 PDC process. Detuning of the secondary down-conversion source allows for non-degenerate operation such that the overall cascaded decay of a green pump photon into three telecom photons is described by

$$\begin{aligned} 532\,\text{nm} &\rightarrow 1625\,\text{nm} + 1551\,\text{nm} + 1611\,\text{nm} \\ \text{pump} &\rightarrow \text{idler}\,1 + \text{signal}\,2 + \text{idler}\,2. \end{aligned} \tag{7.18}$$

In the case of primary signal photons we expect loss figures of $\alpha_{\text{WG,s1}} \leq 0.2\,\text{dB/cm}$ and we measured $\alpha_{\text{WG}}(\text{C} + \text{L} - \text{band}) = 0.08\,\text{dB/cm}$ for telecom photons, which can exit the device through the deposited end-face coating with efficiency $\eta_{\text{EF}} = 0.995$.

The following analysis applies also to bulk, hybrid and guided-wave cascaded parametric down-conversion sources, as long as the systems are pumped with a pulsed laser. Of course the individual parameters have to be adapted appropriately.

7.2.2.2. Estimation of the mean photon number in the primary PDC process

In this section we model the outcome of the primary parametric down-conversion process in terms of the click probability for idler 1 photons at binary detectors. We assume the signal and idler photon number per optical pulse to be Poisson-distributed, since both of our type-0 PDC processes are multi-mode in the spectral domain (compare Sec. 6.1).

The density vector element, describing the probability that an m-photon state is generated in the first PDC process, contributes to the average photon number $\langle m \rangle$ per signal or idler pulse. It is given by

$$\rho_m = \frac{e^{-\langle m \rangle} \cdot \langle m \rangle^m}{m!}. \tag{7.19}$$

Depending on the photon number density per pump pulse, we can deduce the mean photon number per output pulse fairly well by measuring idler 1 clicks events

with a binary free-running detector. This is only valid under the precondition that the detector does not saturate due to dead-time effects.

For the (lossless) case of an arbitrary m-photon input state impinging the idler 1 detector, we can model the click response of the detector. If no photons arrive ($m = 0$), only noise counts will influence the zero-photon click probability, which reads

$$P'_{\mathrm{i1}}\,(m = 0) = p_{\mathrm{noise,i1}}. \tag{7.20}$$

The noise count probability of a free-running detector, $p_{\mathrm{noise,i1}}$, can be inferred from the specified dark count rate $R_{\mathrm{dc,i1}}$, and from the count rate of additional blackbody photons, R_{bb}. The latter becomes significant, when we heat up our cascaded PDC source to around 164°C. We relate the sum of the two rates, $R_{\mathrm{noise,i1}}$, to appropriate timing units in order to get the noise probability $p_{\mathrm{noise,i1}}$. For our pulsed system, the pulse duration in combination with the joint timing jitter of the involved detection devices appears to be a reasonable timing choice.

Second, when we know that there is exactly one photon impinging to the detector ($m = 1$), a click can occur due to a noise count or due to the primary idler photon itself with efficiency $\eta_{\mathrm{Det,i1}}$ or both, i. e., noise counts "blind" the detector for the incoming photon. Therefore, the are treated as stochastically independent similar to a logic OR operation, and we get the click probability for the one-photon state:

$$P'_{\mathrm{i1}}\,(m = 1) = p_{\mathrm{noise,i1}} + \eta_{\mathrm{Det,i1}} - p_{\mathrm{noise,i1}} \cdot \eta_{\mathrm{Det,i1}}. \tag{7.21}$$

As soon as there are (higher-order) m-photon states arriving at the detector, the latter will give only one click, since it is not photon-number resolving. The click probability corresponds to the counter event of the case, where the detector neither clicks due to noise events (that is $p = 1 - p_{\mathrm{noise,i1}}$), nor due to any of the impinging photons (i. e., $p' = (1 - \eta_{\mathrm{Det,i1}})^m$). This is equivalent to a logical NAND operation on the negated zero- and one-photon click probabilities, and we write

$$P'_{\mathrm{i1}}\,(m) = 1 - (1 - p_{\mathrm{noise,i1}}) \cdot (1 - \eta_{\mathrm{Det,i1}})^m. \tag{7.22}$$

Since this formula is consistent with equations 7.20 and 7.21 for the cases $m = 0$ and $m = 1$, respectively, we generalize equation 7.22 for arbitrary m-photon states with $m \geq 0$.

We expect primary idler photons to undergo optical loss of $1 - \eta_{\mathrm{i1}}$ on their path from the point of generation to the point of being detected. In detail, the transmittance η_{i1} can be calculated as the product of individual transmittances and efficiencies of lossy optical elements and the detector (logical AND), that is

$$\eta_{\mathrm{i1}} = \eta_{\mathrm{int,1}} \cdot \eta_{\mathrm{EF}} \cdot \eta_{\mathrm{OC,i1}} \cdot \eta_{\mathrm{Det,i1}}. \tag{7.23}$$

Herein $\eta_{\mathrm{int,1}} = \eta_{\mathrm{coupler,i1}} \cdot \eta_{\mathrm{WG,i1}}$ denotes the intrinsic transmittance of our model device for idler 1 photons behind the first PDC stage. The factor $\eta_{\mathrm{OC,i1}}$ is the transmittance of supplementary optical components in the idler 1 measurement arm,

and the detector efficiency is still labeled $\eta_{\mathrm{Det,i1}}$. With this in mind, we substitute equation 7.22 by the loss-dependent m-photon click probability

$$P_{\mathrm{i1}}(m) = 1 - (1 - p_{\mathrm{noise,i1}})(1 - \eta_{\mathrm{i1}})^m. \tag{7.24}$$

Third, we calculate the overall click probability $P_{\mathrm{i2}}(\langle m \rangle)$ for an ensemble measurement of optical pulses, carrying Poisson-distributed photons with mean photon number $\langle m \rangle$. We weight the individual m-photon contributions with their occupation probabilities ρ_{m} and get for the overall idler 1 click probability

$$P_{\mathrm{i1}}(\langle m \rangle) = \sum_{m \geq 0}^{\infty} [1 - (1 - p_{\mathrm{noise,i1}})(1 - \eta_{i1})^m] \cdot \rho_m. \tag{7.25}$$

We find that $P_{\mathrm{i1}}(\langle m \rangle)$ is equal to the noise count probability $p_{\mathrm{noise,i1}}$ for $\langle m \rangle \to 0$. Conversely, for large mean photon numbers $\langle m \rangle \gg 1$, $P_{\mathrm{i1}}(\langle m \rangle)$ asymptotically approaches unit click probability. Another consequence of equation 7.25 is its linearity with respect to $\langle m \rangle$ for low arm efficiencies $\eta_{\mathrm{i1}} \ll 1$. This means that an m-photon state will yield a click about m-times more often than a one-photon state. Furthermore, there exists a linear relation between $P_{\mathrm{i1}}(\langle m \rangle)$ and $\langle m \rangle$ for $\langle m \rangle \ll 1$, where only zero- and one-photon components play a predominant role.

Next, we model the response of the binary detector for our real-world scenario. If η_{i1} is properly known, we can calculate the click rate of the idler 1 detector to be approximately

$$R_{\mathrm{i1}} \approx R_{\mathrm{noise,i1}} + R_{\mathrm{rep}} \cdot P_{\mathrm{i1}}(\langle m \rangle), \tag{7.26}$$

where R_{rep} is our pump laser repetition rate.

By comparing the measured and calculated click rates, we are able deduce the mean photon number of the first PDC process by solving equation 7.26 for $P_{\mathrm{i1}}(\langle m \rangle)$ and get

$$P_{\mathrm{i1}}(\langle m \rangle) = \frac{R_{\mathrm{i1}} - R_{\mathrm{noise,i1}}}{R_{\mathrm{rep}}} \approx \frac{R_{\mathrm{i1}}}{R_{\mathrm{rep}}}. \tag{7.27}$$

For small Klyshko efficiencies $\eta_{\mathrm{i1}} \ll 1$, we infer that the mean photon number per pulse is approximately given by

$$\langle m \rangle \approx \frac{R_{\mathrm{i1}}}{\eta_{\mathrm{i1}} \cdot R_{\mathrm{rep}}}. \tag{7.28}$$

Note that we assumed in the measured click rates in equation 7.27 to be at moderate levels, where neither dead-time nor saturation effects of the detector become significant. The validity of the latter condition depends on the efficiency η_{i1}. However, the overall count rate should exceed the noise count rate significantly, i. e., $R_{\mathrm{i1}} \gg R_{\mathrm{noise,i1}}$, for the approximations in equations 7.27 and 7.28 to hold.

7.2.2.3. Secondary PDC process

Accessing the mean photon number of the first PDC process by measuring idler 1 clicks also allows us to predict the outcome of the secondary PDC process, since the primary photons share temporal correlations and have the same mean photon number per pulse at the point of their generation. Thus, we are able to estimate the contributions of individual m-photon states in an ensemble of optical pulses. We can be sure that, at the output of our first PDC process, the photon number distribution of the signal 1 photons is not only Poisson-like, but also equal to the corresponding idler 1 distribution, if we neglect different loss values inside the chip.

In the following, we model the transfer of signal 1 photons towards the secondary conversion stage as well as the second PDC process itself in terms of a lossy channel with subsequent deterministic pair generation. An incoming m-photon state behaves as if it is reflected (and lost), when no conversion occurs, but gets transmitted *and* duplicated, when a conversion takes place. *After* conversion, we treat the generated pair photons as individual but time-correlated entities.

The linear optical device efficiency,

$$\eta_{\mathrm{Dev,s1}} = \eta_{\mathrm{coupler,s1}} \cdot \eta_{\mathrm{WG,s1}}, \tag{7.29}$$

describes the transmission of signal 1 photons through the integrated directional coupler towards the secondary PDC stage, while $\eta_{\mathrm{coupler,s1}}$ is the efficiency that the signal photon remains in the original coupler arm. The term $\eta_{\mathrm{WG,s1}}$ denotes the waveguide transmittance for the signal 1 photon from the average point of its generation to the average point of its decay to a secondary photon pair.

The secondary PDC process takes place with the *nominal* internal conversion efficiency per signal 1 photon, $P'_{\mathrm{PDC,2}}$, which includes the spectral overlap of the primary signal photon mode with the phase-matched pump mode of the secondary process. Note that the mutual spatio-spectral mode compatibility between signal 1 photons and the pump input of the second PDC process is important (see Sec. 5.4.2), but here we restrict ourselves to include this precondition to $P'_{\mathrm{PDC,2}}$. We multiply the involved probabilities and efficiencies accordingly, since they describe stochastically independent events, and we get the second PDC's *internal* conversion probability per signal 1 (pump) photon:

$$P_{\mathrm{PDC,2}} = \eta_{\mathrm{Dev,s1}} \cdot P'_{\mathrm{PDC,2}}, \tag{7.30}$$

which acts similar to a "loss factor" on primary signal photons. Note that $\eta_{\mathrm{Dev,s1}}$ can be replaced by the transmittance of other interfacing devices, if the considered model system is a pulsed bulk or hybrid cascaded parametric down-conversion source.

We write the resulting photon number transformation in a matrix representation:

$$\vec{\rho}_k = \mathbf{L}_{\mathrm{PDC,2}} \cdot \vec{\rho}_m. \tag{7.31}$$

The vector $\vec{\rho}_m$ comprises the incoming photon number occupation probabilities for

different m-photon states according to equation 7.19. The elements

$$L_{km} = \binom{m}{k} P_{\mathrm{PDC},2}^{k} \left(1 - P_{\mathrm{PDC},2}\right)^{m-k}, \; m \geq k \tag{7.32}$$

contribute to the loss matrix $\mathbf{L}_{\mathrm{PDC},2}$ and describe the probability that k secondary photon pairs are generated, given an m-photon state in the signal 1 (and idler 1) mode is present behind the first PDC stage.

This leads to *individual* photon number contributions ρ_k of the time-correlated signal 2 and idler 2 photons. We write

$$\rho_k = \sum_{m \geq k \geq 0}^{\infty} \binom{m}{k} P_{\mathrm{PDC},2}^{k} \left(1 - P_{\mathrm{PDC},2}\right)^{m-k} \cdot \rho_m. \tag{7.33}$$

In the limit of unit internal conversion probability $P_{\mathrm{PDC},2} = 1$, we expect $\rho_k = \rho_m$ to hold true, whereas real-world conditions lead to drastically decreased mean photon numbers per pulse for secondary photons, i. e., $\langle k \rangle \ll \langle m \rangle$, since internal conversion probabilities are typically of the order of $10^{-5} \leq P_{\mathrm{PDC},2} \leq 10^{-10}$ pairs per input photon.

7.2.2.4. Spectral splitting of secondary photons

We showed in Sec. 5.4.2 that the spectral characteristics of secondary photon pairs is tunable such that quasi-deterministic spatio-spectral splitting can be achieved. Experimentally, this is realized by implementing appropriate filters and by driving the secondary PDC at non-degenerate photon pair emission. More specifically, we use a cascade of band-pass filters in order to define two beam paths for signal 2 and idler 2. This is depicted in the setup schematic in Fig. 7.13. That technique provides us also with the reduction of noise events, which are related to the blackbody emission of a heated cascaded parametric down-conversion source.

For our modeling, we combine the wavelength dependent transmission at supplementary optical elements (filters, fiber-couplings etc.) with the splitting behavior of the filter cascade and with the detection efficiency in the two individual measurement arms:

$$\eta_{\mathrm{s2}}\left(\lambda_{\mathrm{s2}}\right) = T_{\mathrm{CWDM},1}\left(\lambda_{\mathrm{s2}}\right) \cdot \eta_{\mathrm{OC,s2}}\left(\lambda_{\mathrm{s2}}\right) \cdot \eta_{\mathrm{Det,s2}}\left(\lambda_{\mathrm{s2}}\right) \cdot \eta_{\mathrm{EF}} \tag{7.34}$$

and

$$\eta_{\mathrm{i2}}\left(\lambda_{\mathrm{i2}}\right) = R_{\mathrm{CWDM},1}\left(\lambda_{\mathrm{i2}}\right) \cdot T_{\mathrm{CWDM},2}\left(\lambda_{\mathrm{i2}}\right) \cdot \eta_{\mathrm{OC,i2}}\left(\lambda_{\mathrm{i2}}\right) \cdot \eta_{\mathrm{Det,i2}}\left(\lambda_{\mathrm{i2}}\right) \cdot \eta_{\mathrm{EF}}. \tag{7.35}$$

Herein, $T_{\mathrm{CWDM},1}\left(\lambda_{\mathrm{s2}}\right)$ denotes the transmittance of the first coarse wavelength division multiplexer for the signal wavelength at $(1551 \pm 7)\,\mathrm{nm}$, and $R_{\mathrm{CWDM},1}\left(\lambda_{\mathrm{i2}}\right)$ is the reflectance for the idler 2 photons at 1611 nm. The second CWDM in the cascade acts only as a band-pass filter for the idler 2 photons at $(1611 \pm 7)\,\mathrm{nm}$ with transmittance $T_{\mathrm{CWDM},2}\left(\lambda_{\mathrm{i2}}\right)$. The additional optical components provide transmittances $\eta_{\mathrm{OC}}\left(\lambda\right)$ in the respective beam path. Note that η_{EF} describes the wavelength-dependent transmittance of telecom photons in the C- and L-band at the device's

end-facet. Individual detector efficiencies are labeled with $\eta_{\mathrm{Det}}(\lambda)$, the wavelength dependence of which must be taken seriously, if common InGaAs-based detectors are used.

The aforementioned considerations allow us to anticipate the click probabilities of our binary detectors in the secondary measurement arms. The derivation is similar to equation 7.25, but we take the significant changes of the photon number distribution, caused by the second PDC process (see equation 7.33), into account. Additionally, we pay attention to the spectral dependence of the transmittances in equations 7.34 and 7.35.

A click event in one of the free-running detectors is given as the counter event of having neither a dark count, nor signal/idler photons, respectively. For the click probabilities of single detection events in the respective secondary arm we write

$$P_{\mathrm{s2/i2}}(\langle m\rangle) = \sum_{k\geq 0}^{\infty}\left\{1-\left(1-p_{\mathrm{noise,s2/i2}}\right)\left[1-\eta_{\mathrm{s2/i2}}\left(\lambda_{\mathrm{s2/i2}}\right)\right]^{k}\right\}\cdot\rho_k \tag{7.36}$$

$$= \sum_{k\geq 0}^{\infty}\left\{1-\left(1-p_{\mathrm{noise,s2/i2}}\right)\left[1-\eta_{\mathrm{s2/i2}}\left(\lambda_{\mathrm{s2/i2}}\right)\right]^{k}\right\} \times \sum_{m\geq k}^{\infty}\binom{m}{k}P_{\mathrm{PDC,2}}^{k}\left(1-P_{\mathrm{PDC,2}}\right)^{m-k}\rho_m. \tag{7.37}$$

We consider $p_{\mathrm{noise,s2/i2}}$ to be the individual noise count probabilities of the signal 2 and idler 2 detectors. With the realistic assumption of $P_{\mathrm{PDC,2}}\approx 10^{-7}$, we can conclude that all $(m\geq 1)$-photon states of the primary PDC process will be converted mainly to $k=0$ and few $k=1$ photon contributions in the secondary PDC process.

In the following, we assume that the wavelength dependent arm efficiencies can be described by analytical expressions, being continuous for reasonable intervals around the expected signal/idler wavelengths, i. e., $\lambda_{\mathrm{s2/i2}}^{\mathrm{min}}\leq\lambda_{\mathrm{s2/i2}}\leq\lambda_{\mathrm{s2/i2}}^{\mathrm{max}}$. Proper intervals are given by the filter bandwidths of considered fiber-optic band-pass filters. Thus, we write for the overall arm efficiencies η^{tot}, which are experimentally accessible with the method described in Sec. 7.2.1 above:

$$\eta_{\mathrm{s2}}^{\mathrm{tot}} = \frac{\int_{\lambda_{\mathrm{s2}}^{\mathrm{min}}}^{\lambda_{\mathrm{s2}}^{\mathrm{max}}}\eta_{\mathrm{s2}}(\lambda_{\mathrm{s2}})\,\mathrm{d}\lambda}{\lambda_{\mathrm{s2}}^{\mathrm{max}}-\lambda_{\mathrm{s2}}^{\mathrm{min}}} \equiv \eta_{\mathrm{K,s2}} \tag{7.38}$$

and

$$\eta_{\mathrm{i2}}^{\mathrm{tot}} = \frac{\int_{\lambda_{\mathrm{i2}}^{\mathrm{min}}}^{\lambda_{\mathrm{i2}}^{\mathrm{max}}}\eta_{\mathrm{i2}}(\lambda_{\mathrm{i2}})\,\mathrm{d}\lambda}{\lambda_{\mathrm{i2}}^{\mathrm{max}}-\lambda_{\mathrm{i2}}^{\mathrm{min}}} \equiv \eta_{\mathrm{K,i2}} \tag{7.39}$$

We furthermore approximate $(1-P_{\mathrm{PDC,2}})^{m-k}\approx 1$ in equation 7.33 for reasonable internal PDC conversion probabilities. Additionally, we expect $p_{\mathrm{noise,s2}}\ll\eta_{\mathrm{s2}}^{\mathrm{tot}}$ and $p_{\mathrm{noise,i2}}\ll\eta_{\mathrm{i2}}^{\mathrm{tot}}$.

With all these assumptions and preconditions, the evaluation of equation 7.37 for both photon species yields the click probabilities for secondary PDC photons:

$$\begin{aligned} P_{\mathrm{s2}}(\langle m\rangle) &\approx p_{\mathrm{noise,s2}} + \eta_{\mathrm{s2}}^{\mathrm{tot}} \sum_{m\geq 1}^{\infty} m \cdot P_{\mathrm{PDC,2}} \cdot \rho_m \\ &= p_{\mathrm{noise,s2}} + \eta_{\mathrm{s2}}^{\mathrm{tot}} \cdot P_{\mathrm{PDC,2}}^{\mathrm{gen}} \\ &= p_{\mathrm{noise,s2}} + \eta_{\mathrm{s2}}^{\mathrm{tot}} \cdot P_{\mathrm{PDC,2}} \cdot \langle m\rangle. \end{aligned} \tag{7.40}$$

and

$$\begin{aligned} P_{\mathrm{i2}}(\langle m\rangle) &\approx p_{\mathrm{noise,i2}} + \eta_{\mathrm{i2}}^{\mathrm{tot}} \sum_{m\geq 1}^{\infty} m \cdot P_{\mathrm{PDC,2}} \cdot \rho_m \\ &= p_{\mathrm{noise,i2}} + \eta_{\mathrm{i2}}^{\mathrm{tot}} \cdot P_{\mathrm{PDC,2}}^{\mathrm{gen}} \\ &= p_{\mathrm{noise,i2}} + \eta_{\mathrm{i2}}^{\mathrm{tot}} \cdot P_{\mathrm{PDC,2}} \cdot \langle m\rangle. \end{aligned} \tag{7.41}$$

In equations 7.40 and 7.41 we notice, that higher-order m-photon states from the first PDC stage will each contribute to the secondary conversion process approximately m-times more often than one-photon states. Note that the term $P_{\mathrm{PDC,2}}^{\mathrm{gen}}$ labels the effective pair generation probability per optical pulse, whereas $P_{\mathrm{PDC,2}}$ is the pair generation probability per pump photon. However, pumping at the single photon level leads to the conclusion that both measures for the PDC generation probability are at around the same order of magnitude.

We see that individual click probabilities depend linearly not only on $p_{\mathrm{noise,i2}}$, $P_{\mathrm{PDC,2}}$, and on $\eta_{\mathrm{s2/i2}}^{\mathrm{tot}}$, but also on the mean photon number of the first PDC output pulses, $\langle m\rangle$, since

$$\sum_{m\geq 1}^{\infty} m \cdot \rho_m \equiv \langle m\rangle. \tag{7.42}$$

This means that four parameters have an influence on each single-click probabilities $P_{\mathrm{s2}}(\langle m\rangle)$ and $P_{\mathrm{i2}}(\langle m\rangle)$. While the noise probability should be minimized for best possible SNR, the efficiency $\eta_{\mathrm{s2/i2}}^{\mathrm{tot}}$ has to be as high as possible.

Increasing $P_{\mathrm{PDC,2}}$ to values higher than 10^{-6} is technologically hard in lithium niobate waveguide structures. This fact implies, for experiments with commercially available equipment, that the noise count probability (per optical pulse) is typically of the same order as $P_{\mathrm{PDC,2}}^{\mathrm{gen}}$, and we will not be able to identify photon triplets with good signal-to-noise ratios just by measuring the generation of signal 2 or idler 2 photons. Instead, we make use of the temporal correlations of the photon triplets and perform coincidence measurements, as described in the following. This will lift the genuine triplets above the inevitable noise-related accidental contributions.

Note that equations 7.40 and 7.41 reflect what we derived in Sec. 7.2.1 for direct pumping of the secondary PDC process with attenuated laser pulses instead of single photons from the first PDC stage.

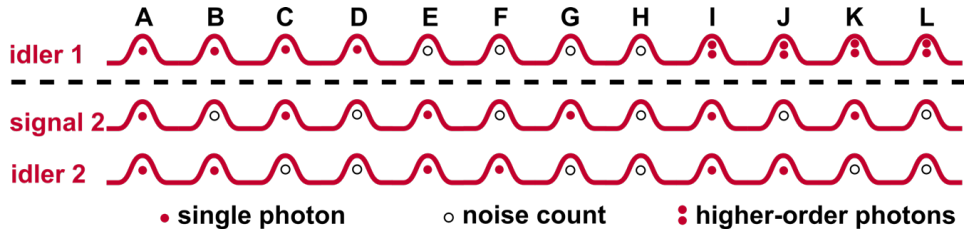

Figure 7.16.: Possible outcome of two- and three-fold coincidence measurements between the primary and secondary detection events. Only case A represents genuine photon-triplet preparation, whereas all other options denote noise-related and accidental coincidences. The dashed line marks the spatial separation of events with high (top) and low (bottom) detection probabilities.

7.2.2.5. Two-fold coincidences of secondary PDC photons

For the evaluation of two- and three-fold coincidences, we look at the possible outcome options: in practice, we must accept that clicks at free-running binary detectors will stem from noise contributions OR genuine PDC photons.

We distinguish between the twelve cases shown in Fig. 7.16, where only case A represents a genuine photon triplet. All other options cannot be discarded, but have to be taken into account as uncorrelated noise contributions.

We recognize the similarities of equations 7.40 and 7.41 and equations 7.11 and 7.12, respectively. Hence, we infer the probability for the coincidental detection of the time-correlated secondary photons from equation 7.13, and we write for the ideal case of noise-less detection:

$$P^{\mathrm{corr}}_{2-\mathrm{fold}}\left(\mathrm{s2}\cap\mathrm{i2},\langle m\rangle\right) = \eta^{\mathrm{tot}}_{\mathrm{s2}}\eta^{\mathrm{tot}}_{\mathrm{i2}}\sum_{m\geq 1}^{\infty} m\cdot P_{\mathrm{PDC},2}\cdot\rho_m \tag{7.43}$$

$$= \eta^{\mathrm{tot}}_{\mathrm{s2}}\eta^{\mathrm{tot}}_{\mathrm{i2}}\cdot P^{\mathrm{gen}}_{\mathrm{PDC},2} \tag{7.44}$$

$$= \eta^{\mathrm{tot}}_{\mathrm{s2}}\eta^{\mathrm{tot}}_{\mathrm{i2}}\cdot P_{\mathrm{PDC},2}\cdot\langle m\rangle. \tag{7.45}$$

This means that the coincidence probability of secondary pairs scales linearly with the mean photon number of the primary process as we would also expect for coherently pumped PDC processes. With our measured parameters given in Tab. 7.1 and a mean photon number of $\langle m\rangle = 0.25$ per pulse, we calculate $P^{\mathrm{corr}}_{2-\mathrm{fold}}\left(\mathrm{s2}\cap\mathrm{i2},\langle m\rangle\right) = (1.33\pm 0.01)\cdot 10^{-9}$ per pulse, which can be referred to as the experimentally accessible success probability for the two-fold coincidences. We anticipate the measurable photon coincidence rate accordingly as

$$R^{\mathrm{corr}}_{2-\mathrm{fold}} = P^{\mathrm{corr}}_{2-\mathrm{fold}}\left(\mathrm{s2}\cap\mathrm{i2},\langle m\rangle\right)\cdot R_{\mathrm{rep}} \tag{7.46}$$

$$= (47.9\pm 0.4)\,\mathrm{h}^{-1}.$$

We estimate the noise-related accidental coincidences such that we include the noise-count probabilities per coincidence time window, which we determine as one nanosecond including the joint timing jitter of the measurement apparatus. We get

$$\begin{aligned} P^{\text{noise}}_{2-\text{fold}}\left(\text{s2}\cap\text{i2},\langle m\rangle\right) &= \eta^{\text{tot}}_{\text{s2}}\cdot P_{\text{PDC},2}\cdot\langle m\rangle\cdot p_{\text{noise,i2}} \\ &\quad +\eta^{\text{tot}}_{\text{i2}}\cdot P_{\text{PDC},2}\cdot\langle m\rangle\cdot p_{\text{noise,s2}} \\ &\quad +p_{\text{noise,s2}}\cdot p_{\text{noise,i2}}, \end{aligned} \tag{7.47}$$

which is dominated by the last term for our experimental setup, because the individual noise count probabilities are expectedly higher than the single photon detection probabilities for the assumed $\langle m\rangle$. We calculate around $P^{\text{noise}}_{2-\text{fold}}\left(\text{s2}\cap\text{i2},\langle m\rangle\right) = 1.19\pm0.05\cdot10^{-12}$ per coincidence time window of 1 ns, and we expect signal-to-noise ratios for secondary coincidence detection of

$$\begin{aligned} SNR_{\text{PDC},2} &= \frac{P^{\text{corr}}_{2-\text{fold}}\left(\text{s2}\cap\text{i2},\langle m\rangle\right)}{P^{\text{noise}}_{2-\text{fold}}\left(\text{s2}\cap\text{i2},\langle m\rangle\right)} \\ &= 1117\pm45. \end{aligned} \tag{7.48}$$

This result indicates that we could already verify photon-triplet generation by detecting coincidences of secondary PDC photons. However, for our guided-wave device and its on-chip coupling behavior at idler 1 wavelengths, we have to consider the spatio-spectral splitting behind the first PDC stage to be non-deterministic. As long as the fiber-based CWDMs for secondary PDC wavelengths provide sufficient extinction for primary idler wavelengths in both measurement arms, we can assume that the probability of detecting idler 1 photons is negligible there and, thus, does not contribute to accidental coincidences of the secondary photon detection.

The situation is different and more critical if higher-order mode combinations contribute to the first PDC process. We denote these competing or "parasitic" processes with primes in the following description. Assuming the 532 nm pump and/or the signal 1' photons to be exited, say, in the TM_{01} mode, we must also assume that the corresponding parasitic idler 1' photons, although in the fundamental TM_{00} mode, can have wavelengths similar to the secondary PDC photons. This is due to waveguide dispersion and only slightly different phase-matching conditions for higher-order PDC generation. As soon as the wanted and the unwanted PDC processes show similar idler wavelengths, $\lambda_{\text{i1}'}\approx\lambda_{\text{i1}}$, which the on-chip coupler might not be optimized for, the competing idler 1' photons will pass the on-chip directional coupler through the original arm with transmittance $\eta^{\text{acc}}_{\text{coupler,i1}'} = 1-\eta_{\text{coupler,i1}'}(\lambda_{\text{i1}'})$. These parasitic photons can also pass subsequent optical elements and the CWDM filters towards the secondary detectors, and will contribute to secondary detection and coincidence events. This is expressed by the arm transmittances at idler 1' wavelengths, $\eta^{\text{tot}}_{\text{s2}}(\lambda_{\text{i1}'})$ and $\eta^{\text{tot}}_{\text{i2}}(\lambda_{\text{i1}'})$. The probabilities, describing that at least one of the accidental idler 1' photon survives in the respective secondary photon measurement arm, are given by

$$P^{\text{acc}}_{\text{i1}'\to\text{s2}} = \eta^{\text{tot}}_{\text{s2}}(\lambda_{\text{i1}'})\cdot\sum_{m'\geq1}^{\infty}\left[1-(1-\eta^{\text{acc}}_{\text{coupler,i1}'})^{m'}\right]\cdot\rho'_{m'} \tag{7.49}$$

and

$$P^{\mathrm{acc}}_{\mathrm{i1'}\rightarrow\mathrm{i2}} \quad = \quad \eta^{\mathrm{tot}}_{\mathrm{i2}}(\lambda_{\mathrm{i1'}}) \cdot \sum_{m'\geq 1}^{\infty} \left[1-(1-\eta^{\mathrm{acc}}_{\mathrm{coupler,i1'}})^{m'}\right] \cdot \rho'_{m'}. \tag{7.50}$$

For simplicity we assume that the internal conversion probability of the first PDC process is the same for all spatial mode combinations. Thus, the photon number occupation vector elements, $\rho'_{m'} = \rho_m$, are identical to the ones of the fundamental PDC process and contribute to the formulas above. In practice, the conversion efficiencies depend on the waveguide properties (i. e., the effective refractive indices of the involved modes) as well as on the possibility for quasi-selective excitation of different spatial pump modes.

We notice in equations 7.49 and 7.50 that the detection probabilities for accidental idler 1' photons in the secondary measurement arms not only depend on the properties of the integrated directional coupler structure, but also on the injected pump power and internal conversion probabilities for primary higher-order PDC processes. The latter both determine the photon number occupation densities $\rho'_{m'}$. We conclude a linear increase of $P^{\mathrm{acc}}_{\mathrm{i1}\rightarrow\mathrm{s2}}$ and $P^{\mathrm{acc}}_{\mathrm{i1}\rightarrow\mathrm{i2}}$ with the average photon number $\langle m'\rangle$ for small values of $\eta^{\mathrm{acc}}_{\mathrm{coupler,i1}}$.

Falsely directed idler 1' photons have also an impact on the coincidence detection probability of the secondary PDC process. These events occur on the one hand due to coincidences of a genuine secondary photon with at least one idler 1' photon. On the other hand, higher-order idler 1' photon contributions with $m' \geq 2$ could also survive the on-chip coupler and the filtering process as a spatio-spectrally separated pair. The probability that $k' \geq 2$ idler 1' photons of the first PDC process remain in the original waveguide behind the on-chip directional coupler is given by

$$P^{\mathrm{acc}}_{\mathrm{i1'}}\left(k'\geq 2\right) = \sum_{m'\geq k'\geq 2}^{\infty} \left[\binom{m'}{k'} \cdot (\eta^{\mathrm{acc}}_{\mathrm{coupler,i1'}})^{k'} \cdot (1-\eta^{\mathrm{acc}}_{\mathrm{coupler,i1'}})^{m'-k'}\right] \cdot \rho'_{m'}. \tag{7.51}$$

For small values $\langle m'\rangle \ll 1$ we have $\rho'_2 \gg \rho'_{m'}$, and the two-photon contributions will predominantly occupy the resulting photon number density vector. We calculate the accidentals' probability for the case that two out of two idler 1' photons survive the directional coupler and approximate $P^{\mathrm{acc}}_{\mathrm{i1'}}\left(k'\geq 2\right)$:

$$P^{\mathrm{acc}}_{\mathrm{i1'}}\left(m'=k'=2\right) = (\eta^{\mathrm{acc}}_{\mathrm{coupler,i1'}})^2 \cdot \rho'_2 \approx P^{\mathrm{acc}}_{\mathrm{i1'}}\left(k'\geq 2\right). \tag{7.52}$$

An accidental coincidence due to these two-photon states can only occur, if one of the idler 1' photon passes the signal 2 measurement arm and the other passes the idler 2 arm or vice versa. Neglecting loss of idler 1' photons on chip, the coincidence probability for this scenario is given by

$$P^{\mathrm{acc}}_{\mathrm{i1'}\rightarrow\mathrm{s2}\cap\mathrm{i2}}\left(k'\geq 2\right) \approx 2 \cdot \eta^{\mathrm{tot}}_{\mathrm{s2}}(\lambda_{\mathrm{i1'}}) \cdot \eta^{\mathrm{tot}}_{\mathrm{i2}}(\lambda_{\mathrm{i1'}}) \cdot P^{\mathrm{acc}}_{\mathrm{i1'}}\left(k'\geq 2\right) \tag{7.53}$$

With this approximation, we expect that accidental coincidences occur with the joint probability

$$\begin{aligned} P_{\text{coinc}}^{\text{acc,i1}'}\left(\text{s2} \cap \text{i2}, \langle m \rangle\right) &= P_{\text{i1}' \rightarrow \text{s2}}^{\text{acc}} \cdot P_{\text{i2}}(\langle m \rangle) \\ &\quad + P_{\text{i1}' \rightarrow \text{i2}}^{\text{acc}} \cdot P_{\text{s2}}(\langle m \rangle) \\ &\quad + P_{\text{i1}' \rightarrow \text{s2} \cap \text{i2}}^{\text{acc}}\left(k' \geq 2\right), \end{aligned} \tag{7.54}$$

which also includes coincidences of accidental idler 1' photons with noise contributions. Note that the approximation made in Eq. 7.52 denotes a simplification and neglects the impact of higher-order photon number contributions $m' \geq 3$ of idler 1' photons at increasing pump powers. Thus, we derive for the CAR of the secondary photon detection process a lower bound

$$CAR_{\text{PDC,2}} \leq \frac{P_{\text{coinc}}^{\text{corr}}\left(\text{s2} \cap \text{i2}, \langle m \rangle\right)}{P_{\text{coinc}}^{\text{acc,i1}'}\left(\text{s2} \cap \text{i2}, \langle m \rangle\right)}, \tag{7.55}$$

The CAR depends not only on the amount of idler 1' photons passing the measurement arms with $\eta_{\text{s2}}^{\text{tot}}(\lambda_{\text{i1}'})$ and $\eta_{\text{i2}}^{\text{tot}}(\lambda_{\text{i1}'})$, but we also notice that the coincidences-to-accidentals ratio decreases rapidly with stronger excitation of the higher-order mode combinations, which is expressed by an increase of $P_{\text{i1}'}^{\text{acc}}\left(k' \geq 2\right)$ in Eq. 7.52. This circumstance marks a fundamental limitation of an imperfect integrated device.

As an example, let us assume that the transmittances for idler 1' photons through the secondary measurement arms are $\eta_{\text{s2}}^{\text{tot}}(\lambda_{\text{i1}'}) = \eta_{\text{i2}}^{\text{tot}}(\lambda_{\text{i1}'}) = 0.001$ due to acceptable filtering at the fiber-optic CWDMs. Furthermore, let the on-chip coupling efficiency at idler 1' wavelengths into the bar waveguide be $\eta_{\text{coupler,i1}'}^{\text{acc}} = 0.05$. For a mean photon number per pulse at the first PDC output, $\langle m \rangle = \langle m' \rangle = 0.25$, the one-photon contributions occupy around $\rho_1' = 0.195$ and the two-photon components around $\rho_2' = 0.024$ of the photon number density vector behind the directional coupler. We neglect other higher-order photon number contributions of the parasitic idler 1' and calculate for lower bound of the accidental coincidences probability using Eq. 7.54:

$$P_{\text{coinc}}^{\text{acc,i1}'}\left(\text{s2} \cap \text{i2}, \langle m \rangle\right) \geq (2.15 \pm 0.5) \cdot 10^{-10}$$

per detection time window, and with Eq.7.55 we approximate the upper bound for CAR, i. e.,

$$CAR_{\text{PDC,2}} \leq 6.2 \pm 1.5.$$

This relatively low CAR value underlines the strict requirements for the filtering of parasitic idler 1' photons, but also the importance of selective coupling of the pump light in order to prevent higher-order mode excitation. The latter significantly reduces the mean photon number per pulse $\langle m' \rangle$, which has an inverse quadratic influence on CAR.

Another way to overcome the fidelity limitations is to provide the suppression of higher-order PDC processes in the first stage by waveguide engineering techniques. Linearly tapered waveguides, for example, can prevent higher-order pump modes at

532 nm to be guided. Likewise, tapering our waveguides between the on-chip directional coupler and the secondary poled region can provide that signal 1 photons are guided only in the fundamental spatial mode, whereas higher-order spatial modes at parasitic signal 1' wavelengths and also telecom photons from the first PDC process will scatter to the substrate due to the changed cut-off conditions. These future technological countermeasures are expected to remove the necessity for narrow-band filtering in the signal 2 and idler 2 measurement arms.

7.2.2.6. Three-fold coincidence probabilities

Although the coincidental detection of photon pairs generated in the second PDC process (provided that values of $SNR_{\mathrm{PDC,2}}$ and $CAR_{\mathrm{PDC,2}}$ are sufficiently high) can be seen as the sufficient condition to verify the generation of photon triplets, the necessary condition is fulfilled only if we also detect the corresponding idler 1 photon in its dedicated measurement arm.

We rely on the detection scheme in Fig. 7.11 and 7.13, where all detector outcomes are fed into a multi-channel time-tagging unit, and we post-select the three-fold coincidences (see next Section 7.2.3). In this configuration, we benefit from having access to accidental events by analyzing coincidences between neighboring pulses, which appear at multiple integers of the inverse repetition time of the pulsed pump laser.

The three-fold coincidence probability of detecting time-correlated photons, including the genuine photon triplets, is given by

$$\begin{aligned} P\left(\mathrm{i2} \cap \mathrm{s2} \cap \mathrm{i1}, \langle m \rangle\right) &= \eta_{\mathrm{i2}}^{\mathrm{tot}} \cdot \eta_{\mathrm{s2}}^{\mathrm{tot}} \qquad (7.56) \\ &\quad \times \sum_{m \geq 1}^{\infty} m \cdot P_{\mathrm{PDC,2}} \cdot \left(1 - P_{\mathrm{PDC,2}}\right)^{m-1} \cdot \left[1 - \left(1 - \eta_{i1}\right)^{m}\right] \cdot \rho_m \\ &\approx \eta_{\mathrm{i2}}^{\mathrm{tot}} \cdot \eta_{\mathrm{s2}}^{\mathrm{tot}} \cdot P_{\mathrm{PDC,2}} \cdot \sum_{m \geq 1}^{\infty} m \cdot \left[1 - \left(1 - \eta_{i1}\right)^{m}\right] \cdot \rho_m. \qquad (7.57) \end{aligned}$$

Here, we also take the low values of $P_{\mathrm{PDC,2}} \ll 1$ into account. However, the photon-triplet detection probability is approximately given by

$$P\left(\mathrm{i2} \cap \mathrm{s2} \cap \mathrm{i1}, m = 1\right) \approx \eta_{\mathrm{i2}}^{\mathrm{tot}} \cdot \eta_{\mathrm{s2}}^{\mathrm{tot}} \cdot P_{\mathrm{PDC,2}} \cdot \eta_{i1} \cdot \rho_1. \qquad (7.58)$$

Thus, we can rewrite equation 7.57 as

$$\begin{aligned} P\left(\mathrm{i2} \cap \mathrm{s2} \cap \mathrm{i1}, \langle m \rangle\right) &\approx P\left(\mathrm{i2} \cap \mathrm{s2} \cap \mathrm{i1}, m = 1\right) \qquad (7.59) \\ &\quad \times \left\{ 1 + \sum_{m \geq 2}^{\infty} m \cdot \left[1 - \left(1 - \eta_{i1}\right)^{m}\right] \cdot \frac{\rho_m}{\rho_1} \right\}, \end{aligned}$$

if we neglect noise contributions and assume, again, $\left(1 - P_{\mathrm{PDC,2}}\right)^{m-1} \approx 1$. We notice the influence of higher-order photons on the overall three-fold coincidence probability $P\left(\mathrm{i2} \cap \mathrm{s2} \cap \mathrm{i1}, \langle m \rangle\right)$. Thus, we calculate the factor $r\left(\langle m \rangle\right)$ as the ratio of three-fold

coincidences, stemming from $\langle m \rangle$-photon contributions, and $(m = 1)$-photon events using equations 7.58 and 7.59:

$$\begin{aligned} r\left(\langle m \rangle\right) &= \frac{P\left(\mathrm{i2} \cap \mathrm{s2} \cap \mathrm{i1}, \langle m \rangle\right)}{P\left(\mathrm{i2} \cap \mathrm{s2} \cap \mathrm{i1}, m = 1\right)} \\ &\approx 1 + \sum_{m \geq 2}^{\infty} m \cdot \left[1 - (1 - \eta_{i1})^m\right] \cdot \frac{\rho_m}{\rho_1}. \end{aligned} \tag{7.60}$$

This indicates that higher-order photons in the first PDC stage have a nonlinear impact on the three-fold coincidences. We note that the ratio $\frac{\rho_m}{\rho_1}$ is linear only for $m \equiv 2$. For $m \geq 3$ we expect quasi-linear behavior only for low mean photon numbers $\langle m \rangle \ll 1$, whereas the higher-order photon impact is super-linear otherwise.

The three-fold coincidence probability increase is depicted in Fig. 7.17, where we plotted $r\left(\langle m \rangle\right)$ color-coded and dependent on the mean photon number $\langle m \rangle$ and the primary idler arm efficiency η_{i1}. We deduce from the adjacent graphs that, on the one hand, the idler 1 arm efficiency impacts $r\left(\langle m \rangle\right)$ quasi-linearly for $\langle m \rangle \approx 0.25$. On the other hand, $r\left(\langle m \rangle\right)$ increases super-linearly with $\langle m \rangle$, which limits the scalability of a pulsed source fundamentally in terms of the injected pump power. Note that the inverse of $r\left(\langle m \rangle\right)$ is a measure for the ratio, with which genuine photon triplets contribute to the overall three-fold coincidence probability. This ratio decreases accordingly with increasing pump powers at the cascaded PDC source input. Specifically for $\langle m \rangle = 0.25$ we deduce

$$r\left(\langle m \rangle\right) = 1.30 \pm 0.07,$$

which means that the measurable three-fold coincidence rate will be around 30% higher than the genuine photon-triplet rate. Inversely, only $\sim 77\%$ of the three-fold coincidences can be expected to be genuine photon triplets. Consequently, we treat three-fold coincidences, which involve higher-order photon contributions of the first PDC process, as accidentals.

We have experimental access to the approximate value of $r\left(\langle m \rangle\right)$ by analyzing three-fold coincidences, which include neighboring pulses of the idler 1 detection at multiple integers of $\tau_{\mathrm{rep}} = R_{\mathrm{rep}}^{-1}$. The probability of detecting three-fold coincidences in two consecutive pulses is equal to the probability of registering a three-fold coincidence between a secondary photon pair and a two-photon idler 1 pulse. Thus, for mean photon numbers $\langle m \rangle \leq 1$, where the higher-order photon states are dominated by two-photon contributions, we can approximate the accidentals in this manner. Note that this method is only possible in pulsed systems, whereas cw realizations would have to rely either directly on photon-number-resolving detectors, or on measurements of the second-order autocorrelation function of primary idler photons.

We calculate the achievable coincidences-to-accidentals ratio for three-fold coinci-

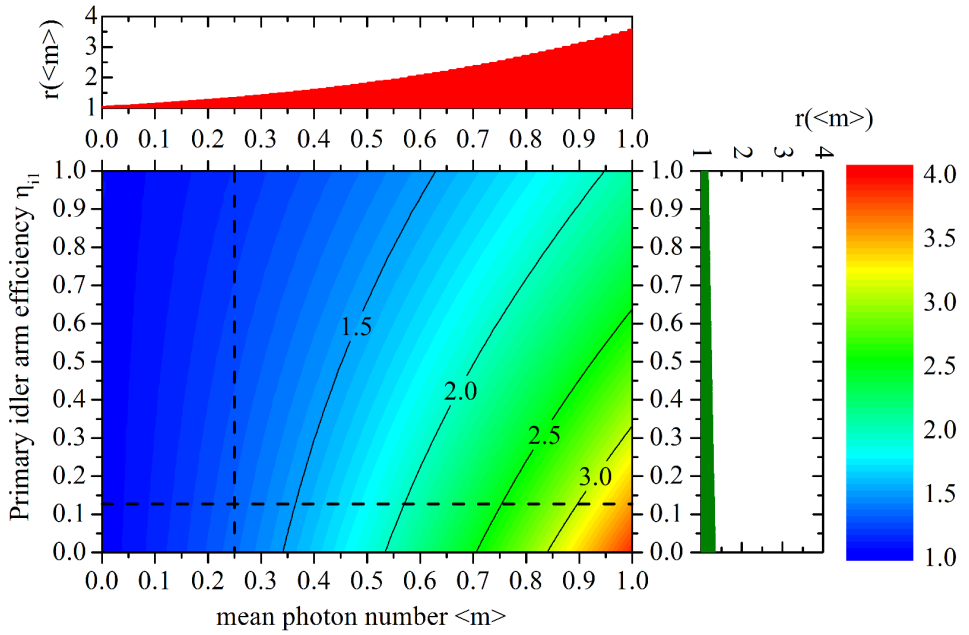

Figure 7.17.: Increase of the three-fold coincidence click probability dependent on the mean photon number and the idler arm efficiency of the primary PDC stage. The adjacent graphs show the individual dependencies for the dotted cross-cut lines, which represent reasonable values of η_{i1} and $\langle m \rangle$. In general, we notice a nonlinear dependence of $r\left(\langle m \rangle\right)$ on both axis parameters, which represents a fundamental limitation on the generation and verification of genuine photon triplets in a pulsed system in conjunction with binary detectors.

dence measurements as

$$\begin{aligned} CAR_{3-\text{fold}} &= \frac{P\left(\text{i2} \cap \text{s2} \cap \text{i1}, m = 1\right)}{\sum_{m \geq 2}^{\infty} P\left(\text{i2} \cap \text{s2} \cap \text{i1}, m\right)} \\ &= \frac{1}{r\left(\langle m \rangle\right) - 1}, \end{aligned} \tag{7.61}$$

which does not include noise-related contributions. The coincidences-to-accidentals ratio approaches values of $CAR_{3-\text{fold}} < 1$ for $r\left(\langle m \rangle\right) > 2$. This means that less than half of the three-fold coincidences stem from genuine photon triplets for that case.

We estimate $CAR_{3-\text{fold}} \approx 3.3$ for reasonably low pump powers, i. e., $\langle m \rangle = 0.25$, and an idler 1 arm efficiency of $\eta_{i1} = 0.129$. In Fig. 7.18 we plot the dependencies of $CAR_{3-\text{fold}}$ on the mean photon number as well as on the Klyshko efficeincy of the idler 1 arm. We see that the impact of increasing mean photon numbers is dramatic: At arm efficiencies of $\eta_{i1} = 0.129$, the coincidences-to-accidentals ratio drops rapidly from around 100 to only around 0.4 in the range of $0.01 \leq \langle m \rangle \leq 1.0$. At $\langle m \rangle \approx 0.6$

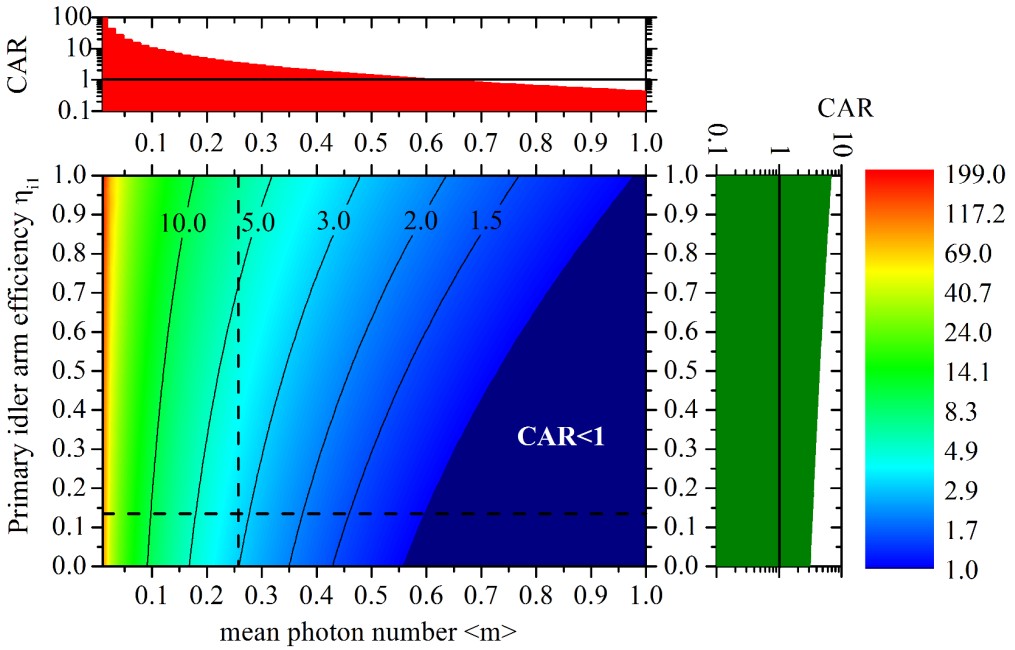

Figure 7.18.: Decay of the coincidences-to-accidentals ratio dependent on the mean photon number and the idler arm efficiency of the primary PDC stage. The adjacent graphs show the individual dependencies for the dotted cross-cut lines, which represent $\eta_{i1} = 0.129$ and $\langle m \rangle = 0.25$. We notice the rapid decrease of CAR with increasing mean photon number $\langle m \rangle$. This fundamental limitation prohibits the scaling of photon-triplet generation by increasing the pump power.

we notice that CAR value crosses the break-even point, which means that we can expect as many accidental three-fold coincidences as genuine photon triplets for the given idler 1 arm efficiency. It is also obvious that with higher arm transmittances the coincidences-to-accidentals ratio increases. However, this positive influence is less pronounced as the impact of lower mean photon numbers per pulse behind the first PDC stage.

Now the question arises: how many genuine photon-triplet states we can expect to measure in our setup? From the approximation in equation 7.58 and the measured Klyshko efficiencies and internal PDC probabilities given in Tab. 7.1, we derive for the expectable photon-triplet rate:

$$\begin{aligned} R_{\text{triplet}} &= P\left(\text{i2} \cap \text{s2} \cap \text{i1}, m = 1\right) \cdot R_{\text{rep}} \\ &= \eta_{\text{i2}}^{\text{tot}} \cdot \eta_{\text{s2}}^{\text{tot}} \cdot P_{\text{PDC},2} \cdot \eta_{\text{i1}} \cdot \rho_1 \cdot R_{\text{rep}} \\ &= (4.8 \pm 0.3)\,\text{h}^{-1}, \end{aligned} \tag{7.62}$$

where a reasonable mean photon number of $\langle m \rangle = 0.25$ per optical pulse in the first

PDC process as well as a pump laser repetition rate of $R_{\mathrm{rep}} = 10\,\mathrm{MHz}$ are included. Note that the photon-number-density-matrix element depends on the chosen mean photon number, i. e. $\rho_1 = \rho_1(\langle m \rangle)$.

From the result in equation 7.62 and the individual measurement arm efficiencies, we derive a photon-triplet generation rate inside the monolithic model system of $R^{\mathrm{gen}}_{\mathrm{triplet}} \sim 1765\,\mathrm{h}^{-1}$. The theoretical generation rate is dependent on the repetition rate of the pump laser and the internal conversion efficiency of the secondary PDC process.

Another method of benchmarking the photon-triplet generation process is to define a success probability, which relates the verified photon-triplet number in the whole measurement time to the number of pulses within that duration. As an example, we divide the expected photon-triplet generation rate in Eq. 7.62 to the number of pulses per hour for our 10 MHz pump laser. Given these values, we end up at the success probability per pump pulse of

$$\begin{aligned} P^{\mathrm{succ}}_{\mathrm{triplet}} &= \frac{R_{\mathrm{triplet}}\left[\mathrm{h}^{-1}\right]}{R_{\mathrm{rep}} \cdot 3600\,\mathrm{s}} \\ &= (1.11 \pm 0.44) \cdot 10^{-10} \end{aligned} \tag{7.63}$$

This figure of merit includes all experimental imperfections as well as the internal PDC generation probabilities of both PDC stages. In that manner, $P^{\mathrm{succ}}_{\mathrm{triplet}}$ is a valuable measure for the efficiency and scalability of the pulsed cascaded PDC source as well as for the experimental implementation.

We assume picosecond pump pulses and expect the three-fold coincidences to be distributed over a temporal width of $\sim 1\,\mathrm{ns}$, which includes the joint timing jitter of the detection apparatus. By analogy to the case of secondary photon pair coincidences, as discussed in Section 7.2.2.5, we derive the signal-to-noise ratio $SNR_{3-\mathrm{fold}}$ by relating the probability of generating three-fold coincidences by cascaded PDC, i. e., $P(\mathrm{i2} \cap \mathrm{s2} \cap \mathrm{i1}, \langle m \rangle)$, to the probability of detecting noise-contributed three-fold coincidences. A valid approximation of $SNR_{3-\mathrm{fold}}$ includes three-fold coincidences, where the idler 1 detection events (PDC photons and noise contributions, see equation 7.25) as well as the two-fold coincidences of the secondary photon detection are involved:

$$\begin{aligned} P^{\mathrm{noise}}_{3-\mathrm{fold}}(\mathrm{i2} \cap \mathrm{s2} \cap \mathrm{i1}, \langle m \rangle) &\approx P^{\mathrm{corr}}_{2-\mathrm{fold}}(\mathrm{s2} \cap \mathrm{i2}, \langle m \rangle) \cdot p_{\mathrm{noise,i1}} \\ &\quad + P^{\mathrm{noise}}_{2-\mathrm{fold}}(\mathrm{s2} \cap \mathrm{i2}, \langle m \rangle) \cdot P_{\mathrm{i1}}(\langle m \rangle) \\ &= \eta^{\mathrm{tot}}_{\mathrm{s2}} \eta^{\mathrm{tot}}_{\mathrm{i2}} \cdot P_{\mathrm{PDC,2}} \cdot \langle m \rangle \cdot p_{\mathrm{noise,i1}} \\ &\quad + P^{\mathrm{noise}}_{2-\mathrm{fold}}(\mathrm{s2} \cap \mathrm{i2}, \langle m \rangle) \cdot \sum_{m \geq 0}^{\infty} \left[1 - (1 - \eta_{i1})^m\right] \cdot \rho_m \\ &\approx P^{\mathrm{noise}}_{2-\mathrm{fold}}(\mathrm{s2} \cap \mathrm{i2}, \langle m \rangle) \cdot \sum_{m \geq 0}^{\infty} \left[1 - (1 - \eta_{i1})^m\right] \cdot \rho_m . \end{aligned} \tag{7.64}$$

The approximations in Eq. 7.64 are valid for $SNR_{\mathrm{PDC,2}} \cdot p_{\mathrm{noise,i1}} \ll \eta_{i1}$ and $P^{\mathrm{noise}}_{2-\mathrm{fold}}(\mathrm{s2} \cap \mathrm{i2}, \langle m \rangle) \ll P^{\mathrm{corr}}_{2-\mathrm{fold}}(\mathrm{s2} \cap \mathrm{i2}, \langle m \rangle) \ll P_{\mathrm{i1}}(\langle m \rangle)$, which is a realistic case

for our measurement apparatus. For the upper bound of the signal-to-noise ratio of three-fold coincidences, we calculate

$$\begin{aligned} SNR_{3-\text{fold}} &\leq \frac{P\left(\text{i2} \cap \text{s2} \cap \text{i1}, \langle m \rangle\right)}{P_{3-\text{fold}}^{\text{noise}}\left(\text{i2} \cap \text{s2} \cap \text{i1}, \langle m \rangle\right)} \\ &\approx \frac{P\left(\text{i2} \cap \text{s2} \cap \text{i1}, \langle m \rangle\right)}{P_{2-\text{fold}}^{\text{noise}}\left(\text{s2} \cap \text{i2}, \langle m \rangle\right) \cdot P_{\text{i1}}\left(\langle m \rangle\right)}. \end{aligned} \tag{7.65}$$

We see that $SNR_{3-\text{fold}}$ depends strongly on the probability of noise-related two-fold coincidences and, in turn, on the detector properties as well as on the thermal conditions, i. e., the emitted blackbody radiation of the integrated waveguide device.

It is important to mention that $SNR_{3-\text{fold}}$ does not represent the signal-to-noise ratio of genuine photon triplets with respect to the noise-related background, but it depends on the overall three-fold coincidence probability. Thus, it is highly recommended to verify the generation of photon triplets by post-processing analysis of the signal-to-noise ratio *and* the coincidences-to-accidentals ratio in pulsed cascaded parametric down-conversion processes.

In summary we have studied and analyzed pulsed cascaded parametric down-conversion based on our monolithically integrated device as a model system. For our real-world scenario, we have derived the expected two- and three-fold coincidence probabilities for the photon-triplet detection process, for which we have included transmission and detection inefficiencies as well as noise contributions.

Taking the experimental apparatus in Fig. 7.13 into account, we predict photon-triplet generation rates of $R_{\text{triplet}} \sim 4$ per hour, when the mean photon number of the primary PDC stage is adjusted to $\langle m \rangle = 0.25$ at pump repetition rates of 10 MHz. The impact of uncorrelated noise contributions to the signal-to-noise ratio of three-fold coincidences has been predicted, and we have inferred that a careful analysis of higher-order photon contributions is as essential as the estimation of higher-order PDC processes in the first stage.

7.2.3. Experimental verification of low-noise photon-triplet generation

Now that we have studied the photon triplet generation process in our cascaded PDC source intensively, we perform measurements and present the results in this section. We expect that higher-order photon contributions of the first PDC process will not only influence the measurable two- and three-fold coincidences, but will also lead to bad signal-to-noise and coincidences-to-accidentals ratios, we have to chose appropriate pump power levels. We calculate the mean photon number per pulse by rearranging Eq. 7.17 and get

$$\langle m \rangle = \frac{\mathbf{P}_{\text{p}} \cdot \lambda_{\text{p}}}{R_{\text{rep}} \cdot h \cdot c} \cdot P_{\text{PDC},1}. \tag{7.66}$$

For $\mathbf{P}_{\text{p}} = 10\,\mu\text{W}$ of fundamental pump power at $\lambda_{\text{p}} = 531.75\,\text{nm}$, we yield $\langle m \rangle = 0.215 \pm 0.005$. This value is slightly below $\langle m \rangle = 0.25$, which we assumed in our

studies in the section above. We can expect to measure slightly lower photon triplet rates and signal-to-noise ratios. However, higher values of $CAR_{3-\mathrm{fold}} \approx 4.0 \pm 0.2$ can be expected.

We stabilize our photon-triplet source to the expected optimal point of operation, $\theta = (163.8 \pm 0.1)°\mathrm{C}$, which provides us with signal 1 and idler 1 photons at wavelengths of $\lambda_{\mathrm{s1}} = (790.3 \pm 0.04)\,\mathrm{nm}$ and $\lambda_{\mathrm{i1}} = 1625\,\mathrm{nm}$, respectively. Furthermore, we achieve spectrally non-degenerate photon pair emission in the second PDC stage. The signal 2 and idler 2 photon wavelengths peak at the central transmission wavelengths of our implemented CWDM fiber-filters at $\lambda_{\mathrm{s2}} = 1551\,\mathrm{nm}$ and $\lambda_{\mathrm{i2}} = 1611\,\mathrm{nm}$, respectively.

The photon-triplet generation measurements are performed for a duration of $\tau_{\mathrm{meas}} = 11.5\,\mathrm{h}$, and we collect the individual detection events with a time-tagging module (TTM) (TTM8000, Austrian Institute of Technology). The data acquisition system offers up to eight inputs, which would allow us to include the pump laser trigger for noise count suppression. This requires high data transfer rates, which the TTM is also able to process. However, for the long measurement durations in our experiments, high data rates also mean huge amounts of data to be stored and post-processed. Thus, we do not take the laser-trigger signal into account, but restrict ourselves to the three detector inputs.

7.2.3.1. Long-term stability of source and experimental implementation

During the measurements we logged the single count rates of the idler 1 photon detection in intervals of 10 seconds. These rates (including noise counts) represent not only directly the generation of primary PDC photon pairs, but also indirectly their susceptibility to thermal drifts of the setup: if the pump coupling changes due to temperature fluctuations, the phasematching conditions for both processes will change accordingly and the mutual compatibility of our cascaded PDC process might suffer from this. The idler 1 count rate will also change as a consequence. Hence, the drift of the primary idler count rates over time is a direct measure of the thermal stability and robustness of our device against environmental changes.

In Fig. 7.19 (left) we plot the relative change of the idler 1 count rate with respect to its average value over the full measurement duration. We recognize that, in conjunction with the histogram (right), the single count rate deviates by only $\sigma = 0.497\%$ and no more than $\pm 2\%$ from the mean value. This means that our integrated device as well as the measurement setup is extremely stable over longer terms, and the triplet-generation process benefits from the monolithic source's ruggedness against thermal fluctuations.

7.2.3.2. Data analysis strategy

Our time-tagging module collects a string of (absolute) time stamps with temporal resolution of $\tau_{\mathrm{bin}} 82.3045\,\mathrm{ps}$, for which any of the addressed input channels registers

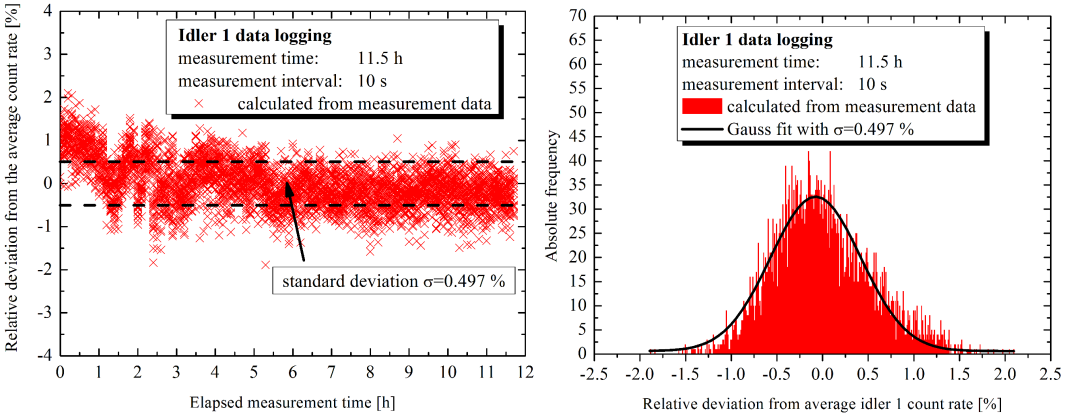

Figure 7.19.: The relative change of the single idler 1 count rate with respect to its mean value **(left)** is lower than 2% over 11.5 hours of measurement time, which indicates a high degree of long-term stability for our source and experimental implementation. After two hours there are practically no drifts due to thermal fluctuations. The histogram **(right)** exhibits Gaussian-like shape with a standard deviation of less than $\sigma = 0.5\%$, which means that the relative count rate changes happen solely due to the statistical fluctuations of our Poisson-distributed idler 1 photon generation.

the rising edge of a voltage pulse. In principle, each time stamp is encoded as a 60 bit integer value, which means that two consecutive time stamps have a relative time difference equivalent to the temporal resolution. As soon as one of our binary detector fires due to a photon or a noise contribution, the events will be addressed in terms of a time bin. A coincidence is recorded, if two or three detection events at different input channels occur in the same or at least in nearest-neighbor time bins. Our whole data analysis relies on the temporal information of the detectors' click events.

We compensated the optical and electronic delays in our setup such that there is practically no relative arrival time difference between the three electronic detector signals stemming from genuine photons of the triplet generation process. This means that the time stamps for idler 1, signal 2 and idler 2 photon-detection events have either the same 60 bit encoded value or they differ by only few bits.

In order to verify the generation of photon triplets, we developed a data analysis strategy which takes the different single click probabilities at the three detectors into account. First, we analyze the data for time stamps, where the signal 2 detector clicks, because the detection probability as well as the count rate are the lowest in our setup. This significantly reduces the computational effort for the search for coincidences with click events in the remaining detectors.

For each signal 2 detection event at arrival times τ_2, we define a coincidence window of ~ 600 ns around the absolute timing information of these events. We chose this large temporal width, because it includes also ± 3 neighboring pulses in our

10 MHz pulsed system. Within the coincidence window, we search for events from the idler 2 detector at times τ_3, which shows the second lowest click probability. For the relative times of arrival $\tau_3 - \tau_2$, corresponding to the time bin number differences, we register the coincident events of signal 2 and idler 2 detection. Doing so for the whole set of data provides us with an indicator for photon-triplet generation, because two-fold coincidences in the secondary PDC process denote the necessary condition for it as explained in Sec. 7.2.2.5.

For the full proof of having generated genuine photon triplets, we also define another coincidence time window of of ~ 600 ns around the absolute timings of the two-fold coincidences of signal 2 and idler 2 detection events. Within this temporal area, we search for detection events in the remaining idler 1 arm at arrival times τ_1 and, thus, get three-fold coincidences dependent on the relative arrival time $\tau_1 - \tau_2 = \tau_1 - \tau_3$ as the general outcome. The data format has now the structure of a matrix, where the individual matrix elements represent the two relative arrival times $\tau_3 - \tau_2$ and $\tau_1 - \tau_2$, respectively, whereas the values of the matrix elements stand for the number of three-fold coincidences.

7.2.3.3. Experimental results and discussion

With our developed data analysis strategy, we are able to perform the photon-triplet verification in a a pseudo-heralded manner, because we make use of individual detection (and noise) events in order to find two- and three-fold coincidences efficiently within our 11.5 hours of measurement data.

Figure 7.20 shows the measured and analyzed coincidences between signal 2 and idler 2 detection events dependent on the relative arrival time $\tau_3 - \tau_2$. We find a signature for temporal correlations at around $\tau_3 - \tau_2 \approx -9$ ns in the raw data (top graph). From a detailed view on the peak we infer a temporal width of the correlated events of $\Delta(\tau_3 - \tau_2) = (1.20 \pm 0.08)$ ns. Thus, we conclude that merging of temporal bins offers a valuable tool for the increase of visibility, because we have to consider timing-jitter effects of the detectors and electronics. Likewise, we notice a small peak at around $\tau_3 - \tau_2 \approx -109$ ns, which indicates the appearance of accidental two-fold coincidences of signal 2 photons with photons from the neighboring idler 2 pulses.

In the left graph of Fig. 7.21 we combine the measurement data of eight and sixteen temporal bins, respectively. While the eight-fold merged data still shows two bins containing time-correlated coincidence events, the 16-fold merged data has only one peak at the expected relative time delay. The corresponding bin width of $\tau_{16-\mathrm{bin}} = 1.3168$ ns matches the temporal peak width $\Delta(\tau_3 - \tau_2)$ very well, and we conclude that 16-fold merging is a good option to visualize and analyze the time-correlated coincidence events. Note that the signal-to-noise ratio in Fig. 7.21 appears to be higher for the eight-fold merged data set. However, we rely on the 16-fold merged data, since the corresponding temporal bin width includes all jitter effects with higher confidence.

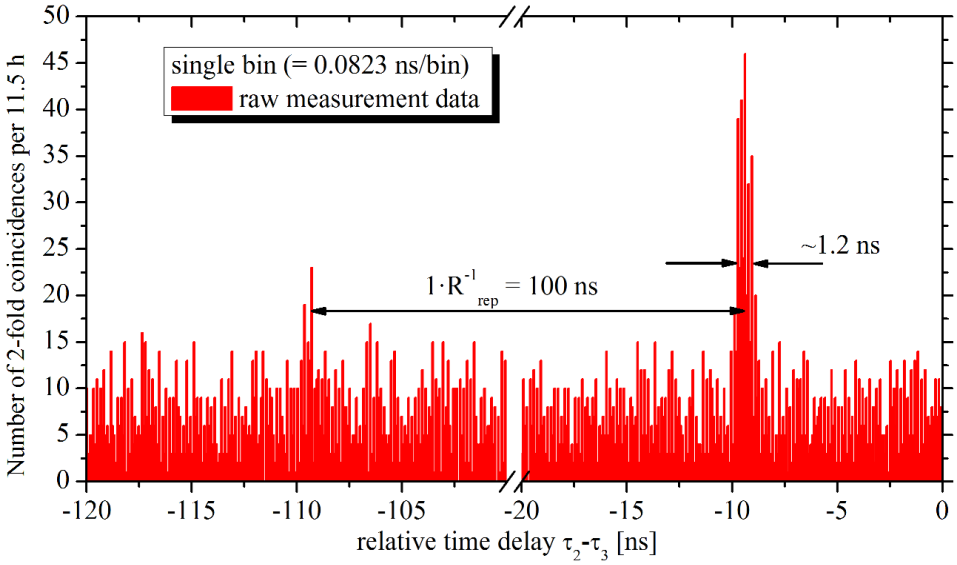

Figure 7.20.: The two-fold coincidences of signal 2 and idler 2, dependent on the relative arrival-time and measured over 11.5 hours, show a clear signature of temporal correlations in the raw measurement data at $\tau_3 - \tau_2 \approx -9\,\mathrm{ns}$. From the temporal width of the peak, we conclude that 16-fold time binning of the data includes the joint timing jitter of the detectors and electronics. At multiple integers of the laser repetition time, e. g. at $\tau_3 - \tau_2 \approx -109\,\mathrm{ns}$, we identify accidental two-fold coincidences between consecutive pulses.

From the statistical analysis of the full data set, which includes not only one neighboring pulse, we deduce that the time-correlated peak overcomes the surrounding noise-related coincidences by a factor of $SNR'^{\mathrm{exp}}_{\mathrm{PDC},2} = 2.99 \pm 0.30$ as shown in the right graph in Fig. 7.21. This value is significantly lower than the theoretical value, $SNR_{\mathrm{PDC},2} = 1117$, which could be expected according to Eq. 7.48. We might try to explain this discrepancy with the temporal windows of 1 ns, which we defined the noise count probabilities of the signal 2 and idler 2 detectors for in Tab. 7.1. But taking the slightly larger bin width, $\tau_{16-\mathrm{bin}} = 1.3168\,\mathrm{ns}$ used in our data analysis, into account does not bridge the gap between the theoretical and the experimentally determined SNR values. By comparing the absolute number of the 16-bin two-fold coincidences in Fig. 7.21 with our expectations for a mean photon number of $\langle m \rangle = 0.25$ per pulse behind the first PDC stage, we see that we have generated $R^{\mathrm{corr}}_{2-\mathrm{fold}} = 29.4 \pm 5.4$ coincidences per hour at a mean photon number of $\langle m \rangle = 0.215$ per pulse behind the first PDC stage. Our prediction in Eq. 7.46 is only a factor of 1.62 higher, and it also does not explain the discrepancy between theoretical and experimental SNR for two-fold coincidences.

We do not measure any significant changes in the single count rates of signal 2 and idler 2, if the pump laser is blocked. Thus, we can also rule out the influence of electronic cross-talk in our time-tagging module, which would lead to noise count

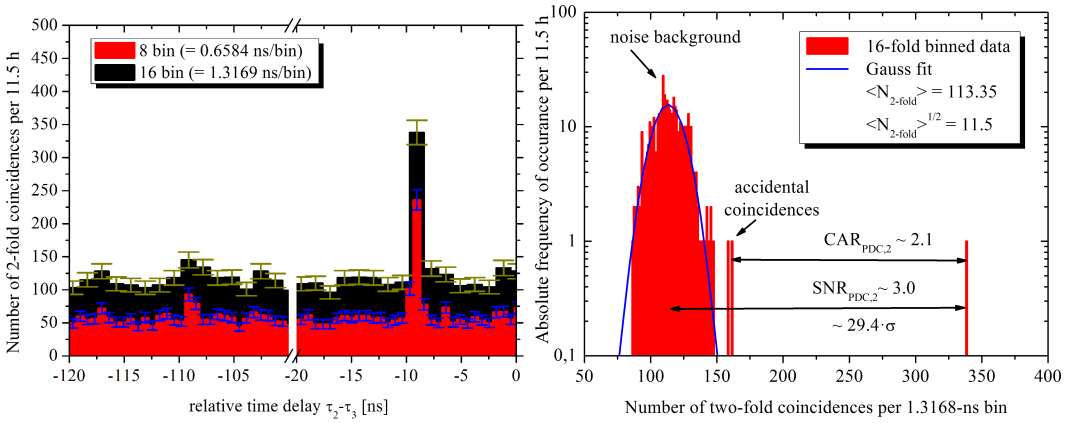

Figure 7.21.: The eight- and 16-fold merging of the 0.0823 ns-wide time-bins of the time-tagging module increases the visibility of the time-correlated peak over the noise background and the accidental coincidences (left). The statistical evaluation of the 16-fold merged data shows that our correlated peak is more than 29 standard deviations above the average noise background (right). We also deduce a coincidences-to-accidentals ratio of $CAR^{\mathrm{exp}}_{\mathrm{PDC},2} \sim 2.1$ from the average number of accidental coincidences of the 16-fold merged data as well as a signal-to-noise ratio of $SNR^{\mathrm{exp}}_{\mathrm{PDC},2} \sim 3.0$.

probabilities different to those assumed in our theoretical estimation. Instead, we suspect the huge discrepancy between the theoretically and experimentally determined $SNR_{\mathrm{PDC},2}$ to be intrinsic to our data analysis strategy: per detected signal 2 photon we scan a 600 ns-wide coincidence window for events in the idler 2 detector in order to identify also coincidences with neighboring pulses. Due to the fact that we do not have an absolute timing reference, such as an additional electronic laser trigger, we count the noise many-fold more often than in our theoretical model, where we assumed only $\tau_{\mathrm{coinc}} = 1\,\mathrm{ns}$ in our calculations. Thus, our data analysis can be seen as an intermediate between pulsed and continuous-wave coincidence counting. Dividing the theoretically predicted noise count probability for the idler 2 detection by the factor of $600\,\mathrm{ns}/1.317\,\mathrm{ns} = 456$ yields a corrected theoretical signal-to-noise ratio of $SNR_{\mathrm{PDC},2} = 2.45 \pm 0.11$, which is closer to our experimentally determined value. However, a detailed analysis of the impact of the coincidence time window on the noise-related two-fold coincidence probability could explain the gap between theory and experiment in future work.

We determine the impact of higher-order mode contributions in the first PDC process, which is introduced by mislead and improperly filtered idler 1 photons in the secondary photons' detection arms, by calculating the coincidences-to-accidentals $CAR_{\mathrm{PDC},2}$ ratio for the two-fold coincidences. We calculate the accidentals as the average number of two-fold coincidences appearing in neighboring (non-correlated)

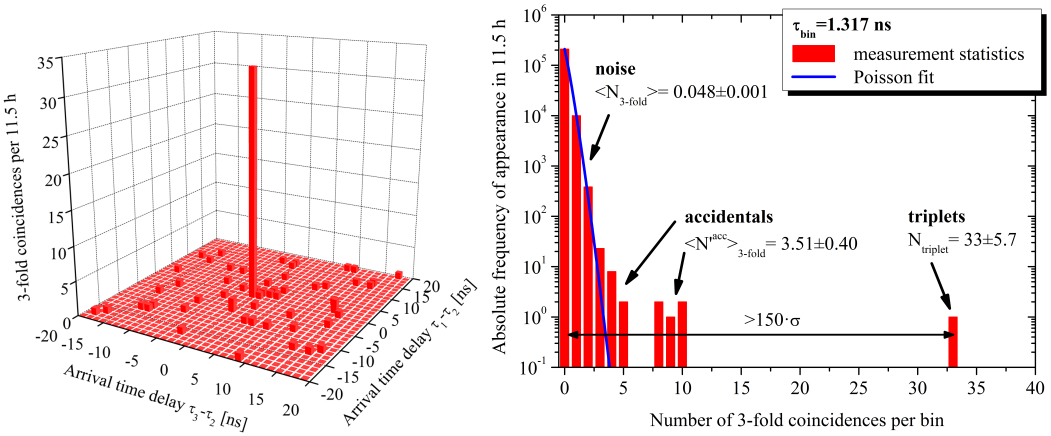

Figure 7.22.: The 3D graph shows the three-fold coincidences at around zero relative time delays between the three detector events. We see a clear signature of time-correlated coincidences in the center of the graph, which indicates genuine photon-triplet generation (left). The histogram (right) shows the absolute frequency of certain bin occupation by three-fold coincidences. We see that only one 16-fold merged data point carries 33 triple coincidences, whereas the noise background follows Poisson statistics very well. We deduce that the time-correlated bin overcomes the noise background by over 150 standard deviations. Only a small amount of the whole set of $\sim$ 210000 bins exhibit also higher absolute frequencies of occupation, which we suspect to stem from accidental three-fold coincidences with neighboring peaks.

peaks and get $CAR^{\mathrm{exp}}_{2-\mathrm{fold}} = 2.11 \pm 0.03$.

Analyzing the dataset for three-fold coincidences yields the left graph shown in Fig. 7.22, which visualizes the number of three-fold coincidences dependent on the relative arrival times $\tau_3 - \tau_2 = (0 \pm 20)$ ns and $\tau_1 - \tau_2 = (0 \pm 20)$ ns. We identify a clear indication for time-correlated triple coincidences around zero delays. Specifically, the absolute number of three-fold coincidences per 11.5 hours of measurement time is $N^{\mathrm{corr}}_{3-\mathrm{fold}} = 33 \pm 5.8$. This corresponds to a three-fold coincidence rate of $R^{\mathrm{exp}}_{3-\mathrm{fold}} = 2.9 \pm 1.7\,\mathrm{h}^{-1}$ and is already close to the predicted value of $R_{\mathrm{triplet}} = 4.8 \pm 0.3\,\mathrm{h}^{-1}$ in Eq. 7.62. As mentioned before, we assumed a slightly higher mean photon number in our theoretical calculations.

The rate $R^{\mathrm{exp}}_{3-\mathrm{fold}}$ might also contain three-fold coincidences stemming from higher-order photon contributions and/or from higher-order mode combinations of the first PDC process. Thus, we estimate the impact of these contributions by performing a statistical analysis for the full dataset including neighboring pulses. The resulting histogram is shown in the right graph of Fig. 7.22. We see that the Poisson fit curve matches the measurement data very well, and we calculate a mean number of three-fold coincidences per 11.5 hours of $\langle N_{3-\mathrm{fold}} \rangle = 0.048 \pm 0.004$ with the standard

deviation $\sigma^{\mathrm{acc}}_{3-\mathrm{fold}} = \sqrt{\langle N_{3-\mathrm{fold}} \rangle} = 0.283$. From these values we determine the signal-to-noise ratio for the three-fold coincidences, $SNR^{\mathrm{exp}}_{3-\mathrm{fold}} = 687 \pm 138$, which means that the number of three-fold coincidences overcomes the noise-related background by over $150 \cdot \sigma^{\mathrm{acc}}_{3-\mathrm{fold}}$. This underlines the strength of correlated photons over stochastically independent noise contributions: even if individual noise count probabilities dominate the single detection events as in our case, coincidences are obviously the method of choice for using and verifying the PDC photons' temporal correlations.

From the graph we also infer the overall coincidences-to-accidentals ratio by calculating the average number of accidental coincidence events $\langle N'^{\mathrm{acc}}_{3-\mathrm{fold}} \rangle = 3.51 \pm 0.40$ from all 41 neighboring peaks in the considered time windows of 600 ns × 600 ns. We get for the coincidences-to-accidentals ratio $CAR'^{\mathrm{exp}}_{3-\mathrm{fold}} = 9.40 \pm 1.96$, which is higher than expected from Eg. 7.61. This result can be explained on the one hand by the lower experimental mean photon number $\langle m \rangle = 0.215$ behind the first PDC stage and the resulting decreased impact of higher-order photon contributions on the three-fold coincidences. On the other hand, the influence of higher-order mode contributions of the primary PDC process, i. e. mislead idler 1 photons, on the secondary photon detection is noticeably decreased.

In the histogram Fig. 7.22 we identify 5 time bins, which contain $\langle N^{\mathrm{acc}}_{3-\mathrm{fold}} \rangle = 9.0 \pm 1.3$ accidental three-fold coincidences on average. We suspect these time bins to belong to the neighboring peaks along the $\tau_1 - \tau_2$ temporal axis. This means that these bins are related only to higher-order photon contributions stemming from the idler 1 detection. In our theoretical prediction in Eg. 7.61 we considered exactly this case. If we calculate the coincidences-to-accidentals ratio for this $\langle N^{\mathrm{acc}}_{3-\mathrm{fold}} \rangle$, we get

$$CAR^{\mathrm{exp}}_{3-\mathrm{fold}} = 3.67 \pm 0.84,$$

which matches the predictable $CAR_{3-\mathrm{fold}} = 4.04 \pm 0.16$ very well, when the mean photon number of $\langle m \rangle = 0.215$ per pulse behind the primary PDC stage is assumed (see Eq. 7.61 and 7.62).

Although this information, obtained from the bin occupation histogram, is already proof of having generated genuine photon triplets in our experiment, we visualize this fact in Fig. 7.23, where the number of three-fold coincidences is plotted, again, versus the relative arrival time delays $\tau_1 - \tau_2$ and $\tau_3 - \tau_2$. We perform a stronger merging to our measurement data and achieve temporal widths of around 10 ns per bin and plot the full measurement range in the central, color-coded graph. With this merging method, the number of noise-related three-fold coincidences inevitably increases and the $SNR_{3-\mathrm{fold}}$ drops. Likewise the $CAR^{\mathrm{exp}}_{3-\mathrm{fold}}$ decreases, but the visibility to the eye of the central peak, including our time-correlated photon triplets, is improved significantly. We notice that the neighboring peaks along the $(\tau_1 - \tau_2)$-axis dominate the accidentals in the three-fold coincidences. This confirms our suspicion stated above that the higher-order photon number contributions of the idler 1 photons have the highest impact on the accidental triple coincidences. This fact is separately visualized in the top graph of Fig. 7.23.

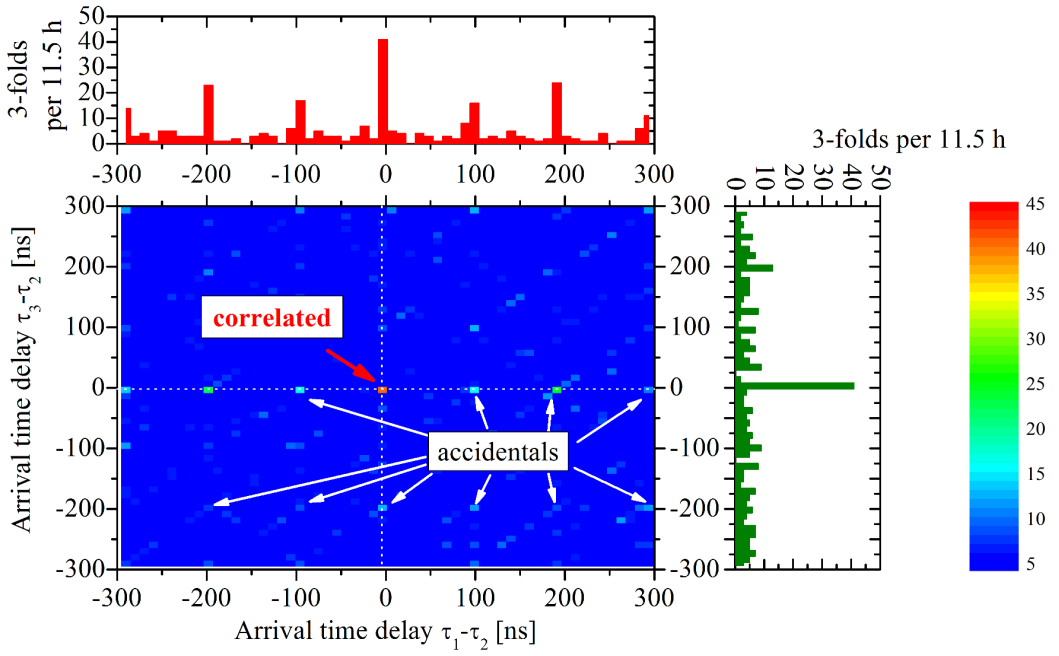

Figure 7.23.: The color-coded graph shows the three-fold coincidences dependent on the relative time delays, where the bins of the complete dataset are merged to temporal widths of around $10\,\mathrm{ns} \times 10\,\mathrm{ns}$ for visualization purposes. We see that the time-correlated peak is situated around zero arrival time delays, whereas the neighboring peaks appear prominently along the $(\tau_1 - \tau_2)$-axis at $\tau_3 - \tau_2 \approx 0\,\mathrm{ns}$. This means that accidental three-fold coincidences occur mainly because higher-order idler 1 photon number states are involved, rather than improperly filtered idler 1 photons stemming from higher-order mode contributions, that disturb the secondary detection. The two side graphs denote cuts along the dotted lines and show the three-fold coincidences for fixed arrival time delays.

By contrast, the idler 1 photons from higher-order mode combinations in the first PDC process do not significantly contribute large absolute numbers to the three-fold coincidences in neighboring peaks. This also confirms our findings from the two-fold coincidence analysis between signal 2 and idler 2 photons: The $CAR^{\mathrm{exp}}_{\mathrm{PDC},2}$ value is not significantly lower than $SNR^{\mathrm{exp}}_{\mathrm{PDC},2}$, which means that the absolute number of accidental two-fold coincidences per time bin is (on average) not significantly larger than the noise-related background.

From the $CAR^{\mathrm{exp}}_{3-\mathrm{fold}}$ value we can infer the increase factor for the three-fold coincidence probability, $r\,(\langle m \rangle) = 1.27 \pm 0.29$ according to Eq. 7.61. In turn, we find that the detected genuine photon-triplet rate is

$$R^{\mathrm{exp}}_{\mathrm{triplet}} = 2.26 \pm 0.39\,\mathrm{h}^{-1},$$

which is around half the expected value and corresponds to a triplet generation rate of

$$R_{\text{triplet}}^{\text{gen,exp}} = 983 \pm 171\,\text{h}^{-1},$$

where the individual transmittances and the detector imperfections are not included.

We also derive the success probability for the photon-triplet generation by using the determined triplet generation rate in conjunction with Eq. 7.63 and get

$$P_{\text{triplet}}^{\text{succ,exp}} = (6.25 \pm 1.09) \cdot 10^{-11}$$

experimentally verified photon triplets per pump pulse. This benchmark is, by contrast to the triplet generation rate, dependent on the individual arm transmittances, the efficiencies of the tree detectors *and* the pump laser repetition rate. Thus, it can be increased by improving the path transmittances and detection efficiencies of the three photon detection systems. Likewise, pump lasers with higher repetition rate but identical pulse energies as in our experiments can be deployed in order to improve $P_{\text{triplet}}^{\text{succ,exp}}$.

We compare the experimentally derived success probability per pump pulse with what we could expect by taking the pump power $\mathbf{P}_\text{p} = 10\,\mu\text{W}$, the individual PDC conversion efficiencies and the detection path efficiencies into account. Using Eq. 7.66, we could have expected a success probability per pulse of

$$\begin{aligned} P_{\text{triplet}}^{\text{succ,th}} &= \frac{\eta_{\text{i1}} \cdot \eta_{\text{s2}}^{\text{tot}} \cdot \eta_{\text{i2}}^{\text{tot}} \cdot P_{\text{PDC,1}} \cdot P_{\text{PDC,2}} \cdot \mathbf{P}_\text{p} \cdot \lambda_\text{p}}{h \cdot c \cdot R_{\text{rep}}} \\ &= (1.49 \pm 0.11) \cdot 10^{-10}. \end{aligned}$$

The experimental value is of the same order of magnitude as the theoretical prediction, but still a factor of ~ 2 smaller, even with the relatively large experimental error bars. We suspect the reason for this gap to be the pump power, which we measured prior to the coupling objective. Although its transmittance as well as the transmittance of the input end-face coating are known for the green pump light, we have no information about the amount of pump light, which is coupled to the input waveguide of our source.

Our approach to generate photon triplets using an integrated cascaded parametric down-conversion source together with pulsed pump light, however, allows for unprecedented signal-to-noise ratios and, thus purity of the triplet verification process on the one hand. On the other hand, the scalability of the absolute photon-triplet generation and detection rate is given, if a pump laser with higher repetition rate would be used. We also benefit from the fact that a pulsed source provides intrinsic temporal information, which can be used to determine accidental contributions very accurately. Third, the pulsed excitation and the excellent long-term stability make our integrated source an ideal candidate for applications in synchronized quantum networks. Finally, our monolithically integrated device intrinsically does not suffer from interface losses, although the spectral mode overlap between the two cascaded PDC processes could be optimized in the future.

Since other approaches for the generation of photon triplet states mostly rely on cw pumping in conjunction with cascaded nonlinearities, it is non-trivial to compare the figures of merit with the ones pointed out in this thesis. Although the absolute numbers of detected photon triplets are around two orders of magnitude higher than in our work [92, 93], the scalability of those systems is potentially limited by higher-order photon components, the impact of which has to be determined. Additionally, we suspect that cw photon-triplet sources are scalable only by applying higher pump powers in the order of several milliwatts, which can cause optical damage and resulting long-term instabilities, if the primary PDC source is based on lithium niobate waveguides. By contrast, our pulsed source requires relatively low cw-equivalent pump powers, while the pulse duty-cycle seemingly reduces the negative impact of photo-refractive effects on the stability.

All other cascaded nonlinear triplet generation methods rely on the interfacing of different types of photon-pair generation processes. This causes inevitable loss, because the different nature of the involved and cascaded subsystems (bulk crystals, atomic vapor, waveguides etc.) do typically not share perfect spatial mode overlap. Our integrated approach, however, offers unit spatial mode-matching intrinsically, while the current spectral mode mismatch can be optimized and brought closer to unity in future work.

Conclusion

In the first section of this chapter, we characterized the cascaded conversion of classical light at λ_{p1} to the visible. Performing cascaded SHG/SFG at low pump powers $\mathbf{P}_{\mathrm{p1}}$ and $\mathbf{P}_{\mathrm{p2}}$ we were able to prove the tunability of the generated light by temperature tuning and adapting the pump wavelengths. For the temperature range $174.1°\mathrm{C} \leq \theta \leq 175.6°\mathrm{C}$ we achieved tuning of the quasi-phase-matched output signal in the range of $531.73\,\mathrm{nm} \leq \lambda_{\mathrm{SFG,2}} \leq 531.81\,\mathrm{nm}$ with phase-matching bandwidths of $\lambda_{\mathrm{SFG,2}}^{\mathrm{FWHM}} = (0.045 \pm 0.005)\,\mathrm{nm}$.

In a second experiment, where we injected idler light at $\lambda_{\mathrm{i}} = 1615\,\mathrm{nm}$ and with low powers, we were able to generate green classical light at $\lambda_{\mathrm{SFG,2}} = 531.78\,\mathrm{nm}$ in two consecutive sum-frequency processes with a maximum overall efficiency of $\eta_{\mathrm{cSFG/SFG}}^{\mathrm{max}} = (35.7 \pm 0.2)\%$. We derived almost identical coupling parameters for the individual up-conversion processes. For the individual SFG processes, we inferred maximum conversion efficiencies of $\eta_{\mathrm{SFG,1}}^{\mathrm{max}} = (78.5{\pm}1.0)\%$ and $\eta_{\mathrm{SFG,2}}^{\mathrm{max}} = (47.5{\pm}0.2)\%$, respectively. These results indicate that the application of our device as a tunable source of green laser light is feasible, but utilizing the cascaded SFG/SFG processes as part of a hybrid up-conversion detector does not provide significant advantage over commercially available detector in terms of joint detection efficiency.

For the up-conversion of quasi-single-photon states, our device does not provide the desired performance. Both the overall system detection efficiency of the first up-conversion stage, $\eta_{\mathrm{SPUC,1}}^{\mathrm{PDE,max}} = (6.00 \pm 0.09)\%$, and, more prominently, the noise count rate are outperformed by state-of-the-art commercial systems. Nevertheless, our

results indicate that the up-conversion of spontaneous Raman scattering, induced and converted by a tunable strong pump 1, could be applied as a spectroscopy method for studying the Stokes- and anti-Stokes-shift as waveguide properties of our device [280]. In order to utilize an integrated source like ours for cascaded single-photon up-conversion, significant technological improvements are required in future work.

We also investigated the generation of photon triplets by cascaded parametric down-conversion theoretically and experimentally. Specifically, we took the experimental circumstances for the commercially available optical components as well as the measured properties of our integrated waveguide device into account. Following this path, we were able to predict the photon pair detection outcome of the secondary PDC stage, when being pumped at the single photon level. Likewise, we derived the theory for the detection and verification of genuine photon triplets, noise-related background contributions and also accidental coincidences.

Experimentally, we verified the photon-triplet generation in our integrated device by analyzing the measurement data for two- and three-fold coincidences. We found that for cw-equivalent pump powers of only $\mathbf{P}_\mathrm{p} = 10\,\mu\mathrm{W}$ a generation rate of $R^{\mathrm{exp}}_{\mathrm{triplet}} = 2.26 \pm 0.39$ genuine photon triplets per hour is possible with coincidences-to-accidentals ratios between $3.67 \leq CAR^{\mathrm{exp}}_{3-\mathrm{fold}} \leq 9.4$, depending on the type of accidental contributions. Furthermore, we determined an extraordinarily high signal-to-noise ratio of $SNR^{\mathrm{exp}}_{3-\mathrm{fold}} \geq 680$ with respect to the noise-related three-fold coincidences.

Our experimental results matched the theoretical predictions reasonably well, and we discussed remaining differences. We can conclude that our modeling approach is not only adaptable to the specific experimental circumstances discussed here, but it can be extended also to hybrid versions of cascaded parametric down-conversion processes. From our general experimental approach of pulsed excitation we infer the natural compatibility of the photon-triplet source to synchronized quantum networks, being supported by the excellent long-term stability of our device.

CHAPTER 8

Conclusions and Outlook

Although and because science often deals with the precognition, the application and the description of Mother Nature's gifts for mankind, the efforts of researchers on the uncovering of new phenomena will probably never become less. Therefore, this thesis cannot be more, but also not less than a grain of sand in the desert or rather a drop in the ocean. During the time of preparing and writing this thesis we have taken the chance to explore some exciting aspects of applied quantum optics, which we briefly summarize at this point. Likewise, we try to connect our work to the future creation of new grains of sand by providing an outlook on possible extensions.

After a short introduction to the general purpose and the topic of integrated quantum optics, we briefly described the theoretical framework for the target-oriented application of nonlinear waveguides in the generation, propagation and conversion of photons in quantum optics. Based on the well-established model of *Strake et al.* [107], we designed and fabricated an integrated device in our clean-room facility by making use of the mature technology of photolithography and periodic domain inversion on titanium-diffused waveguides in lithium niobate.

Our monolithic device with several integrated functionalities bears some extraordinary features, which other technological approaches are not yet competitive with. For example, our $\chi^{(2)}$-nonlinear waveguides show among the lowest loss values reported so far. Their optical modes in the telecommunication wavelength regime let us expect very good spatial overlaps to optical single-mode fibers for both polarizations. This allows for the feasibility of fiber-packaged devices in the future.

In basic experiments we characterized the nonlinear properties of the two type-0 nonlinear frequency-conversion stages. The first stage allows for the bright generation of heralded single photons with efficiencies of $\eta_{\mathrm{H}} = 60\%$ via parametric down-

conversion [256]. In this process we converted green pump pulses at $\lambda_{p1} = 532\,\text{nm}$ to signal photons at $\lambda_{s1} = 803\,\text{nm}$ and idler photons at $\lambda_{i1} = 1573\,\text{nm}$ with probabilities of around $P_{\text{PDC},1} = 8 \cdot 10^{-8}$ pairs per pump photon. This conversion efficiency is two orders of magnitude lower than the actual record in waveguiding devices [48]. Nevertheless, the primary down-conversion stage, in conjunction with the on-chip directional coupler, provides us with the opportunity to generate higher-order photon states, which we proved to match the requirements for passive decoy state quantum key distribution (QKD) in quasi-photon-number-resolved measurements [257]. Therein, we heralded n-photon states up to $n = 4$ at very low input powers of only around $\mathbf{P}_{p1} \leq 2\,\mu\text{W}$, and we conclude that photon-number splitting attacks can be detected and averted by the application of our source in practical QKD systems.

Furthermore, we showed that the second PDC stage can be pumped with light around $\lambda_{p2} = 790.5\,\text{nm}$ and emitting spectrally broad-band around $\lambda_{s2/i2} = (1581 \pm 35)\,\text{nm}$ with conversion efficiencies around $P_{\text{PDC},2} = 2.7 \cdot 10^{-7}$ photon pairs per pump photon. Like the first stage, our secondary conversion stage is conveniently tunable in its pump acceptance and emission. Thus, we were able to make both conversion processes mutually compatible in the spectral degree of freedom. This prerequisite was required by the mail goal of this work: the cascading of two frequency-conversion stages on a single integrated device.

On the one hand, we managed to convert coherent light from the telecom L-band to the green in a cascaded manner with efficiencies of around $\eta_{\text{cSFG}} = 35\%$, by which we have realized an efficient temperature-tunable green laser source. This overall efficiency can be increased in our opinion by overcoming the surface-related scattering losses with the technology of highly efficient, reverse-proton-exchanged waveguides [172, 275]. On the other hand, our integrated device, at this state of development, does not meet the requirements for the (cascaded) up-conversion of single telecom photons to the near-infrared or the visible wavelength regime. The necessary strong pump for the up-conversion process induces spontaneous Raman scattering - an effect which could be minimized in the future by pump wavelengths much longer than the input to convert. Then, Raman scattering [281] as well as disorder-induced quasi-phase-matching pedestals [275, 279] play no significant role, anymore.

Additionally, we have put a lot of effort into the inverse process, i. e. the generation of photon-triplet states by cascaded parametric down-conversion. In detail, we benefited from the basic characterization of our device previously mentioned, and we conceived and built an experimental setup, which allowed us to prove with high confidence that our world's first monolithic photon-triplet source emits around $R_{\text{triplet}} = 2$ triplets per hour at only $\mathbf{P}_{p} = 10\,\mu\text{W}$. This corresponds to a success probability of $P_{\text{triplet}}^{\text{succ,exp}} = 6.25 \cdot 10^{-11}$ verified photon triplets per pump pulse, a benchmark that takes detector imperfections and optical transmittances of supplementary components into account. In coincidence measurements we inferred experimental signal-to-noise ratios larger than $SNR_{3-\text{fold}}^{\text{exp}} = 410$ with respect to uncorrelated background noise, whereas the coincidences-to-accidentals ratio with respect to average non-correlated neighboring pulses is $CAR_{3-\text{fold}}^{\text{exp}} = 10.75 \pm 2.24$.

In parallel, we developed a theoretical model, which describes our pulsed triplet-generation and detection setup, but is also applicable to more generalized schemes of pulsed cascaded parametric down-conversion. We found that our predictions in terms of expectable photon-triplet output, the signal-to-noise ratios and the coincidences-to-accidentals ratios agree well with the experimental results. This means that our assumptions and experimental circumstances, which we included to the model, were precise enough for reasonable anticipation. According to our model and experimental findings, the impact of higher-order photon-number contributions from the first PDC stage limits the applicable pump power for the photon-triplet generation via cascaded PDC. From our measurements we also infer an unprecedented long-term stability of our triplet source, which is less than 0.5% from the average over a measurement time of around 11.5 hours. This result underlines another benefit of our integrated and compact approach, i. e. it ruggedness against environmental/thermal influences.

The high purity of our results shows the benefits of the pulsed excitation on the one hand, while our device is capable of being synchronized with clocked quantum networks on the other hand. Likewise, the presented photon-triplet source is scalable in terms of its emission rate, when pump lasers with higher repetition rate are employed in future work. Thus, we can expect to increase the output by around one order of magnitude with state-of-the-art laser sources. At least one additional order of magnitude in triplet detection probability can be gained by the reduction of filtering. Therefore, future efforts should concentrate on technological developments, which improve the on-chip coupling behavior on the one hand, and which help to reduce the impact of higher-order photon contributions of the first PDC stage on the other hand. Tapered waveguide structures and electro-optically supported directional couplers [148] can be implemented in future versions of our device for optimization of its performance. Further improvement on the internal conversion efficiencies can be achieved by changing the technological basis to reverse-proton-exchanged waveguide structures, which have been shown to be the most efficient frequency conversion devices to date [172, 275, 279] due to their reduced mode dispersion, i. e. improved mode symmetry and overlap.

At the end of a thesis it is always useful to have a look into the future. We want to take this opportunity and propose two logical expansions of the integrated quantum optical device, presented in this thesis, as an outlook on forthcoming activities. Within these proposals, we turn the current limitations of our photon-triplet source into real benefits.

Taking the current status of our device into account we can exploit the cascaded nonlinear conversion processes such that we seed one or both of our integrated PDC stages with weak coherent pulses, which are synchronized with the green pump. Doing so would allow for the generation of either photon pairs being accompanied by a single-photon-added coherent state [301] (only one seed) or with a pair of single-photon-added coherent states accompanied by a single photon (both PDC stages seeded individually). In either case, the output states are expected to be

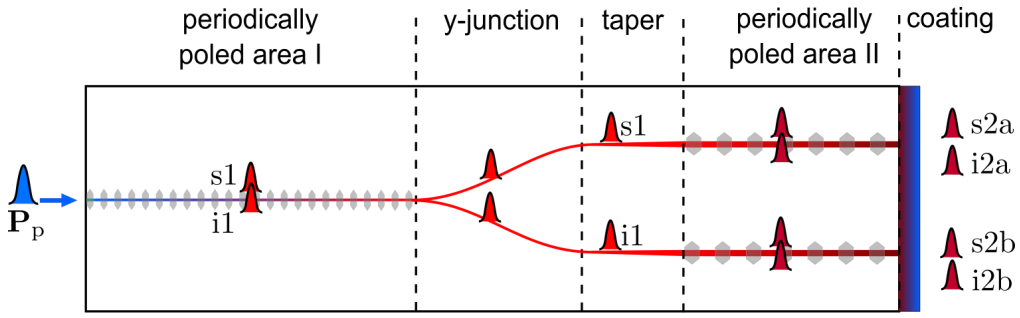

Figure 8.1.: Schematic of the proposed four-photon source. A narrow input waveguide ($w_{\mathrm{WG},1} = 3\,\mu\mathrm{m}$) is pumped with pulsed light at $\lambda_\mathrm{p} = 405\,\mathrm{nm}$, which is converted to primary signal 1/idler 1 photons at $\lambda_{\mathrm{s1}} = \lambda_{\mathrm{i1}} = 810\,\mathrm{nm}$ in a degenerate type-0 PDC process. The integrated y-junction splits the generated photon pairs with 50% chance and directs them, after passing linearly tapered waveguide structures, to individual periodically poled waveguides of $w_{\mathrm{WG},2} = 7\,\mu\mathrm{m}$ width

non-classical at first sight, but depending on the strength of the seeding light it is possible to study the transition from quantum to the classical world. Thus, it appears feasible to generate Schrödinger-cat-like states [8] in terms of micro-macro-entangled states with ours or similar integrated devices in future work.

Another logical extension of our integrated source can be seen in a cascaded PDC source, which emits genuine four-photon-states instead of photon-triplets. In the schematic in Fig. 8.1 we have sketched a device very similar to our current source, but with slight technological changes, which are summarized in Tab. 8.1. In order to generate four non-degenerate photons in the telecom wavelength regime, say $\lambda_{\mathrm{s2a}} = \lambda_{\mathrm{s2b}} = 1595\,\mathrm{nm}$ and $\lambda_{\mathrm{i2a}} = \lambda_{\mathrm{i2b}} = 1646\,\mathrm{nm}$, we will have to pump the proposed source in the blue wavelength region at $\lambda_\mathrm{p} = 405\,\mathrm{nm}$. This requires additional technological effort in terms of dispersion engineering as well as improved periodic poling techniques. Pump wavelengths in the blue require waveguide widths around $w_{\mathrm{WG},1} = 3\,\mu\mathrm{m}$ in order to provide the first down-conversion to $\lambda_{\mathrm{s1}} = \lambda_{\mathrm{i1}} = 810\,\mathrm{nm}$ to address predominantly the fundamental mode combination. Besides, this wavelength combination requires poling periods for a type-0 PDC process of $\Lambda_{\mathrm{PDC},1} < 3.0\,\mu\mathrm{m}$, which are technologically challenging with standard pulsed electric field poling methods. Additionally, an integrated 50/50 beam-splitter must provide the splitting within reasonable coupling length. A y-junction will meet these requirements best. Furthermore, we will have to include linearly tapered waveguide segments behind the coupler in order to widen the two output ports to standard widths of $w_{\mathrm{WG},2} = 7\,\mu\mathrm{m}$, where the secondary PDC photons will typically not suffer from the waveguides' cut-off. The poling periods for the two individual but identical secondary PDC stages are expected to be $\Lambda_{\mathrm{PDC},1} \approx 18.0\,\mu\mathrm{m}$. Finally, the initial titanium layer thickness

Table 8.1.: Estimated technological parameters for an integrated four-photon source

parameter	**value**
Waveguide width 1st PDC stage $w_{\mathrm{WG,1}}$	$2.0\,\mu$m
Waveguide width 2nd PDC stage $w_{\mathrm{WG,2}}$	$7.0\,\mu$m
1st PDC poling period $\Lambda_{\mathrm{G,1}}$	$< 3.0\,\mu$m
2nd PDC poling period $\Lambda_{\mathrm{G,2a/b}}$	$\approx 18.0\,\mu$m
y-junction opening angle $\alpha_{\mathrm{y-j}}$	$\approx 0.5^{\circ}$

must be increased such that light at $\lambda_{\mathrm{i2a/b}} = 1646\,\mathrm{nm}$ is still guided.

One major difference of the proposed source compared with the investigated one in this thesis is the positive impact of higher-order photon contributions behind the primary PDC stage. Both of the secondary PDC stages must be pumped simultaneously with intermediate signal 1/idler 1 photons for the generation of a time-correlated four-photon state. For this purpose the on-chip y-junction must guide at least one photon in each output arm, which address the secondary PDC stages. If only a single photon pair per pulse is present behind the primary PDC stage, the probability for the desired splitting is only 50% for ideal y-junction behavior, since both photons could end up in the same branch with 25% each. Thus, higher mean output photon numbers per pulse of the primary PDC process will increase the chance that both secondary PDC stages are pumped with at least one signal 1/idler 1 photon, simultaneously. In parallel, the total output probability of four-photon states will increase as well. Of course, a full statistical model of the splitting process and the resulting four-photon probabilities has to be developed. Note, however, that care must me taken of the impact of high pump powers at the blue wavelength on possible optical damage [155].

This possible and feasible architecture for a monolithically integrated four-photon device can offer new ways for the generation of multi-qubit entanglement and, thus for proving the non-locality of quantum mechanics in a deterministic manner [9, 11, 33, 287, 289, 294–296]

Acknowledgments

In about five years of working on this small contribution to science, I have received a lot of support by many people. It is my pleasure to say thank you to all of those who made the success of this work possible by their scientific and mental assistance.

First of all, I would like to thank Dr. Hubertus Suche for his furtherance, which he provided to me already in the first semesters of my undergraduate studies. I will never forget his endorsement to become a doctoral student in this group.

Likewise, my sincere thanks are dedicated to Prof. Dr. Christine Silberhorn, whose style of leading the group without any hierarchical boundaries was and still is overwhelming. Thank you for accepting me as your student. Thank you for the journal club, without which the topic of this thesis would be a different one. Thank you for the freedom to do research without recognizable monetary and topical limitations. Thank you for believing with me in the success of this work. Thank you for the supervision and for reviewing this thesis.

I thank Prof. Dr. Artur Zrenner very much for being the second reviewer of this thesis.

There are many group members, who I bothered with my questions in the past years. In particular, I want to say thank you very much to Dr. Harald Herrmann, Dr. Benjamin Brecht, Raimund Ricken and Viktor Quiring for your support with theoretical and technological issues. I gained a decent part of my knowledge on integrated quantum optical devices because of you.

Thanks also to my colleagues Dr. Michael Stefszky, Dr. Kai-Hong Luo, Vahid Ansari, Georg Harder, Helge Rütz and Dr. Malte Avenhaus for their help to deal with that bunch of technical, experimental and software-related details.

But also those members and alumni of the group, who I have not mentioned by their names, deserve my honest thanks for the climate in our group. You all will be part of my life, being the best colleagues one could have. Cheers.

Very special thanks are dedicated to Jun.-Prof. Dr. Timothy John Bartley, whose

advice as a native English speaker helped me a lot to write this thesis. I also very much appreciate your endorsement for what comes next.

Finally, I want to thank my family in general and my love Anja in particular for the patience during the last years. I do very much appreciate your backing, your understanding for coming home late sometimes, and your efforts to make my life good. I love you.

Bibliography

[1] Max Planck. Ueber das gesetz der energieverteilung im normalspectrum. Annalen der Physik, 309(3):553–563, 1901.

[2] W. Wien. Ueber die energievertheilung im emissionsspectrum eines schwarzen körpers. Annalen der Physik, 294(8):662–669, 1896.

[3] F.R.S. Lord Rayleigh. Liii. remarks upon the law of complete radiation. Philosophical Magazine Series 5, 49(301):539–540, 1900.

[4] J.H. M.A. Jeans. On the partition of energy between matter and Ã†ther. Philosophical Magazine Series 6, 10(55):91–98, 1905.

[5] W. Heisenberg. über quantentheoretische umdeutung kinematischer und mechanischer beziehungen. Zeitschrift für Physik, 33(1):879–893, 1925.

[6] E. Schrödinger. An undulatory theory of the mechanics of atoms and molecules. Phys. Rev., 28:1049–1070, Dec 1926.

[7] M. Born. Zur quantenmechanik der stoßvorgänge. Zeitschrift für Physik, 37(12):863–867, 1926.

[8] E. Schrödinger. Die gegenwärtige situation in der quantenmechanik. Naturwissenschaften, 23(48):807–812, 1935.

[9] A. Einstein, B. Podolsky, and N. Rosen. Can quantum-mechanical description of physical reality be considered complete? Physical Review, 47(10):777–780, May 1935.

[10] B. Brecht. Engineering ultrafast quantum frequency conversion. PhD thesis, 2014.

[11] J. S. Bell. On the einstein podolsky rosen paradox. Physics, 1(3):195–200, 1964.

[12] J. P. Gordon, H. J. Zeiger, and C. H. Townes. The maser-new type of microwave amplifier, frequency standard, and spectrometer. Phys. Rev., 99:1264–1274, Aug 1955.

[13] T. H. Maiman. Stimulated optical radiation in ruby. Nature, 187(4736):493–494, August 1960.

[14] Roy J. Glauber. Coherent and incoherent states of the radiation field. Phys. Rev., 131:2766–2788, September 1963.

[15] J. A. Armstrong, N. Bloembergen, J. Ducuing, and P. S. Pershan. Interactions between light waves in a nonlinear dielectric. Physical Review, 127(6):1918–1939, September 1962.

[16] P. A. Franken and J. F. Ward. Optical harmonics and nonlinear phenomena. Rev. Mod. Phys., 35:23, 1963.

[17] D. C. Burnham and D. L. Weinberg. Observation of simultaneity in parametric production of optical photon pairs. Physical Review Letters, 25(2):84–87, July 1970.

[18] J. F. Clauser, M. A. Horne, A. Shimony, and R. A. Holt. Proposed experiment to test local hidden-variable theories. Phys. Rev. Lett., 23:880–884, Oct 1969.

[19] S. J. Freedman and J. F. Clauser. Experimental test of local hidden-variable theories. Phys. Rev. Lett., 28:938–941, Apr 1972.

[20] S. E. Miller. Coupled wave theory and waveguide applications. Bell System Technical Journal, 33(3):661–719, 1954.

[21] E. A. J. Marcatili. Dielectric rectangular waveguide and directional coupler for integrated optics. Bell System Technical Journal, 48:2071–2102, 1969.

[22] S. Somekh and A. Yariv. Phase matching by periodic modulation of the nonlinear optical properties. Optics Communications, 6(3):301 – 304, 1972.

[23] I. P. Kaminow, V. Ramaswamy, R. V. Schmidt, and E. H. Turner. Lithium niobate ridge waveguide modulator. Applied Physics Letters, 24(12):622–624, 1974.

[24] D. Marcuse. Theory of dielectric optical waveguides. Academic Press, 1974.

[25] R. V. Schmidt and I. P. Kaminow. Metal-diffused optical waveguides in LiNbO3. Applied Physics Letters, 25(8):458–460, October 1974.

[26] H. J. Kimble, M. Dagenais, and L. Mandel. Photon antibunching in resonance fluorescence. Phys. Rev. Lett., 39:691–695, September 1977.

[27] C. K. Hong, Z. Y. Ou, and L. Mandel. Measurement of subpicosecond time intervals between two photons by interference. Physical Review Letters, 59(18):2044, November 1987.

[28] J. G. Rarity, K. D. Ridley, and P. R. Tapster. Absolute measurement of detector quantum efficiency using parametric downconversion. Appl. Opt., 26(21):4616–4619, November 1987.

[29] J. Huang and P. Kumar. Photon-counting statistics of multimode squeezed light. Physical Review A, 40(3):1670, 1989.

[30] Paul G. Kwiat, Klaus Mattle, Harald Weinfurter, Anton Zeilinger, Alexander V. Sergienko, and Yanhua Shih. New high-intensity source of polarization-entangled photon pairs. Physical Review Letters, 75(24):4337–4341, December 1995.

[31] Paul G. Kwiat, Edo Waks, Andrew G. White, Ian Appelbaum, and Philippe H. Eberhard. Ultrabright source of polarization-entangled photons. Physical Review A, 60(2):R773–R776, 1999.

[32] A. B. U'Ren, C. Silberhorn, K. Banaszek, and I. A. Walmsley. Efficient conditional preparation of high-fidelity single photon states for fiber-optic quantum networks. Physical Review Letters, 93(9):093601, 2004.

[33] D. M. Greenberger, M. A. Horne, and A. Zeilinger. Bell's Theorem, Quantum Theory, and Conceptions of the Universe, page 73–76. Kluwer Academic, Dordrecht, 1989.

[34] J.-W. Pan, D. Bouwmeester, M. Daniell, H. Weinfurter, and A. Zeilinger. Experimental test of quantum nonlocality in three-photon greenberger-horne-zeilinger entanglement. Nature, 403(6769):515–519, February 2000.

[35] C. Maurer, C. Becher, C. Russo, J. Eschner, and R. Blatt. A single-photon source based on a single ca + ion. New Journal of Physics, 6(1):94, 2004.

[36] P. Maunz, D. L. Moehring, S. Olmschenk, K. C. Younge, D. N. Matsukevich, and C. Monroe. Quantum interference of photon pairs from two remote trapped atomic ions. Nat Phys, 3(8):538–541, 2007.

[37] H. G. Barros, A. Stute, T. E. Northup, C. Russo, P. O. Schmidt, and R. Blatt. Deterministic single-photon source from a single ion. New Journal of Physics, 11(10):103004, October 2009.

[38] H. H. Arnaut and G. A. Barbosa. Orbital and intrinsic angular momentum of single photons and entangled pairs of photons generated by parametric down-conversion. Physical Review Letters, 85(2):286, July 2000. Copyright (C) 2009 The American Physical Society; Please report any problems to prola@aps.org.

[39] S. Franke-Arnold, S. M. Barnett, M. J. Padgett, and L. Allen. Two-photon entanglement of orbital angular momentum states. Physical Review A, 65(3):033823, February 2002. Copyright (C) 2009 The American Physical Society; Please report any problems to prola@aps.org.

[40] S. Franke-Arnold, L. Allen, and M. Padgett. Advances in optical angular momentum. Laser & Photonics Review, 2(4):299–313, 2008.

[41] S. Chen, Y.-A. Chen, T. Strassel, Z.-S. Yuan, B. Zhao, J. Schmiedmayer, and J.-W. Pan. Deterministic and storable single-photon source based on a quantum memory. Phys. Rev. Lett., 97:173004, Oct 2006.

[42] E. Bimbard, R. Boddeda, N. Vitrant, A. Grankin, V. Parigi, J. Stanojevic, A. Ourjoumtsev, and P. Grangier. Homodyne tomography of a single photon retrieved on demand from a cavity-enhanced cold atom memory. Phys. Rev. Lett., 112:033601, Jan 2014.

[43] P. Michler, A. Kiraz, C. Becher, W. V. Schoenfeld, P. M. Petroff, Lidong Zhang, E. Hu, and A. Imamoglu. A quantum dot single-photon turnstile device. Science, 290(5500):2282 –2285, December 2000.

[44] J. Claudon, J. Bleuse, N. S. Malik, M. Bazin, P. Jaffrennou, N. Gregersen, C. Sauvan, P. Lalanne, and J.-M. Gerard. A highly efficient single-photon source based on a quantum dot in a photonic nanowire. Nat Photon, 4(3):174–177, March 2010.

[45] C. Kurtsiefer, S. Mayer, P. Zarda, and H. Weinfurter. Stable solid-state source of single photons. Phys. Rev. Lett., 85:290–293, Jul 2000.

[46] A. Beveratos, S. Kühn, R. Brouri, T. Gacoin, J.-P. Poizat, and P. Grangier. Room temperature stable single-photon source. The European Physical Journal D - Atomic, Molecular, Optical and Plasma Physics, 18(2):191–196, 2002.

[47] M. Leifgen, T. Schröder, F. Gädeke, R. Riemann, V. Metillon, E. Neu, C. Hepp, C. Arend, C. Becher, K. Lauritsen, and O. Benson. Evaluation of nitrogen- and silicon-vacancy defect centres as single photon sources in quantum key distribution. New Journal of Physics, 16(2):023021, 2014.

[48] S. Tanzilli, H. de Riedmatten, H. Tittel, H. Zbinden, P. Baldi, M. De Micheli, D.B. Ostrowsky, and N. Gisin. Highly efficient photon-pair source using periodically poled lithium niobate waveguide. Electronics Letters, 37(1):26–28, Jan 2001.

[49] A. Eckstein, B. Brecht, and C. Silberhorn. A quantum pulse gate based on spectrally engineered sum frequency generation. Opt. Express, 19(15):13770–13778, July 2011.

[50] G. Harder, V. Ansari, B. Brecht, T. Dirmeier, C. Marquardt, and C. Silberhorn. An optimized photon pair source for quantum circuits. Opt. Express, 21(12):13975–13985, Jun 2013.

[51] S. Aaronson and A. Arkhipov. The computational complexity of linear optics. In Proceedings of the Forty-third Annual ACM Symposium on Theory of Computing, STOC '11, pages 333–342, New York, NY, USA, 2011. ACM.

[52] S. Aaronson and A. Arkhipov. Bosonsampling is far from uniform. ArXiv e-prints, September 2013.

[53] C. Bennett and G. Brassard. Quantum cryptography: Public key distribution and coin tossing. In Proceedings of IEEE International Conference on Computers, Systems, and Signal Processing, pages 175–179, 1984.

[54] H.-J. Briegel, W. Dür, J. I. Cirac, and P. Zoller. Quantum repeaters: The role of imperfect local operations in quantum communication. Phys. Rev. Lett., 81:5932–5935, Dec 1998.

[55] C. Simon, H. de Riedmatten, M. Afzelius, N. Sangouard, H. Zbinden, and N. Gisin. Quantum repeaters with photon pair sources and multimode memories. Physical Review Letters, 98:190503, 2007.

[56] N. Curtz, E. Koller, H. Zbinden, M. Decroux, L. Antognazza, Ã˜. Fischer, and N. Gisin. Patterning of ultrathin ybco nanowires using a new focused-ion-beam process. Superconductor Science and Technology, 23(4):045015, 2010.

[57] S. Tanzilli, A. Martin, F. Kaiser, M.P. De Micheli, O. Alibart, and D.B. Ostrowsky. On the genesis and evolution of integrated quantum optics. Laser & Photonics Reviews, 6(1):115–143, 2012.

[58] A. Martin, O. Alibart, M. P. De Micheli, D. B. Ostrowsky, and S. Tanzilli. A quantum relay chip based on telecommunication integrated optics technology. New Journal of Physics, 14(2):025002, 2012.

[59] N. Sangouard, B. Sanguinetti, N. Curtz, N. Gisin, R. Thew, and H. Zbinden. Faithful entanglement swapping based on sum-frequency generation. Phys. Rev. Lett., 106(12):120403, March 2011.

[60] D. Bonneau, E. Engin, K. Ohira, N. Suzuki, H. Yoshida, N. Iizuka, M. Ezaki, C. M. Natarajan, M. G. Tanner, R. H. Hadfield, S. N. Dorenbos, V. Zwiller, J. L. O'Brien, and M. G. Thompson. Quantum interference and manipulation of entanglement in silicon wire waveguide quantum circuits. New Journal of Physics, 14(4):045003, 2012.

[61] T. Meany, L. A. Ngah, M. J. Collins, A. S. Clark, R. J. Williams, B. J. Eggleton, M. J. Steel, M. J. Withford, O. Alibart, and S. Tanzilli. Hybrid photonic circuit for multiplexed heralded single photons. Laser & Photonics Reviews, 8(3):L42–L46, 2014.

[62] E. Pomarico, B. Sanguinetti, T. Guerreiro, R. Thew, and H. Zbinden. Mhz rate and efficient synchronous heralding of single photons at telecom wavelengths. Opt. Express, 20(21):23846–23855, October 2012.

[63] A. Politi, M.J. Cryan, J. G. Rarity, S. Yu, and J. L. O'Brien. Silica-on-silicon waveguide quantum circuits. Science, 320:646, 2008.

[64] G. D. Marshall, A. Politi, J. C. F. Matthews, P. Dekker, M. Ams, M. J. Withford, and J. L. O'Brien. Laser written waveguide photonic quantum circuits. Opt. Express, 17(15):12546–12554, July 2009.

[65] A. Peruzzo, A. Laing, A. Politi, T. Rudolph, and J. L. O'Brien. Multimode quantum interference of photons in multiport integrated devices. Nature Communications, 2(224):224, March 2011.

[66] J. C. F. Matthews, A. Politi, A. Stefanov, and J.L. O'Brien. Manipulation of multiphoton entanglement in waveguide quantum circuits. Nature Photonics, 3(6):346–350, June 2009.

[67] P. J. Shadbolt, T. Vértesi, Y.-C. Liang, C. Branciard, N. Brunner, and J. L. O'Brien. Guaranteed violation of a bell inequality without aligned reference frames or calibrated devices. Sci. Rep., 2:470, June 2012.

[68] H. W. Li, S. Przeslak, A. O. Niskanen, J. C. F. Matthews, A. Politi, P. Shadbolt, A. Laing, M. Lobino, M. G. Thompson, and J. L. O'Brien. Reconfigurable controlled two-qubit operation on a quantum photonic chip. New Journal of Physics, 13(11):115009, 2011.

[69] B. J. Smith, D. Kundys, N. Thomas-Peter, P. G. R. Smith, and I. A. Walmsley. Phase-controlled integrated photonic quantum circuits. Opt. Express, 17(16):13516–13525, August 2009.

[70] B. J. Metcalf, N. Thomas-Peter, J. B. Spring, D. Kundys, M. A. Broome, P. C. Humphreys, X.-M. Jin, M. Barbieri, W. Steven K., J. C. Gates, B. J. Smith, N. K. Langford, P. G.R. Smith, and I. A. Walmsley. Multiphoton quantum interference in a multiport integrated photonic device. Nat Commun, 4:1356–, January 2013.

[71] J. B. Spring, B. J. Metcalf, P. C. Humphreys, W. St. Kolthammer, X.-M. Jin, M. Barbieri, A. Datta, N. Thomas-Peter, N. K. Langford, D. Kundys, J. C. Gates, B. J. Smith, P. G. R. Smith, and I. A. Walmsley. Boson sampling on a photonic chip. Science, 339(6121):798–801, 2013.

[72] K. Banaszek, A. B. U'Ren, and I. A. Walmsley. Generation of correlated photons in controlled spatial modes by downconversion in nonlinear waveguides. Opt. Lett., 26(17):1367–1369, September 2001.

[73] M. C. Booth, M. Atatüre, G. Di Giuseppe, B. E. A. Saleh, A. V. Sergienko, and M. C. Teich. Counterpropagating entangled photons from a waveguide with periodic nonlinearity. Physical Review A, 66(2):023815, 2002.

[74] J. Chen, A. J. Pearlman, A. Ling, J. Fan, and A. L. Migdall. A versatile waveguide source of photon pairs for chip-scale quantum information processing. Optics Express, 17(8):6727–6740, April 2009.

[75] D. Bonneau, M. Lobino, P. Jiang, C. M. Natarajan, M. G. Tanner, R. H. Hadfield, S. N. Dorenbos, V. Zwiller, M. G. Thompson, and J. L. O'Brien. Fast path and polarization manipulation of telecom wavelength single photons in lithium niobate waveguide devices. Phys. Rev. Lett., 108:053601, January 2012.

[76] F. Kaiser, A. Issautier, L. A. Ngah, O. Danila, H. Herrmann, W. Sohler, A. Martin, and S. Tanzilli. High-quality polarization entanglement state preparation and manipulation in standard telecommunication channels. New Journal of Physics, 14(8):085015, 2012.

[77] M. Karpinski, C. Radzewicz, and K. Banaszek. Dispersion-based control of modal characteristics for parametric down-conversion in a multimode waveguide. Opt. Lett., 37(5):878–880, March 2012.

[78] A. S. Solntsev, A. A. Sukhorukov, D. N. Neshev, and Y. S. Kivshar. Spontaneous parametric down-conversion and quantum walks in arrays of quadratic nonlinear waveguides. Physical Review Letters, 108(2):023601, January 2012.

[79] L. A. Ngah, O. Alibart, L.t Labonte, V. D'Auria, and S. Tanzilli. Ultra-fast heralded single photon source based on telecom technology. Laser & Photonics Reviews, 9(2):L1–L5, 2015.

[80] E. Pomarico, B. Sanguinetti, N. Gisin, R. Thew, H. Zbinden, G. Schreiber, A. Thomas, and W. Sohler. Waveguide-based opo source of entangled photon pairs. New Journal of Physics, 11(11):113042, 2009.

[81] O. Alibart, D. B. Ostrowsky, P. Baldi, and S. Tanzilli. High-performance guided-wave asynchronous heralded single-photon source. Opt. Lett., 30(12):1539–1541, June 2005.

[82] A. Martin, A. Issautier, H. Herrmann, W. Sohler, D. B. Ostrowsky, O. Alibart, and S. Tanzilli. A polarization entangled photon-pair source based on a type-ii ppln waveguide emitting at a telecom wavelength. New Journal of Physics, 12(10):103005, 2010.

[83] M. Fiorentino, S. M. Spillane, R. G. Beausoleil, T. D. Roberts, P. Battle, and M. W. Munro. Spontaneous parametric down-conversion in periodically poled ktp waveguides and bulk crystals. Opt. Express, 15(12):7479–7488, June 2007.

[84] R. Regener and W. Sohler. Loss in low-finesse ti:linbo3 optical waveguide resonators. Applied Physics B: Lasers and Optics, 36:143–147, 1985.

[85] R. V. Roussev, C. Langrock, J. R. Kurz, and M. M. Fejer. Periodically poled lithium niobate waveguide sum-frequency generator for efficient single-photon detection at communication wavelengths. Opt. Lett., 29(13):1518–1520, Jul 2004.

[86] E. Pomarico, B. Sanguinetti, R. Thew, and H. Zbinden. Room temperature photon number resolving detector for infared wavelengths. Optics Express, 18(10):10750–10759, 2010.

[87] G. Giorgi, P. Mataloni, and F. De Martini. Frequency hopping in quantum interferometry: Efficient up-down conversion for qubits and ebits. Phys. Rev. Lett., 90:027902, Jan 2003.

[88] M. A. Albota and F. N. C. Wong. Efficient single-photon counting at 1.55 μm by means of frequency upconversion. Opt. Lett., 29(13):1449–1451, Jul 2004.

[89] A. P. Vandevender and P. G. Kwiat. High efficiency single photon detection via frequency up-conversion. Journal of Modern Optics, 51(9-10):1433–1445, 2004.

[90] R. Ikuta, Y. Kusaka, T. Kitano, H. Kato, T. Yamamoto, M. Koashi, and N. Imoto. Wide-band quantum interface for visible-to-telecommunication wavelength conversion. Nat Commun, 2:537–, November 2011.

[91] H. Hübel, D. R. Hamel, A. Fedrizzi, S. Ramelow, K. J. Resch, and T. Jennewein. Direct generation of photon triplets using cascaded photon-pair sources. Nature, 466(7306):601–603, July 2010.

[92] L. K. Shalm, D. R. Hamel, Z. Yan, C. Simon, K. J. Resch, and T. Jennewein. Three-photon energy-time entanglement. Nat Phys, 9(1):19–22, January 2013.

[93] D. R. Hamel, L. K. Shalm, H. Hübel, A. J. Miller, F. Marsili, V. B. Verma, R. P. Mirin, S. W. Nam, K. J. Resch, and T. Jennewein. Direct generation of three-photon polarization entanglement. Nat Photon, 8(10):801–807, October 2014.

[94] W. Mauerer and C. Silberhorn. Quantum key distribution with passive decoy state selection. Phys. Rev. A, 75:050305, May 2007.

[95] R. S. Weis and T. K. Gaylord. Lithium niobate: Summary of physical properties and crystal structure. Applied Physics A, 37(4):191–203, 1985.

[96] T. Suhara and M. Fujimura. Waveguide Nonlinear-Optic Devices. Springer, 1 edition, June 2003.

[97] M. Luennemann, U. Hartwig, G. Panotopoulos, and K. Buse. Electrooptic properties of lithium niobate crystals for extremely high external electric fields. Applied Physics B, 76(4):403–406, 2003.

[98] G. Schreiber. Quasi-phasenangepasste frequenzkonversion mit periodisch gepolten ti:linbo$_3$-wellenleitern, 2001.

[99] R. W. Boyd. Nonlinear Optics. Academic Press, 3 edition, 2008.

[100] J. M. Manley and H. E. Rowe. Some general properties of nonlinear elements-part i. general energy relations. Proceedings of the IRE, 44(7):904–913, July 1956.

[101] A. Yariv. Quantum Electronics. John Wiley & Sons, Inc., 3 edition, 1989.

[102] J. Crank. The mathematics of diffusion. Clarendon Press Oxford [England], 2nd ed. edition, 1975.

[103] W. K. Burns, P. H. Klein, E. J. West, and L. E. Plew. Ti diffusion in ti:linbo3 planar and channel optical waveguides. Journal of Applied Physics, 50(10):6175–6182, 1979.

[104] Gian Paolo Bava, I. Montrosset, W. Sohler, and H. Suche. Numerical modeling of ti:linbo3integrated optical parametric oscillators. Quantum Electronics, IEEE Journal of, 23(1):42–51, Jan 1987.

[105] G. B. Hocker and W. K. Burns. Mode dispersion in diffused channel waveguides by the effective index method. Appl. Opt., 16(1):113–118, Jan 1977.

[106] Makoto Minakata, Shoichi Saito, and Masashi Shibata. Two-dimensional distribution of refractive index changes in ti-diffused linbo3 strip waveguides. Journal of Applied Physics, 50(5):3063–3067, 1979.

[107] E. Strake, G.P. Bava, and I. Montrosset. Guided modes of ti:linbo3 channel waveguides: a novel quasi-analytical technique in comparison with the scalar finite-element method. Lightwave Technology, Journal of, 6(6):1126–1135, June 1988.

[108] Toshiaki Suhara, Yuichi Handa, Hiroshi Nishihara, and Jiro Koyama. Analysis of optical channel waveguides and directional couplers with graded-index profile. J. Opt. Soc. Am., 69(6):807–815, Jun 1979.

[109] W. Grundkötter. Theoretische beschreibung quai-phasenangepasster optisch frequenzkonversion in periodisch gepolten wellenleitern, 1999.

[110] D. Marcuse. Optimal electrode design for integrated optics modulators. Quantum Electronics, IEEE Journal of, 18(3):393–398, Mar 1982.

[111] D. Zhang, G. Ding, and C. Chen. Theoretical analysis of guided mode and effective refractive index at 1.53 um in ti:linbo3 strip waveguides. J. Lightwave Technol., 16(3):459, Mar 1998.

[112] G. Hocker and W.K. Burns. Modes in diffused optical waveguides of arbitrary index profile. Quantum Electronics, IEEE Journal of, 11(6):270–276, Jun 1975.

[113] M. L. Bortz. Quasi-Phasematched Optical Frequency Conversion in Lithium Niobate Waveguides. PhD thesis, 1994.

[114] R. V. Roussev. Optical-Frequency Mixers in Periodically Poled Lithium Niobate: Materials, Modeling, and Characterization. PhD thesis, Stanford University, 2006.

[115] K. R. Parameswaran, J. R. Kurz, R. V. Roussev, and M. M. Fejer. Observation of 99% pump depletion in single-pass second-harmonic generation in a periodically poled lithium niobate waveguide. Opt. Lett., 27(1):43–45, Jan 2002.

[116] L. Bersiner, U. Hempelmann, and E. Strake. Numerical analysis of passive integrated-optical polarization splitters: comparison of finite-element method and beam-propagation method results. J. Opt. Soc. Am. B, 8(2):422–433, February 1991.

[117] A. Yariv. Coupled-mode theory for guided-wave optics. Quantum Electronics, IEEE Journal of, 9(9):919–933, Sep 1973.

[118] A. Hardy and W. Streifer. Coupled mode theory of parallel waveguides. Lightwave Technology, Journal of, 3(5):1135–1146, Oct 1985.

[119] W. K. Burns, A. F. Milton, A. B. Lee, and E. J. West. Optical modal evolution 3-dB coupler. Appl. Opt., 15(4):1053–1065, April 1976.

[120] L. D. Hutcheson. Losses in titanium-diffused lithium-niobate channel waveguides due to directional changes. PhD thesis, The University of Arizona, 1980.

[121] S. K. Korotky, E. A. J. Marcatili, J. J. Veselka, and R. H. Bosworth. Greatly reduced losses for small-radius bends in ti:linbo3 waveguides. Applied Physics Letters, 48(2):92–94, 1986.

[122] M. Fox. Quantum Optics. Ox, 2006.

[123] A. Lenhard. Quantum Photonic Interfaces between Atomic and Telecommunication Wavelengths. PhD thesis, 2015.

[124] R. Q. Hanbury Brown, R.and Twiss. Correlation between photons in two coherent beams of light. Nature, 177:27–29, 1956.

[125] R. J. Glauber. The quantum theory of optical coherence. Phys. Rev., 130:2529–2539, June 1963.

[126] A. Christ and C. Silberhorn. Limits on the deterministic creation of pure single-photon states using parametric down-conversion. Phys. Rev. A, 85:023829, February 2012.

[127] A. Christ, B. Brecht, W. Mauerer, and C. Silberhorn. Theory of quantum frequency conversion and type-ii parametric down-conversion in the high-gain regime. New Journal of Physics, 15(5):053038, 2013.

[128] A. Christ, K. Laiho, A. Eckstein, K. N. Cassemiro, and C. Silberhorn. Probing multimode squeezing with correlation functions. New Journal of Physics, 13:033027, March 2011.

[129] A. Eckstein, A. Christ, P. J. Mosley, and C. Silberhorn. Highly efficient single-pass source of pulsed single-mode twin beams of light. Phys. Rev. Lett., 106:013603, January 2011.

[130] W. H. Zachariasen. Skrifter Norske Videnskaps Akad. Oslo, Mat.-Naturv. Kl. I(4), 1928.

[131] B. T. Matthias and J. P. Remeika. Ferroelectricity in the ilmenite structure. Phys. Rev., 76:1886–1887, Dec 1949.

[132] Wikipedia The Free Encyclopedia. Lithium niobate. 07/23/2015.

[133] Wikipedia Die Freie Enzyklopädie. Lithiumniobat. 07/23/2015.

[134] J. Czochralski. Ein neues verfahren zur messung der kristallisationsgeschwindigkeit der metalle. Zeitschrift für physikalische Chemie, 92:219–221, 1918.

[135] D. E. Zelmon, D. L. Small, and D. Jundt. Infrared corrected sellmeier coefficients for congruently grown lithium niobate and 5 mol.% magnesium oxide –doped lithium niobate. J. Opt. Soc. Am. B, 14(12):3319–3322, Dec 1997.

[136] U. Schlarb and K. Betzler. Refractive indices of lithium niobate as a function of temperature, wavelength, and composition: A generalized fit. Phys. Rev. B, 48:15613–15620, Dec 1993.

[137] D. H. Jundt. Temperature-dependent sellmeier equation for the index of refraction, ne, in congruent lithium niobate. Opt. Lett., 22(20):1553–1555, Oct 1997.

[138] G. J. Edwards and M. Lawrence. A temperature-dependent dispersion equation for congruently grown lithium niobate. Optical and Quantum Electronics, 16(4):373–375, 1984.

[139] I. P. Kaminow and E. H. Turner. Electrooptic light modulators. Proceedings of the IEEE, 54(10):1374–1390, Oct 1966.

[140] I. P. Kaminow, J. R. Carruthers, E. H. Turner, and L. W. Stulz. Thin-film linbo3 electro-optic light modulator. Applied Physics Letters, 22(10):540–542, 1973.

[141] I. P. Kaminow, L. W. Stulz, and E. H. Turner. Efficient strip-waveguide modulator. Applied Physics Letters, 27(10):555–557, 1975.

[142] R. V. Schmidt and P. S. Cross. Efficient optical waveguide switch/amplitude modulator. Opt. Lett., 2(2):45–47, Feb 1978.

[143] R. C. Alferness. Electrooptic guided-wave device for general polarization transformations. Quantum Electronics, IEEE Journal of, 17(6):965–969, Jun 1981.

[144] R. C. Alferness and L. L. Buhl. Waveguide electro-optic polarization transformer. Applied Physics Letters, 38(9):655–657, 1981.

[145] T. R. Ranganath and S. Wang. Ti-diffused linbo3 branched-waveguide modulators: Performance and design. Quantum Electronics, IEEE Journal of, 13(4):290–295, Apr 1977.

[146] R. C. Alferness. Guided-wave devices for optical communication. Quantum Electronics, IEEE Journal of, 17(6):946–959, Jun 1981.

[147] M. Lawrence. Lithium niobate integrated optics. Reports on Progress in Physics, 56(3):363, 1993.

[148] R. V. Schmidt and H. Kogelnik. Electro-optically switched coupler with stepped $\delta\beta$ reversal using ti-diffused $linbo_3$ waveguides. Applied Physics Letters, 28(9):503–506, 1976.

[149] H. Kogelnik and R.V. Schmidt. Switched directional couplers with alternating $\delta\beta$. Quantum Electronics, IEEE Journal of, 12(7):396–401, Jul 1976.

[150] R. V. Schmidt, I. P. Kaminow, and J. R. Carruthers. Acousto-optic diffraction of guided optical waves in linbo3. Applied Physics Letters, 23(8):417–419, 1973.

[151] M. L. Shah. Fast acousto-optical waveguide modulators. Applied Physics Letters, 23(2):75–77, 1973.

[152] J. M. White, P. F. Heidrich, and E. G. Lean. Thin-film acousto-optic interaction in linbo¡sub¿3¡/sub¿. Electronics Letters, 10:510–511(1), November 1974.

[153] F. S. Chen. Optically induced change of refractive indices in linbo3 and litao3. Journal of Applied Physics, 40(8):3389–3396, 1969.

[154] D. A. Bryan, Robert Gerson, and H. E. Tomaschke. Increased optical damage resistance in lithium niobate. Applied Physics Letters, 44(9):847–849, 1984.

[155] T. Fujiwara, A. Terashima, and H. Mori. Photorefractive effect in ti-diffused channel waveguides using linbo3 substrates with reduced optical absorption. Applied Physics Letters, 55(26):2718–2720, 1989.

[156] F. S. Chen, J. T. LaMacchia, and D. B. Fraser. Holographic storage in lithium niobate. Applied Physics Letters, 13(7):223–225, 1968.

[157] D. Marcuse. Mode conversion caused by surface imperfections of a dielectric slab waveguide. Bell System Technical Journal, 48:3187–3215, 1969.

[158] K. Noguchi, O. Mitomi, K. Kawano, and M. Yanagibashi. Highly efficient 40-ghz bandwidth ti:linbo/sub 3/ optical modulator employing ridge structure. Photonics Technology Letters, IEEE, 5(1):52–54, Jan 1993.

[159] Q. Xu, V. R. Almeida, R. R. Panepucci, and M. Lipson. Experimental demonstration of guiding and confining light in nanometer-size low-refractive-index material. Opt. Lett., 29(14):1626–1628, Jul 2004.

[160] J. L. Jackel and J. J. Johnson. Reverse exchange method for burying proton exchanged waveguides. Electronics Letters, 27(15):1360–1361, July 1991.

[161] J. Rams, J. Olivares, and J.M. Cabrera. Shg-capabilities of reverse pe-linbo3 waveguides. Electronics Letters, 33(4):322–323, Feb 1997.

[162] Yu. N. Korkishko, V. A. Fedorov, T. M. Morozova, F. Caccavale, F. Gonella, and F. Segato. Reverse proton exchange for buried waveguides in linbo3. J. Opt. Soc. Am. A, 15(7):1838–1842, Jul 1998.

[163] Y.N. Korkishko, V.A. Fedorov, and F. Laurell. The shg-response of different phases in proton exchanged lithium niobate waveguides. Selected Topics in Quantum Electronics, IEEE Journal of, 6(1):132–142, Jan 2000.

[164] J. L. Jackel, C. E. Rice, and J. J. Veselka. Proton exchange for high-index waveguides in LiNbO3. Applied Physics Letters, 41(7):607–608, October 1982.

[165] K. M. Davis, K. Miura, N. Sugimoto, and K. Hirao. Writing waveguides in glass with a femtosecond laser. Opt. Lett., 21(21):1729–1731, Nov 1996.

[166] Y. Nishida, H. Miyazawa, M. Asobe, O. Tadanaga, and H. Suzuki. Direct-bonded qpm-ln ridge waveguide with high damage resistance at room temperature. Electronics Letters, 39(7):609–611, April 2003.

[167] T. R. Volk, V. I. Pryalkin, and N. M. Rubinina. Optical-damage-resistant linbo3:zn crystal. Opt. Lett., 15(18):996–998, Sep 1990.

[168] Yu. N. Korkishko, V. A. Fedorov, M. P. De Micheli, P. Baldi, K. El Hadi, and A. Leycuras. Relationships between structural and optical properties of proton-exchanged waveguides on z-cut lithium niobate. Appl. Opt., 35(36):7056–7060, Dec 1996.

[169] C. Canali, A. Carnera, G. Della Mea, P. Mazzoldi, S. M. Al Shukri, A. C. G. Nutt, and R. M. De La Rue. Structural characterization of proton exchanged linbo3 optical waveguides. Journal of Applied Physics, 59(8):2643–2649, 1986.

[170] P. G. Suchoski, T. K. Findakly, and F. J. Leonberger. Stable low-loss proton-exchanged linbo3 waveguide devices with no electro-optic degradation. Opt. Lett., 13(11):1050–1052, Nov 1988.

[171] L. Chanvillard, P. AschiÃ©ri, P. Baldi, D. B. Ostrowsky, M. de Micheli, L. Huang, and D. J. Bamford. Soft proton exchange on periodically poled linbo3: A simple waveguide fabrication process for highly efficient nonlinear interactions. Applied Physics Letters, 76(9):1089–1091, 2000.

[172] K. R. Parameswaran, R. K. Route, J. R. Kurz, R. V. Roussev, M. M. Fejer, and M. Fujimura. Highly efficient second-harmonic generation in buried waveguides formed by annealed and reverse proton exchange in periodically poled lithium niobate. Opt. Lett., 27(3):179–181, February 2002.

[173] N. L. Thomas-Peter, B. J. Smith, D. Kundys, P. G. Smith, and I. A. Walmsley. Phase-controlled photonic quantum circuits in laser written integrated optics. In Quantum Electronics and Laser Science Conference, page QThG2. Optical Society of America, 2010.

[174] A. Martin, O. Alibart, J.-C. Flesch, J. Samuel, Supurna Sinha, S. Tanzilli, and A. Kastberg. Non-local geometric phase in two-photon interferometry. EPL (Europhysics Letters), 97(1):10003, 2012.

[175] H. Jin, F. M. Liu, P. Xu, J. L. Xia, M. L. Zhong, Y. Yuan, J. W. Zhou, Y. X. Gong, W. Wang, and S. N. Zhu. On-chip generation and manipulation of entangled photons based on reconfigurable lithium-niobate waveguide circuits. Phys. Rev. Lett., 113:103601, Sep 2014.

[176] J. W. Silverstone, D. Bonneau, K. Ohira, N. Suzuki, H. Yoshida, N. Iizuka, M. Ezaki, C. M. Natarajan, M. G. Tanner, R. H. Hadfield, V. Zwiller, G. D. Marshall, J. G. Rarity, J. L. O'Brien, and M. G. Thompson. On-chip quantum interference between silicon photon-pair sources. Nat Photon, 8(2):104–108, February 2014.

[177] B. Stern, X. Zhu, C. P. Chen, L. D. Tzuang, J. Cardenas, K. Bergman, and M. Lipson. On-chip mode-division multiplexing switch. Optica, 2(6):530–535, Jun 2015.

[178] S. E. Harris. Proposed backward wave oscillation in the infrared. Applied Physics Letters, 9(3):114–116, 1966.

[179] M. M. Fejer, G. A. Magel, D. H. Jundt, and R. L. Byer. Quasi-phase-matched second harmonic generation: tuning and tolerances. IEEE Journal of Quantum Electronics, 28(11):2631 –2654, November 1992.

[180] A. Christ, A. Eckstein, P. J. Mosley, and C. Silberhorn. Pure single photon generation by type-i PDC with backward-wave amplification. Optics Express, 17(5):3441–3446, March 2009.

[181] M. Yamada, N. Nada, M. Saitoh, and K. Watanabe. First-order quasi-phase matched LiNbO3 waveguide periodically poled by applying an external field for efficient blue second-harmonic generation. Applied Physics Letters, 62(5):435–436, February 1993.

[182] W. K. Burns, W. McElhanon, and L. Goldberg. Second harmonic generation in field poled, quasi-phase-matched, bulk linbo/sub 3/. Photonics Technology Letters, IEEE, 6(2):252–254, Feb 1994.

[183] J. Webjorn, V. Pruneri, P.S.J. Russell, J.R.M. Barr, and D.C. Hanna. Quasi-phase-matched blue light generation in bulk lithium niobate, electrically poled via periodic liquid electrodes. Electronics Letters, 30(11):894–895, May 1994.

[184] L. E. Myers, R. C. Eckardt, M. M. Fejer, R. L. Byer, W. R. Bosenberg, and J. W. Pierce. Quasi-phase-matched optical parametric oscillators in bulk periodically poled linbo3. J. Opt. Soc. Am. B, 12(11):2102–2116, Nov 1995.

[185] G. D. Miller. Periodically poled lithium niobate: modeling, fabrication, and nonlinear-optical performance. PhD thesis, University of Stanford, 1998.

[186] E. J. Murphy, T. Rice, L. McCaughan, G. T. Harvey, and P.J. Read. Permanent attachment of single-mode fiber arrays to waveguides. Lightwave Technology, Journal of, 3(4):795–799, Aug 1985.

[187] K.-Y. Lee, C.-J. Hsieh, J.-R. Sze, and G.-J. Jaw. Optimal direct coupling from single-mode fibers to ti:linbo3, channel waveguides. Fiber and Integrated Optics, 15(4):365–371, 1996.

[188] Homepage Corning Inc. Smf-28e+ optical fiber product specification sheet, 2015.

[189] W. Karthe and R. Müller. Integrierte Optik. Akademische Verlagsgesellschaft Geest & Portig K.-G., 1991.

[190] R. Nouroozi. All optical wavelength conversion and parametric amplification in Ti:PPLN channel waveguides for telecommunication applications. PhD thesis, University of Paderborn, 2010.

[191] L. Zhang, C. Silberhorn, and I. A. Walmsley. Secure quantum key distribution using continuous variables of single photons. Phys. Rev. Lett., 100:110504, March 2008.

[192] F. Pignatiello, M. De Rosa, P. Ferraro, S. Grilli, P. De Natale, A. Arie, and S. De Nicola. Measurement of the thermal expansion coefficients of ferroelectric crystals by a moire interferometer. Optics Communications, 277(1):14 – 18, 2007.

[193] M. Avenhaus, A. Eckstein, P.J. Mosley, and C. Silberhorn. Fiber-assisted single-photon spectrograph. Opt. Lett., 34(18):2873–2875, September 2009.

[194] G. Harder. Private communication, 2013.

[195] E. Knill, R. Laflamme, and G. J. Milburn. A scheme for efficient quantum computation with linear optics. Nature, 409(6816):46–52, January 2001.

[196] N. J. Cerf, C. Adami, and P. G. Kwiat. Optical simulation of quantum logic. Phys. Rev. A, 57:R1477–R1480, Mar 1998.

[197] J. F. Clauser and J. P. Dowling. Factoring integers with young's N -slit interferometer. Phys. Rev. A, 53:4587–4590, Jun 1996.

[198] P. G. Kwiat, J. R. Mitchell, P. D. D. Schwindt, and A. G. White. Grover's search algorithm: An optical approach. Journal of Modern Optics, 47(2-3):257–266, 2000.

[199] T. B. Pittman, B. C. Jacobs, and J. D. Franson. Single photons on pseudodemand from stored parametric down-conversion. Physical Review A, 66(4):042303, October 2002.

[200] D. N. Klyshko. Use of two-photon light for absolute calibration of photoelectric detectors. Soviet Journal of Quantum Electronics, 10(9):1112, 1980.

[201] P. Grangier, G. Roger, and A. Aspect. Experimental evidence for a photon anticorrelation effect on a beam splitter: A new light on single-photon interferences. EPL (Europhysics Letters), 1(4):173, 1986.

[202] J. F. Clauser. Experimental distinction between the quantum and classical field-theoretic predictions for the photoelectric effect. Phys. Rev. D, 9:853–860, February 1974.

[203] A. B. U'Ren, C. Silberhorn, J. L. Ball, K. Banaszek, and I. A. Walmsley. Characterization of the nonclassical nature of conditionally prepared single photons. Physical Review A, 72(2):021802, 2005.

[204] W. Mauerer. On Colours, Keys, and Correlations: Multimode Parametric Downconversion in the Photon Number Basis. PhD thesis, Universitat Erlangen-Nurnberg, Universitatsstrasse. 4, 91054 Erlangen, Germany, 2008.

[205] W. Mauerer, M. Avenhaus, W. Helwig, and C. Silberhorn. How colors influence numbers: Photon statistics of parametric down-conversion. Phys. Rev. A, 80:053815, November 2009.

[206] S. Fasel, O. Alibart, S. Tanzilli, P. Baldi, A. Beveratos, A. Gisin, and H. Zbinden. High-quality asynchronous heralded single-photon source at telecom wavelength. New Journal of Physics, 6(1):163, 2004.

[207] G. Brida, I. P. Degiovanni, M. Genovese, A. Migdall, F. Piacentini, S. V. Polyakov, and I. Ruo Berchera. Experimental realization of a low-noise heralded single-photon source. Opt. Express, 19(2):1484–1492, January 2011.

[208] G. Brida, I. P. Degiovanni, M. Genovese, F. Piacentini, P. Traina, A. Della Frera, A. Tosi, A. Bahgat Shehata, C. Scarcella, A. Gulinatti, M. Ghioni, S. V. Polyakov, A. Migdall, and A. Giudice. An extremely low-noise heralded single-photon source: A breakthrough for quantum technologies. Applied Physics Letters, 101(22):221112, 2012.

[209] H. B. Coldenstrodt-Ronge and C. Silberhorn. Avalanche photo-detection for high data rate applications. Journal of Physics B: Atomic, Molecular and Optical Physics, 40(19):3909, 2007.

[210] F. Steinlechner, M. Gilaberte, M. Jofre, T. Scheidl, J. P. Torres, V. Pruneri, and R. Ursin. Efficient heralding of polarization-entangled photons from type-0 and type-ii spontaneous parametric downconversion in periodically poled ktiopo4. J. Opt. Soc. Am. B, 31(9):2068–2076, Sep 2014.

[211] P. J. Mosley, J. S. Lundeen, B. J. Smith, P. Wasylczyk, A. B. U'Ren, C. Silberhorn, and I. A. Walmsley. Heralded generation of ultrafast single photons in pure quantum states. Phys. Rev. Lett., 100:133601, April 2008.

[212] C. Söller, O. Cohen, B. J. Smith, I. A. Walmsley, and C. Silberhorn. High-performance single-photon generation with commercial-grade optical fiber. Phys. Rev. A, 83:031806, March 2011.

[213] F. Steinlechner, P. Trojek, M. Jofre, H. Weier, D. Perez, T. Jennewein, R. Ursin, J. Rarity, M. W. Mitchell, J. P. Torres, H. Weinfurter, and V. Pruneri. A high-brightness source of polarization-entangled photons optimized for applications in free space. Opt. Express, 20(9):9640–9649, April 2012.

[214] J. B. Spring, P. S. Salter, B. J. Metcalf, P. C. Humphreys, M. Moore, N. Thomas-Peter, M. Barbieri, X.-M. Jin, N. K. Langford, W. S. Kolthammer, M. J. Booth, and I. A. Walmsley. On-chip low loss heralded source of pure single photons. Opt. Express, 21(11):13522–13532, Jun 2013.

[215] S. Ramelow, A. Mech, M. Giustina, S. Gröblacher, W. Wieczorek, J. Beyer, A. Lita, B. Calkins, T. Gerrits, S. W. Nam, A. Zeilinger, and R. Ursin. Highly efficient heralding of entangled single photons. Opt. Express, 21(6):6707–6717, Mar 2013.

[216] F. Hargart, C. A. Kessler, T. Schwarzböck, E. Koroknay, S. Weidenfeld, M. Jetter, and P. Michler. Electrically driven quantum dot single-photon source at 2 ghz excitation repetition rate with ultra-low emission time jitter. Applied Physics Letters, 102(1):–, 2013.

[217] T. Schröder, F. Gädeke, M. J. Banholzer, and O. Benson. Ultrabright and efficient single-photon generation based on nitrogen-vacancy centres in nanodiamonds on a solid immersion lens. New Journal of Physics, 13(5):055017, 2011.

[218] A. E. Lita, A. J. Miller, and S. W. Nam. Counting near-infrared single-photons with 95% efficiency. Opt. Express, 16(5):3032–3040, Mar 2008.

[219] T. Gerrits, N. Thomas-Peter, J. C. Gates, A. E. Lita, B. J. Metcalf, B. Calkins, N. A. Tomlin, A. E. Fox, A. Lamas-Linares, J. B. Spring, N. K. Langford, R. P. Mirin, P. G. R. Smith, I. A. Walmsley, and S. W. Nam. On-chip, photon-number-resolving, telecommunication-band detectors for scalable photonic information processing. Phys. Rev. A, 84:060301, Dec 2011.

[220] V. B. Verma, B. Korzh, F. Bussières, R. D. Horansky, S. D. Dyer, A. E. Lita, I. Vayshenker, F. Marsili, M. D. Shaw, H. Zbinden, R. P. Mirin, and S. W. Nam. High-efficiency superconducting nanowire single-photon detectors fabricated from mosi thin-films. ArXiv e-prints, April 2015.

[221] M. A. Broome, M. P. Almeida, A. Fedrizzi, and A. G. White. Reducing multiphoton rates in pulsed down-conversion by temporal multiplexing. Optics Express, 19(23):22698–22708, November 2011.

[222] G. S. Vernam. Secret signaling system, July 1922.

[223] D. Gottesman, H.-K. Lo, N. Lütkenhaus, and J. Preskill. Security of quantum key distribution with imperfect devices. Quantum Information & Computation, 4(5):325–360, 2004.

[224] A. Niederberger, V. Scarani, and N. Gisin. Photon-number-splitting versus cloning attacks in practical implementations of the bennett-brassard 1984 protocol for quantum cryptography. Phys. Rev. A, 71:042316, April 2005.

[225] V. Makarov and D. R. Hjelme. Faked states attack on quantum cryptosystems. Journal of Modern Optics, 52(5):691–705, 2005.

[226] V. Makarov, A. Anisimov, and J. Skaar. Effects of detector efficiency mismatch on security of quantum cryptosystems. Phys. Rev. A, 74:022313, August 2006.

[227] C.-H. F. Fung, B. Qi, K. Tamaki, and H.-K. Lo. Phase-remapping attack in practical quantum-key-distribution systems. Phys. Rev. A, 75:032314, March 2007.

[228] B. Qi, C.-H. F. Fung, H.-K. Lo, and X. Ma. Time-shift attack in practical quantum cryptosystems. Quantum Info. Comput., 7(1):73–82, January 2007.

[229] A. Lamas-Linares and C. Kurtsiefer. Breaking a quantum key distribution system through a timing side channel. Opt. Express, 15(15):9388–9393, July 2007.

[230] L. Lydersen, C. Wiechers, C. Wittmann, D. Elser, J. Skaar, and V. Makarov. Hacking commercial quantum cryptography systems by tailored bright illumination. Nature Photonics, 4(10):686–689, October 2010.

[231] F. Xu, B. Qi, and H.-K. Lo. Experimental demonstration of phase-remapping attack in a practical quantum key distribution system. New Journal of Physics, 12(11):113026, November 2010.

[232] Z. Peng and L. Chao. Feasibility of double-click attack on a passive detection quantum key distribution system. Chinese Physics Letters, 28(7):070304, 2011.

[233] H.-W. Li, S. Wang, J.-Z. Huang, W. Chen, Z.-Q. Yin, F.-Y. Li, Z. Zhou, D. Liu, Y. Zhang, G.-C. Guo, W.-S. Bao, and Z.-F. Han. Attacking a practical quantum-key-distribution system with wavelength-dependent beamsplitter and multiwavelength sources. Phys. Rev. A, 84:062308, Dec 2011.

[234] S. Zhang, J. Wang, and C.-J. Tang. Improved fake-state attack to the quantum key distribution systems. International Journal of Theoretical Physics, 51(9):2719–2726, 2012.

[235] M.-S. Jiang, S.-H. Sun, C.-Y. Li, and L.-M. Liang. Wavelength-selected photon-number-splitting attack against plug-and-play quantum key distribution systems with decoy states. Phys. Rev. A, 86:032310, September 2012.

[236] Y.-L. Tang, H.-L. Yin, X. Ma, C.-H. F. Fung, Y. Liu, H.-L. Yong, T.-Y. Chen, C.-Z. Peng, Z.-B. Chen, and J.-W. Pan. Source attack of decoy-state quantum key distribution using phase information. Phys. Rev. A, 88:022308, Aug 2013.

[237] M. G. Tanner, V. Makarov, and R. H. Hadfield. Optimised quantum hacking of superconducting nanowire single-photon detectors. Opt. Express, 22(6):6734–6748, Mar 2014.

[238] A. N. Bugge, S. Sauge, A. M. M. Ghazali, J. Skaar, L. Lydersen, and V. Makarov. Laser damage helps the eavesdropper in quantum cryptography. Phys. Rev. Lett., 112:070503, Feb 2014.

[239] S. Sajeed, P. Chaiwongkhot, J.-P. Bourgoin, T. Jennewein, N. Lütkenhaus, and V. Makarov. Security loophole in free-space quantum key distribution due to spatial-mode detector-efficiency mismatch. Phys. Rev. A, 91:062301, Jun 2015.

[240] S. Sajeed, I. Radchenko, S. Kaiser, J.-P. Bourgoin, A. Pappa, L. Monat, M. Legré, and V. Makarov. Attacks exploiting deviation of mean photon number in quantum key distribution and coin tossing. Phys. Rev. A, 91:032326, Mar 2015.

[241] G. Brassard, N. Lütkenhaus, T. Mor, and B. C. Sanders. Limitations on practical quantum cryptography. Phys. Rev. Lett., 85:1330–1333, August 2000.

[242] H.-K. Lo, X. Ma, and K. Chen. Decoy state quantum key distribution. Phys. Rev. Lett., 94:230504, June 2005.

[243] X.-B. Wang. Beating the photon-number-splitting attack in practical quantum cryptography. Phys. Rev. Lett., 94:230503, June 2005.

[244] W.-Y. Hwang. Quantum key distribution with high loss: Toward global secure communication. Phys. Rev. Lett., 91:057901, August 2003.

[245] D. Achilles, C. Silberhorn, and I. A. Walmsley. Direct, loss-tolerant characterization of nonclassical photon statistics. Physical Review Letters, 97(4):043602, July 2006.

[246] T. Horikiri and T. Kobayashi. Decoy state quantum key distribution with a photon number resolved heralded single photon source. Phys. Rev. A, 73:032331, Mar 2006.

[247] Y. Adachi, T. Yamamoto, M. Koashi, and N. Imoto. Simple and efficient quantum key distribution with parametric down-conversion. Phys. Rev. Lett., 99:180503, Nov 2007.

[248] X. Ma and H.-K. Lo. Quantum key distribution with triggering parametric down-conversion sources. New Journal of Physics, 10(7):073018, July 2008.

[249] M. Curty, X. Ma, B. Qi, and T. Moroder. Passive decoy-state quantum key distribution with practical light sources. Phys. Rev. A, 81:022310, February 2010.

[250] Z.-Q. Yin, H.-W. Li, Y. Yao, C.-M. Zhang, S. Wang, W. Chen, G.-C. Guo, and Z.-F. Han. Counterfactual quantum cryptography based on weak coherent states. Phys. Rev. A, 86:022313, Aug 2012.

[251] D. Achilles, C. Silberhorn, C. Śliwa, K. Banaszek, and I. A. Walmsley. Fiber-assisted detection with photon number resolution. Opt. Lett., 28(23):2387–2389, December 2003.

[252] M. J. Fitch, B. C. Jacobs, T. B. Pittman, and J. D. Franson. Photon-number resolution using time-multiplexed single-photon detectors. Phys. Rev. A, 68:043814, October 2003.

[253] M. Avenhaus, H. B. Coldenstrodt-Ronge, K. Laiho, W. Mauerer, I. A. Walmsley, and C. Silberhorn. Photon number statistics of multimode parametric down-conversion. Phys. Rev. Lett., 101:053601, August 2008.

[254] W. Helwig, W. Mauerer, and C. Silberhorn. Multimode states in decoy-based quantum-key-distribution protocols. Phys. Rev. A, 80:052326, November 2009.

[255] A. Christ, K. Laiho, A. Eckstein, T. Lauckner, P. J. Mosley, and C. Silberhorn. Spatial modes in waveguided parametric down-conversion. Phys. Rev. A, 80:033829, September 2009.

[256] S. Krapick, H. Herrmann, V. Quiring, B. Brecht, H. Suche, and Ch. Silberhorn. An efficient integrated two-color source for heralded single photons. New Journal of Physics, 15(3):033010, 2013.

[257] S. Krapick, M. S. Stefszky, M. Jachura, B. Brecht, M. Avenhaus, and C. Silberhorn. Bright integrated photon-pair source for practical passive decoy-state quantum key distribution. Phys. Rev. A, 89:012329, January 2014.

[258] C. Q. Xu, H. Okayama, K. Shinozaki, K. Watanabe, and M. Kawahara. Wavelength conversions 1.5 μm by difference frequency generation in periodically domain-inverted linbo3 channel waveguides. Applied Physics Letters, 63(9):1170–1172, 1993.

[259] J. Midwinter. Image conversion from 1.6 μm to the visible in lithium niobate. Quantum Electronics, IEEE Journal of, 4(5):319–320, May 1968.

[260] H. de Riedmatten, M. Afzelius, M. U. Staudt, C. Simon, and N. Gisin. A solid-state light-matter interface at the single-photon level. Nature, 456(7223):773–777, December 2008.

[261] K. F. Reim, J. Nunn, V. O. Lorenz, B. J. Sussman, K. C. Lee, N. K. Langford, D. Jaksch, and I. A. Walmsley. Coherent optical memory with ghz bandwidth. In Quantum Electronics and Laser Science Conference, page QWH3. Optical Society of America, 2010.

[262] W. Tittel, M. Afzelius, T. Chaneliere, R.L. Cone, S. Kröll, S.A. Moiseev, and M. Sellars. Photon-echo quantum memory in solid state systems. Laser & Photonics Reviews, 4(2):244–267, 2010.

[263] H. P. Specht, C. Nolleke, A. Reiserer, M. Uphoff, E. Figueroa, S. Ritter, and G. Rempe. A single-atom quantum memory. Nature, 473(7346):190–193, May 2011.

[264] K.-H. Luo, H. Herrmann, S. Krapick, R. Ricken, V. Quiring, H. Suche, W. Sohler, and C. Silberhorn. Two-color narrowband photon pair source with high brightness based on clustering in a monolithic waveguide resonator. ArXiv e-prints, June 2013.

[265] D. Rieländer, K. Kutluer, P. M. Ledingham, M. Gündoğan, J. Fekete, M. Mazzera, and H. de Riedmatten. Quantum storage of heralded single photons in a praseodymium-doped crystal. Phys. Rev. Lett., 112:040504, Jan 2014.

[266] K.-H. Luo, H. Herrmann, S. Krapick, B. Brecht, R. Ricken, V. Quiring, H. Suche, W. Sohler, and C. Silberhorn. Direct generation of genuine single-longitudinal-mode narrowband photon pairs. New Journal of Physics, 17(7):073039, 2015.

[267] Y. H. Min, J. H. Lee, Y. L. Lee, W. Grundkoetter, V. Quiring, and W. Sohler. Tunable all-optical control of wavelength conversion of 5 ps pulses by cascaded sum- and difference frequency generation (csfg/dfg) in a ti:ppln waveguide. In Optical Fiber Communication Conference, page FP4. Optical Society of America, 2003.

[268] R. Nouroozi, H. Suche, A. Hellwig, R. Ricken, V. Quiring, and W. Sohler. Phase control of double-pass cascaded shg/dfg wavelength conversion in ti:ppln channel waveguides. Opt. Express, 18(13):14225–14231, June 2010.

[269] R. Schiek, Y. Baek, G. Krijnen, G. I. Stegeman, I. Baumann, and W. Sohler. All-optical switching in lithium niobate directional couplers with cascaded nonlinearity. Opt. Lett., 21(13):940–942, July 1996.

[270] M. H. Chou, I. Brener, M. M. Fejer, E. E. Chaban, and S. B. Christman. 1.5-um-band wavelength conversion based on cascaded second-order nonlinearity in linbo3 waveguides. Photonics Technology Letters, IEEE, (6):653–655, June 1999.

[271] X. Xie and M. M. Fejer. Cascaded optical parametric generation in reverse-proton-exchange lithium niobate waveguides. J. Opt. Soc. Am. B, 24(3):585–591, March 2007.

[272] H. Hu, R. Nouroozi, R. Ludwig, C. Schmidt-Langhorst, H. Suche, W. Sohler, and C. Schubert. 110 km transmission of 160 Gbit/s RZ-dqpsk signals by midspan polarization-insensitive optical phase conjugation in a ti:ppln waveguide. Opt. Lett., 35(17):2867–2869, September 2010.

[273] G. Porat, Y. Silberberg, A. Arie, and H. Suchowski. Two photon frequency conversion. Opt. Express, 20(4):3613–3619, Feb 2012.

[274] K. Kintaka, M. Fujimura, T. Suhara, and H. Nishihara. Third harmonic generation of nd:yag laser light in periodically poled linbo3 waveguide. Electronics Letters, 33(17):1459–1461, Aug 1997.

[275] J. S. Pelc, Q. Zhang, C. R. Phillips, L. Yu, Y. Yamamoto, and M. M. Fejer. Cascaded frequency upconversion for high-speed single-photon detection at 1.55 um. Opt. Lett., 37(4):476–478, 2012.

[276] OptoElectronic Components Homepage. Super conducting nanowires product overview, 2015.

[277] ID Quantique Homepage. id280 superconducting nanowire product overview, 2015.

[278] Excelitas Technologies Homepage. Spcm-nir product brief, 2015.

[279] J. S. Pelc, C. Langrock, Q. Zhang, and M. M. Fejer. Influence of domain disorder on parametric noise in quasi-phase-matched quantum frequency converters. Opt. Lett., 35(16):2804–2806, Aug 2010.

[280] J. S. Pelc, L. Ma, C. R. Phillips, Q. Zhang, C. Langrock, O. Slattery, X. Tang, and M. M. Fejer. Long-wavelength-pumped upconversion single-photon detector at 1550 nm: performance and noise analysis. Opt. Express, 19(22):21445–21456, Oct 2011.

[281] J. S. Pelc, G.-L. Shentu, Q. Zhang, M. M. Fejer, and Jian-Wei Pan. Upconversion of optical signals with multi-longitudinal-mode pump lasers. Phys. Rev. A, 86:033827, Sep 2012.

[282] Excelitas Technologies Homepage. Spcm-aqrh datasheet, 2015.

[283] ID Quantique Homepage. id230 single photon counting module product overview, 2015.

[284] R. F. Schaufele and M. J. Weber. Raman scattering by lithium niobate. Phys. Rev., 152:705–708, Dec 1966.

[285] C. Langrock, E. Diamanti, R. V. Roussev, Y. Yamamoto, M. M. Fejer, and H. Takesue. Highly efficient single-photon detection at communication wavelengths by use of upconversion in reverse-proton-exchanged periodically poled linbo3 waveguides. Opt. Lett., 30(13):1725–1727, Jul 2005.

[286] A. Lenhard, S. Zaske, and C. Becher. Lock-in detection of single photons after two-step frequency conversion. Opt. Lett., 37(20):4254–4256, Oct 2012.

[287] D. M. Greenberger, M. A. Horne, A. Shimony, and A. Zeilinger. Bell's theorem without inequalities. American Journal of Physics, 58(12):1131–1143, 1990.

[288] D. Bouwmeester, J.-W. Pan, M. Daniell, H. Weinfurter, and A. Zeilinger. Observation of three-photon greenberger-horne-zeilinger entanglement. Phys. Rev. Lett., 82:1345–1349, Feb 1999.

[289] J. S. Bell. On the problem of hidden variables in quantum mechanics. Rev. Mod. Phys., 38:447–452, Jul 1966.

[290] C. Sliwa and K. Banaszek. Conditional preparation of maximal polarization entanglement. Phys. Rev. A, 67:030101, Mar 2003.

[291] S. Barz, G. Cronenberg, A. Zeilinger, and P. Walther. Heralded generation of entangled photon pairs. Nat Photon, 4(8):553–556, August 2010.

[292] T. E. Keller, M. H. Rubin, Y. Shih, and L.-A. Wu. Theory of the three-photon entangled state. Phys. Rev. A, 57:2076–2079, Mar 1998.

[293] T. Guerreiro, A. Martin, B. Sanguinetti, S. Pelc, J. C. Langrock, M. Fejer, M. N. Gisin, H. Zbinden, N. Sangouard, and T. Thew, R.˙ Nonlinear interaction between single photons. Phys. Rev. Lett., 113:173601, Oct 2014.

[294] N. D. Mermin. What's wrong with these elements of reality? Physics Today, 43:9–11, 1990.

[295] N. D. Mermin. Extreme quantum entanglement in a superposition of macroscopically distinct states. Phys. Rev. Lett., 65:1838–1840, Oct 1990.

[296] N. D. Mermin. Quantum mysteries revisited. American Journal of Physics, 58(8):731–734, 1990.

[297] Z. Qin, L. Cao, H. Wang, A. M. Marino, W. Zhang, and J. Jing. Experimental generation of multiple quantum correlated beams from hot rubidium vapor. Phys. Rev. Lett., 113:023602, Jul 2014.

[298] J. Jing, Z. Qin, L. Cao, H. Wang, A. Marino, and W. Zhang. Experimental generation of triple quantum correlated beams from cascaded four-wave mixing processes. In CLEO: 2014, page JTu4A.41. Optical Society of America, 2014.

[299] X. Jia, Z. Yan, Z. Duan, X. Su, H. Wang, C. Xie, and K. Peng. Experimental realization of three-color entanglement at optical fiber communication and atomic storage wavelengths. Phys. Rev. Lett., 109:253604, Dec 2012.

[300] D.-S. Ding, W. Zhang, S. Shi, Z.-Y. Zhou, Y. Li, B.-S. Shi, and G.-C. Guo. Hybrid-cascaded generation of tripartite telecom photons using an atomic ensemble and a nonlinear waveguide. Optica, 2(7):642–645, Jul 2015.

[301] G. S. Agarwal and K. Tara. Nonclassical properties of states generated by the excitations on a coherent state. Phys. Rev. A, 43:492–497, January 1991.

Appendix

APPENDIX A

Refractive indices of lithium niobate

In this section we provide an overview of the Sellmeier coefficients for bulk lithium niobate [137,138], which constitute the dispersion relation for both refractive indices. Note that all coefficients are given unit-less, which implies that the wavelength has to be implemented in micrometer and the temperature in degree Celsius.

Figure A.1 shows the dispersion relation of bulk congruent lithium niobate according to the Sellmeier coefficients given in Tab. A.1. The red curves describe the ordinary refractive index at room temperature (solid) and at 170°C (dashed), while blue curves demonstrate the Sellmeier relation of the extraordinary refractive index. Note that the increasing gap between both index types at infrared wavelengths is owed to the different mathematical models behind.

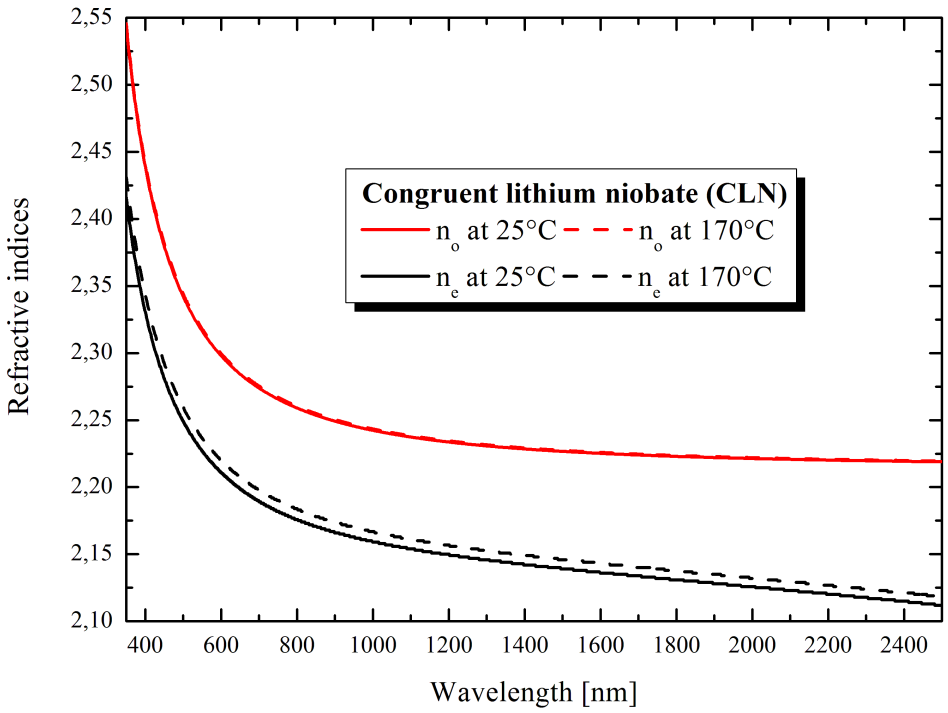

Figure A.1.: Refractive index dispersion of bulk congruent lithium niobate at room temperature (solid lines) and 170°C (dashed lines).

Table A.1.: Sellmeier coefficients for bulk lithium niobate.

ordinary		**extraordinary**	
Sellmeier coefficient	**value**	**Sellmeier coefficient**	**value**
$A_{1,o}$	4.9048	$A_{1,e}$	5.35583
$A_{2,o}$	0.11775	$A_{2,e}$	0.100473
$A_{3,o}$	0.21802	$A_{3,e}$	0.20692
$A_{4,o}$	0.027153	$A_{4,e}$	100.0000
		$A_{5,e}$	11.3493
		$A_{6,e}$	$1.5334 \cdot 10^{-2}$
$B_{1,o}$	$2.2314 \cdot 10^{-8}$	$B_{1,e}$	$4.6390 \cdot 10^{-7}$
$B_{2,o}$	$-2.9671 \cdot 10^{-8}$	$B_{2,e}$	$3.8620 \cdot 10^{-8}$
$B_{3,o}$	$2.1429 \cdot 10^{-8}$	$B_{3,e}$	$-8.9000 \cdot 10^{-9}$
		$B_{4,e}$	$2.6570 \cdot 10^{-5}$

APPENDIX B

Brief derivation of Electro-optical tensor entries

The wavelength dependent nonlinear optical coefficient $\bar{\bar{d}}(\lambda)$ in general constitutes of 27 independent entries. It can be reduced to a 3×6 matrix with 18 elements by the Einstein summation convention $d_{ijk} = d_{ikj}$, when taking the crystal structure and the Kleinman symmetry [Kleinman] properties of lithium niobate into account. If we assume the nonlinear susceptibility to be independent of the wavelength, the number of independent tensor elements is further reduced to 10 entries, and we end up with the following representation in a contracted matrix notation, where $d_{ijk} = d_{ikj}$:

$$d_{il,\mathrm{LiNbO_3}} = \begin{pmatrix} 0 & 0 & 0 & 0 & d_{31} & -d_{22} \\ -d_{22} & d_{22} & 0 & d_{31} & 0 & 0 \\ d_{31} & d_{31} & d_{33} & 0 & 0 & 0 \end{pmatrix}. \tag{B.1}$$

Herein, the indices were replaced according to the following rules [Boyd]:

$$d_{il,\mathrm{LiNbO_3}} = \begin{pmatrix} jk, kj: & 11 & 22 & 33 & 23, 32 & 31, 13 & 12, 21 \\ l: & 1 & 2 & 3 & 4 & 5 & 6 \end{pmatrix}. \tag{B.2}$$

APPENDIX C

Overview of the device design parameters

Here, we summarize the parameters for the design of our monolithic cascaded parametric down-conversion source in Tab. C.1. The choice of parameters is based on the detailed explanation in Sec. 4.4, and they match the parameters theoretically derived in the literature [111].

Table C.1.: Parameter settings for the device design.

device design parameter	**nominal value**	**remarks**
Ti thickness t_{Ti}	80 nm	got 76 nm
Ti stripe width w_{Ti}	7.0 μm	got 7.0 ± 0.1 μm
		tapered to 3.0 μm
# of coupled WG pairs	42	+7 test WGs
# of waveguide groups	7	3 pairs + test WG
S-bend bending radius R_{B}	160 mm	for low loss
WG separation	13.0 μm (coupler region)	13.0 ∓ 0.0 μm
	127.0 μm (input/output)	127.0 ∓ 0.0 μm
coupler stem length L_{C}	$2750 \leq L_{\mathrm{C}} \leq 4250$ μm	$\Delta L_{\mathrm{C}} = 250$ μm
poled waveguide length	30 mm	each poling
1$^{\mathrm{st}}$ poling period $\Lambda_{\mathrm{G},1}$	$6.71 \leq \Lambda_{\mathrm{G},1} \leq 6.91$ μm	$\Delta\Lambda_{\mathrm{G},1} = 0.04$ μm
1$^{\mathrm{st}}$ poling duty-cycle	72/28 (mask)	$50/50 \pm 5\%$ (chip)
2$^{\mathrm{nd}}$ poling period $\Lambda_{\mathrm{G},2}$	$17.45 \leq \Lambda_{\mathrm{G},2} \leq 18.27$ μm	$\Delta\Lambda_{\mathrm{G},2} = 0.02$ μm
2$^{\mathrm{nd}}$ poling duty-cycle	67/33 (mask)	$50/50 \pm 5\%$ (chip)

APPENDIX D

Propagation constant mismatch model

From our model we derived exponential dependencies of the propagation constant differences $\Delta\beta\left(d(z),\lambda\right)$ on the center-to-center separation in coupled waveguide structures and on the chosen wavelength. For the modeling we applied the design parameters given in Appendix C above. By fitting curves of the form

$$\Delta\beta\left(d(z),\lambda\right) = A\left(\lambda\right) + e^{-\frac{d(z)}{B(\lambda)}} \tag{D.1}$$

we infer the two parameters as summarized in Tab. D.1

Table D.1.: Fit parameters for the coupler modeling.

wavelength [nm]	**polarization**	$A\left(\lambda\right)$ [m^{-1}]	$B\left(\lambda\right)$ [μm]
532	TM	$1.415600 \cdot 10^{13}$	0.36367
	TE	$6.502656 \cdot 10^{10}$	0.51187
790	TM	$1.127139 \cdot 10^{9}$	0.66363
	TE	$2.060349 \cdot 10^{7}$	1.04293
1550	TM	$5.633821 \cdot 10^{5}$	1.94182
	TE	$6.078484 \cdot 10^{4}$	3.27898
1575	TM	$4.035683 \cdot 10^{5}$	2.00335
	TE	$5.554472 \cdot 10^{4}$	3.37811
1600	TM	$3.527679 \cdot 10^{5}$	2.06667
	TE	$5.093461 \cdot 10^{4}$	3.47866
1625	TM	$3.094686 \cdot 10^{5}$	2.13184
	TE	$4.686464 \cdot 10^{4}$	3.58056

APPENDIX E

Common versus laser triggered coincidence measurements

In this appendix, we give provide a brief comparison of measurements on Klyshko efficiencies and PDC conversion probabilities. Specifically, we perform measurements with and without taking the electronic laser trigger for the direct pumping of our secondary PDC process into account. If the laser trigger is included to the coincidence measurements, we can reduce the singles and also the coincidence detection time windows to a minimum width in the time-tagging module, where the vast majority of randomly distributed noise events is excluded from. Thus, the remaining detection events reflect the true rates and inferred probabilities more precise than without laser triggering. In Fig. E.1 we show this effect. While for the common measurements without laser triggering there is a significant decrease of the Klyshko efficiencies at low pump powers, we reduce the impact significantly with laser triggering. Due to the decreased single count rates (most noise counts are missing), our absolute Klyshko efficiencies are increased. Consequently, the internal PDC conversion probability per pump photon decreases in comparison to the non-triggered measurements, because the coincidence rates remain almost constant for both types of analysis.

We also calculate the differences in the individual singles-detection rates for both types of measurements. Subtracting the laser-triggered count rates from the non-triggered ones provides us with the pump-power dependent graph shown in Fig. E.2. Our expectations for after-pulsing-free detectors would lead to constant count-rate differences at the noise count level of the individual detector. However, we notice a significant increase of the signal 1 count rate difference with increasing pump powers, while the y-axis offset is equal to the noise count rate of the InGaAs-APD.

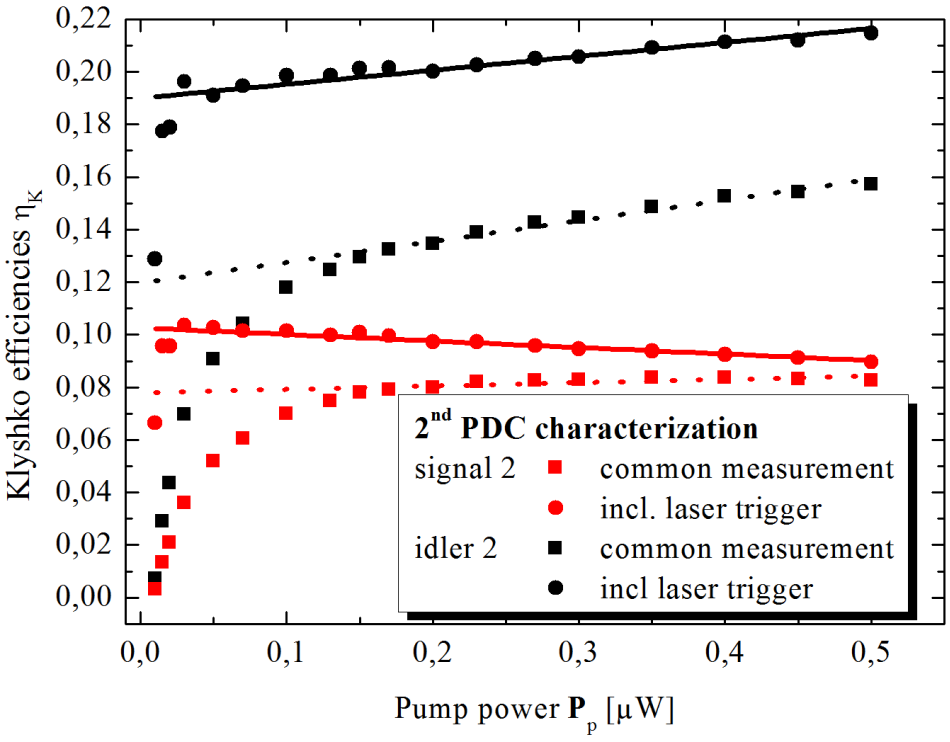

Figure E.1.: The comparison of the Klyshko efficiencies for the secondary PDC process underlines the positive effect of including the electronic laser trigger to the singles and coincidences measurements. While for common measurements the influence of noise counts is very much pronounced at low pump powers, the Klyshko efficiencies have strongly decreased values. With laser triggering, this effect is significantly reduced even at very low pump powers. We conclude that laser triggering leads to measured Klyshko efficiencies, which reflect the true values for η_{s2}^{tot} and η_{i2}^{tot} much better than the common method without. Only in pulsed PDC we can benefit from this effect.

For the idler 2 single detection-rate difference we register a significantly shallower increase with higher pump powers as compared to the signal 2 arm. Again, the y-axis offset of the curve is equivalent to the noise count rate of the SNSPD detector.

We explain the differences of the singles-detection behavior with the two different detector technologies: although InGaAs-based avalanche photo-diodes are usually quenched after detection (actively or passively), they show significant after-pulsing probabilities at low operation temperatures. This is intrinsic to the semiconductor material and requires additional dead times in the order of $\tau_{dead} \approx 20\,\mu s$. Suppressing the detection for durations longer than the repetition times of the pulsed system to investigate leads to saturation effects for our 10 MHz-pulsed experimental setup. The saturation effect also explains the dissimilarities between the pump power de-

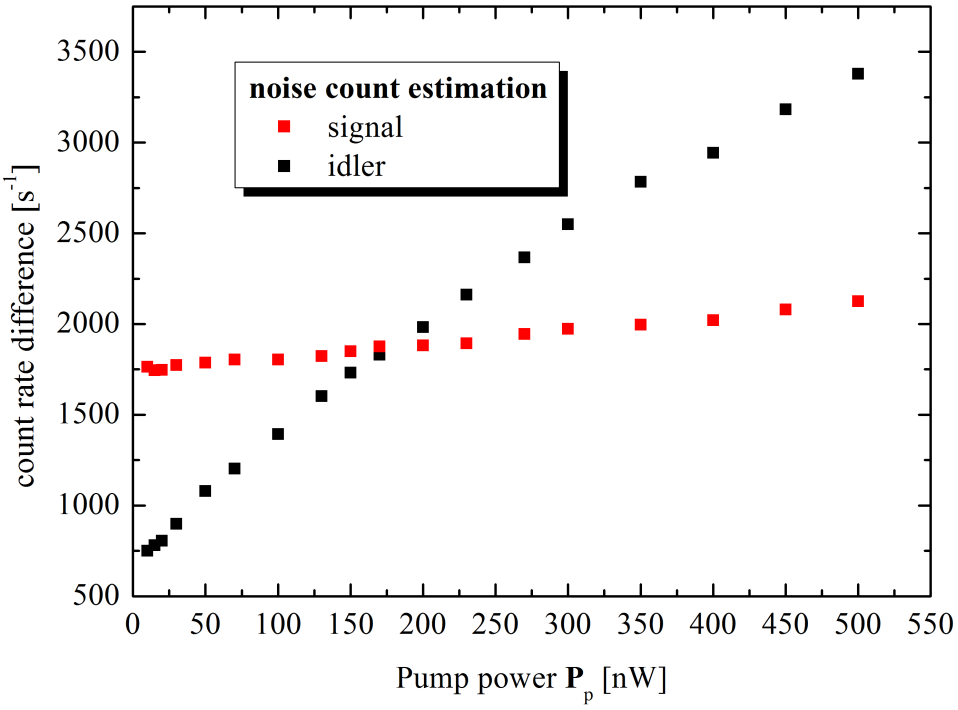

Figure E.2.: The difference of single count rates, deduced from the two different types of coincidence measurements, is plotted for both secondary detectors dependent on the pump power. We see that the y-axis offsets correspond to individual noise count rates of the detectors. The InGaAs-based avalanche photo-diode shows a significant increase of the count rate difference, which is dedicated to the intrinsic afterpulsing tendency of this kind of detector technology.

pendent Klyshko efficiency behavior shown in Fig. 7.14 and 7.15: only the idler 2 arm shows a decreasing Klyshko efficiency, because the detected signal 2 rates are lower than what we could expect at higher pump powers.

Contrarily, our superconducting nanowire detectors show practically no afterpulsing and very short recovery times of the order of $\tau_{\mathrm{rec}} \approx 60\,\mathrm{ns}$. This allows for saturation-free detection with the pulse repetition rates used in this thesis. We assume that the slight increase of the singles-rate difference stems from parasitic fluorescence, induced to the implemented silicon filter by the residual pump light.

Despite the dead time of $20\,\mu\mathrm{s}$ in our experiments, the InGaAs-APD exhibits obviously significant after-pulsing, which we deduce from the graph in Fig. E.2. This means the more photons impinge at the signal 2 detector, the larger the contributions of afterpulses to the absolute count rates, but it also means that saturation effects become significant even at lower pump powers.

APPENDIX F

List of Publications

Main publications

The following work has been published or prepared for publication during the conception of this thesis. The scientific content of this thesis is partially inherent to the publications.

- **On-chip generation of genuine photon triplet states**
  Stephan Krapick, Benjamin Brecht, Harald Herrmann, Viktor Quiring, and Christine Silberhorn
  in preparation

- **Analysis of photon triplet generation in pulsed cascaded parametric down-conversion sources**
  Stephan Krapick and Christine Silberhorn
  submitted

- **Bright Integrated Photon-Pair Source for Practical Passive Decoy State Quantum Key Distribution**
  Stephan Krapick, Michael Stefszky, Michal Jachura, Benjamin Brecht, Malte Avenhaus, and Christine Silberhorn
  Physical Review A 89, 012329 (2014)

- **An Efficient Integrated Two-Color Source for Heralded Single Photons**
  Stephan Krapick, Harald Herrmann, Viktor Quiring, Benjamin Brecht, Hubertus Suche, and Christine Silberhorn
  New Journal of Physics 15, 033010 (2013)

Author Contributions

The author has contributed to the following works during his doctoral studies, but these are not the focus of this thesis.

- **Direct generation of genuine single-longitudinal-mode narrowband photon pairs**
  Kai-Hong Luo, Harald Herrmann, Stephan Krapick, Benjamin Brecht, Raimund Ricken, Viktor Quiring, Hubertus Suche, Wolfgang Sohler, and Christine Silberhorn
  New Journal of Physics 17, 073039 (2015)

- **Liquid-nitrogen cooled, free-running single-photon sensitive detector at telecommunication wavelengths**
  Matthias Covi, Benedikt Pressl, Thomas Günthner, Kaisa Laiho, Stephan Krapick, Christine Silberhorn, and Gregor Weihs
  Applied Physics B 118, 489-495 (2015)

- **Two-color narrowband photon pair source with high brightness based on clustering in a monolithic waveguide resonator**
  Kai-Hong Luo, Harald Herrmann, Stephan Krapick, Raimund Ricken, Viktor Quiring, Hubertus Suche, Wolfgang Sohler, and Christine Silberhorn
  arXiv:1306.1756 (2014)

APPENDIX G

List of acronyms

AOM acousto-optic modulator

APD avalanche photo-diode

APE annealed proton exchange

AR anti-reflective

ASE amplified spontaneous emission

BD beam dump

BPF band-pass filter

CAR coincidences-to-accidentals ratio

CHSH Clauser-Horne-Shimony-Holt

CLN congruent lithium niobate

cSFG/SFG cascaded SFG/SFG

cSHG/SFG cascaded SHG/SFG

cw continuous-wave

CWDM coarse wavelength division multiplexer

DCM dichroic mirror

DFG difference-frequency generation

ECL external cavity laser

EDFA erbium-doped fiber-amplifier

EIM effective index method

EOM electro-optic modulator

FC fiber coupling stage

FEM finite element method

FPGA field-programmable gate array

FR free-running

FR-APD free-running avalanche photo-diode

FUC frequency up-conversion

FWHM full width at half maximum

GHZ Greenberger-Horne-Zeilinger states

HBT Hanbury Brown-Twiss

HR high-reflective

HWHM half-width at half maximum

HWP half-wave plate

InGaAs-APD indium-gallium-arsenide avalanche photo-diode

IR infrared

KTP potassium titanyl phosphate

LN lithium niobate

LPF long-pass filter

MMF multi-mode fiber

Nd:YAG neodymium-doped yttrium aluminum garnet

NIR near-infrared

NMP 1-Methyl-2-pyrrolidone

ONF optical noise factor

OPA optical parametric amplification

PDC parametric down-conversion

PE proton exchange

PPLN periodically poled lithium niobate

PM power-meter

PNS photon-number-splitting attack

PR photo-resist

QBER quantum bit error rate

QIP quantum information processing

QKD quantum key distribution

QPM quasi-phase-matching

QWP quarter-wave plate

RGxyz home-coated colorglass filter

RI refractive index

RPE reverse proton exchange

SAW surface acoustic wave

SFG sum-frequency generation

SFWM spontaneous four-wave mixing

SHG second-harmonic generation

Si-APD silicon avalanche photo-diode

SiF silicon filter

SMF single-mode fiber

SNR signal-to-noise-ratio

SNSPD superconducting nanowire single-photon detector

SPE soft proton exchange

SPF short-pass filter

SPUC single-photon up-conversion

TC temperature controller

TDC time-to-digital converter

TE transverse electric

THG third-harmonic generation

Ti:LN titanium-diffused lithium niobate

Ti:PPLN titanium-diffused periodically poled lithium niobate

TM transverse magnetic

TMD time-multiplexed detector

TTM time-tagging module

UV ultra-violet

VAtt variable attenuator

WDM wavelength division multiplexer

WG waveguide

List of Figures

List of Tables